CORNEOCYTES AS POTENTIAL BIOMARKERS OF SKIN INTEGRITY

by

ANA SOFIA MARQUES MENDES ÉVORA

A thesis submitted to the University of Birmingham for the degree of

DOCTOR OF PHILOSOPHY

School of Chemical Engineering
College of Engineering and Physical Sciences
University of Birmingham
June 2023

To my parents,
António and Lúcia

ABSTRACT

A healthy skin barrier is crucial for protecting against environmental threats and maintaining skin health. Pressure ulcers (PUs) remain a prevalent issue in European hospitals (around 11% incidence). This thesis investigates the role of the stratum corneum (SC) and corneocytes in early skin damage and PU development.

To accurately measure corneocyte mechanical properties, a meticulous protocol using Atomic Force Microscopy nanoindentation was developed. Corneocytes exhibited Young's moduli (~0.4–1.5 GPa) similar to glassy organic polymers and, at stresses greater than the yield value, they displayed viscoplastic behaviour describable by the Herschel-Bulkley model. Immersed in water, corneocytes swelled, becoming more compliant (~2 MPa), less rigid, and more strain-tolerant. In-depth analysis of corneocytes from different anatomical sites revealed variations in topography, cornified envelope (CE) maturity, and corneodesmosome distribution, indirectly assessed through desmoglein-1 staining (Dsg1). Corneocytes from the volar forearm, neck, and sacrum had similar topographies, CE maturity (17–20%), and Dsg1 expression (18–24%). Cheek cells presented circular nano-objects and increased Dsg1 levels (46%). Medial heel cells displayed villi-like structures, along with high levels of immature CEs (48%) and Dsg1 (68%). The cell stiffness showed significant inter-subject variability, correlating with the level of immature CEs at the cheek, neck, and sacrum.

Two cohort studies investigated corneocyte properties in the context of skin integrity: in respirator usage among healthcare professionals during the COVID-19 pandemic and in category I PUs. The first study linked elevated levels of immature CEs to self-reported adverse reactions. The second study observed differences in cell topography, immature CEs, and corneodesmosome distribution in category I PUs, indicating the presence of immature SC markers even in early skin damage. Although no significant variations in Young’s modulus were found, corneocytes from elderly patients tended to be more compliant than those from young individuals (patient cells: ~0.05–0.60 GPa).

Together, these findings contribute to our understanding of the properties of corneocyte and skin mechanical and barrier functions and are the first step in investigating the potential of using superficial skin cells as prediction and/or diagnostic markers for early skin damage.

ACKNOWLEDGMENTS

First and foremost, I owe a special thanks to my supervisors **Prof Mike Adams** and **Prof Zhibing Zhang** and to the STINTS project manager, **Dr Simon Johnson**, who have put a great deal of time into advising me and have made themselves available with little or no notice. They regarded me as a valuable member of their team, to whom I am extremely grateful. Their scientific integrity and honesty revived my hope in Science and helped me grow as a person and a professional. Thank you for always giving me the room to grow and the freedom to test my own ideas, and for always giving me your honest feedback. I also thank **Dr Pete Worsley** for all his kindness and support.

A word of gratitude to the late **Emeritus Professor Dan Bader**, who loved science with passion. His enthusiasm will stay with me.

To the **STINTS** colleagues and consortium, I want to say thank you for all the meetings, collaborations, interesting discussions, conferences, and socials. With you, even if for most of the time far away, I felt there was a community I belonged to. To **Dr Nicola Piasentin**, thank you for being the best pen-pal friend I could have asked for!

I would also like to express my gratitude to my **friends on campus**. Wanting it or not, the UK is the best example of what Europe means: a home in the middle of strange languages, a community of very different individuals with very different tastes, beliefs, and journeys, but with the same drive: to live more and to live better. To my international friends I say farewell, not goodbye.

To **my life-long friends** I say thank you for giving me the strength to never quit and reminding me that we are always the same, even when we change.

To **my family**, some words in my native tongue. Obrigada. Por sempre me terem ensinado a persistir, a enfrentar os obstáculos de frente, a partir mesmo quando a vontade era ficar. Esta tese é vossa.

Lastly, I want to express my heartfelt thank you to **Dr Ioannis Kiratzis**. Your support, your kindness, your patience, and love helped me through all the stressful times. Your kind smile did the rest. Ευχαριστώ.

TABLE OF CONTENTS

LIST OF FIGURES

LIST OF TABLES

LIST OF ABBREVIATIONS

AFM	Atomic force microscopy
ATR-FTIR	Attenuated total reflection Fourier transform infrared
BMI	Body mass index
CCD	Charge-coupled device
CD	Corneodesmosome
CE	Cornified envelope
CLE	Cornified lipid envelope
CNO	Circular nano-object
CV	Coefficient of variation
DMT	Derjaguin, Muller, and Toporov adhesion theory
Dsg1	Desmoglein-1
DTI	Dermal Texture Index
EDTA	Ethylenediaminetetraacetic acid
ESEM	Environmental Scanning Electron Microscopy
FEG	Field Emission Gun
FSD	Fourier self-deconvolution
HBRC	Human Biomaterials Resource Centre
HCW	Healthcare worker
INV	Involucrin
JKR	Johnson–Kendall–Roberts model
NMF	Natural moisturising factor
NMR	Nuclear magnetic resonance
OP	Oliver-Pharr

PBS	Phosphate Buffered Saline
PDMS	Polydimethylsiloxane
PE	Photoexposed cheek
PP	Photoprotected post-auricular
PPE	Personal protective equipment
PU	Pressure ulcer
QC	Quality control
RGB	Red-green-blue colour model
RH	Relative humidity
RPE	Respiratory protective equipment
SC	Stratum corneum
SD	Standard deviation
SDS	Sodium dodecyl sulphate
SEM	Scanning Electron Microscopy
SG	Stratum granulosum
SI	Supplementary information
S-Urine	Synthetic urine
TEWL	Trans-epidermal water loss
TM	Tapping mode
TREC	Topographic and recognition imaging
UV	Ultraviolet

LIST OF PUBLICATIONS

Évora AS, Johnson SA, Zhang Z, Adams MJ. *Corneocytes: Relationship between Structural and Biomechanical Properties.* Skin Pharmacol Physiol, 2021. 34(3):146-161.

Évora AS, Zhang, Z, Johnson SA, Zhang Z, Adams MJ. *Atomic force microscope protocols for characterising the elastoviscoplastic biomechanical properties of corneocytes*. Peer review in Communications Biology

Évora AS, Johnson SA, Zhang Z, Adams MJ. *Characterization of topographical, biomechanical and maturation properties of corneocytes with respect to anatomical location.* Skin Res Tech, 2023. 10.1016/j.jdermsci.2023.08.008.

Évora AS, Johnson SA, Zhang Z, Adams MJ. *The effect of hydration on the topographical and mechanical properties of corneocyte.* Submitted to JMBBM

Évora AS, Abiakam N, Jayabal, H, Worsley, PR, Zhang, Z, Johnson, SA, Adams, MJ, Bader, DL. *Characterisation of superficial corneocytes in skin areas of the face exposed to prolonged usage of respirators by healthcare professionals during COVID-19 pandemic.* J Tissue Viability, 2023. 32(2):305-313.

Évora AS, Abiakam N, Jayabal, H, Zhang, Z, Johnson, SA, Adams, MJ, Bader, DL, Worsley, PR. *Changes in the properties of superficial corneocytes over a category I pressure ulcer.* J Dermatol Sci, 2023. 10.1016/j.jdermsci.2023.08.008.

CONFERENCE COMMUNICATIONS

Évora AS, Johnson SA, Zhang Z, Adams MJ. *Corneocytes – bricks against mechanical load? Biomechanical and topographical characterization of corneocytes.* Summer School 2021: A Boost To The Skin Barrier, Leo Foundation Skin Immunology Research Centre, University of Copenhagen, Hornbæk, Denmark. (Oral communication)

Évora AS, Johnson SA, Zhang Z, Adams MJ. *Biomechanical and topographical characterization of corneocytes using AFM with respect to anatomical location.* EPUAP 2021 Virtual Meeting. (Oral communication)

Évora AS, Piasentin N, Johnson SA, Lian G, Cai Q, Zhang Z, Adams MJ. *Biomechanics and of corneocytes using AFM – Effect of hydration.* ISBS World Congress on Biophysics and Imaging of Skin. June 2022. Berlin, Germany. (Oral communication)

Évora AS, Piasentin N, Johnson SA, Lian G, Cai Q, Zhang Z, Adams MJ. *Relationship between hydration and stratum corneum structure.* Skin Forum International Skin Science Network. June 2022. Mälmo, Sweden. (Poster communication)

Évora AS, Abiakam N, Jayabal H, Worsley PR, Johnson SA, Zhang Z, Adams MJ., Bader DL. *Properties of corneocytes in the context of skin health.* EPUAP 2022. Prague, Czech. (Oral communication)

CHAPTER I GENERAL INTRODUCTION

The modern world strives to teach us on *how to feel comfortable in our own skin* with just a few easy steps. However, for patients suffering from skin diseases and conditions, this commonplace expression can be painfully literal and far from easy. This is particularly true for individuals with pressure ulcers (PUs). PUs are localized injuries to the skin and underlying tissue, typically occurring over bony prominences due to pressure or a combination of pressure and shear forces [1]. Surprisingly, PUs remain prevalent in European hospitals, affecting approximately 10.8% of patients [2]. Despite significant efforts to understand the causes of PUs, the aetiology of these wounds continues to be a topic of strong interest to the scientific community. In fact, as late Emeritus Professor Dan Bader suggested in his *The Last hurrah* [3], there has been an emphasis on deep tissue injury in this field of research, sometimes ignoring that most PUs are category I wounds, i.e., consisting in early damage at the skin surface, rather than at the deep tissue level [1]. The, sometimes, fiery debate on PU aetiology arises from the different hypothesis of mechanistic pathways by which skin damage occurs.

Theories involve localized ischaemia [4, 5], impaired interstitial fluid flow and lymphatic drainage [6, 7], reperfusion injury [8, 9], and sustained deformation of cells [10, 11]. Ischaemia and lymphatic drainage hypothesis have been based on *in vivo* studies that generally confirm sustained tissue loading influence on tissue perfusion and/or lymph flow, thereby affecting the transport of nutrients and metabolic waste to and from the tissue, respectively. This, however, is mostly valid for muscle tissue, which is much more active than skin and so, such theories can only in part explain soft tissue breakdown at the skin surface. The same is valid for reperfusion injury through oxygen free radicals, which states that restoration of blood flow after load removal exacerbates

damage to the tissue. Although a mouse model for ischaemia-reperfusion injuries has been used to study pressure ulcer development [12], there is still a lack of evidence that restoration of blood flow aggravates skin damage in real-life clinical settings. Moreover, histopathological data suggest that pressure ulcer development has a cellular origin, considering cellular damage to be caused by sustained cell deformation [11, 13]. In fact, cell deformation affects volume changes and cytoskeletal reorganization, which may result in tissue breakdown. *In vitro* models of cultured cells or engineered tissues under compressive or shear loading have demonstrated certain thresholds for cellular breakdown [14, 15].

These theories focus on the different components of soft tissue, which might be affected by mechanical loading to varying degrees and so have different relevance in tissue damage. It is likely that PUs result from a combination of factors uncovered by these theories, even though their individual and combined role may vary depending on the nature of the mechanical insult and on patient characteristics such as comorbidities and age. In addition, the role of skin mechanics must also be considered [16], as these can vary considerably depending on intrinsic factors, such as anatomical site, age, and nutrition, and on extrinsic factors as exposure to UV or the use of creams.

The effective first barrier between the external environment and an organism is the Stratum Corneum (SC). The SC, which is usually described by a “bricks and mortar” structural model [17], is composed of corneocytes, flattened cells filled with keratin enveloped in a protein and lipid envelope [18] and connected via corneodesmosomes (CDs) [19]. The intercellular space is filled with the so-called lipid lamellae consisting of ceramides, cholesterol, and fatty acids [18]. The SC can be considered a semi-rigid thin film (~ 20-30 µm thickness in non-glabrous skin) [20] seating on top a soft material (viable

epidermis, dermis, and hypodermis). In fact, the Young's modulus of the SC has been calculated to be in the range 1-3 GPa, for a low relative humidity of 35% [21]. It is much stiffer than the viable epidermis (1.5 MPa), dermis (20 kPa) and hypodermis (2 kPa) [22]. Interestingly, however, the role of the SC in skin mechanics and tissue integrity has been largely disregarded. Consequently, the primary motivation behind this thesis was to comprehensively explore the pivotal role of SC cells, known as corneocytes, in preserving skin integrity, particularly under conditions of mechanical loading that may eventually lead to the development of pressure ulcers. The work is also very important for cosmetic science. In fact, understanding the properties of corneocytes and how they change in different conditions can help create skincare products that strengthen the protective barrier of the skin and emphasize the need for cosmetics that support skin integrity under stress. Moreover, insights into the properties of corneocytes of the elderly can guide the development of anti-aging products.

Therefore, the role of corneocytes in SC mechanics and early mechanical damage was studied following a structured approach outlined as follows:

1. Chapter II: to review the state-of-the-art knowledge on SC and, particularly, on corneocyte properties.
2. Chapter III: to establish experimental protocols for the study of the mechanical properties of single cells using Atomic Force Microscopy (AFM).
3. Chapter IV: to characterize the maturation and mechanical properties of corneocytes in healthy young skin according to anatomical site by collecting cells from 10 participants and investigating 5 locations: forearm, cheek, neck, sacrum, and medial heel.

4. Chapter V: To study the effects of hydration on skin cell mechanics and morphology.
5. Finally, to study the changes in corneocyte properties in early skin damage through two cohort studies: Chapter VI - the changes of superficial corneocytes during prolonged respirator application in the clinical setting during the COVID19 pandemic; and Chapter VII - the first characterization of superficial corneocytes at the site of category I pressure ulcers in elderly individuals.
6. Chapter VIII summarizes the key findings illustrating the relevance of studying the role of the SC in maintaining skin integrity and presents overarching future work.

CHAPTER II - CORNEOCYTES: RELATIONSHIP BETWEEN STRUCTURAL AND BIOMECHANICAL PROPERTIES

This chapter is based on the published paper Évora, A.S., et al., *Corneocytes: Relationship between Structural and Biomechanical Properties.* Skin Pharmacol Physiol, 2021. 34(3):146-161.

2.1 Abstract

Background: Skin is the interface between an organism and the external environment and hence the Stratum Corneum (SC) is the first to withstand mechanical insults that, in certain conditions, may lead to integrity loss and the development of pressure ulcers. The SC comprises corneocytes, which are vital elements to its barrier function. These cells are differentiated dead keratinocytes, without organelles, composed of a cornified envelope and a keratin-filled interior, and connected by corneodesmosomes.

Summary: The current review focusses on the relationship between the morphological, structural, and topographical features of corneocytes and their mechanical properties, to understand how they assist the SC in maintaining skin integrity and in responding to mechanical insults.

Key messages: Corneocytes create distinct regions in the SC: the inner SC is characterized by immature cells with a fragile cornified envelope and a uniform distribution of corneodesmosomes; the upper SC has resilient cornified envelopes and a honeycomb distribution of corneodesmosomes, with a smaller surface area, and greater thickness than cells from the inner layer. The literature indicates that this upward maturation process is one the most important steps in the mechanical resistance and barrier function of the SC. The morphology of these cells is dependent on the body site: the surface area in non-exposed skin is about 1000-1200 μm^2, while for exposed skin, e.g., the cheek and forehead, is about 700-800 μm^2. Corneocytes are stiff cells compared to other cellular types, e.g., the Young's modulus of muscle and fibroblasts cells are typically a few kPa, while those of corneocytes is reported to be about hundreds of MPa. Moreover, these skin cells have two distinct mechanical regions: the cornified envelope (100–250 MPa) and the keratin matrix (250–500 MPa).

2.2 The Skin and the Stratum Corneum

Human skin is composed of three main dynamic layers, namely the hypodermis, dermis, and epidermis [23]. The latter is the outermost layer (Figure 2.1), being a waterproof barrier protecting the body against the entry of foreign bodies and physical and mechanical insults [24]. It is a stratified and squamous epithelium that can be subdivided into four discrete layers, in which keratinocytes, the main cell type, undergo a differentiation process, from the inner layer, at the epidermal-dermal interface (stratum germinativum or basal cell layer), to the SC [25, 26].

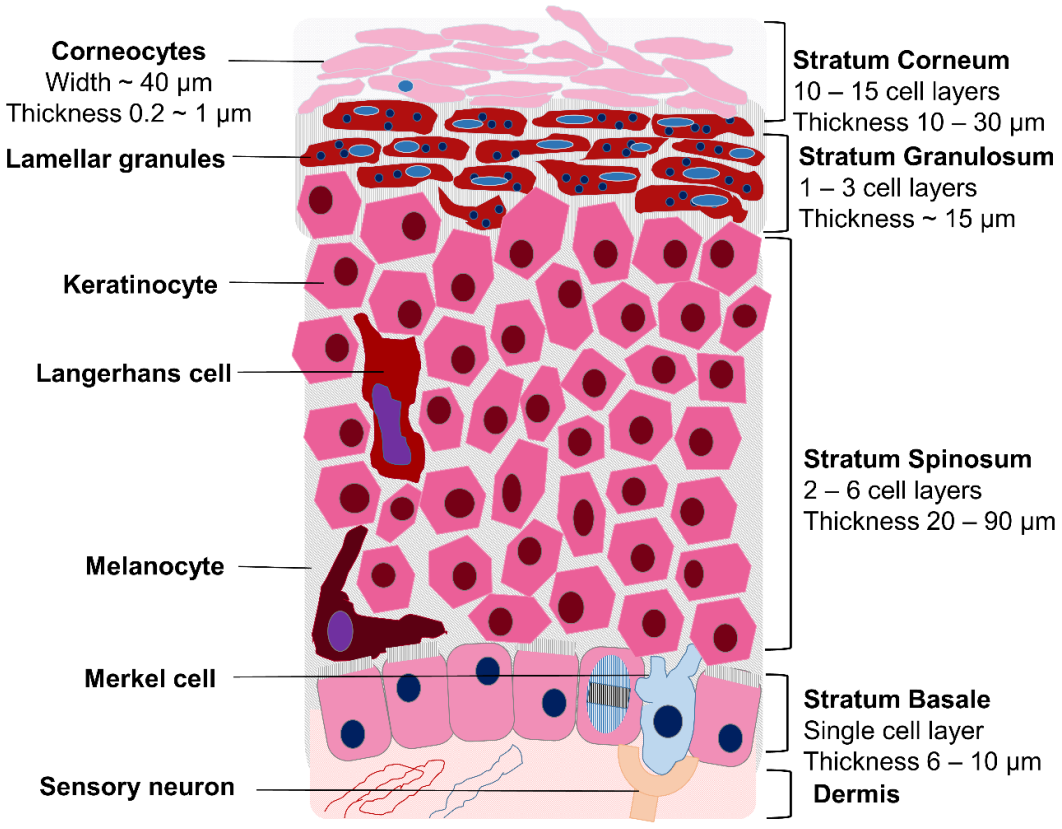

Figure 2.1. Schematic diagram of the epidermis. Keratinocytes proliferate in the basal cell layer and move upwards in the stratum spinosum where they start to suffer a differentiation process while migrating upwards in the epidermis. This process involves a synthesizing step in the stratum granulosum and culminates with death by cornification and maturation of corneocytes in the outermost layer of the stratum corneum.

The SC is usually described by a “brick and mortar” structural model [17] (Figure 2.2) where the corneocytes are completely flattened and their keratin filled-interior is surrounded by protein and lipid envelopes (cornified envelopes and cornified lipid envelopes, CE and CLE, respectively) [18]. Adjacent corneocytes are connected by corneodesmosomes (CDs) for which localization and density depends on the depth of localization of the cells in the SC [19]. Intercellular lamellae of lipids, such as ceramides, cholesterol, and fatty acids, are first synthesized in the stratum granulosum [18] and compose the “mortar” of the SC.

The SC functions as a barrier between the organism and the external environment, being responsible for the control of trans-epidermal water loss (TEWL) and the selective absorption of compounds [27]. The thickness of the SC varies depending on body site - that of the cheek and back of the hand being 17 and 30 µm, respectively, while that from the palm being much thicker (173 µm) [20] - although this will vary somewhat for different individuals. The complex hierarchical structure of the SC has two main functions: while corneocytes and CDs mainly contribute to the mechanical resistance of the layer, the intercellular lipids are mainly involved in the barrier function [28], preventing water loss and the entry of foreign bodies. The mechanical resistance of the skin to environmental insults is a critical function of the structural cohesion of the SC and the mechanical resilience of the corneocytes, which depends on the differentiation process of the keratinocytes in the epidermis. There are several reviews on the composition and biochemistry of the stratum corneum (SC) that mainly reveal the mechanisms underlying its barrier function in healthy skin and several disorders [29, 30, 31]. However, the mechanical function of SC has been addressed in less detail. Many studies have examined the pathways leading to the loss of skin integrity under the

action of applied stresses, but there is still not a consensus on the underlying mechanisms.

The current review aims to consider the relationship between the structure and morphology of corneocytes and their biomechanical properties since these dead cells are the first elements to sense load and friction.

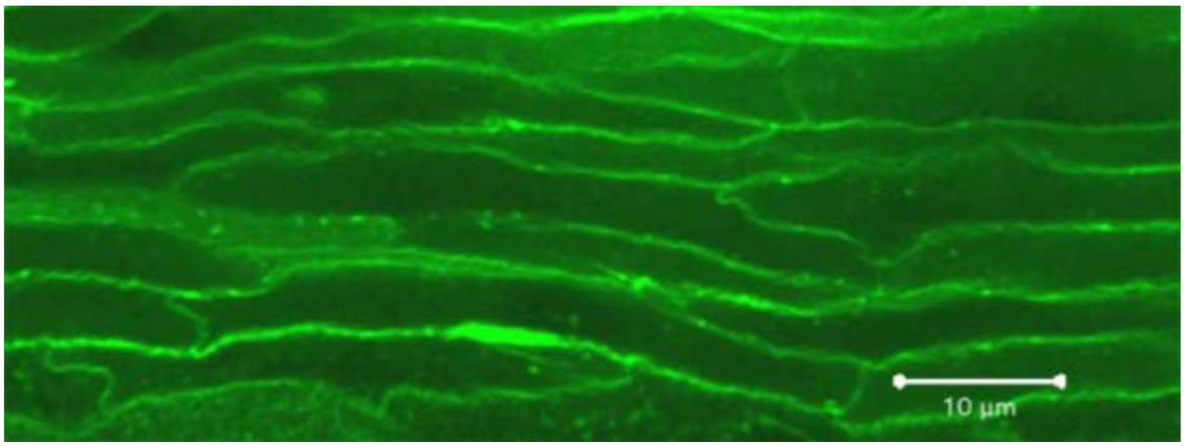

Figure 2.2. Confocal fluorescence images of the SC. Images obtained after staining with Nile red in alkali solution to swell the corneocytes in order to render them visible in an optical microscope (cells are expanded by a factor of 5 in the thickness dimension). The specimen was mechanically and optically cross-sectioned in the same apical-to-basal plane, dorsum skin. The image illustrates the 'bricks and mortar' structure of the SC. Reproduced, with permission, from Talreja et al. [17]. SC, stratum corneum.

2.3 Corneocytes

Keratinocytes proliferate in the basal layer of the epidermis and migrate upwards, undergoing a sequential differentiation that culminates with death by cornification [32]. Cornification is usually described by three main events: formation of an intracellular keratin network (with the loss of organelles); assembly of the CE with the CLE covalently attached and selective degradation of CDs. The maturation of the corneocytes of the SC and desquamation of superficial cells are well-controlled processes that depend on several different elements such as proteases and their inhibitors, a controlled pH gradient, and regulated hydration of the SC [19]. The different

steps of corneocyte maturation are reflected by their morphology and surface topography as discussed below.

2.4 Morphology and Topography

The morphology of corneocytes (Table 2.1, Figure 2.3) was first studied in 1939 [33], which reported a diameter of approximately 25-35 μm and a single-sided surface area of 700-900 μm^2 and it is of great interest in dermatology and cosmetic science since the appearance of corneocytes is increasingly associated with several skin conditions. Later, cells from the forehead and hand were observed to have the smallest surface area of 700-800 μm^2, and those from the upper arm, thigh, and axilla had the greatest surface area of 1000-1200 μm^2 [34, 35, 36], which indicated that corneocytes from high proliferative regions are usually smaller [37].

An increase in surface area of corneocytes with age has also been reported [35, 38, 39], e.g., corneocytes from the axilla have a surface area of ~ 750 μm^2 for babies, ~ 1000μm^2 for children, ~ 1200 μm^2 for adults, and, finally, ~ 1400 μm^2 for the elderly. Using AFM, Gorzelanny et al. showed that corneocytes from aged SC (Figure 2.3(b)) presented a surface area of 753 ± 120 μm^2, and those from young subjects' skin (Figure 2.3(a)), a smaller area of 555 ± 80 μm^2 [40].

Moreover, the thickness of corneocytes has been reported to be inversely related to the cross-sectional area of the cells: the largest cells are usually the thinnest [41]. Furthermore, it was reported that there is a 40% decrease in thickness for corneocytes sampled from the upper SC (first tape strip), compared to those in the inner SC (20th tape strip) [38], and a corresponding increase in the surface area [42].

Table 2.1. Surface area of corneocytes from different body sites, ages, and genders.

Surface area (μm^2)					
Body region	**Babies**	**Children**		**Adults**	**Aged**
Scalp	~ 700 [35]	~ 800 [35]	Male	~ 900 [35]	1000 [35]
			Female	~ 1100 [35]	
Forehead	~ 750 [35]	~ 750 [35]	Male	~ 750 [35]	900 [35]
			Female	~ 900 [34, 35]	
Axilla	~ 800 [35]	~ 1000 [35]	Male	~ 1200 [35]	1400 [34]
				~ 1148 ± 11 [37]	
			Female	~ 1250 [35]	
				1176 ± 11 [37]	
Upper arm	~ 800 [35]	~ 1000 [35]	Male	~ 1000 [34, 35]	1200 [35]
				1098 ± 12 [37]	
			Female	~ 1050 [35]	
				1145 ± 14 [37]	
			-	~ 1000 [38]	
Forearm	~ 700 [35]	~ 900 [35]	Male	~ 850 [35]	1100 [35] 753 ± 120 [40] 1000-1300 [39]
				~ 1004 ± 12 [37]	
			Female	~ 1100 [35]	
				~ 1018 ± 21 [37]	
			-	~ 840 [36]	
			-	555 ± 80 [40]	
			-	600 – 1000 [39]	
			-	1000 ± 200 [42]	
Hand	~ 650 [35]	~ 700 [35]	Male	~ 800 [35]	~ 1000 [35]
			Female	~ 1000 [35]	800 – 1050 [39]
				600-850 [39]	
Abdomen	~ 800 [35]	~ 800 [35]	Male	~ 1000 [35]	~ 1300 [35]
				1130 ± 8 [37]	
			Female	~ 1400 [35]	
				1180 ± 18 [37]	
				~ 850 [36]	
Thigh	~ 750 [35]	~ 800 [35]	Male	~ 1100 [35]	~ 1300 [35]
				1184 ± 17 [37]	
			Female	~ 1300 [35]	
				1188 ± 14 [37]	
Heel	-	-	Male	~ 800 [35]	-
				1104 ± 12 [37]	
			Female	~ 1000 [35]	
				1101 ± 12 [37]	
Cheek	-	-	-	~ 680 [38]	-
			-	750 ± 150 [42]	
			-	800 – 1000 [38]	

In the context of representing the 3D morphology of a corneocyte, a flattened Kelvin tetrakaidecahedron geometry has both a hexagonal cross-section as well as hexagonal upper and lower faces that are consistent with a simple 2D top-view model of the SC [43, 44]. Close packing of SG keratinocytes of this shape allows them to maintain an effective tight junction barrier as cells suffer cornification and move upward to the SC. This geometry represents an optimal shape for space-filling and those authors propose that it also represents the basis for the barrier function and physical strength of the horny layer.

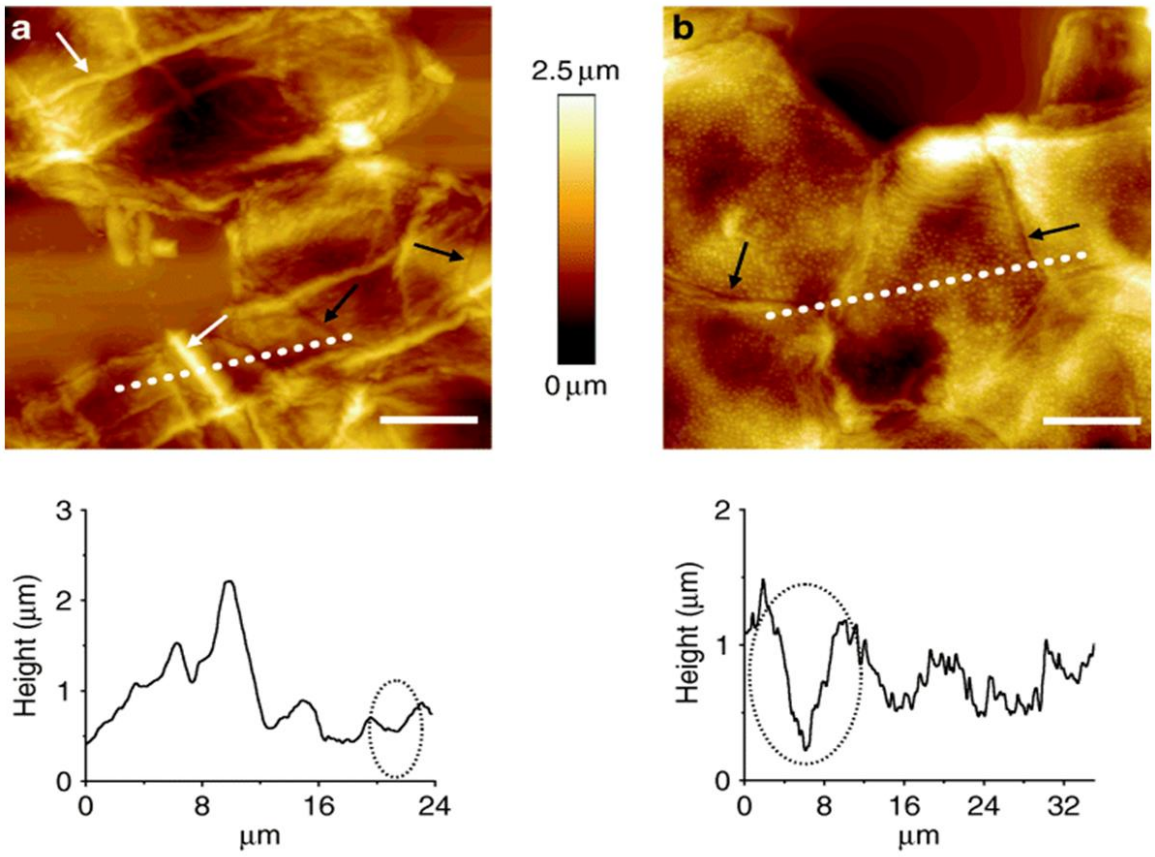

Figure 2.3. 3D image of corneocytes. Corneocytes from a young donor **(a)** and from an aged donor **(b)**. Height is given in colour brightness – lateral dimension by scale bar (10 µm). The white arrows point to filamentous structures so far unidentified, while the black arrow indicates cell–cell contacts between two corneocytes. The dotted line indicates a cross-section that is displayed below. The dotted circle indicates the intercellular gap. Reproduced with permission from Gorzelanny et al. [40].

2.5 Mechanical properties of corneocytes

The mechanical properties of corneocytes are important since the dead envelope of cells that constituting the SC must have physical properties that enable them to experience deformation in response to body movement and physical insults [45]. The skin regularly endures a range of physical challenges e.g., walking and wearing tight shoes, wearing belts and tight clothes, and when in contact with skincare and grooming products such as shavers.

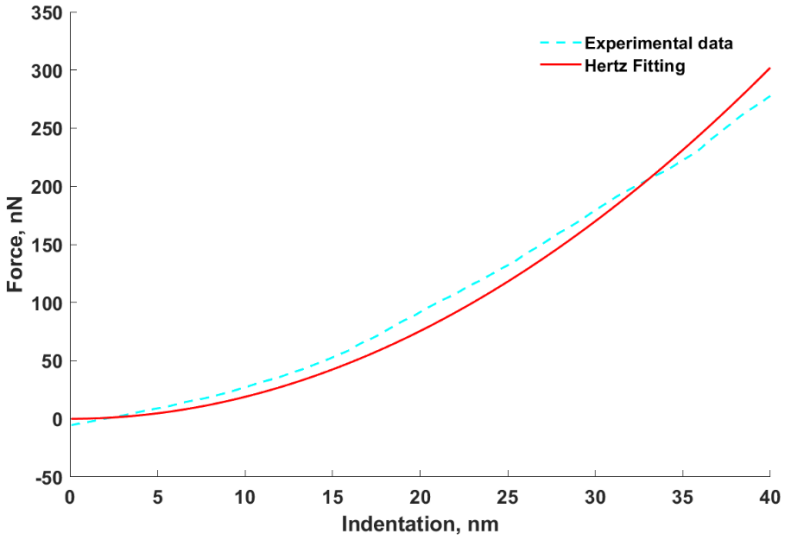

Figure 2.4. Representative AFM force curve. Force as a function of indentation depth and Hertz-Sneddon fitting obtained on inner forearm superficial corneocyte (2nd tape strip) at room temperature using a JPK Nanowizard instrument with a 26 N/m stiffness cantilever and a pyramidal tip [46].

The stretched or compressed SC must be able to return to its original state without structural changes. Hence, understanding the mechanical properties of single cells assist us in delineating the phenomena underlying the mechanical resistance of the skin, the maintenance of integrity, and damage processes. Corneocytes were observed to fold readily but to strongly resist elongating forces [45], and the Young's modulus was calculated to be ~ 0.45 GPa. Later, using a micromanipulation technique, two populations of corneocytes were identified in normal skin based on the force

required to compress the cornified envelope: resilient (833 ± 431 μN) and fragile CEs (135 ± 32 μN) [47] and a greater ratio of fragile to resilient CEs was observed in dry skin.

Table 2.2. Mechanical properties of corneocytes measured by different techniques as defined by the value of the Young's modulus.

Methods	Young's Modulus
Fontbrune's double micromanipulation system Corneocytes dispersed in water	450 MPa [45]
Scanning Probe Microscopy Indentation: < 10 nm Cantilever spring constant: - Probe: spherical Contact mechanics model: Hertz	0.4 GPa [48]
Treatment of skin with moisturizer for 10 days *Scanning Probe Microscopy* Indentation: < 10 nm Cantilever spring constant: 0.1 N/m Probe: pyramidal Contact mechanics model: JKR	Before treatment: 50 ± 20 MPa After treatment: 25 ±15 MPa [49]
Treatment of skin with moisturizer for 5 days *Scanning Probe Microscopy* Indentation: < 10 nm Cantilever spring constant: 0.6 N/m Probe: spherical Contact mechanics model: JKR	Before treatment: 1.34 ± 0.46 MPa After treatment: 1.87 ± 0.85 MPa [50]
Scanning Probe Microscopy Indentation: < 50 nm (cornified envelope) and > 50 nm (cell interior) Cantilever spring constant: 35 N/m Probe: nanoneedles (diameters of 40 and 75 nm) Contact mechanics model: Oliver-Pharr	For < 50 nm: 100 MPa For > 50 nm: 500 MPa [51]
Scanning Probe Microscopy Indentation: < 50 nm (cornified envelope) and > 50 nm (cell interior) Cantilever spring constant: 2.5 N/m Probe: pyramidal Contact mechanics model: Hertz	*Upper SC (1st Tape strip):* For < 50 nm: 250 MPa For > 50 nm: 300 – 520 MPa *Inner SC (14th Tape strip):* For < 50 nm: 150 MPa; For > 50 nm: 250 – 300 MPa [52]

More recently, the mechanical properties of corneocytes have been mainly investigated using AFM to measure indentation loading curves and applying contact mechanics models, e.g., Hertz-Sneddon, DMT or JKR [53], to obtain the Young's modulus (a representative loading curve is shown in Figure 2.4).

There is a large variability in the Young's modulus determined for corneocytes: from 1.34 MPa up to 0.4 GPa [48, 49, 50] (Table 2.2). The force spectroscopy mode of AFM requires great control of the method and a rigorous analysis of the data such that the contact mechanics model and the geometry of the probe greatly influence the results. Pyramidal and conical probes, for example, can be regarded as spheres or paraboloids of revolution for small indentations, in which a nominal radius is usually assigned.

However, for larger indentations, the probe can be treated as either a cone or pyramid with half-angles dependent on the indentation depth. Another important point to consider is the stiffness of the cantilever: if it is softer than the sample, the measured stiffness of the sample will be mainly that of the probe. We speculate that some of the probes used in the literature were too soft in this respect and resulted in under and overestimated Young's moduli.

The influence of the different components of the cells was assessed using nanoneedles mounted on cantilevers with a spring constant of 35 N/m [51] and the Oliver-Pharr model [54] to fit the data. The reduced Young's modulus was calculated to be ~ 100 MPa for indentations < 50 nm and 500 MPa at greater depths. This work can be related to that by Milani et al. [52], in which the authors calculated the apparent Young's modulus for different depths by applying the Hertz model to intervals of force as a function of indentation. Using pyramidal probes and 2.5 N/m stiffness cantilevers, the stiffness of cells from 3 different SC depths (1st, 7th, 14th tape strips) was measured.

A decrease in the Young's modulus was established as a function of the depth of indentation. For the 1st strip, an apparent modulus of ~ 250 MPa for the CE and 300-520 MPa for the keratin bundles, while for cells deeper in the SC, a modulus of about 150 MPa for the CE and 250-300 MPa for the keratin-matrix were calculated. The increase in stiffness with proximity to the skin surface correlates with the enlargement and the thinning of cells along that axis.

However, the protocol for the collection of corneocytes might influence the results obtained. While most authors use the tape stripping method to collect cells, the influence of the tape on the compliance of the AFM force curves is not described. Moreover, Richter et al. [55] studied the swelling of corneocytes by AFM Tapping Mode (TM), using a silanization technique to firmly attach the cells to a silicon substrate. In their TM images, they did not find phase contrast differences between cells in air and the silicon substrate. However, cells in water showed a considerable phase contrast when compared to the substrate. The authors attributed this to the viscoelasticity of the swollen cells and concluded that the absence of phase contrast in the case of the cells in air was consistent with the description of corneocytes as being brittle and hard [55]. More rigorous viscoelasticity experiments, such as stress-relaxation using AFM, are nonetheless needed to confirm this assumption. Additionally, it should be noted that this procedure includes an overnight drying step of the sample followed by a washing step. Because the cells are allowed to dry overnight, it is difficult to state that their mechanical properties are close to those measured when the tape stripping method is employed to collect corneocytes.

Moreover, a divergence of the mechanical properties of single cells from those obtained when cells are integrated in the SC is expected. When integrated in the tissue,

corneocytes are subjected to different forces, such as interplanar and peripheral adhesion forces (explored in the Section below regarding the CE), which may influence their mechanical properties.

2.6 Keratins: role in cell mechanical strength

Keratins have long been recognized as the main component contributing to the mechanical strength of keratinocytes [32, 56]. Their expression is selective and matches the degree of differentiation of cells across the epidermis. Basal keratinocytes are mitotically active and express keratins 5 and K14, with a minor amount of K15 [57]. As keratinocytes migrate upwards and suffer differentiation, they start expressing keratin 1 and keratin 10, with a loss of K5 and K14 expression [58]. Additionally, there is expression of K2 in the upper spinous and granular layers [59]. Furthermore, in the palmar-plantar epidermis K9 is prominently expressed in the suprabasal differentiating layers [60] and K6, K16, K17, and K19 are also expressed in specific spatial patterns and their expression can be rapidly induced upon various challenges, such as wounding and infection [61]. Since corneocytes are dead cells composed of a strong protein-lipid envelope surrounding these keratin bundles, studies of the isolated influence of keratin filaments on their mechanical properties are difficult to perform.

Nevertheless, as seen in the previous section, it is possible to make a distinction between the contribution of the cornified envelope and the cell interior using AFM force spectroscopy. Furthermore, by studying the phenomena occurring with the viable cells of the epidermis, it is possible to extrapolate knowledge to the product of their differentiation i.e., corneocytes. For example, it has been observed in multiple studies that mutations in keratin genes, such as in the disruption of filament formation or alteration of properties and dynamics of bundle assembly, reduce the strength of cells

[62, 63]. Living human keratinocytes were studied under loading and unloading cycles of single cells by AFM and it was observed that a typical force of 0.4 ± 0.1 μN was required to reach 30% compression and 6.0 ± 2.0 μN for an 80% compression of the original height [62]. The Young's moduli of the keratinocyte membrane and cytoplasm were calculated to be 23–38 MPa and 120–340 kPa, respectively, which is a factor of 25–30 greater than that of the cytoskeleton of T cells. This shows that keratins are responsible for the high stiffness of keratinocytes. A correlation between molecular integrity of keratin filaments (K5 and K14) and mechanical toughness of epithelial cells was also found [64]. The modulus of mutant cells (not expressing K14) was 343 ± 18 and 412 ± 74 Pa for the nucleus and cytoplasm, respectively, while for controls, a greater cell stiffness was observed of 459 ± 31 Pa for the nucleus and 752 ± 100 Pa for cytoplasm.

In a different study, Akinshina et al. [65], attempted to verify the results obtained by Jokura et al. [66]. The latter studied the effects of the Natural Moisturising Factor (NMF) components on the SC using nuclear magnetic resonance (NMR), rheology, and Scanning Electron Microscopy (SEM). They observed that treating excised SC with water would release the NMF component, leading to a reduction in the mobility of keratin intermediate filaments (IFs) and a smaller value of the elastic modulus. The electron micrographs suggested that, in the absence of NMF, the keratin filaments tend to associate more tightly. They concluded that the former results indicated that the increase in corneocyte rigidity is due to increased intermolecular attractive forces between keratin filaments. They modelled the interactions between keratin IFs suspended in different media and found that the N-tails of the keratin filaments act as the 'glue', while the C-tails are responsible for maintaining a certain distance between

the IFs. The small charged species comprising the NMF then act in the prevention of the attractive forces between the protruding terminal domains of IF helical cores. When they are eliminated, the attractive forces are sufficiently large to ‘glue’ the filaments together and thus increase the stiffness of the corneocyte. This denotes the complex relationships existing in SC cells in order to maintain mechanical integrity.

The stretching of cultured keratinocytes also provides an insight into the response of cells to certain types of mechanical stimuli. When normal human keratinocytes and HaCat cells are stretched, the expression of K10 was completely suppressed after 24 h, and the K6 expression was induced; that is, the mechanical stimulus suppressed the differentiation of the cells [67]. The response of cultured cells to mechanical stimuli raises the question of what happens to keratin expression when the skin is subjected to clinically relevant pressures, such as those of a patient lying in bed or seated in a wheelchair: are the keratinocytes able to adapt in the presence of mechanical loading? Using a device to periodically stimulate keratinocytes (over 80 h), it was observed that the keratin distribution of the cells was amorphous and partly granular, as described for corneocytes [68]. The expression of a 67 kDa keratin was found in mechanically stimulated HaCat cells, which is not normally expressed by cultured keratinocytes. Furthermore, Yamaguchi et al. [69] found that non-palmoplantar keratinocytes gained the ability to express K9 when co-cultured with palmoplantar fibroblasts.

The influence of the morphology and composition of plantar skin on the tolerance to load has been studied [70]. Plantar SC was found to be a factor of 16 thicker than the SC from nonplantar skin, with greater interdigitation between the epidermis and dermis and with a 2.1 increase in fluorescence intensity of desmoglein 1 (Dsg1), a key component of CDs. Moreover, plantar skin was observed to deform less with loading

(factors of 1.6 and 3.4 less under compression and shear, respectively). Moreover, the SC showed a factor of 3 increase in the Young's modulus, and factors of 4.8 and 7.2 increase for viable epidermis and dermis respectively. Using a pyramidal probe, the change of the Young's modulus with depth proved to be more gradual for plantar skin (18% decrease per 100 μm) than for nonplantar skin (84% decrease per 100 μm). The authors suggested this may assist in mitigating stress concentrations by eliminating "hotspot" areas of stress. Plantar skin seems to mitigate the effect of mechanical insults by diverse structures and mechanisms: thicker SC is associated with greater stiffness and more cohesion since there is a greater number of desmosomes. To study the mechanical properties of individual corneocytes would be a logical next step to complement the knowledge about this type of SC.

2.7 Cornified Envelope (CE)

Apart from keratin bundles that fill the interior of corneocytes, two other components contributing to the mechanical strength of these cells and the mechanical resistance of SC must be considered. These are the CD and the CE. Extensive reviews on the formation and composition of both structures have been presented elsewhere [19, 27, 32, 71]. Briefly, the cornification process begins with the synthesis of an immature CE beneath the plasma membrane of the keratinocytes. This envelope undergoes maturation by the covalent attachment of certain precursor proteins (such as involucrin, loricrin, and SPRs - small proline-rich proteins) to produce a quite rigid structure [71]. Transglutaminase activity allows the cross-linking of proteins via γ-gamma-glutamyl-ϵ-lysine isopeptide bonds, which reinforces the envelope [72]. Some authors have observed that the composition of CEs is variable and dependent on the type of substrate available to the transglutaminases [73], with some considering the possibility

of the incorporation of CD proteins later in the CE maturation [74]. Additionally, the maturation of CEs culminates with the covalent attachment of ceramides, fatty acids, and others to involucrin and loricrin, creating a hydrophobic coating [75, 76]. These bound lipids are called the cornified lipid envelope and are thought to be a scaffold for the intercellular lipids of the SC [77, 78, 79], further stabilizing and promoting the flexibility of this top layer.

The maturation of the CE follows the movement of corneocytes in the SC and many authors have attempted to discriminate mature from immature CEs using microscopy and immunostaining techniques. CEs from different SC depths were first observed by Normarski contrast microscopy, which allowed the identification of two different populations of CEs: 'fragile' (CEf) and 'resilient' (CEr) [73]. These two states of maturation can be found in the most superficial layer of SC, although the amount of CEf is small in normal skin and elevated in dry skin [47]. Moreover, the ratio between resilient and fragile CEs in the case of inflammatory skin disorders was found to be decreased in Psoriasis and Atopic Dermatitis (AD) [80].

Most recently, the standard technique for assessing CE maturity is the double staining of lipids with Nile red and immunostaining of involucrin. Nile red is used to stain lipids covalently bound to the CE, the last step of corneocyte maturation, while immunostaining of involucrin is performed to distinguish non-matured CEs [81]. It is suggested that the loss of involucrin staining during corneocyte maturation must be a result of the covalent attachment of lipids to CE proteins, in which case the epitope of involucrin might be hidden for recognition by the antibody upon immunostaining. Corneocytes were reported to become less and less mature with increasing SC depth [82, 83]. This morphological feature is related to the mechanical strength of corneocytes

as discussed previously: a decrease in Young's modulus of corneocytes with depth from the first strip (250 MPa) to the seventh strip (150 MPa) for the cornified envelope [52] and a similar trend reported when measuring the force necessary to compress both CE types [47].

Guneri et al. applied conventional methods and a novel one to evaluate the maturity of CEs [75]. They found that the anti-involucrin and Nile red approach was limited in discriminating the maturity of CEs in the deeper SC layers of photo exposed cheek (PE) and photoprotected post-auricular (PP). With this method, both deep layers (PP9 and PE9, ninth tape strip) would be considered immature. Although, when relying on the mechanical integrity of CEs, by analysing the morphology after sonication, differences were found in the proportion of immature CEs in the deeper layers of PE cheek (43 ± 6.5 % less maturity), but PP9 seemed to be less perturbed by this mechanical stress. This means that, although the traditional method would regard PP9 CEs to be immature, they cannot be considered immature in their response to mechanical stress, suggesting that the maturation of corneocytes depends both on the formation of a mechanical resistant cornified envelope and on the establishment of a lipid envelope [78] surrounding the rigid CE. In summary, the maturation of CEs is intimately related to the stiffness of corneocytes: matured corneocytes are stiffer not only because of the type of keratin bundles composing their matrix but also because of the cross-linking occurring in the cornified envelope.

2.8 Corneodesmosomes

In addition to the maturation of the cornified envelope, another important step in cornification is related to the formation and degradation of CDs. These structures are responsible for the cohesion of the deeper layers of SC that bind the corneocytes

together. The importance of these components was demonstrated by the absence of corneodesmosin expression, which results in the premature detachment of corneocytes from SC in mice and humans [84]. The precise distribution of Dsg1 in corneocytes as they transit in SC has been studied (Figure 2.5) [85].

The outer layer or mature SC is characterized by a honeycomb-like structure, in which the cornified cells are attached only laterally in the same cell layer [86]. This feature is only absent in palmar and plantar regions, where CDs are found to be dispersed over the whole surface of the cells. These junctional structures are modified desmosomes [87, 88] involved in desquamation, a complex process regulated by several proteases and inhibitors, first expressed in the stratum granulosum and secreted to the extracellular space. Peripheral CDs are thought to persist in the outer SC, being protected from enzymatic degradation by tight junctions that surround them [89]. A correlation between TEWL readings and the localization of Dsg1 has also been established, with the presence of Dsg1 on the periphery of cells being associated with a healthy SC (lower values of TEWL), and if dispersed on the whole surface, corresponding to a reduced barrier function (higher TEWL) [85]. Moreover, the honeycomb feature of mature SC seems to result in improved flexibility of the whole layer by attenuating mechanical insults, such as bending or flexing, allowing the shape of corneocytes to adapt and the outer SC to perform minimal “slide” over the inner SC [90].

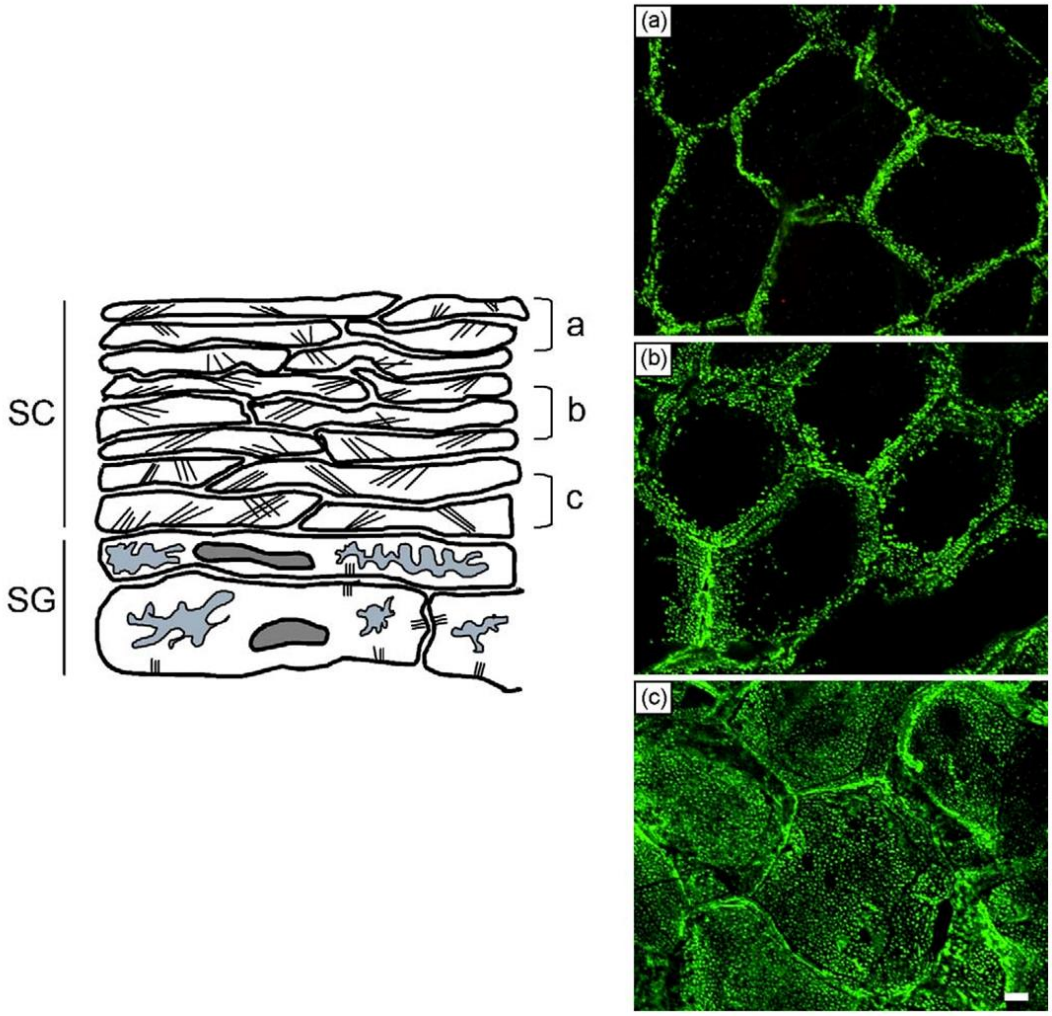

Figure 2.5. Desmoglein 1 immunostaining in the stratum corneum from the inner to outer SC. 11 tape strips were performed on the inner upper arm. In the inner SC **(c)**, desmoglein 1 was localized over the entire surface of the corneocytes, while in the middle layer **(b)** it was localized mainly in the periphery, persisting in this region in the outermost layer **(a)**. Bar = 5 µm. Reproduced with permission from Naoe et al. [85].

Furthermore, the digestion of CDs increases with increasing relative humidity (RH) [91]. It was also found that at high (80% RH), but not at low (44% RH) humidity, glycerol further enhances CD digestion. When the glycerol treated SC was extended at 80% RH, the extensibility of the SC increased dramatically, indicating a reduction of inter-corneocyte cohesion.

This behaviour is suggested to be caused by the influence of humidity on the activity of desquamatory enzymes. When an inhibitor of serine proteases was introduced, the moisture-dependent increase in tissue extensibility was prevented. Finally, the stiffness of the SC was largely unchanged even at high doses of UV radiation, while the fracture strength and fracture strain of the SC decreased with increasing UV exposure [92, 93], indicating that UV influences cellular cohesion, dominated by both intercellular lipids and CDs, while not interfering with the mechanical resistance of the tissue, which is mainly controlled by the keratin matrix and the rigid cornified envelope of corneocytes. A dispersion in the localization of Dsg1 in the tissue, indicating degradation of CDs after UV radiation treatment was also observed [93].

Corneodesmosomes seem to play a major role in the cohesion of SC, which can be divided into two main regions: the deeper-immature SC, which is much more cohesive, and the outer SC, for which flexibility and plasticity may depend on intercellular lipids and the honeycomb localization of CDs. It is important to note that the honeycomb structure of the outer SC seems to be preferred in most body regions, but not for the palmar and plantar zones [93, 94]. In these regions, there prevails a strong cohesion between corneocytes, with CDs dispersed on the whole surface. This cohesiveness in combination with greater Young's modulus (greater stiffness) may be an evolutionary advantage since they are subjected to greater pressures and other forces even if it is associated with decreased suppleness and barrier function.

2.9 Maturation of corneocytes and surface texture

When analysing the surface of corneocytes using SEM and AFM, small circular protrusions of a few hundreds of nanometres (termed circular nano-objects - CNOs)

are observed on the basal side of the cells (Figure 2.6c [46]). Cells from the palms and soles were observed to have an irregular shape, with excessive wrinkling on their surfaces and sometimes villi-like structures, while those from the axilla, umbilical region, and the back presented a hexagonal shape, with trabeculae that were parallel to the cell border, forming a regular network [95]. Similar differences were found using AFM TM to analyse the topography of cells from the forearm (smooth topography) and the palm of the hand (with the presence of numerous small protrusions) [96].

The distribution of these structures is not homogenous: some cells are covered with CNOs, while some cells are smooth with a subcellular preference of CNOs at the periphery. Such protrusions have been associated with cell-to-cell adhesion [97] and assigned to aging [40] and some skin states and disorders [35, 40, 98, 99, 100], as reviewed in detail by Riethmüller [101]. Using a computer vision algorithm, Franz et al. [102] were able to determine the mean number densities of CNOs over cell surfaces; they termed this parameter the Dermal Texture Index (DTI). It was found to be greatest on lesion areas of AD skin (DTI - 200-800), but also to be greater in non-lesion areas, when compared to healthy skin controls (DTI ~ 100). An increase in DTI was also found in cases of loss of function of filaggrin [103]. The same authors observed corneodesmosin (a key component of CDs) to be present in CNOs by immunogold electron microscopy. Although the literature does not define a conclusive connection between CNOs and CDs, it is reasonable to explore such relations.

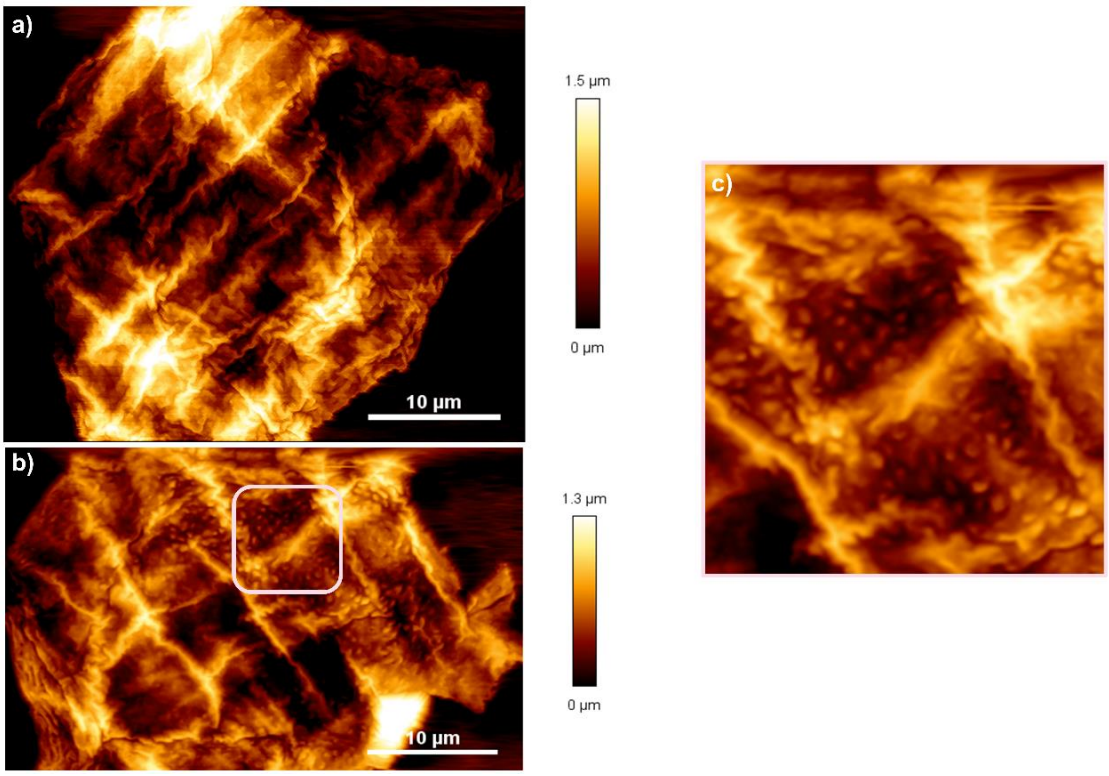

Figure 2.6. Topographical analysis of corneocytes. AFM reveals surface topographical features on superficial corneocytes (2nd strip) from the inner forearm of one volunteer. Height is given in colour brightness – lateral dimension by scale bar (10 µm). The images were obtained in the contact mode (cantilever stiffness of 1 N/m and a pyramidal tip). **(a)** A smooth corneocyte presenting ridges on its surface. **(b)** A corneocyte presenting CNOs on its surface, highlighted by the white box. **(c)** Zoom image of (b) of CNOs present on the cell surface. [46].

It is known that the degradation of filaggrin leads to an increase in NMF concentration that is responsible for water retention, which is an important factor for the activation of proteases involved in the degradation of CDs, as mentioned above. Consequently, it is reasonable to relate a mutation of the filaggrin loss-of-function gene with a greater number of CNOs by the impaired degradation of CDs when the water content is decreased. If CD degradation is impaired, corneocyte maturation might be compromised, which would explain the defect in barrier function attributed to the intercellular lipids that might not have the space to rearrange viz., a greater number of CDs implies a greater cohesion of the SC, but a loss in barrier function.

Additionally, corneodesmosin was detected on the surface of SC using simultaneous topographic and recognition imaging (TREC) technique based on AFM [104]. The authors found the density of corneodesmosin to be about 1000 proteins/μm^2 on the surface of corneocytes from superficial SC and about 1200 in deeper layers of SC. Additionally, the size of the recognition spots was larger in the deeper SC, which is in agreement with the described progressive degradation of corneodesmosin during the desquamation process [105]. The topographic and recognition images showed that the protein is located mainly on 'bead-like' structures observed by the authors, although not every structure presented recognition sites [104]. Using the same technique (TREC), Danzberger et al. studied the location of glycans on the corneocyte surface [106]. Glycan moieties were demonstrated to protect CDs from proteolysis, and so to be involved in the desquamation process [107]. In this study, almost all recognition sites for glycans were on top of 'bead-like' topographical elevations (height between 1.1–4.0 nm) [106]. The authors suggested that these structures could be remnants of CDs [29].

An unequivocal correlation between morphology and function of these structures is still lacking, and work to relate the above topographical feature with the mechanical characteristics and maturation states of corneocytes should be done. A study by Guo et al. carried out relevant research by exploring the adhesion of single corneocytes in different layers of the SC. Both peripheral and interplanar adhesion increased with depth. Moreover, cells from the most superficial layers showed a weaker interplanar adhesion compared to the peripheral one, which is consistent with the localization of CDs in the superficial SC [108]. This anisotropy of adhesion forces agrees with the protective barrier role of the SC, allowing for a resistance to stretching and shearing forces, while not compromising the integrity of the layer.

2.10 Conclusions

Corneocytes are the “bricks” of the SC (Figure 2.7) primarily responsible for the mechanical strength and stiffness and contributing to the barrier function. Being the product of differentiation of keratinocytes, these cells create distinct regions in the SC: the inner SC characterized by immature cells with a fragile cornified envelope and a uniform distribution of CDs; and the upper SC with resilient CEs and a honeycomb distribution of CDs.

Regarding their morphology, it is important to note: 1) the regional differences in the surface area and thickness (200 nm to ≤ 1 μm). Corneocytes from body sites usually more protected from chemical, physical and mechanical insults (ventral region of arms and legs and abdomen, for example) generally have a greater surface area (1000-1200 μm^2) and are thinner than those exposed to insults, such as the forehead, cheek, palms, and soles (700-800 μm^2) [109]. 2) The increase in the surface area of corneocytes with age, and finally, 3) the correlation between the surface area, thickness, and location of these cells in the SC, with upper cells presenting a greater surface area and smaller thickness than deeper cells, which depends upon the sequential maturation of corneocytes along the SC [38, 110, 111]. This morphological maturation is ultimately related to the mechanical properties of corneocytes [52], with immature cells from the deeper regions of the SC being less stiff than those at the surface [47, 52].

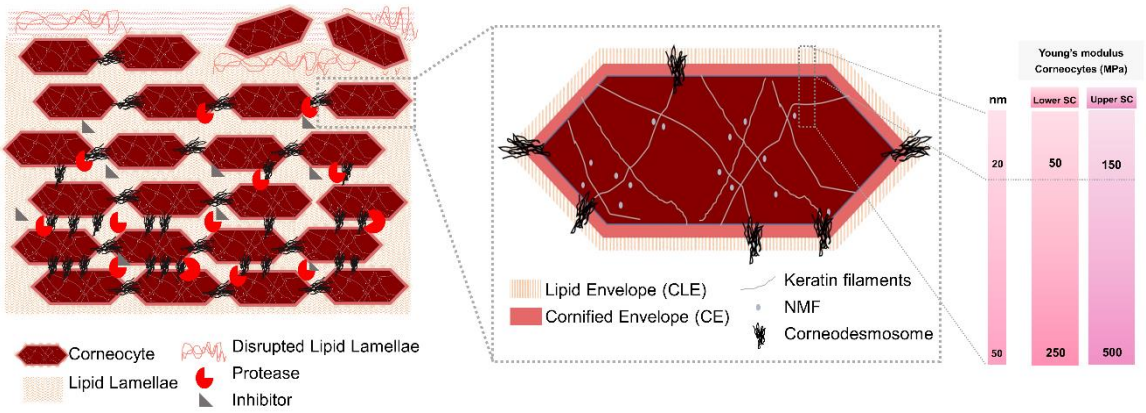

Figure 2.7. "Brick and mortar" illustration of SC (stratum corneum). The SC which can be theoretically classified into two main zones. Deeper SC (stratum compactum) that is close to the stratum granulosum, which represents the compact SC with CDs present over the whole surface of the corneocytes. Outer SC (stratum disjunctum) with the transition to desquamating surface, which is characterized by looser corneocytes (CDs create a honeycomb pattern). The lipid lamellae are well formed and imparts some plasticity compared to the cohesive deeper SC. Moreover, the morphology and strength of the corneocytes is consistent with this classification since the inner corneocytes are softer than those at the surface. The maturation of the cornified envelope may assist in compensating for the loss of cohesion of the outer SC with a greater mechanical strength of the individual cells.

Corneocytes are more rigid compared to other cell types (the Young's modulus of other cell types such as muscle [112] and fibroblasts [113] are typically a few kPa) and presenting two distinct mechanical regions: the cornified envelope (100–250 MPa) and the keratin matrix (250–500 MPa).

The SC is usually described as having two different regions, the stratum compactum, and the stratum disjunctum relating to the maturation of corneocytes, particularly in the distribution of CDs over the cell surface, as represented in Figure 2.5. There is a progressive degradation of CDs from the inner to the outer SC, the latter being characterized by a honeycomb structure. The presence of CNOs seems to be related to CDs, since these structures have been observed to contain corneodesmosin. However, a clear relation between their presence in normal skin and their function is still lacking. Moreover, the SC from different body sites possesses different

characteristics, particularly that from palmar and plantar regions, which is much stiffer and cohesive with a uniform distribution of CDs over the surface of the cell [9594]. Although the stiffness of plantar corneocytes seems to arise from the expression of K9, further mechanical studies are needed to comprehend the maturation of the cornified envelope in such regions, particularly how it is affected by the persistence of CDs in the upper SC.

To understand the morphological and mechanical properties of corneocytes is a crucial step in revealing the mechanisms underpinning skin barrier function and integrity loss. Intercellular lipids are normally considered to be the barrier function elements of SC; however, the optimal arrangement of this “mortar” seems to depend on the correct formation of a cornified protein and lipid envelope that serves as a scaffold. The literature reviewed indicates that the relationship between the maturation of corneocytes and the mechanical resistance is one of the most critical steps in the formation of an effective SC barrier. When the morphology of the corneocytes is perturbed, an impaired barrier function is observed, and some skin disorders may arise. Furthermore, in the presence of water, there is increased degradation of CDs, which may compromise the response of the SC towards loading.

However, there are still gaps in the knowledge about these cells, particularly in their response to mechanical loading and frictional forces and on the role of the structural lipids attached to the CE on the desquamation process, as well as the implications of their presence on the skin microbiome. It has been suggested that the CLE may, on one hand, function as a scaffold for the organization of the extracellular bilayers and, on the other, to contribute to the cohesion of the SC [78]. Moreover, it is thought that the CLE may function as a selective body of permeation; allowing free

transmembrane passage of water, while restricting the loss of larger hygroscopic molecules out of the cell, such as filaggrin breakdown products [78].

It is also relevant to mention the overlooked relationship that seems to exist between the accelerated degradation of CLE and atopic dermatitis [114]. AD is frequently aggravated by the colonization of bacteria secreting ceramidase or the activation of endogenous ceramidase activity [115], which, by contributing to the degradation of the CLE, may induce the release of hygroscopic products from the cell interior, resulting in the appearance of xerosis [116]. A recent study using AFM showed that the adhesion of Staphylococcus aureus to corneocytes from AD patients is controlled by NMF [117]. Reduced filaggrin expression, and consequently low levels of NMF, has been shown previously to facilitate the colonization by these bacteria [118]. The authors postulated that the strong adhesion of Staphylococcus aureus to the cells originates from an increased exposure or expression of ligand proteins on the SC surface. Topographic images show that the surface morphology of corneocytes from low-NMF skin samples present a high density of villous protrusions, which were the regions where strong adhesion bonds were concentrated [117]. The authors also point out that bacterium-skin adhesion is greatly enhanced by physical stress, as shown by the considerable increase in strength of adhesion bonds subjected to tensile forces [117].

Finally, it would be relevant to study the modifications imposed by pressure on the expression of keratins as well as on the maturation of the cornified envelope, both *in vitro* and *in vivo* and to consolidate the knowledge related to mechanical properties of corneocytes of different body sites and site-dependent cell maturation.

CHAPTER III - ATOMIC FORCE MICROSCOPY PROTOCOLS FOR CHARACTERIZING THE ELASTO-VISCOPLASTIC BIOMECHANICAL PROPERTIES OF CORNEOCYTES

This chapter is based on Évora, AS., et al., *Atomic force microscopy protocols for characterising the elasto-viscoplastic biomechanical properties of corneocytes* in peer review at Communications Biology.

3.1 Abstract

Corneocytes, which are dead keratinocytes, are the building blocks of the outer layer of the epidermis, the stratum corneum. Consequently, they are critical in the role of the epidermis as a chemical, biological and mechanical barrier to the external environment. Using nanoindentation by Atomic Force Microscopy, the study aimed to establish a protocol for obtaining accurate results while eliminating experimental artifacts that have contributed to the wide range of Young's modulus values reported in the literature and to obtain a material model that is consistent with their inelastic behaviour. This included the use of a silicone elastomer reference material for determining the effective indenter geometry, which could be described by a polynomial relationship rather than the conventional parabolic or conical assumptions based on their nominal specifications. The study found that the use of a much stiffer supporting substrate was critical in obtaining accurate results, avoiding the interference of substrate compliance. In the dry state, corneocytes exhibited Young's moduli comparable to those of glassy organic polymers. In addition, it was observed that the cells exhibited viscoplastic behaviour that could be described by the Herschel-Bulkley material model, which accounts for the strain rate hardening at stresses greater than the yield value.

3.2 Introduction

Skin is the interface between an organism and the external environment, acting as the first line of defence against a range of external insults, such as mechanical loadings [119, 120]. The contribution of deeper skin layers, such as the dermis, to the architecture and mechanical function of the skin has been studied thoroughly [121, 122]. However, the role of the epidermis, and particularly that of the Stratum Corneum (SC), on the mechanical integrity of skin has been mostly ignored. Nevertheless, the SC is the most superficial layer of the skin, and thus it must adapt to the physiological and boundary requirements of each anatomical location, as exemplified by the special case of glabrous skin [70]. Consequently, it is important to explore to what extent the SC contributes to the mechanical resistance of skin across different body sites and under different conditions.

The stiffness and strength of any tissue depends on the mechanical properties of its constituent cells and extracellular matrix, rendering the mechanical study of single cells as key in understanding many biological processes [123]. The SC and its main cell type (corneocytes) have been characterized topographically and mechanically using Atomic Force Microscopy (AFM) [40, 51, 52, 124]. The Young's modulus of corneocytes has been previously reported in the literature [40, 49, 50, 52, 125], but with a high degree of variability, ranging from a few MPa [50] up to 0.4 GPa [48]. Most of these studies consider that corneocytes deform elastically so that the loading and unloading curves can be described by applying the Hertz or JKR models, with or without an adhesion component respectively, which are based on a spherically capped indenter [49, 52]. However, as demonstrated by Beard et al. [51], when indenting corneocytes there is plastic deformation. These authors performed mechanical tomography with

nanoneedles and used the Oliver-Pharr analysis to calculate the elastic modulus from the unloading curves. The value of the Young's modulus was observed to increase with indentation depth, being about 100 MPa for indentation depths < 50 nm, and 500 MPa for greater depths [51]. Milani et al. [52] also reported an increase in the modulus with indentation depth, being 250 and 300–520 MPa for indentation depths of < 50 nm and > 50 nm, respectively. They used a tomographic technique that was performed with pyramidal probes and relied on a linear elastic model based on a rigid cone indenting a flat surface. Furthermore, corneocytes from the inner SC presented smaller Young's modulus values (250–300 MPa) compared to superficial cells (300–520 MPa) [52]. The main differences in the protocols of these two studies, apart from the contact mechanics models employed, were the geometries of the probes and the stiffnesses of the cantilevers. While Beard et al. [51] used cantilevers with a spring constant of 35 N/m, and cylindrical nanoneedles with a tip radius of 20 and 35 nm, Milani et al. [52] used more compliant cantilevers (2.5 N/m) and three-sided pyramidal probes [52]. There were also differences in how the authors harvested the cells. Beard et al. [51] used hair removal wax melted on a microscope glass slide to strip the SC, as a relatively hard substrate for AFM. Milani et al. [52] stripped the SC using circular adhesive tapes (D-squame, CuDerm Corp., Dallas, TX, US) and adhered the tapes to a microscope glass slide using double-sided tape. The selection of the substrate is of considerable importance for nanoindentation, as will be discussed later; soft substrates may have a large compliance compared with the sample [126].

While the use of AFM as a nanoindentation technique has now been established, there are still many uncertainties in the protocols that must be addressed in order to achieve standard practices that allow comparisons across different studies. Such

uncertainties range from intrinsic calibrations required by the system, including the spring constant of the cantilever, sensitivity of the system, and geometry of the probe, to the analysis of the data, including the appropriate selection of the contact mechanics model. One of the main uncertainties in most AFM nanoindentation studies is the overall geometry and tip radius of the probes since most authors assume that the nominal values given by the manufacturer are accurate [48, 50, 52]. This is critical for selecting the correct contact mechanics model. Colloidal spherical probes are usually used for the mechanical analysis of cells due to their defined geometry. [126]. However, one of the main advantages of AFM is the coupling of topographical and biomechanical analysis that can be achieved with standard imaging probes, also known as sharp AFM tips. This is particularly important for assessing how corneocyte surface properties correlate with their mechanical behaviour. In fact, the presence of circular nano-objects at the surface of skin cells has been associated with certain skin conditions such as Atopic Dermatitis [125], but no attempt has been yet done to correlate these maturation properties with the stiffness of skin cells. Moreover, although tips with well-defined geometries enable a simpler interpretation of mechanical data, they are considerably more costly, which is a disadvantage for examining multiple samples from a large cohort of subjects that involve establishing the potential as biomarkers for applications such as screening for early stage pressure markers.

Standard imaging AFM probes are usually assumed to have spherical tips and to behave either as pyramids or cones for indentations greater than that of the tip radius. Therefore, when assuming a purely linear elastic deformation (as in most studies with cells), the Hertzian model is selected for indentation depths, h, that are much smaller than the nominal tip radius, R. In this case, the tip geometry may be treated as

parabolic and then $F \propto h^{3/2}$, where F is the applied force. When $h > R$, it is often assumed that $F \propto h^{2}$ for a conical geometry [127] since the given nominal tip radius is usually quite small ($R < 10$ nm) using standard AFM probes. These assumptions have been challenged by Fugimani et al. [128] for the case of adhesive elastic contacts. They explored the cone-paraboloid transition for sharp AFM tips and showed that unsuitable geometric assumptions can give large errors. That is, it is important to know the total tip geometry, from the tip to a distance equal to the maximum contact depth, h_c.

Therefore, given the variability of reported values of the Young's modulus and the lack of a comprehensive protocol for measuring the mechanical properties of corneocytes using AFM, the current work aims to explore the main important variables of AFM force spectroscopy, and to describe the appropriate data analysis for characterising the mechanical behaviour. Initially, the effective geometry of the AFM tip was determined by using a silicone elastomer reference material in the presence of an aqueous sodium dodecyl sulphate (SDS) solution to attenuate the adhesion. From nanoindentation unloading curves, it was then possible to calculate the elastic modulus of corneocytes in the dry state collected from three healthy subjects. The mechanical properties of the corneocytes were further studied by performing stress-relaxation experiments. It was observed that the cells exhibited viscoplastic behaviour that could be described by the Herschel-Bulkley material model.

3.3 Methods

3.3.1 Corneocyte collection.

Corneocytes were collected from three healthy adult participants (two males and one female), with ages ranging from 26 to 29 years, in accordance with the UK regulations

and the Declaration of Helsinki. Ethics approval was obtained from the University of Birmingham Research Ethics Committee – ERN-19-1398A. Samples were collected using the tape stripping method (Sellotape, UK). A first layer of corneocytes from the volar forearm was removed and discarded to avoid the presence of contaminants, such as clothing fibres. The second tape strip was used for the AFM measurements. Half of the tape was used directly, while the other half was pressed on a glass slide and immersed in xylene overnight. This detaches the tape, by dissolving the tape adhesive, leaving the corneocytes transferred to the glass. Attached cells were further washed (2× for 30 min) in xylene. FTIR spectra of corneocytes before and after xylene extraction did not reveal any structural differences (Appendix A4). Topographical images of the cells (40 × 40 μm) and a zoom-in TM image (5 × 5 μm) from the central region were obtained (workflow described in Figure A3 of Appendix A).

3.3.2 Environmental Scanning Electron Microscopy (ESEM) and Tapping Mode (TM) AFM for determining the probe geometry.

The overall geometry of the AFM tip was measured using ESEM. The sample was sputter coated with platinum and imaged using a Philips XL30 FEG ESEM operating in high vacuum mode with an accelerating voltage of 20 kV. Image J® version 1.53a (National Institutes of Health, Bethesda, MD, USA) was used to process the ESEM images. The effective tip radius was also evaluated by imaging a calibration sample (TipCheck, Apex Probes, UK) in Tapping Mode (TM) and using a blind tip estimation (partial) algorithm included in Gwyddion, which is an open-source software package for AFM image processing [138]. This algorithm iterated over all the surface data and refined the tip point according to the steepest slope in the direction between the tip point and tip apex.

3.3.3 Silicone elastomer (PDMS) sample preparation for indenter geometry calibration

Polydimethylsiloxane (PDMS) was selected as an ideal material for calibrating the geometry of the indenters since it has a relatively small Young's modulus that is appropriate for the cantilever stiffnesses used for the corneocytes and it is homogeneous, isotropic and, at small strains and strain rates, it is linear elastic. It was cured as in Wang et al. [129]. While there have been a number of studies suggesting that the Young's modulus of PDMS increases with decreasing indentation depths, recently it has been shown that this arises from errors in the surface detection [130]. In the current work, the PDMS was prepared by mixing Sylgard 184 silicone elastomer base and Sylgard 184 silicone elastomer curing agent (Merck KGaA, Darmstadt, Germany) in a mass ratio of 5:1 (base/curing agent). A PDMS sheet (5 mm in thickness) was made by pouring the mixture into a flat bottom polystyrene dish, and PDMS was degassed under vacuum to remove air bubbles. It was cured in an oven at 65 °C for 1 h. The sheet was cut with a biopsy punch and the cast side facing air was used for force spectroscopy measurements. This reference specimen had a mean roughness, S_a, calculated from AFM Tapping Mode of 2.1 nm (from 25 μm^2 AFM image – see Figure 3.2a).

3.3.4 AFM experiments

AFM imaging and indentation experiments were performed in air operated in tapping mode (TM) and Force Spectroscopy, respectively (Nanowizard 4, Bruker, JPK BioAFM, Berlin, Germany). Indentation involved a standard silicon TM tip (NCHV-A, Bruker AFM Probes, Inc). On the basis of the values of Young's modulus described in

the literature for corneocytes (hundreds of MPa), AFM cantilevers with a nominal spring constant of 40 N/m (relatively stiff) and nominal resonance frequency of 320 kHz were selected, with the advantage of being able to perform a topographical characterization using TM-AFM of the regions of interest. All measurements were conducted under a controlled temperature and humidity of 25.5 °C and 35% RH. The loading and unloading data were analysed using customised MATLAB scripts (MathWorks Inc).

Force spectroscopy consists of the nanoindentation of a sample by a tip located on a cantilever. Raw cantilever deflection data is recorded as a change in amplitude (in Volts), which can be converted to force by calibrating both the deflection sensitivity of the system and the spring constant of the cantilever. The deflection sensitivity is calculated before or after each set of experiments by pressing the tip onto a 'relatively' rigid material (e.g., microscope glass slide or sapphire, depending on the cantilever stiffness). Since there should not be a significant indentation on the stiff substrate, the deflection of the cantilever represents the sensitivity of the system (V/nm). Here, the sensitivity of the equipment was calibrated after each set of experiments by pressing onto a sample of sapphire considering that the probe is made of etched silicon, which has a Young's modulus of about 130 GPa [131], and thus, greater than that of glass (E = 72 GPa [131]), but much smaller than that of sapphire (E = 460 GPa [131]). This resulted in a smaller slope (i.e., the sensitivity) of the force curve (18–22 nm/V), when pressing sapphire, than when pressing on the microscope glass slide (28–35 nm/V (see Figure A4).

The spring constant or stiffness of the cantilever (N/m) is usually calibrated using the Sader method [132], which considers the size of the cantilever, as well as a thermal tuning spectrum as a result of the thermal motion, to which a single harmonic oscillator

is fitted in order to extract the resonance frequency and quality factor. In the current study, the cantilever had a spring constant of 28.5 N/m, which, although being in the range of values given by the supplier (20–75 N/m), is significantly different from the nominal value of 40 N/m. Consequently, the spring constant of cantilevers should be calibrated to ensure corrected values of force.

3.3.5 Nanoindentation of PDMS

Nanoindentation measurements were performed on the PDMS specimen in a solution of 0.1% w/w aqueous sodium dodecyl sulphate (SDS) to attenuate adhesion forces [133]. Three different regions were evaluated with 64 force curves (in each 5 × 5 μm region) at a maximum setpoint of 250 nN. The loading and unloading force data as a function of tip displacement were obtained using the AFM force spectroscopy mode, from which the geometry of the probe was determined as summarised below and described in more detail in the Appendix A.

3.3.6 Nanoindentation of corneocytes

Nanoindentation measurements were carried out on corneocytes adhered to Sellotape and after being extracted with xylene and fixed to a microscope glass slide (Figure 3.3a and 3.3b). The selection of the substrate is very important since the tape used here as a substrate is composed of two main components: a backing film, and an adhesive, to which the corneocytes adhere. These adhesives usually belong to the family of polyacrylates, which are characterized by a relatively small value of Young's modulus of less than tens of MPa [134]. Nanoindentation should be performed to a depth of <10% of the sample thickness in order to avoid artifacts arising from the substrate [135]. However, this is only applicable for stiff substrates. When the substrate is softer

than the sample, as in the case of tape, even for techniques at the nano length-scale, such measurements will result in the sample being pushed onto the substrate as it is indented (Figure 3.3a).

For a total of 5 cells per subject, 64 loading and unloading force curves were collected in a 5 x 5 µm region at a velocity of 0.5 µm/s. This included a dwell time of 4 s after loading to allow any viscous component to relax. For each corneocyte, the maximum force setpoint was adjusted by ensuring that the maximum indentation depth was not greater than 10% of the cell thickness (≤ 1 µm) in order to avoid artifacts arising from the supporting substrate [136]. The maximum applied force was 250 nN for cells adhered to Sellotape and 2 µN for cells fixed on a microscope glass slide in order to obtain similar indentation depths with both methods ranging between 30–100 nm (Figure 3.3). Force-relaxation measurements of the corneocytes were obtained during the dwell time of 4 s at constant z-height, after the trigger threshold was achieve. Individual force-time curves (64 curves in a 5 x 5 µm matrix) were obtained for five corneocytes per sample, at a loading velocity of 0.5 µm/s.

3.4 Results

3.4.1 Initial calibration of the tip radius using Environmental Scanning Electron Microscopy (ESEM) and AFM tip characterizer

The approximate overall geometry of the probe used in the current work was obtained from Environmental Scanning Electron Microscopy (ESEM) images (Figure 3.1a), which revealed an overall conical-like shape. For AFM, it is common to use Tapping Mode (TM) imaging of a reference sample to determine the tip geometry by applying a blind tip estimation Gwyddion algorithm [137] to obtain a 3D projection of the tip and a

value for the tip radius [138, 139]. This analysis resulted in an asymmetric paraboloid-like structure for the first 50 nm of the tip apex with a radius of curvature in all directions of 53.2 ± 6.9 nm (Figure 3.1b).

3.4.2 Nanoindentation of PDMS

To derive a more complete quantitative description of the probe geometry, indentations were performed on a reference elastomeric material, polydimethylsiloxane (PDMS). It was assumed to behave as an isotropic linear elastic half-space [140], which is reasonable for small strains and strain rates. A complete description of the calibration methodology is described in Appendix A (A1). The PDMS surface topography and representative force data are presented in Figures 3.2a and 3.2b, respectively.

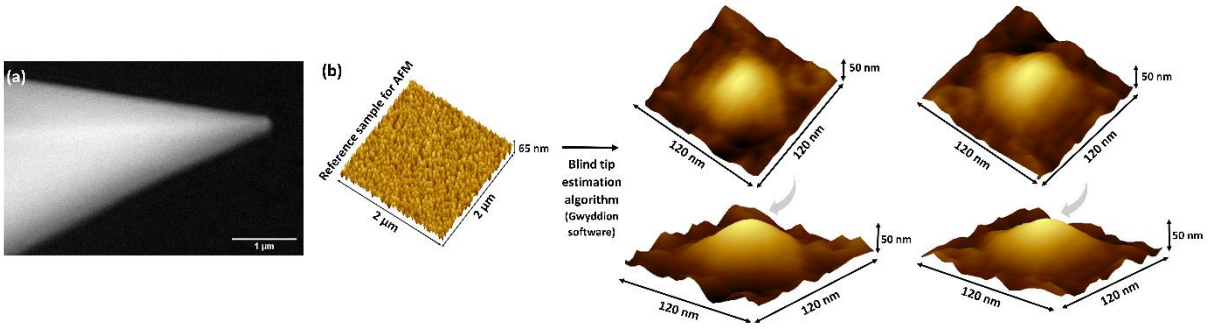

Figure 3.1. Preliminary characterization of the AFM probe geometry. (a) ESEM image. **(b)** Using an AFM reference sample for which the surface topography is shown; a blind tip estimation was performed using Gwyddion software. The tip radius evolution was calculated during imaging (using partial analysis) of a blind estimation applied to 20 horizontal strips of the image. 3D projections show two viewing angles (180° apart) of the tip geometry obtained.

The relationship between the geometry of a probe and the resulting indentation force as a function of indentation depth for PDMS can be obtained by first considering the general expression for the contact stiffness, S [127]. Treating the indenter as being both axisymmetric and rigid:

$$S = \frac{dF}{dh} = \frac{2E}{1-\nu^2}a = 2E^*a \quad (1)$$

where F is the indentation force, h is the indentation depth, and a is the contact radius. E^* is the plane strain elastic modulus such that E and ν are the Young's modulus and Poisson's ratio of the PDMS; it was assumed that ν = 0.5 since PDMS is considered incompressible.

The value of E^* for the PDMS calibration specimen used was measured to be 3.79 ± 0.21 MPa using a micromanipulator equipped with a flat-ended cylindrical probe. This is routinely employed to determine the mechanical properties of micro-particles (Appendix A5) [140, 141]. For the current purpose, the linear slope of the force as a function of the indentation depth gives the contact stiffness and the (constant) contact radius is known so that E^* can be calculated from Eq. (1). In the case of the AFM nanoindentation experiments, E^* is assumed to be given by the same value but the probe geometry is the unknown.

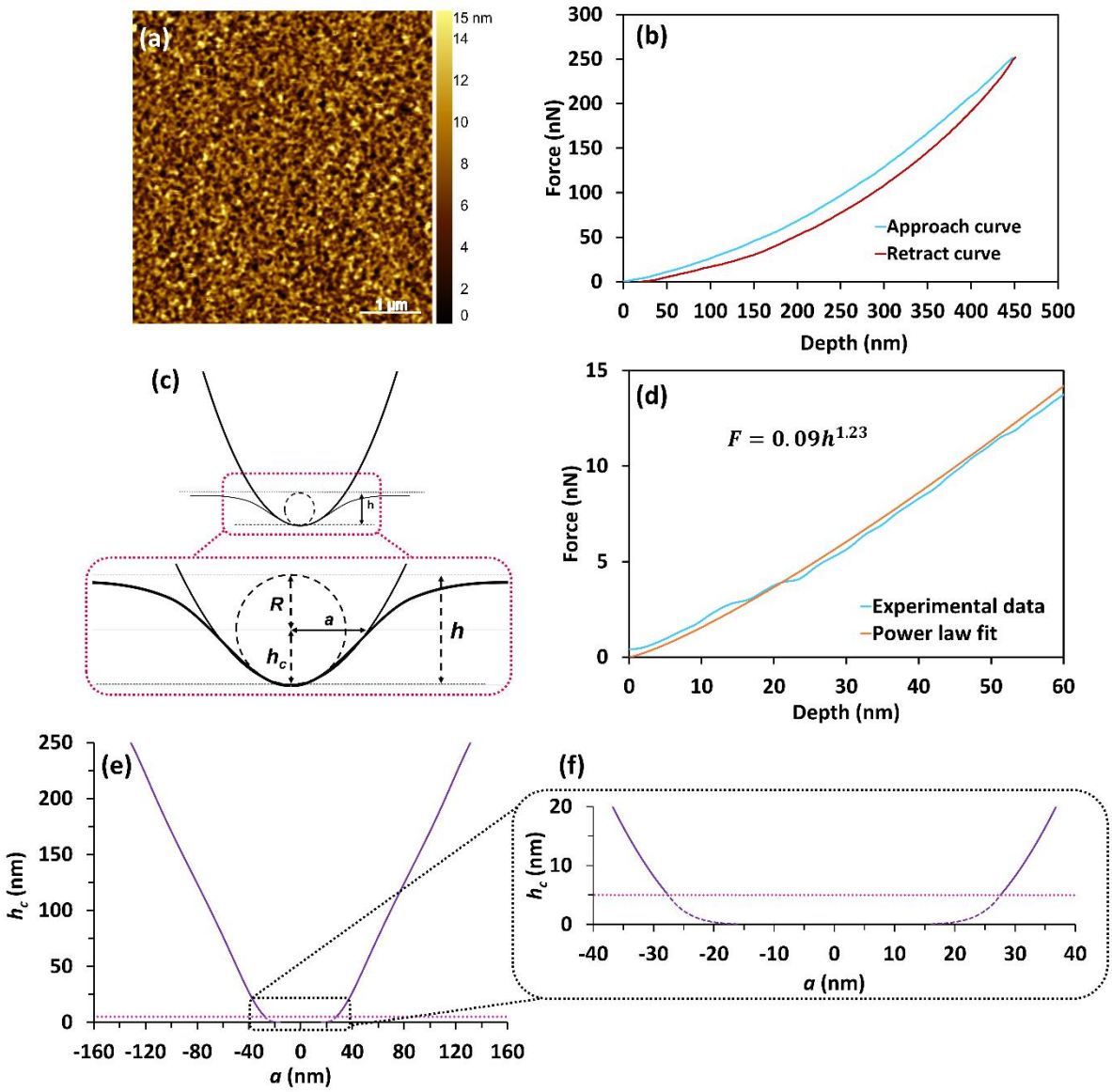

Figure 3.2. PDMS as AFM nanoindentation reference material. (a) Surface topography of the PDMS sample (5:1) used for the characterisation of the probe. **(b)** Representative indentation loading and unloading curve for the PDMS in 0.1% aqueous SDS showing a typical elastic deformation with minimal adhesion. **(c)** Assumption of a hard standard TM AFM tip indenting a soft elastic material as a paraboloid of revolution where h_c is the contact depth, h is the total indentation depth, R is the end radius of curvature of the parabola and a is the contact radius. **(d)** Representative power law fit to the initial 60 nm of a PDMS loading curve presented in (b). **(e)** Average tip radius function obtained from Eq. 10 (see Fig. S2). **(f)** Zoom-in of the tip geometry for a maximum contact depth of 20 nm. The tip geometry was determined from a minimum h_c = 5 nm, as indicated by the dotted magenta line. The dashed line shows the power law for h_c = 5 nm, where n = 7.55 ± 0.20 and c = (7.90 ± 3.90) x 10^{-11} µm$^{-6.82}$, see Eq. (6).

For indentations with a spherically tipped probe, the Hertzian force as a function of depth relationship that is commonly used to obtain E^* from loading curve is [140]:

$$F = \frac{4}{3} E^* R^{1/2} h^{3/2} \quad (2)$$

where R is the radius of the sphere.

Eq. (2) can be obtained by integrating Eq. (1), after approximating the circular contact profile, $h_c(a)$, by a parabola (see Figure 3.2c):

$$h_c = \frac{a^2}{2R} \quad (3)$$

where h_c is the contact depth, and by using the paraboloid relationship between the indentation depth and the contact depth [140]:

$$h = 2h_c \quad (4)$$

Eqs (3) and (4) are a close approximation for a spherical indenter, as is Eq. (2) provided that the contact radius is small compared to the sphere radius. This is not the case for the probes used in the AFM nanoindentation measurements (see Figure 3.2c).

AFM loading curves can be fitted to a power law in order to investigate the applicability of Eq. (2):

$$F = bh^m \quad (5)$$

where b and m are the power law load coefficient and load index respectively.

For PDMS, when analysing the AFM loading curves (Figure 3.2b), it was found that the best-fit for the power law index was not 3/2 but varied with indentation depth,

being slightly greater than 1 for fitting the data close to contact (Figure 3.2d), and ≈ 1.7 for data at deeper depths. In fact, experimentally, a 2nd order polynomial with zero intercept appears to provide a more satisfactory fit over the entire range of the loading curve, rather than a single power law. This indicates that the probe geometry is more closely approximated by a truncated cone than a single power law such as a paraboloid (m = 1.5).

Thus, the blind estimation of the tip is misleading. Consequently, in the current work, an alternative analysis was used to obtain a more accurate geometry of the probe. In summary, this is based on multi-term polynomial smoothing and averaging of multiple loading curves to calculate, firstly, the contact radius as a function of the indentation depth, $a(h)$, using Eq. (1) and, secondly, $m(h)$. The tip radius profile, $a(h_c)$, is derived from these two functions utilising indentation equations for a generalised power law indenter profile:

$$h_c = ca^n \tag{6}$$

where c and n are the power law indenter profile coefficient and indenter profile index respectively. Eq. 6 is the general form of Eq. 3 when n = 2. The two indices are related as follows [140]:

$$n = \frac{1}{m-1} \tag{7}$$

The relationship between the indentation depth and the contact depth is given by:

$$h = \kappa h_c \tag{8}$$

where κ is a scaling factor given by [140]:

$$\kappa = \sqrt{\pi}\frac{\Gamma\left(\frac{n+2}{2}\right)}{\Gamma\left(\frac{n+1}{2}\right)} \tag{9}$$

where $\Gamma(.)$ is the Gamma function. Eq. (8) is the general form of Eq. (4) since κ = 2 when n = 2.

Figures 3.2e and 3.2f show the resulting values of $a(h_c)$ for the probe used in the current work. The prediction of the contact radius is not reliable for h_c < 5 nm because the variability in the experimental results is too great in this region, but the near-contact geometry is shown as a power law cap as a dashed line in Figure 3.2f. In Table 3.1, the geometric parameters of the tip at different indentation depths are reported. A more comprehensive table and the tip area function example can be found in Appendix A.

Table 3.1. Elastic analysis of PDMS. The parameters of the indenter geometry obtained from an elastic analysis of PDMS. E^* was independently calculated from micromanipulation experiments based on the indentation of 3 different regions of a PDMS sample. The load index, m, of the power law was calculated at different contact depths, h_c, based on a polynomial fit of the loading curves of PDMS. The derived parameters c and n define the local geometry of the AFM tip at different contact depths. Mean ± 1 SD

h_c (nm)	10	20	40	60	80	160
m	1.184 ± 0.004	1.240 ± 0.004	1.311 ± 0.002	1.380 ± 0.002	1.45 ± 0.002	1.663 ± 0.005
n	5.41 ± 0.10	4.62 ± 0.08	3.21 ± 0.03	2.63 ± 0.01	2.22 ± 0.01	1.51 ± 0.01
c **(μm^{1-n})**	(7.80 ± 3.11) x 10^{-8}	(5.90 ± 1.31) x 10^{-6}	(1.85 ± 0.21) x 10^{-4}	(1.65 ± 0.09) x 10^{-3}	(8.30 ± 0.02) x 10^{-3}	0.16 ± 0.01

Finally, a best fit polynomial from h_c = 10 nm to h_c = 200 nm is derived for $a(h_c)$:

$$a = d_0 + d_1 h_c + d_2 h_c^2 + d_3 h_c^3 + d_4 h_c^4 + d_5 h_c^5 + d_6 h_c^6 \quad (10)$$

This typically covers the complete range of h_c values obtained from the corneocyte indentation measurements. The first two terms in Eq. (10) have physical relevance as representing a perfect truncated cone, with the higher terms accounting for deviations from this profile.

3.4.5 Nanoindentation and stress relaxation of corneocytes

The loading-unloading data at a speed of 0.5 μm/s obtained for cells attached to tape exhibited a hysteresis loop (Figure 3.3a), which was not observed for the PDMS (Figure 3.2b). This may be the result of viscous, plastic and/or adhesive components [51, 141, 142]. For both elastoplastic and viscoelastic deformations, after the removal of a load, a residual imprint may remain on the surface [143]. For elastoplastic materials, this imprint is irreversible, while for viscoelastic deformations, the imprint is time-dependent and may recover given sufficient time. In the current experiments, a permanent indent was observed on the surface by imaging the cells after indentation (Figures 3.3c–3.3e).

Although the corneocytes exhibited elastoplastic behaviour, the unloading data for such materials is purely elastic and, consequently, the Young's modulus is given by the following expression [54]:

$$E = \frac{\sqrt{\pi}}{2}(1 - \nu^2)\frac{S_0}{\sqrt{A}} \quad (11)$$

where S_0 is the stiffness at the maximum force of the unloading curve, F_{max}, corresponding to the maximum indentation depth, h_{max} , and $A = \pi a^2$ [144] is the contact area. The Poisson's ratio for corneocytes, ν, was assumed to be 0.4, considering what

has been described for keratin [145]. To obtain the contact radius, the tip area function calibrated with PDMS (Figure 3.3e, Table 3.1 and Appendix A1) was used. On the basis that, for an elastoplastic contact, the contact depth, h_c, is related to h_{max} by the expression [54]:

$$h_c = h_{max} - h_s \tag{12}$$

where h_s is the surface elastic deflection at the perimeter of the contact (Figure 3.4b), which is given by the following expression [54]:

$$h_s = \phi \frac{F_{max}}{S_0} \tag{13}$$

The unloading stiffness, $S_0 = dF_{max}/dh$ was obtained by differentiating the following polynomial fit to the upper 80% of the unloading curve and determining the slope at h_{max} [146] (Figure 3.4a):

$$F = C_e h^2 - \left(2C_e h_f\right)h + C_e h_f^2 \tag{14}$$

where C_e and h_f are fitting parameters. The geometric factor, ϕ, was assumed to be 0.73 for a conical indenter, following the work of Oliver and Pharr [147] and considering that the load index, *m*, of the unloading curves of corneocytes was $m \approx 2$. Eq. 14 is an expansion of the following power law with $m = 2$:

$$F = C_e(h - h_f)^m \tag{15}$$

The overall values of Young's moduli of the volar forearm corneocytes on the tape used to harvest the cells and on a microscope glass slide are presented in Table 3.2. Cells adhering to tape showed smaller values in the range of 12–66 MPa, compared to the most recent literature that reports values in the range of 250–500 MPa [51, 52]. However, cells on a microscope glass slide had much greater values ranging from

192–1636 MPa (Table 3.2 and Figures 3.4c–h), which reflects the advantage of a stiff supporting substrate. Although greater than reported previously, they are consistent with those obtained for SC, of about 2 GPa at 30% RH, and decreasing with RH (~1 GPa at 50% RH) [21]. Since corneocytes in this study are in a relatively dry state (35% RH), they display mean Young's modulus values that are similar to polymers in the glassy state [148, 149], which has also been observed for keratin, the major component of these cells [150]. The interpretation of the variability found between cells and participants was not the subject of the current study. Nonetheless, it may be due to the limited number of cells and participants or dependent on the maturation level of individual corneocytes and on the amount of NMF [125].

Table 3.2. The Young's moduli of volar forearm corneocytes either attached to tape strips or fixed to glass microscope slides. The maximum force setpoint used was 250 nN for the tape substrate and 2 µN for the glass substrate. The results for three participants are presented as the median and range (for 5 cells and 64 force curves per cell).

Participant ID	Young's modulus (MPa)	
	Tape	Glass slide
1	15.9 (12.5–21.5)	1183 (482–1263)
2	21.6 (13.8–66.6)	424 (200–533)
3	31.3 (16.3–39.5)	1105 (423–1562)

Such variation is not uncommon when performing mechanical characterization using AFM, particularly for biological samples. For example, previous studies have reported a large range of values when indenting hair [151, 152]. Biological materials are not homogeneous and, in the case of corneocytes, the specific local arrangement of the keratin network and intercellular junctions, differences in the architecture of the CE or other unaccounted factors, such as the surface topography, may give rise to such distributions.

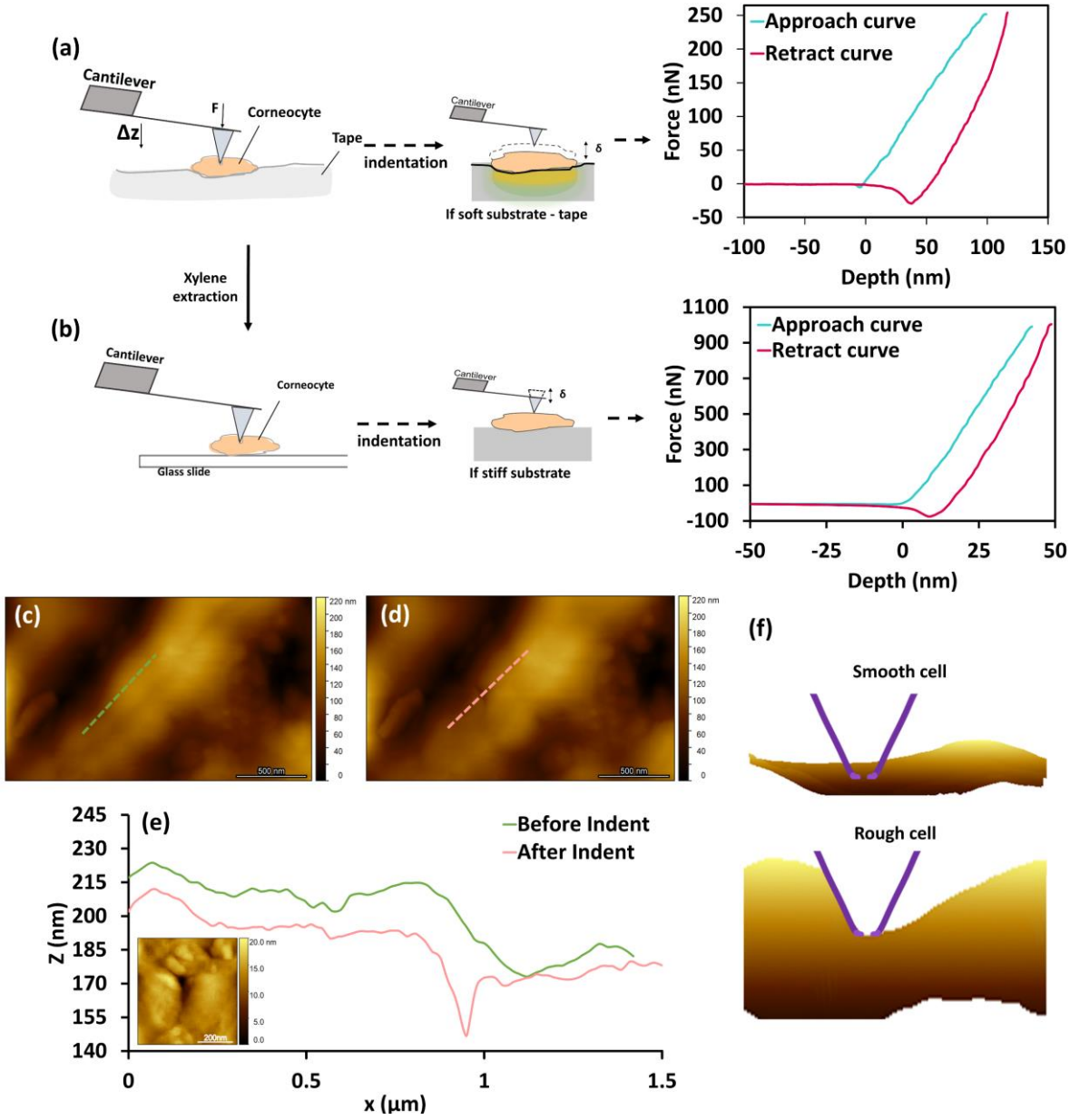

Figure 3.3. Corneocytes present plastic deformation. (a) Schematic steps used to measure the mechanical properties of corneocytes that illustrate the effect of the compliance of the supporting substrate. The cells were initially adhered to Sellotape (soft substrate) and **(b)** were then extracted to a glass slide (stiff substrate) using xylene to dissolve the adhesive. **(c)** and **(d)** correspond to the surface topography of a corneocyte before and after indentation of cells on a glass slide with a force of 2 µN. **(e)** The line profiles from (c) and (d) with an inset showing a zoomed topographical AFM image from (d) of the permanent indent remaining on the surface of the cell. **(f)** Schematic diagram of the AFM tip geometry in comparison to the cell surface topography for rough and smooth cells.

Typical force-relaxation data are shown in Figure 3.5. The aim was to determine the parameters for a viscoplastic material model that would be more representative of the mechanical properties of corneocytes. The data were analysed using a Prony series for which two relaxation times were sufficient (Figure 3.5c) [153]:

$$F(t) = B_0 + B_1 e^{-t/\tau_1} + B_2 e^{-t/\tau_2} \quad (16)$$

where B_0, B_1 and B_2 are constants, τ_1 and τ_2 are relaxation times and t is the time. The corneocytes deform plastically and may be characterised by the hardness, H:

$$F = \pi a^2 H \quad (17)$$

Moreover, the mean contact stress, $\bar{\sigma}$, is equal to the hardness:

$$\bar{\sigma} = H = \frac{F_{max}}{A_{max}} = \psi \sigma_Y \quad (18)$$

where σ_Y is the uniaxial yield stress and $\psi \approx 3$ is the constraint factor assuming that the substrate has fully yielded [154].

For materials that show viscoplastic behaviour, the hardness H is strain rate-dependent. Following the approach described by Yan et al. [153], the time-invariant parameter H in Eq. (18) may be replaced by the time-dependent value $H(t)$ to describe transient measurements, where $H(t)$ can then also be written as a Prony series:

$$H(t) = C_0 + C_1 e^{-t/\tau_1} + C_2 e^{-t/\tau_2} \quad (19)$$

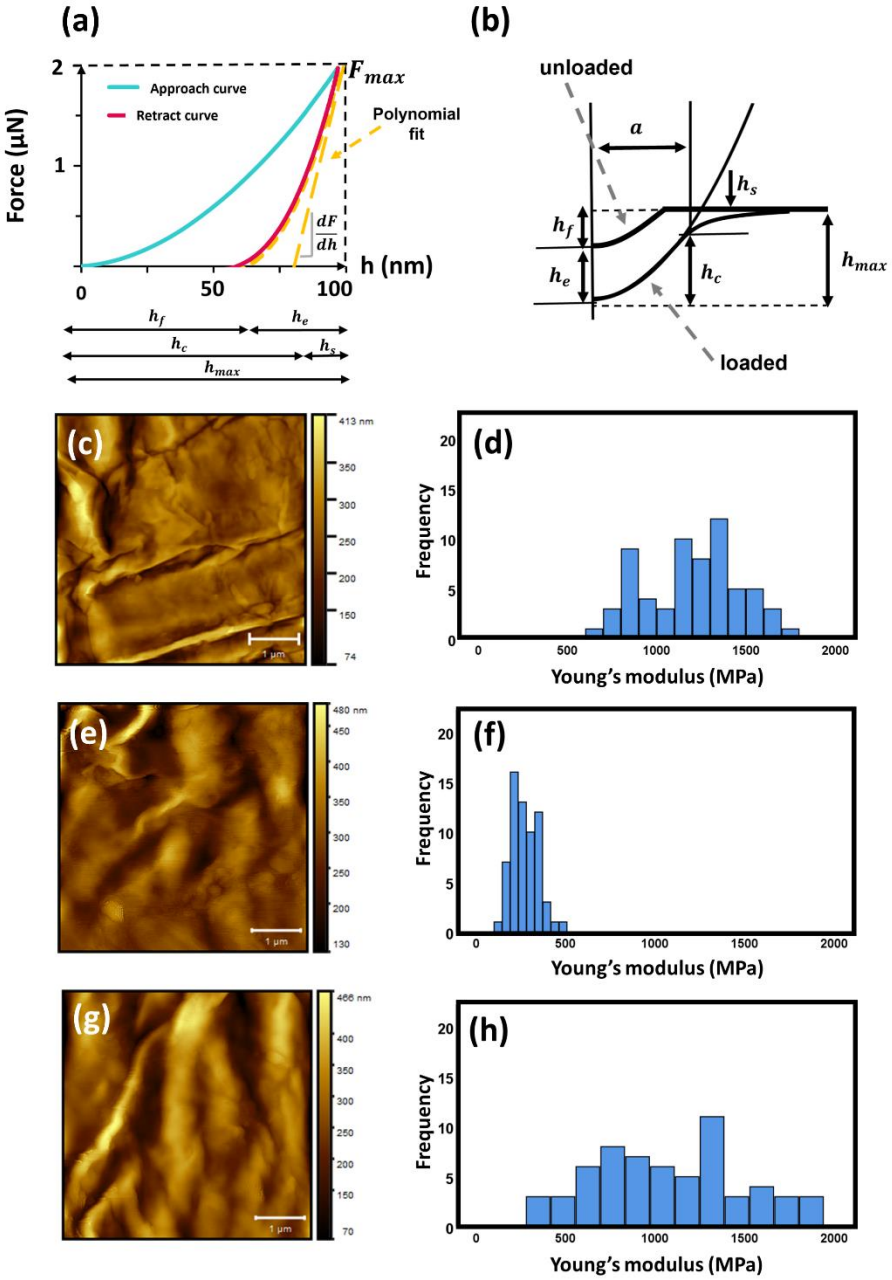

Figure 3.4. Young's modulus of corneocytes can be calculated using Oliver-Pharr analysis. (a) Graphical representation of the load as a function of the indenter displacement showing the quantities used in the analysis and **(b)** a schematic interpretation of these quantities**,** adapted from [28]. a – contact radius; h_{max} – maximum indentation depth; h_c – contact depth; h_s – the surface elastic deflection at the perimeter of the contact; h_f -final impression of the residual hardness impression; h_e – elastic component of the displacement.**(c–h)**TM AFM images of corneocytes and histograms showing values of Young's modulus calculated from 64 force curves in that region for **(c** and **d)** Cell 1 of P1, **(e** and **f)** Cell 3 of P2 and **(g** and **h)** Cell 4 of P3. The cells were fixed on a glass slide and the maximum force setpoint was 2 µN.

The coefficients C_0, C_1 and C_2 are related to B_0, B_1 and B_2 (Eq. (16)) as suggested in [153, 155] by the following expression:

$$C_i = \frac{B_i}{\pi a^2} \tag{20}$$

where $i = (0,1,2)$ and a is obtained from the analysis of the unloading data as described previously.

The instantaneous hardness, H_0, and the long-term hardness, H_∞, can be estimated using the following expressions:

$$H_0 = \sum_{i=0}^{m} C_i \tag{21}$$

and

$$H_\infty = C_0 \tag{22}$$

Table 3.3. Material parameters of the volar forearm corneocytes calculated from force-relaxation AFM curves. The results are presented as median and range (for 5 cells and 64 force curves per cell).

Participant ID	Relaxation times		Hardness	
	τ_1 (s)	τ_2 (s)	H_0 (MPa)	H_∞ (MPa)
1	0.12 (0.10–0.17)	1.99 (1.34–2.17)	198 (128–200)	151 (90–164)
2	0.16 (0.15–0.19)	2.11 (2.07–5.46)	127 (47–162)	76 (21–130)
3	0.14 (0.11–0.16)	2.40 (1.57–4.22)	159 (46–188)	92 (13–128)

The force relaxation data were firstly fitted to Eq. (16) from which the coefficients B_0, B_1 and B_2 were obtained. Then the coefficients C_0, C_1 and C_2 were calculated using Eq. (20). The material parameters describing the viscoplastic behaviour of the corneocytes are presented in Table 3.3.

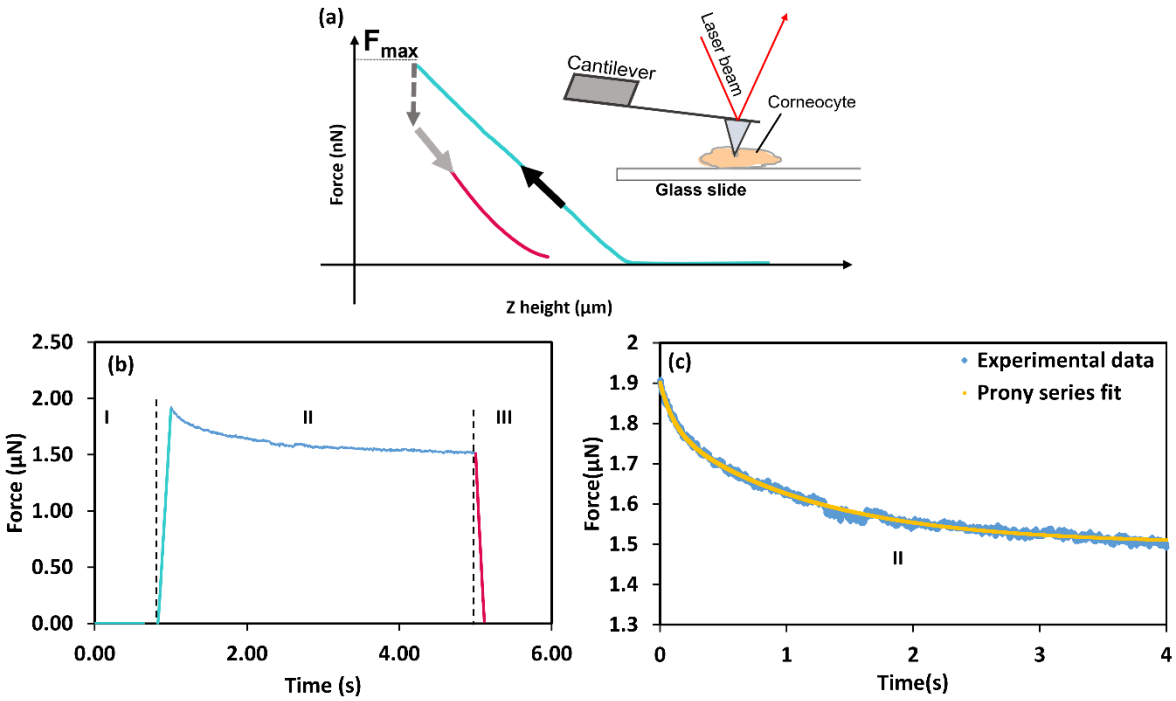

Figure 3.5. Stress-relaxation AFM experiments. (a) Schematic diagram of the stress-relaxation measurement consisting of an approach curve, a pause segment, and a retraction curve. The measurements were performed on cells fixed on a glass slide. **(b)** Representative force as a function of time data consisting of three stages (I) loading curve up to a maximum force setpoint of 2 µN, followed by a 4 s pause at a constant z-height (II) and, finally, the retraction of the probe from the cell surface (III). **(c)** The force-relaxation curve was fitted by a Prony series to obtain the time-independent mechanical properties of corneocytes.

3.5 Discussion

AFM has emerged as the gold standard for studying the mechanical properties of biological cells. Although it was not developed to perform nanoindentation experiments, the nano-resolution allows, not only the characterization of soft samples, but also the ability to generate very shallow indentations in thin materials. Furthermore, the possibility of combining topographical and mechanical analysis considerably enhances the potential of this technique. AFM nanoindentation typically involves obtaining loading-unloading cycles, in which a maximum loading force setpoint is selected by the user, with subsequently retraction of the tip. Although loading curves

contain detailed information about the forces experienced by the AFM probe, the type of deformation (elastic or inelastic) cannot be determined solely by these data and must be elucidated from the unloading curves, during which elastic recovery occurs as the residual indentation impression is formed [54]. However, a viscous component might still exist during unloading. This can be reduced by decreasing the speed of indentation and by allowing a period of relaxation, which here was 4 s. The adhesion component, which can be assessed by the negative part of the unloading curves, was ignored in this study since it was largely attenuated using the aqueous SDS solution for PDMS and was small compared to the positive part of the curves for the corneocytes. Consequently, loading-pause-unloading cycles were performed on individual corneocytes with the Young's modulus values obtained from the unloading curves, since hysteresis was observed as a result of inelastic deformation (Figure 3.3).

Corneocytes are flat dead cells (without a nucleus or organelles) with typical thicknesses and widths of 0.5–1.0 μm and 10–30 μm respectively [78, 125]. They are characterized by a rigid cross-linked protein envelope that is termed the cornified envelope (CE), to which a lipid envelope is covalently attached (CLE) [78, 125]. They encompass an internal matrix that is mainly composed of keratin filaments and natural moisturising factors (NMF) [156]. The thickness of the cornified envelope varies from 20 to 50 nm [52]. The forces required to indent corneocytes were relatively high (1–2 μN) compared to many other cell types (usually a few nN) [157]. In fact, corneocytes cannot be compared to typical cultured cells since their rigid protein envelope surrounds a rigid polymer keratin [125]. At low relative humidity, the SC exhibits glassy state values of the Young's modulus, in the range 1–2 GPa [21] and it is reasonable to assume that this arises mainly from keratin, which was found to account for 85% of the total protein

content of the SC [158]. Previous studies with AFM have measured values of the Young's modulus in the range of 250–500 MPa for corneocytes [51, 52]. Such values are an underestimation on the basis of the various uncertainties of the AFM protocols used, particularly that of the selection of the substrate. Here, the mean Young's modulus of corneocytes on a stiff substrate (microscope glass slide) was in the range 0.6 to 2 GPa (Table 3.2), for an RH of about 35%, which is consistent with the early works of Park and Baddiel on SC [21]. This is much greater than that calculated with a soft substrate by a factor of ~ 20. Unfortunately, the curves obtained on tape could not be simply corrected using the recently developed CoCS model [159], because of the complex elastoviscoplastic behaviour of corneocytes.

A number of attempts have been employed to study the properties of the different components of corneocytes (CLE, CE and keratin matrix), by the use of nanoneedles [51] or using a tomography method relying on the Hertz model [52]. However, they involve the uncertainties in the protocols identified in the current work. Corneocytes may be treated as a composite of two layers: a keratin matrix and a CE film. Independently of which component gives the mechanical strength to the cell, to "quantify" their individual contributions might not be possible because:

1. If the CE is softer than the keratin matrix: considering the restriction for nanoindentation of thin films (< 10% of sample thickness) [136] and the thickness of the CE to be of about 50 nm, indentations would be limited to only ≤ 5 nm.
2. If the CE is stiffer than the keratin matrix, the keratin matrix would be compressed in an analogous way to the tape presented in this work so that the stiffness would mostly arise from the matrix.

That is not to say that differences between cells at different depths [52] or different people [51] are not a result from the different components of the cells, but to reveal which component is responsible for such differences might be difficult to unravel by nanoindentation of cells in the dry state. While there have been models developed for layered elastic and elastoplastic solids, it is complicated analytically to obtain closed-form solutions and generally it is necessary to apply numerical methods such as finite element analysis [160]. Existing analytical models have not been developed for elastoviscoplastic solids or power law indenters and, consequently, a numerical method would be required to quantify the mechanical properties of the two layers.

Furthermore, as observed in Figure 3.3, the tip radius of the AFM tip can be of the same order of magnitude as the cell surface topographical features, particularly for rough corneocytes. This can influence the measured mechanical properties of skin cells and help explain the intra-subject variability observed in this chapter and in chapters IV and V. In fact, as the tip radius approaches the scale of the surface roughness, the indenter is more likely to interact with the surface asperities, which can lead to non-uniform contact and increased contact area, which can lead to an overestimation of the Young's modulus and hardness values. Furthermore, the indentation geometry may become irregular if the indenter encounters roughness features, and the assumed tip geometry in those cases may not be applicable. Finally, these interactions may result in a non-uniformly penetration of the sample, leading to unaccounted variations in the indentation depth. This is a limitation of using sharp indenters to study the properties of skin cells and may be addressed in future work using larger indenters but at a cost of a smaller spatial resolution.

The observed variability in the hardness measurements, in contrast to the consistency in relaxation time data, likely arises from the nature of these measurements. Hardness determination relies heavily on the loading curve from which the maximum indentation force and the contact area are derived. The contact area is influenced by the tip geometry and its interaction with the sample. When the surface roughness plays a role in this interaction, it can significantly impact hardness measurements, potentially explaining the variability in these data. In contrast, relaxation time measurements are less affected by surface roughness. These measurements assess the material's viscoelastic or viscoplastic response after indentation independently of the continued contact with the indenter. As a result, surface roughness may exert less influence on these measurements. This discrepancy suggests that material properties are not uniform across the sample's surface. Hardness, being sensitive to the indenter geometry and interactions, may reflect variations in the surface properties, which can lead to varying results. However, relaxation time measurements may primarily reflect the behaviour of the material's matrix, which exhibits a more homogeneous response to relaxation processes.

The current work has established that corneocytes are elastoplastic with a time dependent yield stress (Table 3.3, Figure 3.5). Material models relate the stress to the strain or strain rate. To obtain a rate-dependent material model from the time dependent data, it may be assumed that the relaxation arises from a conversion of the elastic, ε_e, to the plastic, ε_p, strain so that the total strain, ε, may be decomposed additively as follows:

$$\varepsilon = \varepsilon_e + \varepsilon_p \tag{23}$$

and so, assuming $d\varepsilon/dt = 0$ and a constant value of the Young's modulus $E^* = \sigma/\varepsilon_e$, where σ is the unconfined bulk stress:

$$d\varepsilon_p/dt = -d\varepsilon_e/dt = -d(\sigma/E^*)/dt \approx -\frac{1}{E^*}d\sigma/dt \tag{24}$$

Substituting the derivative of Eq. (19) with the mean stress, $H = \bar{\sigma} = 3\sigma$, the uniaxial strain rate is given by:

$$d\varepsilon_p/dt = \frac{3}{E^*}\left(\frac{C_1}{\tau_1}e^{-t/\tau_1} + \frac{C_2}{\tau_2}e^{-t/\tau_2}\right) \tag{25}$$

so that a material model can be obtained from a plot of σ as a function of $d\varepsilon_p/dt$. Generally, viscoplastic materials are described by a stress overshoot model to account for the strain rate hardening [161]. However, the Herschel-Bulkley model is applied here since it is equivalent for uniaxial deformation [162]:

$$\sigma = \sigma_Y + k\left(d\varepsilon_p/dt\right)^j \tag{26}$$

where σ_Y is the quasi-static uniaxial yield stress, k is the plastic flow consistency and j is plastic flow index. It should be noted that this is a rigid-viscoplastic model since it is assumed that yielding occurs at a zero strain. That is, elastic deformation within the yield surface is treated separately.

Table 3.4. Herschel-Bulkley material parameters. Results are presented as median (range) based on 5 cells per participant, considering the median values for each cell.

Participant ID	σ_Y (MPa)	j	k (MPa s^n)	R^2 (mean ± 1 SD)
1	48 (29–53)	0.33 (0.28–0.36)	16 (15–23)	0.971 ± 0.003
2	21 (7–41)	0.34 (0.14–0.43)	14 (10–22)	0.971 ± 0.009
3	29 (4–43)	0.28 (0.19–0.42)	25 (11–42)	0.955 ± 0.030

Example fits of Eq. (26) to the experimental data for the three participants are shown in Figure 3.6 together with histograms of the yield stresses that reflect the variation in the values of the Young's modulus values described earlier. The median values of the material parameters are given in Table 3.4. They are all of similar order, but further studies are required to elucidate differences between different anatomical locations and under different conditions (moisture content, liquid immersion etc). In addition, the possibility of strain hardening, or softening should be explored. In fact, the advantage of a conical probe is that the strain is independent of the depth of indentation, being only dependent on the cone angle. The representative strain for a spherical tip is proportional to a/R for small values of this ratio. The strain will also increase with indentation depth for a power law tip but would have to be defined by numerical modelling or the use of a strain dependent reference material.

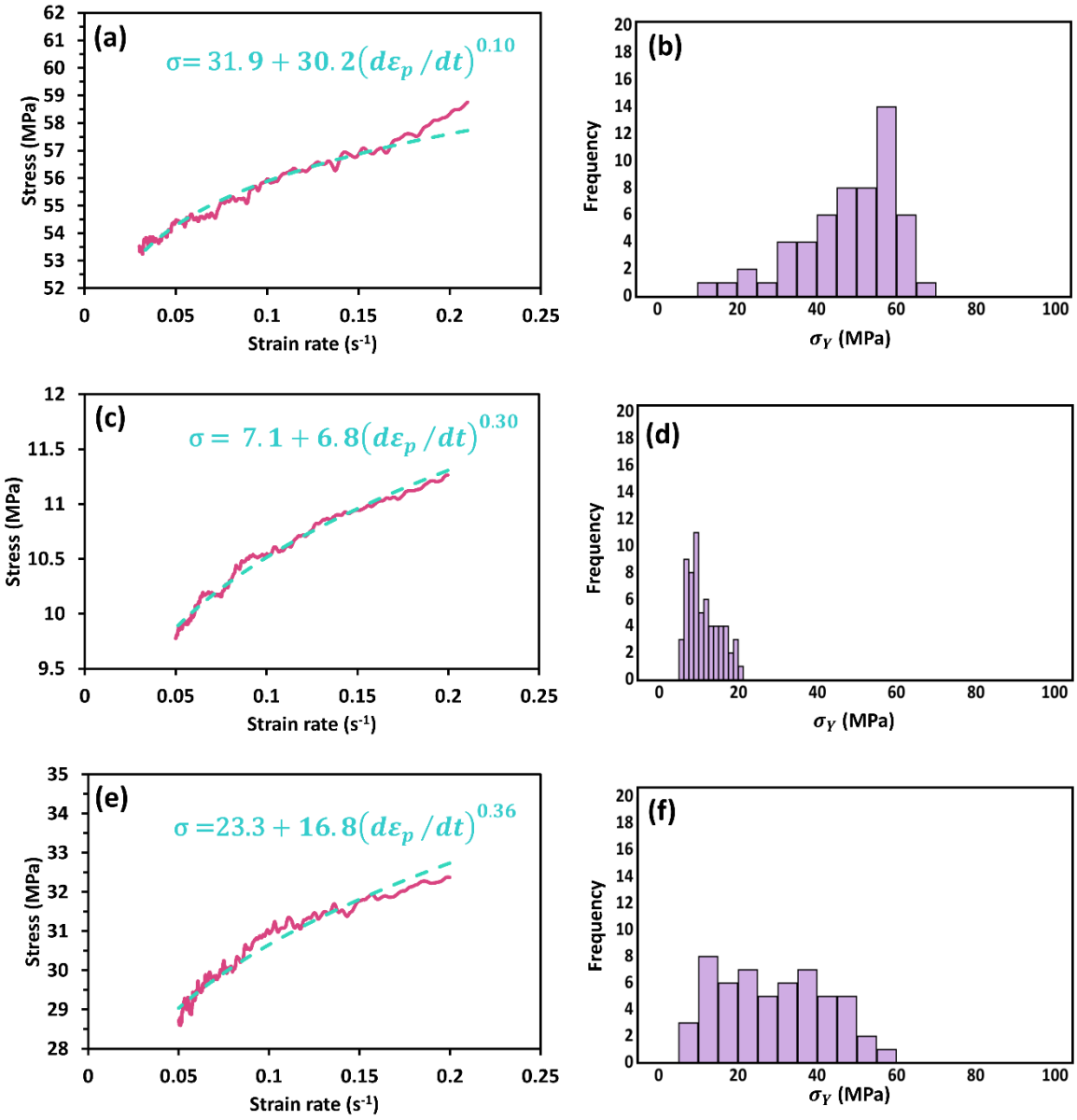

Figure 3.6. Representative Herschel-Bulkley material model fits from single relaxation curves using AFM. (a and b) Cell 2 of P1, **(c and d)** Cell 3 of P2 and **(e and f)** Cell 4 of P3 and corresponding histograms of the calculated yield stresses based on 40–50 stress-relaxation curves. The solid lines are the experimental data. The dashed lines correspond to the Herschel-Bulkley viscoplastic fits.

In summary, the current paper presents nanoindentation protocols to measure the mechanical properties of corneocytes, addressing the most important uncertainties of using AFM to describe the mechanical properties of SC cells. It was concluded that the tape used for stripping corneocytes is unsuitable as a substrate for AFM indentation

measurements since it is much softer than the cells and hence leads to erroneously small Young's modulus values. Moreover, the nominal stiffnesses of the cantilevers and geometries of the tips stated by the supplier should be taken with caution, particularly when using standard TM cantilevers for nanoindentation purposes of relatively stiff materials.

The use of PDMS as a reference material provides an accurate effective geometry of a tip, which demonstrates that the often-employed Hertz analysis for a parabolic geometry is unsuitable. Furthermore, at small stresses, corneocytes exhibit elastic behaviour but viscoplastic behaviour is observed when the stress reaches the yield value, which can be described by the Herschel-Bulkley material model. Future work will focus on the effects of moisture on the properties of corneocytes and the differences across anatomical sites will be explored.

CHAPTER IV - CHARACTERIZATION OF TOPOGRAPHICAL, BIOMECHANICAL AND MATURATION PROPERTICES OF CORNEOCYTES WITH RESPECT TO ANATOMICAL LOCATION

This chapter is based on the submitted article Évora, A.S., et al., *Characterization of topographical, biomechanical and maturation properties of corneocytes with respect to anatomical location* in submitted to Skin Research and Technology.

4.1 Abstract

Background: The Stratum Corneum (SC) is the first barrier of the skin. The properties of individual cells are crucial in understanding how the SC at different anatomical regions maintains a healthy mechanical barrier. The aim of the current study is to present a comprehensive description of the maturation and mechanical properties of superficial corneocytes at different anatomical sites in the nominal dry state.

Methods: Corneocytes were collected from 5 anatomical sites: forearm, cheek, neck, sacrum, and medial heel of 10 healthy young participants. The surface topography was analysed using Atomic Force Microscopy (AFM) and Scanning Electron Microscopy (SEM). The level of positive-involucrin cornified envelopes (CEs) and desmoglein-1 (Dsg1) were used as indirect measures of immature CEs and corneodesmosomes, respectively. In addition, AFM nanoindentation and stress-relaxation experiments were performed to characterise the mechanical properties.

Results: Volar forearm, neck, and sacrum corneocytes presented similar topographies (ridges and valleys) and levels of Dsg1 (13–37%). In contrast, cheek cells exhibited circular nano-objects, while medial heel cells were characterized by villi-like structures. Additionally, medial heel samples also showed the greatest level of immature CEs (32–56%, $p<0.001$) and Dsg1 (59–78%, $p<0.001$). A large degree of inter-subject variability was found for the Young's moduli of the cells (0.19–2.03 GPa), which was correlated with the level of immature CEs at the cheek, neck, and sacrum ($p<0.05$).

Conclusion: A comprehensive study of the mechanical and maturation properties of corneocytes may be used to understand the barrier functions of the SC at different anatomical sites.

4.2 Introduction

Human skin is the interface between an organism and the external environment, hence the Stratum Corneum (SC), apart from posing a barrier against environmental factors [27], and microorganisms and chemicals [163], is also responsible for the barrier function of the skin [164], i.e., to control tissue water loss, and to accommodate mechanical loading [165]. Therefore, the SC must be flexible and able to adapt mechanically to water gradients, body movements and external pressure and shear forces. This layer is primarily composed of corneocytes, which are dead but active cells subject to a maturation process as they move through the SC to the skin surface [125]. This includes the loss of central corneodesmosomes (CDs), which culminates in a honeycomb pattern of intercellular junctions [85, 86], and the maturation of the cornified envelopes (CE) by the cross-linking of proteins and the covalent attachment of lipids [75].

It has been suggested that the mechanical strength of the SC, particularly related to water gradients, must arise from the CEs [47, 51, 52], on the basis that isolated keratin films swell considerably in water, almost to the point of dissolution, such that it does not display detectable elasticity [21]. The properties of the CEs have been studied using different techniques: (i) immuno- and Nile red staining, (ii) mechanical resilience testing against ultrasonic waves [75] and, (iii) micromanipulation evaluation of maximum compression forces [47]. The level of CE maturation has been observed to be greater in the forearm than in the face [81] and smaller in locations of fresh scars [166]. More recently, Guneri et al. showed an increase in maturation in the deeper SC of photoprotected regions of the face, compared to photoexposed ones [75].

Furthermore, changes in the distribution of CDs have been linked to certain skin conditions, with the presence of circular nano-objects and central CDs being observed

in Atopic Dermatitis [101, 103, 167]. These junctions are thought to, not only be involved in the barrier function of the SC [85], but also in the mechanical resilience [108]. In fact, the high peripheral adherence of corneocytes is considered to allow them to form tight layers that are able to resist high stresses, while being impermeable to the outside medium [108].

The previous attempts at characterizing corneocytes from different anatomical sites and skin conditions have been focused on specific cell properties, and a comprehensive understanding of the relationship between maturation (topography, CE, and CDs) and mechanical properties is still lacking. The aim of the current study was to determine the characteristics of superficial corneocytes in healthy young skin at different anatomical sites. Cells were collected from non-glabrous (forearm, cheek, neck, and sacrum) and glabrous (medial heel) skin and surface properties were investigated, viz., topography, CD distribution and CE maturation, and also the mechanical properties.

4.3 Materials and Methods

4.3.1 *Corneocyte collection*

This research project received approval from the University of Birmingham Ethics Committee (ERN-19-1398A). The study recruited a cohort of 10 able-bodied participants (6 males and 4 females). Written, signed, and dated consent was received from each participant prior to sample collection. Participants were screened to exclude those presenting active skin diseases or allergies. The ages of the participants ranged from 24 to 29 (29.6 ± 1.6) years. The mean height and weight were 1.72 ± 0.06 m and 73.1 ± 12.3 kg, respectively, with corresponding mean BMI of 24.4 ±3.5 kg/m^2.

Corneocytes were collected from the five anatomical locations via tape stripping (Sellotape, UK): forearm, cheek, neck, sacrum, and medial heel, by pressing the tape gently onto the skin with gloved hands and gently removing by peeling the tape. The first tape strip was discarded to avoid the presence of contaminants, such as clothing fibres. Each tape strip was cut in four sections and used for the assessment of corneocyte topography via SEM and AFM, analysis of maturation properties (CE maturation and indirect visualization of CDs) and mechanical analysis by AFM.

4.3.2 *Scanning Electron Microscopy (SEM)*

The surface topographies of corneocytes were evaluated with SEM micrographs using a table-top Hitachi TM3030 electron microscope equipped with an integrated 4-segment backscattered electron detector. The samples were prepared by coating with 5 nm of gold using a Quorum Q150R ES gold sputter, utilising argon as the inert gas, with a pressure of 0.5 bar.

4.3.3 CE maturity assay: CE extraction and immunostaining for involucrin and Nile red staining for lipids

Cornified envelopes were isolated from the tape using a previously described methodology [168]. Briefly, each tape section was extracted with 750 mL of dissociation buffer containing 100 mM Tris-HCl pH 8.0, 5 mM EDTA (ethylenediaminetetraacetic acid), 2% SDS (sodium dodecyl sulphate) and 20 mM DL-dithiothreitol (Sigma Aldrich Dorset, UK). Tape sections were extracted in the dissociation buffer for 10 min at 75 °C and centrifuged at room temperature for 10 min at 5000 g. The extracted CEs were washed (three times) in washing buffer: 20 mM Tris-HCl pH 9.0, 5 mM EDTA, 0.2% SDS and 10 mM DL-dithiothreitol and suspended in 1 × PBS buffer (Sigma Aldrich

Dorset, UK). Extracted CEs were transferred on to a Polysine-coated microscope slide (5 µL, VWR international Ltd, Leicestershire, UK) and incubated overnight in a humidified chamber at 4°C with a primary monoclonal antibody against involucrin (1:100, mouse anti-human involucrin SY5, ABCAM, Cambridge, UK). The antibody solution was washed with PBS three times for 5 min before adding the secondary antibody Alexa-Fluor 488-labeled goat anti-mouse IgG antibody (1:200, ABCAM, Cambridge, UK) for 60 min at room temperature (in the dark). The slides were washed with 1 × PBS (three times for 5 min) and mounted with 20 µg/mL Nile red (Sigma Aldrich, Dorset, UK) in 75% glycerol solution (w/w).

4.3.4 Immunostaining for desmoglein-1

The immunostaining protocol for desmoglein-1 (Dsg1) was performed as described in [168]. Briefly, corneocytes attached to the tape section were washed with 1 × PBS (10 min) and incubated with a P23 mouse monoclonal antibody against the extracellular domain of Dsg1 (Progen, Heidelberg, Germany) at 4 °C overnight. This was followed by incubation with Alexa-Fluor 488-labeled goat anti-mouse IgG antibody (1:200, ABCAM, Cambridge, UK), for 60 min at room temperature (20 °C) in the dark. The samples were mounted with anti-fade fluorescence mounting medium (ABCAM, Cambridge, UK).

4.3.5 Image analysis

Schematics of the image analysis protocol can be found in Chapter VI. Five non-overlapping fluorescence images were acquired in total for each CE and each Dsg1 sample with a field of view of 720 × 580 µm. It involved a 10× objective magnification and an analysis using a Leica DMRBE microscope (Leica Microsystems, USA)

equipped with PL-Fluotar 5 × /0.12 and 10 × /0.30 lenses mounted with a Cool-LED pE-300 series blue-illumination source at the wavelength of 460 nm and with a Motic Pro 252 microscope camera. Image analysis was done as in [168]. Briefly, CE maturation was evaluated using a sequential approach: after application of a Gaussian filter, images were converted to either an 8-bit map (for total cell number count) or divided in RGB channels (to count cells staining for Alexa-Fluor 488, i.e., positive to involucrin – green channel). The Huang threshold followed by Watershed command was applied to define CE borders and the cells with a surface area of 300–2000 μm^2 were counted based on average values reported in literature [125]. For the distribution of Dsg1, the ratio of pixels expressing Dsg1 to the total area in pixels was counted in two random regions of interest (ROIs) of 5000 μm^2 that contained corneocytes, as previously established and described [167]. Initially, images were transformed in 8-bit maps and a Huang threshold was applied. This was followed by the Watershed command and using "Analyse Particle" command to count number of pixels.

4.3.6 *Atomic Force Microscopy*

Atomic force microscopy (AFM) imaging and nanoindentation experiments were performed under environmentally controlled conditions (35% RH and 25 °C) using an AFM operated in Tapping Mode (TM) and Force Spectroscopy, respectively (Nanowizard 4, Bruker, JPK BioAFM Berlin, Germany). Standard imaging tips, with a nominal spring constant of 40 N/m and resonance frequency of 300 kHz, were used (NCHV-A, Bruker AFM Probes, Inc). Corneocytes were extracted by pressing the tape section onto a microscope glass slide by overnight incubation in xylene. Cells attached to the glass slide were first imaged to study their surface topography (512 x 512 pixels, 40 x 40 µm), and a zoom-in TM image was then obtained in the centre of each cell (5

x 5 µm, 512 x 512 pixels) and used as a region of interest (ROI) for the nanoindentation measurements. These consisted of the analysis of 64 force curves (indentation force, F,versus indentation depth, *h*) extracted from 8 x 8 matrices, with points spaced 625 nm apart. The geometry of AFM tips was obtained as described in the Supplementary Information (S1). Briefly, an elastomer (polydimethylsiloxane, PDMS) was used as a reference material for nanoindentation; the value of the Young's modulus of the PDMS was measured by micromanipulation as presented in Chapter III and Appendix A. AFM loading curves were analysed using a combination of a 6th order polynomial smoothing function and power law equations to obtain a tip-radius function, i.e., contact radius, a, as a function of contact depth, h_c. Nanoindentation measurements on corneocytes involved loading-pause-unloading cycles, with a maximum applied force of 1.5–2 µN. Stress-relaxation was studied over a 4 s pause period, after the maximum force setpoint at loading was reached. The pause segment was set at constant height and the force relaxation was measured.

4.3.7 AFM data analysis

4.3.7.1 Elastic deformation

The Young's modulus, *E*, of corneocytes was calculated from the unloading portion of the force curves using the Oliver-Pharr method [54]:

$$E = \frac{\sqrt{\pi}}{2}(1-\nu^2)\frac{S_0}{\sqrt{A}} \quad (1)$$

where S_0 is the unloading stiffness at the maximum force, F_{max}, which corresponds to the maximum indentation depth, h_{max} , and $A = \pi a^2$ is the contact area, where a is

the contact radius [144]. The Poisson's ratio for corneocytes, ν, was assumed to be 0.4, based on the value for keratin [145].

Corneocytes are elastoplastic materials [9], so that the contact depth is related to h_{max} by the expression [54]:

$$h_c = h_{max} - h_s \tag{2}$$

where h_s is the surface elastic deflection at the perimeter of the contact, which is given by the following expression [54]:

$$h_s = \phi \frac{F_{max}}{S_0} \tag{3}$$

The unloading stiffness, $S_0 = dF/dh$ at $h = h_{max}$ was obtained by differentiating the following polynomial fit to the upper 80% the unloading curve with respect to *h*, and determining the slope at h_{max} [146]:

$$F = C_e h^2 - \left(2C_e h_f\right)h + C_e h_f^2 \tag{4}$$

where C_e and h_f are fitting parameters. The geometric factor, ϕ, was assumed to be 0.73 for a conical indenter, following the work of Oliver and Pharr [147]. The tip contact radius functions, $a(h_c)$, for all three tips employed in this study are shown in Figure S1. These functions are required to calculate the contact area for each indent at h_{max} in Eq. (1) from the contact depth, h_c, obtained using Eqs (2) and (3).

4.3.7.2 Stress-relaxation analysis

The rate-dependent properties of the corneocytes were calculated by fitting a Prony series to the stress-relaxation curves:

$$F(t) = B_0 + B_1 e^{-t/\tau_1} + B_2 e^{-t/\tau_2} \quad (5)$$

from which the coefficients B_0, B_1 and B_2 were obtained, as well as the characteristic relaxation times, τ_1 and τ_2. Assuming the decay in the force arises from viscoplastic dissipation, the force can be related to the time-dependent hardness $H(t) = F(t)/A$:

$$F(t) = \pi a^2 H(t) \quad (6)$$

and thus,

$$H(t) = C_0 + \sum_{i=1}^{2} C_i e^{-t/\tau_i} \quad (7)$$

So that the coefficients C_0, C_1 and C_2 can be calculated by:

$$C_i = \frac{B_i}{\pi a^2} \quad (8)$$

where $i = (0,1,2)$. Finally, the instantaneous hardness, H_0 and the long-term hardness, H_∞, can, then, be estimated using the following equations:

$$H_0 = \sum_{i=0}^{2} C_i \quad (9)$$

and

$$H_\infty = C_0 \quad (10)$$

4.3.8 Statistical analysis

Raw data were imported into IBM® SPSS® Statistics (version 27) for analysis and assessed for normality using probability plots and the Shapiro-Wilk test for each site and participant. While the topographical data revealed normal distributions, the

maturation properties (%INV+ and %Dsg1) and AFM nanoindentation data showed a non-normal distribution. Accordingly, ANOVA followed by Bonferroni test or Kruskal-Wallis test were employed to investigate whether the anatomical sites had differences in maturation and mechanical properties, respectively. The Mann-Whitney test was used to investigate differences between genders. Tests were considered statistically significant at a 5% level ($p<0.05$). The Spearman's correlational analysis was employed to investigate the relationships between the mechanical and maturation properties.

4.4 Results

4.4.1 *Topography of corneocytes at different anatomical locations*

Representative topographical images of superficial corneocytes from five anatomical locations: forearm, cheek, neck, sacrum, and medial heel, of young adult skin obtained using SEM and AFM tapping mode are shown in Figures 4.1a and 4.1b, respectively. They displayed hexagonal or pentagonal shapes and anatomical site-dependent topographical features. Volar forearm, neck, and sacrum corneocytes showed similar features in the form of ridges across the surface, organized in peaks and valleys. In contrast, most cheek cells showed "circular nano-objects" (CNOs) at the surface, as first described by Riethmüller [101]. Moreover, corneocytes from the plantar region of the foot had a surface divided in 'isles' of 'villi-like' structures. At a greater magnification, villous protrusions in medial heel cells are prominent (Figures 4.1c and 4.1d). They were related to an increase in surface roughness (Table 4.1) as expressed by the root mean square height (S_q) of 102.2 ± 28.4 nm and were significantly different ($p<0.001$) from the forearm, neck, and sacrum, which had values of S_q of about 54, 46 and 31

nm, respectively. The corrugated surface of cheek cells, generally populated by CNOs, also showed significantly greater roughness values (82.8 ±17.8 nm) than the forearm ($p<0.05$), neck ($p<0.01$) and sacrum ($p<0.001$).

Table 4.1. Roughness values measured from Zoom-in TM AFM images of the corneocytes. S_q (root mean square height) and S_a (arithmetical mean height) for an area of 25 μm^2 are given for a cohort of 10 participants (5 cells per participant and anatomical site). The projected cell area was measured directly from AFM topographical images and from extracted CEs. Results are presented as mean ± 1 SD.

Anatomical Region	Roughness (nm)		Cell area (μm^2)	
	S_q	S_a	AFM	CE size
Forearm	54.5 ± 13.0	42.8 ± 10.5	1148.3 ± 230.8	780.5 ± 102.3
Cheek	82.8 ± 17.8	65.6 ± 14.2	695.3 ± 97.4	554.2 ± 81.0
Neck	46.6 ± 12.4	37.5 ± 9.9	956.0 ± 87.7	694.4 ± 173.5
Sacrum	31.2 ± 12.8	24.6 ± 9.8	1079.0 ± 194.6	772.2 ± 227.1
Medial Heel	102.2 ± 28.4	82.5 ± 23.3	811.5 ±125.1	579.8 ± 174.6

The average size of the corneocytes via AFM topography was generally greater than those obtained by fluorescence microscopy of extracted CEs (Table 4.1). This may be due to the multi-step process used to extract CEs from the tape and separate them individually. Although the level of structural changes provoked by the extraction protocol was not studied, some structural changes to the keratin matrix are expected due to the denaturing nature of some materials (e.g., SDS), which may render a less rigid form. Nonetheless, both methods resulted in similar size trends, i.e., cheek cells were generally smaller than forearm (AFM: $p<0.01$; CEs: $p<0.001$), neck (CEs: $p<0.01$), and sacrum cells (CEs: $p<0.001$). Moreover, medial heel cells were statistically smaller than those from the forearm ($p<0.05$) and sacrum (CEs: $p<0.001$).

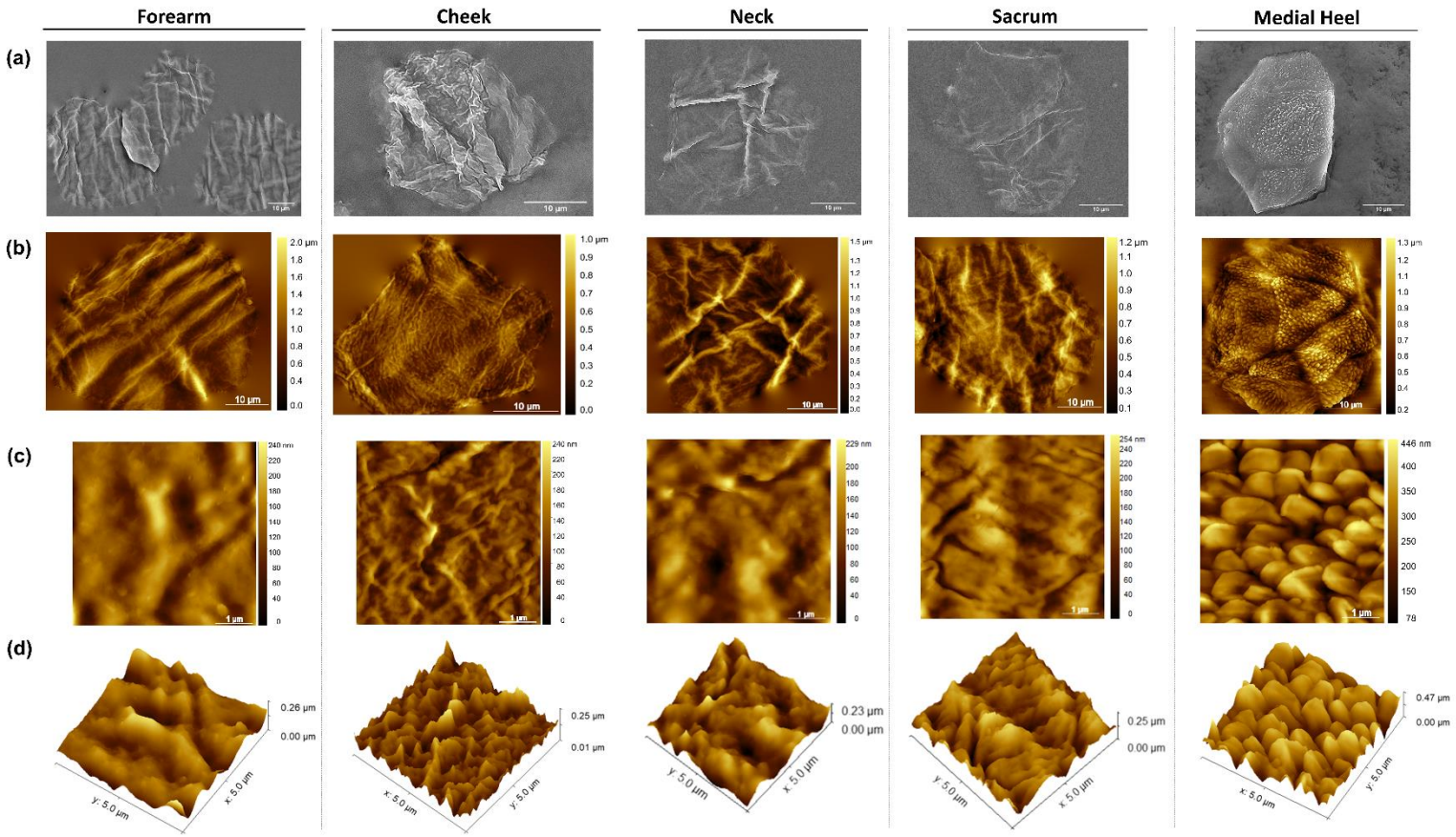

Figure 4.1. Topographical features of superficial corneocytes. (a) SEM and **(b)** AFM analysis revealed differences in the topography of corneocytes from superficial skin. Forearm, neck, and sacrum presented ridges and valleys across the cell surface, while cheek usually exhibited CNOs; and medial heel cells were characterized by villi-like structures. Colour bar corresponds to height (µm) in AFM topography. Scale bars = 10 µm. **(c)** Individual corneocytes were analysed at high magnification (5 × 5 µm) using tapping mode AFM. Scale bars = 1 µm. **(d)** 3D representation of the aforementioned zoomed regions.

4.4.2 CE maturity levels at different anatomical sites

The maturity level of the CEs was evaluated from the percentage of immature CEs, which was defined as the ratio between involucrin-positive CEs to the total number of CEs. Representative fluorescence microscopy images are shown in Figure 4.2a for participants 2 and 7, exemplifying low and high levels of CE maturity, respectively. Individual data are presented in Figure 4.3a. All anatomical sites, apart from the medial heel, which had a coefficient of variation (CV) of 17%, showed considerable inter-subject variability, with the forearm and neck exhibiting the highest (CV 68 and 71%, respectively), followed by the cheek and sacrum (CVs 49%, 48%, respectively). In fact, participants 1–3 and 10 exhibited relatively greater amounts of INV+ CEs at all body sites, while participants 4–9 showed smaller levels of immature CE. The cohort data are presented in Table 4.2. The mean values of immature CEs were similar at the forearm (16.7%), neck (18.4%), and sacrum (20.4%) and relatively greater at the cheek (24.4%). Medial heel had the greatest level of CE immaturity (47.8%, $p<0.001$).

4.4.3 Distribution of Dsg1 at different anatomical sites

The distribution of the CDs was indirectly analysed by immunostaining of Dsg1, which is an intercellular adhesion protein mainly expressed in the upper layers of the skin (Figure 4.2b) [85]. Relatively smaller inter-subject variability was found for %Dsg1 (Figure 4.3b), being the greatest at the forearm and cheek (CV 31 and 28%, respectively), followed by the neck (CV 19%), and the sacrum (CV 15%) and being the smallest at the medial heel (CV 9%).

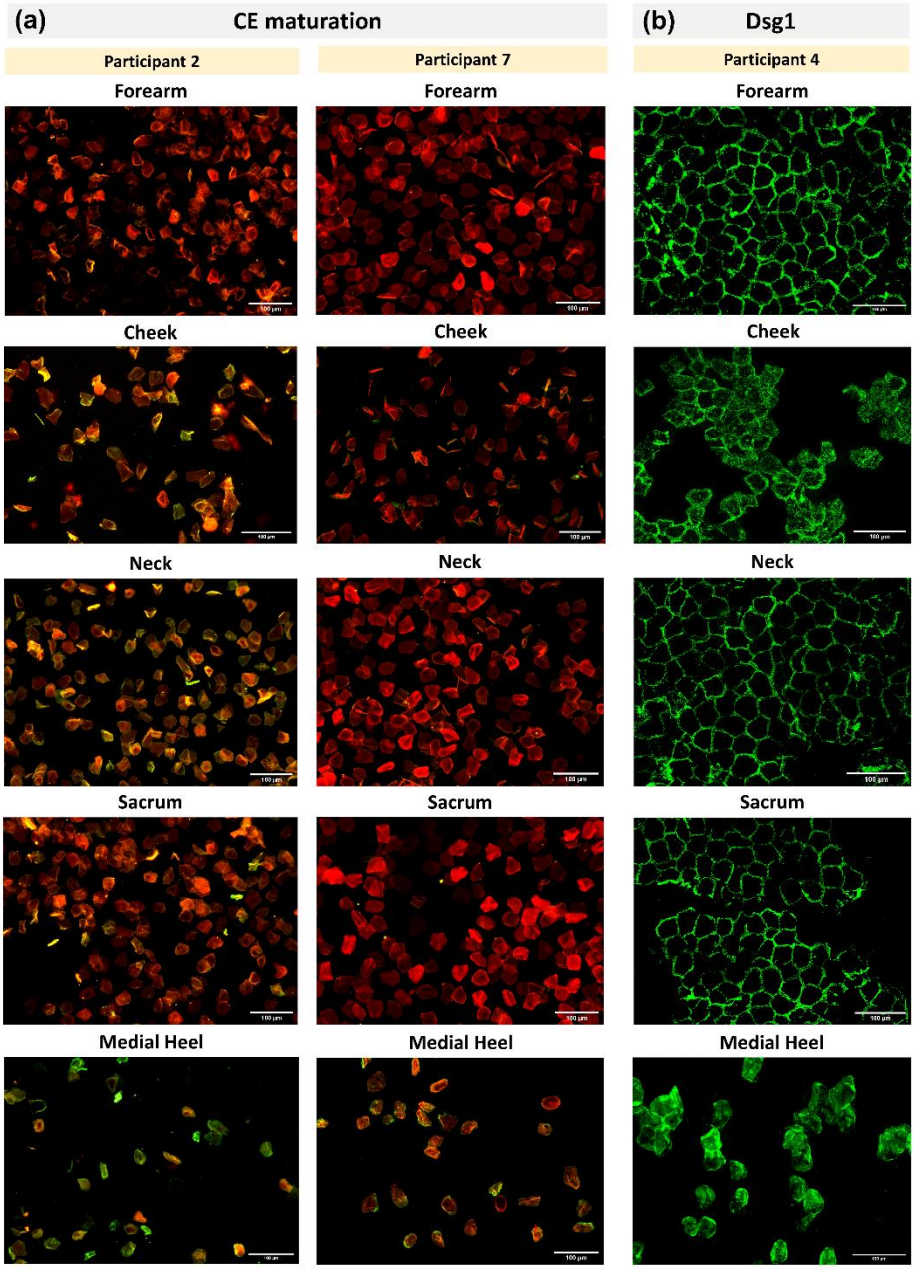

Figure 4.2. Maturation properties of corneocytes. (a) Images of forearm, cheek, neck, sacrum, and medial heel superficial CEs using double staining: immunostaining against INV (green) and Nile red (red) against lipids to quantify the degree of CE maturation. Participants 2 and 7 (P2 and P7) are presented as representative of low and high CE maturity. Forearm, neck, and sacrum corneocytes of P7 stained strongly with Nile red, while the cheek exhibited less lipids at the surface. Medial heel cells stained strongly in green for INV. P2 had higher levels of involucrin-positive CEs at all body sites. **(b)** Distribution of Dsg1 at the surface of superficial corneocytes as an indirect measure of CDs for participant 4. Forearm, neck, and sacrum cells have a typical honeycomb structure with Dsg1 mostly presented at the cell periphery. Cheek corneocytes showed a Dsg1 distribution dispersed on the surface, but not with in a ubiquitous manner as shown in medial heel cells. Scale bar = 100 µm.

A honeycomb pattern of Dsg1 was prevalent in the forearm, neck, and sacrum samples, while cheek samples usually displayed a dispersed signal (Figure 4.2b). This was distinct from medial heel samples, in which Dsg1 was ubiquitously found over the cell surface. In fact, the mean value found for medial heel samples was 67.2%, being the greatest of the anatomical sites studied ($p<0.001$), which was followed by the cheek (46.1%, $p<0.01$) (Table 4.2). Volar forearm, neck, and sacrum samples showed similar amounts of Dsg1, with mean values of 23.0, 21.3 and 18.1%, respectively. Interestingly, while tape strip samples of forearm, neck and sacrum were characterized by uniform layers of cells, cheek samples revealed patches of corneocytes, while the medial heel samples usually showed individual cells or groups of three or four cells, but never in a regular layer.

4.4.4 Biomechanical properties of corneocytes

The biomechanical properties of corneocytes are presented in Table 4.2. Individual moduli data revealed considerable inter-subject variability (Figure 4.3c). In fact, participants 1, 3 and 10 displayed the smallest Young's moduli, with medians of ~ 770, 1231, 465, 490 and 780 MPa for forearm, cheek, neck, sacrum, and medial heel respectively. While the remainder of the cohort presented medians of ~ 994, 1210, 1500, 1320 and 1560 MPa for forearm, cheek, neck, sacrum, and medial heel respectively. Interestingly, the median for the forearm modulus was the smallest (890 MPa, $p = 0.077$), while the greatest was found for the medial heel (1.43 GPa). The time-dependent properties are shown in Table 4.2. Individual data for H_0 (Figure 4.3d) and H_∞ revealed inter-subject variability like that observed for the Young's moduli. Statistical differences were not found between anatomical sites, although there was a trend for lower values for forearm cells and greater for the medial heel.

Correlational analysis between corneocyte biomechanics and CE maturation level

Based on the substantial inter-subject variability found for the corneocyte properties, a correlational analysis was employed to determine if they could be interrelated (Table 4.2). As expected, values of the Young's modulus were correlated to H_0 and H_∞, i.e., greater cell stiffness correlated with greater hardness values as related it is to the yield strain, H_0/E. There were no correlations between these properties and the relaxation times. Furthermore, the cell stiffness was correlated with the level of immature CEs at the cheek, neck, and sacrum, i.e., participants having softer cells, also presented a higher level of immature CEs ($p<0.05$). The hardness values correlated to CE maturity only at the neck and sacrum ($p<0.05$).

4.4.6 Influence of gender on corneocyte properties

To understand the origin of the inter-subject variability found in the maturation and biomechanical properties of corneocytes, intrinsic factors were considered. However, since the cohort was relatively homogeneous in age and BMI, the only apparent intrinsic factor was gender: 4 female and 6 male participants. Consequently, the data were pooled according to gender and tested for differences amongst the two groups, using Mann-Whitney test for pairwise comparisons.

Table 4.2. Maturation and biomechanical properties of corneocytes characterized by elastoviscoplastic behaviour and expressed as % INV+, % Dsg1, Young's modulus, E, relaxation times, τ_1 and τ_2, and hardness, H_0 and H_∞. Given the non-normal distribution of the AFM data, values are presented as median and range of values (min-max) (n = 5 cells per body site and participant and collected from 10 subjects). *p< 0.05. **p< 0.01, ***p< 0.001 by ANOVA followed by Bonferroni test for maturation properties or Kruskal-Wallis test for cell mechanics. The summary of significant Spearman correlations between corneocyte maturation and mechanical properties are also presented.

Anatomical Region	% INV+	% Dsg1	E (MPa)	τ_1 (s)	τ_2 (s)	H_0 (MPa)	H_∞ (MPa)	Parameter		Correlation coefficient
	Mean ± 1 SD		Median (min-max)							
Forearm	16.7 ± 11.4	23.0 ± 7.0	889.6 (258.2-2361.6)	0.12 (0.10-0.16)	1.90 (1.55-2.64)	152.6 (34.2-302.6)	111.0 (21.8-256.8)	E	H_∞	0.678*
									H_0	0.818**
Cheek	24.4 ± 12.0	46.2 ± 12.8 **	1206.5 (772.2-1690.1)	0.12 (0.10-0.14)	1.78 (1.57-2.80)	224.6 (82.0-329.0)	169.9 (68.6-289.1)	E	% INV	-0.791*
Neck	18.4 ± 13.1	21.3 ± 4.1	1379.6 (385.2-1972.9)	0.12 (0.11-0.13)	1.97 (1.57-2.79)	220.8 (36.9-321.1)	164.6 (29.8-262.9)	E	% INV	-0.695*
									H_∞	0.887*
									H_0	0.891**
								H_0	% INV	-0.810*
								H_∞	% INV	-0.781*
Sacrum	20.4 ± 9.9	18.1 ± 2.8	1145.9 (450.7-1876.0)	0.12 (0.11-0.12)	1.75 (1.53-2.19)	232.4 (61.9-333.0)	174.9 (51.3-284.0)	E	% INV	-0.882**
									H_∞	0.777*
									H_0	0.770**
								H_0	% INV	0.666 (p=0.05)
Medial Heel	47.8 ± 8.0 ***	67.2 ± 5.8 ***	1433.6 (422.6-2126.9)	0.12 (0.11-0.13)	2.05 (1.65-2.62)	251.8 (48.5-282.3)	206.9 (40.6-251.2)	E	H_∞	0.602 (p=0.07)
									H_0	**) =0.07)**

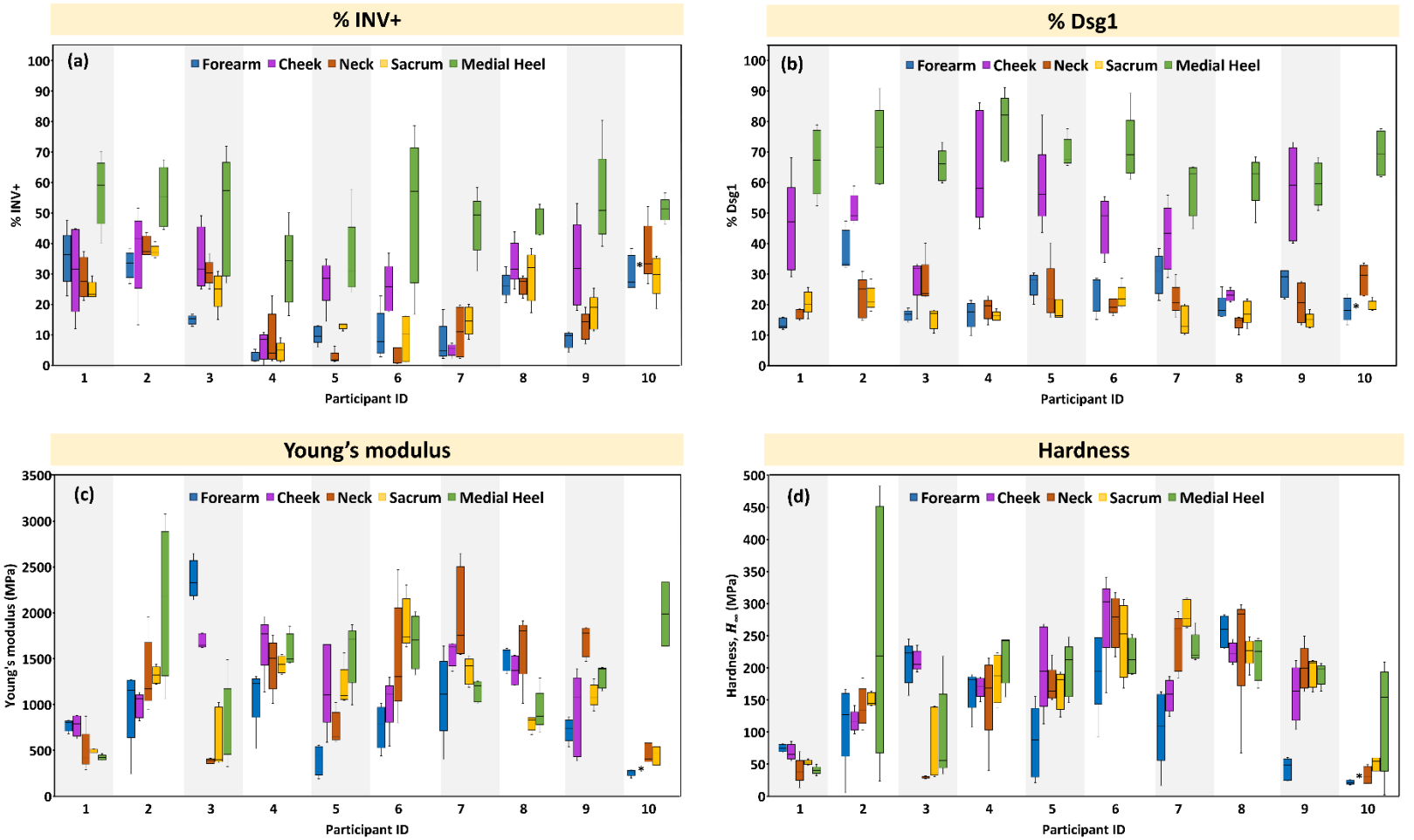

Figure 4.3. Participant individual data of maturation and mechanical properties of corneocytes. Box-and-whisker plots of individual data of **(a)** % INV CEs, **(b)** % Dsg1, **(c)** elastic modulus and **(d)** hardness (H_∞) for 10 subjects. The upper and lower whiskers represent the highest and lowest datum within 1.0 IQR (interquartile range). * indicates missing data – participant sample was not collected

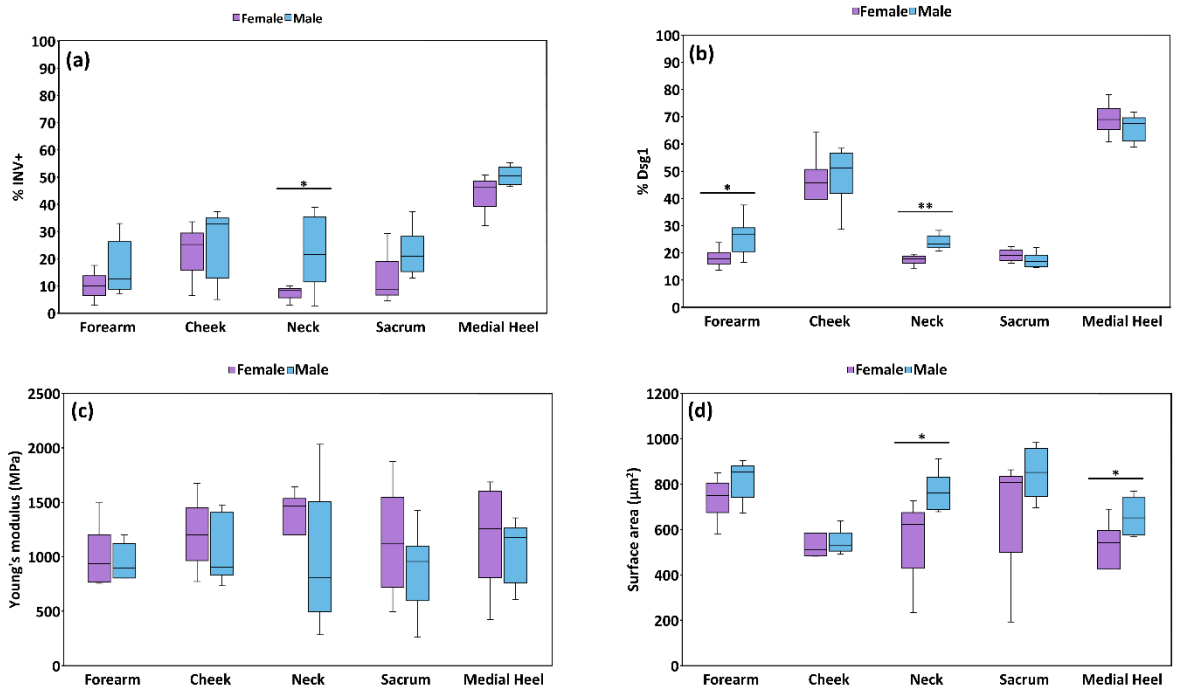

Figure 4.4. Differences between the properties of corneocytes according to gender. Box-whisker plots for the level of immature CEs **(a)**, % Dsg1 **(b)**, Young's modulus **(c)** and cell size **(d)** per body site and gender. The upper and lower whiskers represent the highest and lowest datum within 1.0 IWR (interquartile range). *p< 0.05, **p< 0.01 by the Mann-Whitney test performed for each male-female pair per body site.

A trend was found for female participants to have lower levels of immature have lower levels of immature CEs and Dsg1 (Figures 4.4a and 4.4b) and smaller and stiffer cells (Figure 4.4d) These differences were mainly found at the forearm, neck, and sacrum ($p<0.05$).

4.5 Discussion

Although the different properties of corneocytes have been studied using a range of techniques [47, 51, 75, 85, 86], there has not been a comprehensive examination relating maturation and the biomechanical properties. The aim of the current study was to characterize the superficial corneocytes collected from five anatomical sites from non-

glabrous and glabrous skin. The topographical and maturation properties were similar for volar forearm, neck, and sacrum cells. They had a relatively smooth surface (S_a ~ 25–42 nm) characterized by ridges and valleys. Moreover, they displayed immature CEs levels ranging from ~3–40% and levels of Dsg1 in the range 13–37% (Figure 4.3a and 4.3b). In contrast, cheek and medial heel cells had distinct topographical features with increased surface roughness of ~ 65 and 82% in terms of the values of S_a, respectively, with cheek corneocytes presenting CNOs, and samples from the medial heel revealing prominent villi-like structures (Figures 4.1c and 4.1d). Both sites also showed the highest levels of Dsg1, with mean values of 46 and 67%, respectively (Table 4.2). Moreover, medial heel cells also had the highest levels (around 48%) of immature CEs of the five anatomical sites studied (Table 4.2).

The differences in maturation and topography between the cheek and neck corneocytes demonstrate that anatomically close body sites can have different SC characteristics. Guneri et al. previously showed that corneocytes from different facial sites (photoprotected and photoexposed regions) exhibit different maturation levels, with a greater amount of INV+ CEs being present in the cheek (40%) compared to the post-auricular site (15%) [75]. In the present study, the level of immature CEs tended to be greater at the cheek (24%), compared to the neck (18%). Moreover, the two sites were topographically distinct and showed different levels of Dsg1. In fact, neck corneocytes were smoother (S_a = 37.5 ± 9.9 nm, Table 4.1) and characterized by a honeycomb pattern of Dsg1 (Figure 4.2b). While cheek cells had a rougher surface (S_a = 65.6 ± 14.2 nm, $p<0.01$) and a dispersed pattern of Dsg1 (Figure 4.2b). Cheek corneocytes may be challenged by a variety of external factors, the most relevant being UV radiation. Engebretsen et al. [169] observed significant differences in the Dermal Texture Index (CNOs) for the cheek and hand cells between summer and

winter. In addition, Lipsky et al. observed differences in the pattern and distribution of Dsg1 with increasing doses of UVB irradiation [93], and Biniek et al. proposed that UV radiation influences the intercellular lipids and CD distribution [170]. Nevertheless, neck corneocytes exhibit characteristics of a mature SC (Figures 4.2 and 4.3). In fact, lower levels of transepidermal water loss and greater water contents were previously found at the neck compared to the cheek [171], indicating that the former is characterized by a healthy barrier function, which is consistent with the characteristics observed in this study.

To fully characterize the biomechanical properties, nanoindentation and stress-relaxation experiments were performed using AFM. Interestingly, there were no significant differences in the stiffness and hardness between the anatomical regions studied. However, there was a large inter-subject variability for the stiffness, hardness, and CE maturity level. When employing a correlational analysis between the Young's modulus and % INV+ CEs, a negative correlation was found at the cheek, neck, and sacrum (Table 4.2), suggesting that participants with lower levels of immature CEs, usually have stiffer cells. Guneri et al. challenged the ability of the maturity assay used in the current study to provide biomechanical information about the CE [75]. The authors showed that otherwise considered immature CEs (high level of INV+ CEs) are mechanically mature when their rigidity is evaluated using an ultrasonic wave test. Indeed, the double staining technique used here treats the hydrophobicity of the CE as the indicator of CE maturity. Although most authors relate this to CE rigidity, there is no evidence that this is the case. Cornified lipid envelope formation might not necessarily occur with stiffening of the CE, which depends on the cross-linking of its proteins. However, the analysis of inter-subject variability in this study suggests that there is a relationship between the maturity level of the CE based on its hydrophobicity

and the biomechanical properties at least at three of the five anatomical sites evaluated.

Previously, the stiffness of the SC in full-thickness samples of glabrous skin was shown to be greater than non-glabrous skin measured in AFM experiments [70]. Although the stiffness of cells tended to be greater at the medial heel, there was not a statistical significance in the results, which may arise from the small number of cells analysed per participant. This is surprising considering the load-bearing function of the plantar regions of the skin. In fact, it has been suggested that plantar SC is mechanically adapted to sustain high pressures and keratin 9, only expressed in suprabasal layers of glabrous skin, has been thought to provide such strength [60, 75]. The current study was subject to a relatively small number of participants and, particularly, of cells (5 cells per anatomical site and participant) which may contribute to the lack of statistical significance in the results. This is one of the most important limitations of using AFM since the measurements are extremely time consuming and require a great number of force curves for making valid conclusions.

Samples collected from the male participants were generally more immature than those from the females (Figure 4.4), presenting higher levels of immatures CEs at the neck and sacrum ($p<0.05$) and greater proportions of Dsg1 at the forearm and neck ($p<0.001$). Previous studies found correlations between the CE surface area and their maturity [36, 172], i.e., usually larger cells were associated with greater levels of mature CEs. However, in the current study, although displaying higher levels of immature CEs, the cells from male participants were also the largest (Figure 4.4) at the forearm, sacrum, medial heel ($p<0.001$), and neck ($p<0.05$). A similar trend in cell size for the forearm has been previously observed between pre-menopausal women and men [173].

There was a trend of increased cell softness observed at the neck for the male participants at the sacrum.

The current study was limited to a relatively small cohort of 10 participants from white (Caucasian) ethnicity. In addition, only 4 out of 10 participants were female and there was only a small variation in the age or BMI. Consequently, the results obtained by combining data according to gender must be taken with caution since a larger cohort would be necessary to corroborate any conclusions.

The current results may assist in understanding the role of the SC in sustaining pressure and shear. Differences were not found between cells from non-glabrous skin, except for the cheek, which had increased levels of Dsg1. In contrast, there is an indication that load bearing body sites (heel) benefit from stronger cohesion between SC cells, suggested by a uniform distribution of CDs. Interestingly, although glabrous and non-glabrous skin present different surface maturation properties, they are similar in terms of the mechanical properties.

In summary, the current study evaluated the surface and biomechanical properties of superficial corneocytes in the nominally dry state from five anatomical sites: forearm, cheek, neck, sacrum, and medial heel, which were collected from 10 healthy young participants. Cells at the forearm, neck, and sacrum showed similar surface topography and levels of Dsg1, different from cheek ($p<0.01$) and medial heel ($p<0.001$) corneocytes. The later were characterized by high levels of Dsg1 and distinct topographical features, with cheek cells generally presenting circular nano-objects at the cell surface, and medial heel cells being characterized by villi-like structures. Although there was considerable inter-subject variability, there were no differences in the mechanical properties across anatomical sites either related to cell stiffness (E = 0.25–2.36 GPa) or initial and equilibrium hardness (H_0 = 34–333 MPa

and H_∞ = 22–290 MPa). However, there was a correlation between the proportion of immature CEs and the stiffness of the corneocytes, i.e., stiffer corneocytes were usually associated with a greater proportion of CE maturity. Additionally, the male participants showed a greater proportion of CE immaturity and Dsg1 and larger CEs.

CHAPTER V - THE EFFECTS OF HYDRATION ON THE TOPOGRAPHICAL AND BIOMECHANICAL PROPERTIES OF CORNEOCYTES

This chapter is based on Évora, A.S., et al., *The effects of hydration on the topographical and biomechanical properties of corneocytes* submitted to JMBBM.

5.1 Abstract

It is well established that the biomechanical properties of the Stratum Corneum (SC) are influenced by moisture-induced plasticization rather than its lipid content. This study employs Atomic Force Microscopy to investigate how hydration affects the surface topographical and elasto-viscoplastic characteristics of corneocytes from two anatomical sites. Volar forearm cells underwent swelling when immersed in water, with volar forearm cells experiencing a 50% increase in thickness and volume. Similarly, medial heel cells demonstrated significant swelling in volume, accompanied by increased cell area and reduced cell roughness. Furthermore, as the water activity was increased, they exhibited enhanced compliance, leading to decreased Young's modulus, hardness, and relaxation times. Moreover, the swollen cells also displayed a greater tolerance to strain before experiencing permanent deformation. Despite the greater predominance of immature cornified envelopes in plantar skin, the comparable Young's modulus of medial heel and forearm corneocytes suggests that cell stiffness primarily relies on the keratin matrix rather than on the cornified envelope. The Young's moduli of the cells in distilled water are similar to those reported for the SC, which suggests that the corneodesmosomes and intercellular lamellae lipids junctions that connect the corneocytes are able to accommodate the mechanical deformations of the SC.

5.2 Introduction

During certain body movements or in bedridden patients, human skin is subjected to large deformations causing potentially dangerous strains that may, ultimately, result in open wounds [10, 174]. The mechanical properties of the skin surface, the Stratum Corneum (SC), and sub-surface layers play a crucial role in resisting pressure and shear. The SC is usually described by a “bricks and mortar” structural model in which the corneocytes, its main cell type, are completely flattened and the keratin-filled interior is surrounded by protein and lipid envelopes (CEs and CLEs). Adjacent corneocytes are connected by corneodesmosomes (CDs) and intercellular lamellae lipids, such as ceramides, cholesterol, and fatty acids, which compose the “mortar” of the SC that surrounds corneocytes [125]. Corneocytes are synthesized in the basal layer of the epidermis and mature into comparatively hard structures [32]. Their stiffness arises from an internal network of keratin, a sulphur-containing fibrous protein embedded in a protein matrix and surrounded by a rigid cornified envelope. Park and Baddiel have elegantly explored the mechanical changes occurring in the SC with relative humidity (RH), concluding that effective plasticization depends on the water content rather than the lipid content [21, 175]. Furthermore, there was a reduced water-retaining capacity of the SC upon extraction with organic solvents and followed by an aqueous extraction, due to the removal of hygroscopic substances, namely the natural moisturising factor (NMF) [21].

The swelling of SC in water has been analysed by photographic recordings and determining the thickness by confocal laser scanning microscopy [176]. After 90 min of incubation in distilled water, the through-thickness swelling was 26.0 ± 16.3%. The authors argued that the results were consistent with the orientation of the keratin filaments, which results in cell rigidity and restricts lateral yielding. In the through-

thickness dimension, such restrictions are minimal and the swelling of corneocytes in this direction depends on the elasticity of the cornified envelope. The swelling of individual corneocytes collected from the forehand, close to the wrist, has also been studied using AFM in the tapping mode in air and in distilled water [177]. There was an increase in both the volume and in the mean thickness of ~50 ± 10%, whereas significant lateral swelling was not observed. Additionally, the swelling of corneocytes was found to be replicated by the solvation and elasticity of helical tubes with a woven geometry in a computational model, equivalent to that of a keratin filaments arrangement [178]. Norlén et al. then suggested that the morphology could be described as a cubic (para)crystalline polymer lattice, i.e., the keratin fibres being arranged isotropically possibly with chemical and/or physical attachment points between the fibres. This would ensure that all fibres contribute optimally to the enhanced stiffness and thereby distribute impact loads throughout the entire lattice and thus providing the SC with an optimal strength to weight ratio [56].

Thus far, the effects of hydration on the biomechanical properties of superficial single skin cells have not been investigated. The aim of the present work was to evaluate the relationship between the hydration, surface topography, and mechanical properties of individual corneocytes collected from the forearm and medial heel of three healthy individuals using AFM.

5.3 Materials and Methods

5.3.1 Corneocyte collection

Corneocytes were collected from three healthy female adult participants, with ages ranging from 26 to 31 years, in accordance with the UK regulations and the Declaration of Helsinki. Ethics approval was obtained from the University of Birmingham Research

Ethics Committee – ERN-19-1398B. Samples were collected using the tape stripping method (Sellotape, UK) from two anatomical sites: forearm and medial heel [169179]. The first layer of corneocytes was removed and discarded to avoid the presence of contaminants, such as clothing fibres. The second tape strip was used for the AFM measurements.

5.3.2 Atomic force microscopy

Atomic force microscopy (AFM) imaging and nanoindentation experiments were performed using AFM operated in Tapping Mode (TM) and Force Spectroscopy, respectively (Nanowizard 4, Bruker, JPK BioAFM Berlin, Germany). Standard imaging tips, with a nominal spring constant of 40 N/m and resonance frequency of 300 kHz, were used (NCHV-A, Bruker AFM Probes, Inc). The determination of the geometry of the AFM tips is described in Appendix C. Briefly, an elastomer (polydimethylsiloxane, PDMS) was used as a reference material for nanoindentation; the value of the Young's modulus of the PDMS was measured by micromanipulation as presented in Chapter III and Appendix A [257]. AFM loading curves were analysed using a combination of a 6th order polynomial smoothing function and power law equations to obtain a tip-radius function, i.e., contact radius, a, as a function of contact depth, h_c (Appendix C).

Corneocytes were extracted by pressing the tape onto a microscope glass slide and incubating overnight in xylene. Cells collected from participant 1 (n = 10 cells per site) that were attached to the glass slide were imaged for surface topographical analysis, as well as for cell area, thickness and volume calculations (512 x 512 pixels, 50 x 50 µm). Moreover, forearm and medial heel cells of the three participants were analysed by AFM nanoindentation. This consisted of the analysis of 64 force curves (indentation force, F, as a function of the indentation depth, h) extracted from 8 x 8

matrices, with points spaced 625 nm apart, and involved loading-pause-unloading cycles. Stress-relaxation was studied over a 4 s pause period, after the maximum force setpoint at loading was reached (maximum force setpoint of 2 µN or 50 nN in air and in liquid, respectively). The pause segment was set at constant height and the force relaxation was measured.

To study the effects of hydration on the mechanical properties of single cells, measurements were performed in the dry state (25 °C and 35% RH) and by incubating the samples in different glycerol-water solutions with decreasing glycerol concentration (w/w): 85, 70, 50 % glycerol and distilled water, which corresponded to increasing values of water activity, A_w, of 0.42, 0.62, 0.8 and 1 respectively [180]. The maximum concentration of glycerol was limited to 85% since at greater concentrations the viscosity was too high for the AFM measurements. Measurements were performed for a total of 6 cells per participant and per condition after equilibrating the system for 20 min before measurements.

5.3.3 AFM data analysis

5.3.3.1 Elastic deformation

The Young's modulus, E , of the corneocytes was calculated from the unloading curves using the Oliver-Pharr method [54]:

$$E = \frac{\sqrt{\pi}}{2}(1-\nu^2)\frac{S_0}{\sqrt{A}} \quad (1)$$

where S_0 is the stiffness at the maximum force, F_{max}, which corresponds to the maximum indentation depth, h_{max} , and $A = \pi a^2$ is the contact area, where a is the contact radius [144]. The Poisson's ratio for corneocytes, ν, was assumed to be 0.4, based on the value for keratin [145].

Corneocytes are elastoplastic materials [51], so that the contact depth is related to h_{max} by the expression [54]:

$$h_c = h_{max} - h_s \tag{2}$$

where h_s is the surface elastic deflection at the perimeter of the contact, which is given by the following expression [54]:

$$h_s = \phi \frac{F_{max}}{S_0} \tag{3}$$

The unloading stiffness, $S_0 = dF/dh$ at $h = h_{max}$ was obtained by differentiating the following polynomial fit to the upper 80% of the unloading curve and determining the slope at h_{max} [146]:

$$F = C_e h^2 - \left(2C_e h_f\right)h + C_e h_f^2 \tag{4}$$

where C_e and h_f are fitting parameters. The geometric factor, ϕ, was assumed to be 0.73 for a conical indenter, following the work of Oliver and Pharr [147].

The tip contact radius functions, $a(h_c)$, for all the tips employed in this study are shown in Figure C1 (Appendix C). These functions are required to calculate the contact area for each indent at h_{max} in Eq. (1) from the contact depth obtained using Eqs (2) and (3).

5.3.3.2 Force-relaxation analysis

The time-dependent properties of the corneocytes were calculated by fitting the following Prony series to the force-relaxation curves:

$$F(t) = B_0 + B_1 e^{-t/\tau_1} + B_2 e^{-t/\tau_2} \tag{5}$$

from which the coefficients B_0, B_1 and B_2 were obtained, as well as the characteristic relaxation times, τ_1 and τ_2. Assuming the decay in the force arises from viscoplastic dissipation, the force can be related to the time-dependent hardness $H(t) = F(t)/A$:

$$F(t) = \pi a^2 H(t) \tag{6}$$

and thus,

$$H(t) = C_0 + \sum_{i=1}^{n} C_i e^{-t/\tau_i} \tag{7}$$

So that the coefficients C_0, C_1 and C_2 can be calculated by:

$$C_i = \frac{B_i}{\pi a^2} \tag{8}$$

where $i = (0, 1, 2)$. Finally, the instantaneous hardness, H_0 and the steady state hardness, H_∞, can then be estimated using the following relationships:

$$H_0 = \sum_{i=0}^{m} C_i \tag{9}$$

and

$$H_\infty = C_0 \tag{10}$$

5.3.4 Statistical analysis

Raw data were imported into IBM® SPSS® Statistics (version 27) for analysis and assessed for normality using probability plots and the Shapiro-Wilk test for each site and participant. Two-way ANOVA followed by Dunnett's multiple comparisons test was employed to investigate whether there were differences in the topographical and mechanical properties of cells with different values of A_w. Moreover, paired t-student tests were applied to investigate differences in relaxation times between the dry state

and that in distilled water. Tests were considered statistically significant at a 5% level ($p<0.05$).

5.4 Results

5.4.1 The effect of hydration on the topographical features of corneocytes

Typical topographical images of volar forearm and medial heel corneocytes obtained under ambient conditions and incubated in distilled water are shown in Figure 5.1. Each image represents the map of cell surface heights relative to the underlying glass substrate and is analysed to give the cell dimension values summarised in Table 5.1.

Table 5.1. Thickness, area, volume, and surface roughness (S_q) measured for corneocytes in air and distilled water. Cell volume is calculated based on the projected area and the thickness of the cell. Data are expressed as mean ± 1 SD based on measurements of 10 random cells for each condition and a single participant. * p< 0.05, ** p< 0.01 in t-test performed for each parameter. The mean proportional change in water compared to the measurements under ambient conditions is given as a percentage.

Corneocyte parameter	Air (35% RH)		Distilled Water		Mean Change %	
	Forearm	Medial Heel	Forearm	Medial Heel	Forearm	Medial Heel
Thickness (µm)	0.8 ± 0.1	1.1 ± 0.2	1.1 ± 0.3	1.3 ± 0.3	+ 52*	+ 21
Real surface area (µm²)	1373 ± 327	1095 ± 103	1149 ± 152	1093 ± 188	+ 16	-
Projected area (µm²)	1084 ± 128	745 ± 70	1041 ± 201	851 ± 147	- 4	+ 14
Volume (µm³)	819 ± 135	850 ± 172	1337 ± 407	1283 ± 223	+ 63*	+ 50**
Root mean square height, S_q (nm)	68 ± 21	138 ± 40	47 ± 10	68 ± 10	- 30	- 50**

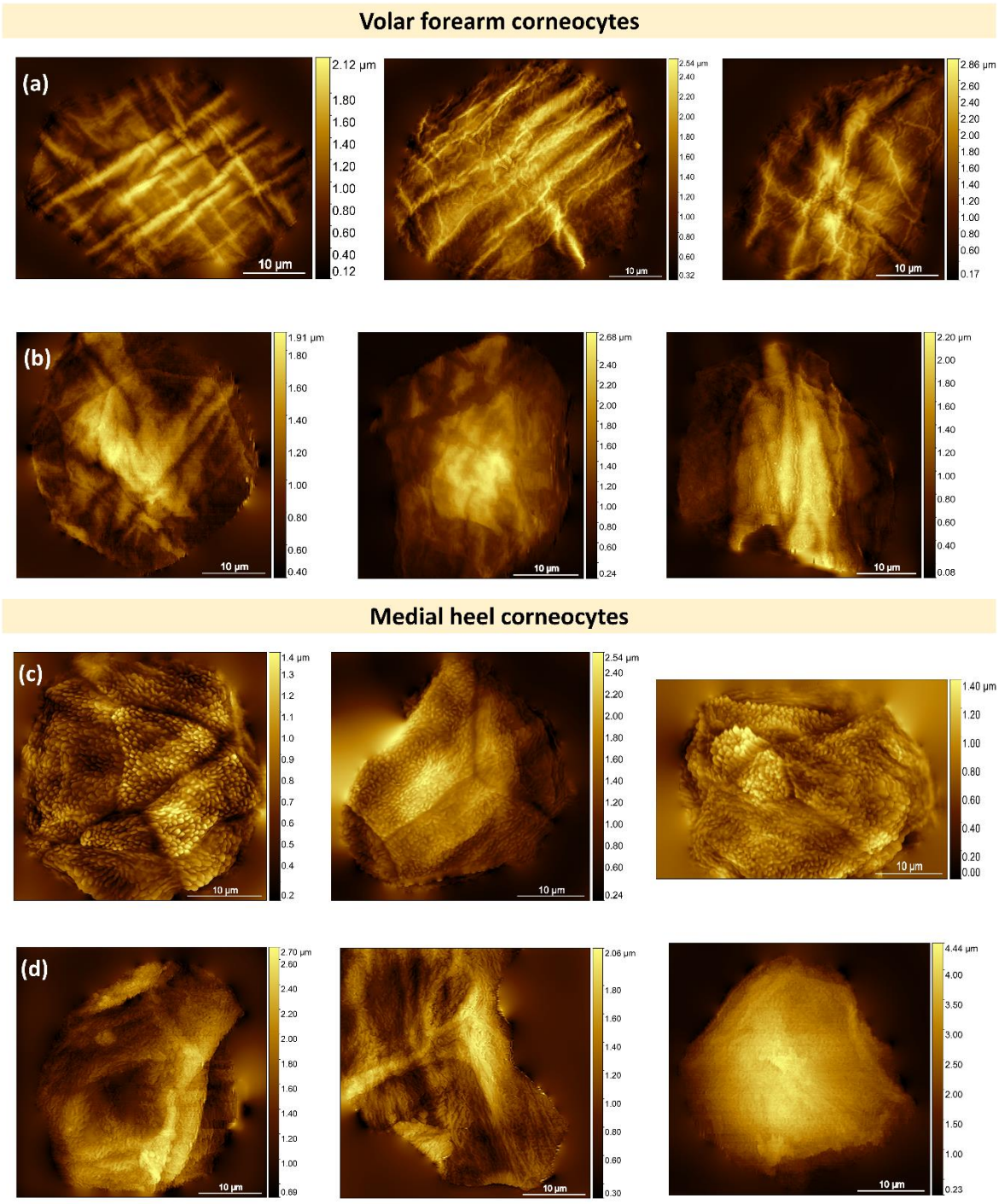

Figure 5.1. TM images of volar forearm and medial heel corneocytes. (a and c) Cells under ambient conditions. **(b and d)** Cells in distilled water. The mean thickness increases from 0.8 ± 0.1 µm and 1.1 ± 0.3 µm in the dry state to 1.14 ± 0.2 µm and 1.3 ± 0.3 µm in water, for forearm and medial heel cells respectively. The scan size in both sets of images was 50 µm × 50 µm. Scale bar = 10 µm.

Forearm corneocytes under ambient conditions (nominally dry state of 35% RH) presented a relatively rough surface, characterized by ridges across the surface,

organized in peaks and valleys (Figure 5.1a). Villi-like features were observed on the surface of medial heel cells (Figure 5.1c). Forearm and medial heel cells incubated in distilled water showed a less corrugated surface (Figure 5.1b and 5.1d), with a decrease in surface roughness of ~30 and 50% ($p<0.01$), respectively. Furthermore, swelling was observed for forearm cells as an increase in the volume (~ 63%, $p< 0.05$) and mean thickness (~ 52%, $p< 0.05$), but significant lateral swelling was not observed (Table 5.1). Similar swelling was found for medial heel cells, with an increase of ~ 20% in thickness, ~ 50 ($p<0.01$) in volume, and a similar trend was observed for the cell area (~ 14%, not statistically significant).

5.4.2 The effect of hydration on the biomechanical properties of corneocytes

The Young's moduli of the corneocytes as a function of the nominal water activity are presented in Table 5.2, and Figures 5.2 and 5.3. Forearm and medial heel cells presented mean moduli of 620 and 540 MPa in the nominally dry state (35% RH), with mean values of the instantaneous hardness of 215 and 161 MPa for the forearm and medial heel cells, respectively. The corresponding steady state mean hardness values were 180 and 140 MPa, respectively.

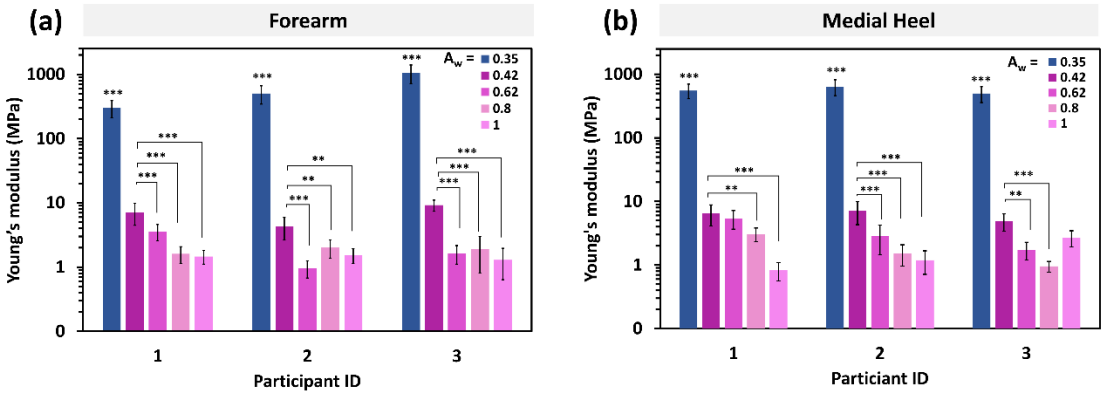

Figure 5.2. Young's moduli of corneocytes. (a) Volar forearm and **(b)** medial heel corneocytes collected from three healthy individuals in the dry state (blue) and immersed in aqueous glycerol solutions with a range of water activities. There were 6 cells per participant per condition. **p< 0.01, ***p< 0.001 based on a two-way ANOVA followed by Dunnett's multiple comparisons test.

With increasing water activity, a clear decrease in the individual modulus values was observed for all participants and both anatomical sites studied (Figure 5.2 and 5.3). For example, cells in 85% glycerol (A_w = 0.42) displayed much smaller moduli of about 6–7 MPa compared to those of the dry state (35% RH) in the range 560–620 MPa. Cells became even softer when incubated in distilled water (A_w = 1), with Young's moduli of about 1.5–2 MPa (p<0.001, Table 5.2). The same trends were observed for the instantaneous and long-term hardness values, i.e., there was a decrease in hardness with increasing water activity (p<0.001). Moreover, there was a faster relaxation time (τ_2) when the cells were incubated in distilled water (Figure 5.3c and 5.3d), compared to the dry state (35% RH). There was also a trend for an increase in the yield strain ($\epsilon_Y = H_0/E$) with increasing water activity, particularly for $A_w > 0.62$ (Table 5.2).

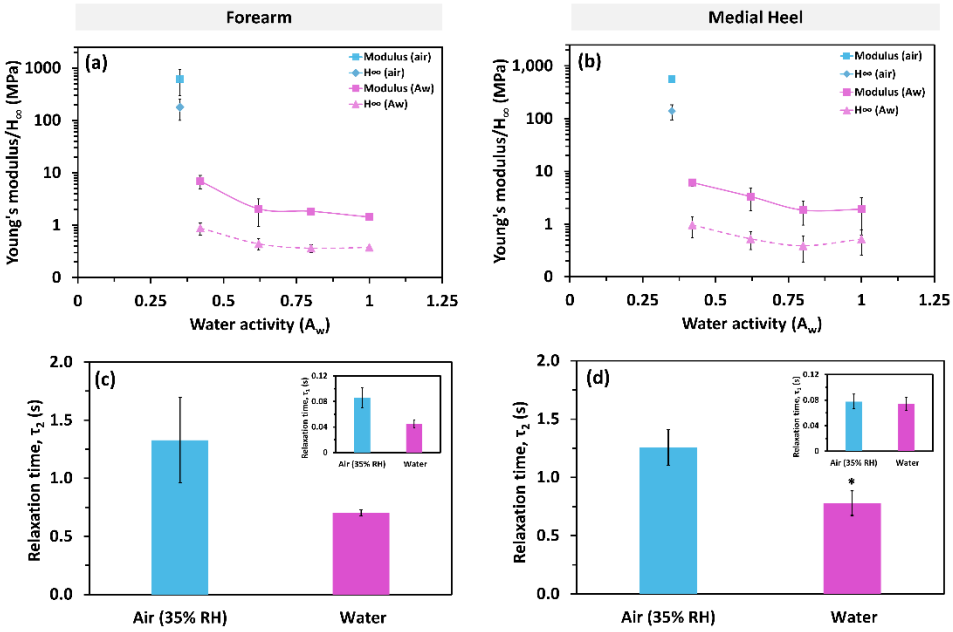

Figure 5.3. A decrease in the Young's modulus and long-term hardness, H_∞, was observed for volar forearm and medial heel corneocytes when exposed to increasing water activity. This was confirmed by two-way ANOVA followed by Dunnett's multiple comparisons test against the dry state (35% RH) and the lowest Aw (85% glycerol), respectively (p< 0.05). The results are presented as mean ± 1 SD based on three healthy participants. *p< 0.05 paired t-student test to compare relaxation times between dry and wet state.

The Herschel-Bulkley model [162] was also applied to the rate-dependent data to characterize the material properties according to the hydration level (the details are given in the Appendix C2 and Table C2), which may be expressed as:

$$\sigma = \sigma_Y + k\left(d\varepsilon_p/dt\right)^j \quad (11)$$

where σ_Y is the quasi-static uniaxial yield stress, k is the plastic flow consistency and j is plastic flow index. The value of j was found to be < 1 for all conditions studied (~0.4–0.5) (Table C2) and approximately independent of A_w. However, there was a decrease in the quasi-static uniaxial yield stress (σ_Y ~30–40 MPa in the nominally dry state, down to 0.30–0.40 and 0.12–0.14 MPa when A_w = 0.42 and 1, respectively). Moreover, there was also a decrease in k with increasing A_w, viz., ~20 MPa s^n in the nominally dry state and 0.20–0.35 MPa s^n when A_w = 0.42, and ~0.10 MPa s^n in distilled water (Table C2).

Table 5.2. Mechanical properties of forearm and medial cells with hydration. (There were 3 participants and 6 cells per participant, mean ± SD).

Hydration level		Young's modulus (MPa)		H_0 (MPa)		H_∞ (MPa)		τ_1 (s)		τ_2 (s)		Yield strain $\varepsilon_Y = H_0/E$	
		Forearm	Medial Heel	Forearm	Medial Heel	Forearm	Medial Heel	Forearm	Medial Heel	Forearm	Medial Heel	Forearm	Medial Heel
Air (RH)	35%	620 ± 320	564 ± 59	214.1 ± 90	161 ± 46	178 ± 79	139 ± 44	0.09 ± 0.02	0.08 ± 0.01	1.33 ± 0.46	1.26 ± 0.15	0.37 ± 0.12	0.29 ± 0.10
Glycerol 85% (A_w)	0.42	6.9 ± 2.0	6.2 ± 0.9	2.1 ± 0.6	2.8 ± 1.3	0.9 ± 0.2	1.0 ± 0.4	0.09 ± 0.05	0.07 ± 0.01	0.87 ± 0.28	0.76 ± 0.03	0.32 ± 0.11	0.46 ± 0.20
Glycerol 70% (A_w)	0.62	2.1 ± 1.1	3.3 ± 1.5	0.9 ± 0.2	1.9 ± 1.2	0.4 ± 0.1	0.5 ± 0.2	0.12 ± 0.06	0.11 ± 0.03	1.14 ± 0.26	0.85 ± 0.12	0.55 ± 0.19	0.64 ± 0.44
Glycerol 50% (A_w)	0.80	1.8 ± 0.2	1.8 ± 0.9	0.8 ± 0.2	1.1 ± .5	0.4 ± 0.1	0.4 ± 0.2	0.06 ± 0.01	0.07 ± 0.01	1.06 ± 0.15	1.03 ± 0.09	0.45 ± 0.10	0.61 ± 0.26
H_2O (A_w)	1.00	1.4 ± 0.1	1.5 ± 0.8	0.8 ± 0.2	1.3 ± 0.7	0.4 ± 0.1	0.52 ± 0.3	0.04 ± 0.01	0.07 ± 0.01	0.70 ± 0.03	0.78 ± 0.10	0.58 ± 0.20	0.87 ± 0.42

5.5 Discussion

This is the first study on the effects of hydration on both the surface topographical and biomechanical properties of single superficial corneocytes. Specifically, this involved the effects of water activity on the Young's modulus, hardness and relaxation times of volar forearm and medial heel corneocytes, which were studied in the nominally dry state and by equilibrating them in aqueous solutions of different glycerol concentrations and in distilled water. Volar forearm corneocytes were found to swell when immersed in distilled water (~ 50%, Table 5.1). A similar swelling of ~ 50% has been previously observed for corneocytes in distilled water [177], as well as for the most superficial layers of the SC [177]. Interestingly, the swelling in medial heel cells was observed as an increase in volume (~ 50%, $p<0.01$) and thickness (~ 20%, not statistically significant), but also in cell area (~ 14%, not statistically significant). This was accompanied by a decrease in cell roughness (~ 50%), which indicates that the swelling of medial heel cells might depend on the flattening of the villi-like structures, with enlargement of the cell area. The smaller increase in cell thickness, compared to forearm cells, may be related to the type of keratin expressed in palmoplantar skin. In fact, while keratins 1 and 10 are expressed in non-glabrous skin, palmoplantar epidermis structural integrity depends on keratin 9 [60], which was suggested to interact with keratin 5, instead of keratin 1 [60]. Future research should investigate the interactions and structure of keratin 9 filaments, to understand if the palmoplantar skin keratin matrix architecture and swelling are similar to those in non-glabrous skin.

Corneocytes become more compliant with increasing A_w, such that the values of the Young's modulus decrease from hundreds of MPa in the nominally dry state (~ 630 MPa) to a few MPa when in distilled water (~ 1.5–2 MPa). This is accompanied

by a decrease in the instantaneous and long-term hardness values (~ 160–215 and 140–180 MPa, down to 0.8–1.3 and 0.4–0.5 MPa, respectively), as well a decrease in the second relaxation time, τ_2, (1.3 s in the dry state down to 0.8 s in the wet state). Moreover, the yield strain tended to increase with an increase in A_w, from about 0.30–0.40 in the dry state (35% RH) up to 0.6–0.9 in distilled water. That is, the swollen cells can accommodate larger strains before undergoing permanent deformation since they are considerably more compliant.

Previously, Park and Baddiel studied the dependence of the mechanical properties of the SC (isolated from pig ears) on the relative humidity using an extensometer [21]. The Young's modulus was found to be ~ 2 GPa, at 30% RH and 25 °C, while at 100% RH, it decreased to ~ 3 MPa. They concluded that this was a result of a glassy-rubbery transition. At low RH values, the SC could be described as a polymeric glass, where long chain movements are restricted, and the extension takes place by the stretching of bonds. They argued that in the wet state, bond scission of the hydrogen bonds and salt linkages occurs due to hydration, but disulphide bonds remain intact, and thus the SC protein chains form a sparse cross-linked entanglement network, that is similar to an elastomer. This could explain the behaviour of single corneocytes, whose mechanical properties may depend upon its main component, keratin. In fact, different studies have proposed the importance of the cornified envelope (CE) in maintaining cell rigidity and integrity [21, 75, 175]. However, in a previous study we were not able to establish a relationship between cell stiffness and CE maturity, i.e., although medial heel cells presented higher levels of immature CEs compared to the forearm, significant differences were not observed for the Young's modulus or the yield stress [181]. This may be interpreted in two possible ways: i) the CE, even if contributing to the

mechanical architecture of corneocytes, is not fundamental in ensuring the mechanical strength of the cell; ii) although medial heel samples exhibited high levels of immature CEs [181], their CE rigidity is similar to that of forearm cells. The later possibility arises from previous observations that the immunostaining method used to analyse CE maturity depends on its hydrophobicity, not on its mechanical properties. In fact, it is possible that medial heel CEs are equally as stiff as forearm cells, but do not display the typical cornified lipid envelope present in mature non-glabrous SC [75, 125].

Interestingly, a correlation between the level of CE maturity and the Young's modulus for forearm cells has been observed in Chapter IV [181], i.e., subjects with greater levels of CE maturity presented generally stiffer cells. This could explain the inter-subject variability found in the current study (Table 5.2). Nonetheless, the absence of a more radical effect of CE maturity on the Young's modulus of corneocytes, might indicate that keratin is indeed mainly responsible for the mechanical properties of the cells, and thus, for the SC stiffness. However, a rigid CE, compared to the typical phospholipidic cell membrane of keratinocytes, might be fundamental towards maintaining cell integrity when cells swell in liquid and towards resisting chemical-induced stresses, such as detergents. In fact, a highly cross-linked and insoluble protein membrane, such as the CE, is more equipped to resist dissolution and denaturation by certain detergents, e.g., sodium dodecyl sulphate, and to resist osmotic pressures induced by cell swelling in water.

Park and Baddiel also studied the effects of A_w on the Young's modulus of the SC, using saturated salt solutions [182]. The mean modulus at small values of A_w = 0.42 (85% glycerol) for corneocytes (6–7 MPa), was much smaller than that of the SC (of ~ 200 MPa) [182]. This may be due to the humectant ability of glycerol aqueous solutions, but

not of the saturated salt solutions in native SC [182], to effectively wet the cells [183]. In fact, native SC retains the lipid lamellae, which acts as a barrier, while, in this study, corneocytes are being studied after xylene extraction, which may have dissolved any extracellular lipids attached to the cell surface. Interestingly, the Young's modulus of the SC in water (~ 5 MPa) was close to that of corneocytes (1.5–2 MPa) [182]. It must be noted that, while in this study, single cells are being studied through nanoindentation, the properties of the SC were measured using an extensometer, and thus the effects of the cell-to-cell junctions (CDs) on the mechanical resilience of the layer cannot be ignored. However, the similar values of Young's modulus obtained in water for single cells and SC layer suggest that the lipid mortar and corneodesmosomes do not seem to restrict the deformability of the SC.

Increasing hydration levels in corneocytes may affect the keratin structure and packing, which, in turn, may change the viscoelastic behaviour of this matrix, with the disruption of intermolecular forces [56,178]. As corneocytes absorb water, they expand, altering the arrangement of the interior keratin proteins that affect the cell mechanical properties. Changes in keratin such as increased spacing (free volume) between keratin filaments packing and water binding that can disrupt hydrogen bonds and other intermolecular forces, can lead to a reduction in Young's modulus and hardness reported in this study. Furthermore, as water molecules interact with keratin proteins, they introduce a degree of plasticity into the structure. Moreover, as corneocytes absorb water and swell, the CE becomes smoother which may increase the permeability to certain compounds. The smoothing and plasticization of corneocytes may be extremely relevant in cosmetic applications. While it is commonly believed that the permeation of compounds primarily occurs via the lipid lamellae, the influence of

well-hydrated skin remains an area warranting further investigation. This may be particularly important in the loss of skin integrity due to moisture damage, an overhydrated SC may be more permeable to certain compounds and more prone to damage due to pressure and friction.

The current study was limited by the number of participants (n = 3) and by using glycerol to vary the water activity, instead of the more commonly used saturated salt solutions. This was due to the high ionic strength of these solutions which prevented accurate AFM measurements due to the high electrostatic interaction interfering with the AFM tip. Although glycerol is not considered a skin plasticizer, in using it to control water activity the behaviour observed may not be fully attributable to the water activity since it may also be dependent on the humectant properties of glycerol [183, 184]. Glycerol was shown to increase molecular mobility of keratin at a given RH, which could not be attributed to an increase in water content [183]. However, given the equipment used in the current work, it was not possible to measure the effects of relative humidity, which is expected to be different from that of incubating cells directly in liquid media. This may explain the large reduction between the dry state (equivalent to A_w= 0.35) and the solution of 85% glycerol (A_w = 0.42) (Figure 5.3 and Table 5.2). The effects of relative humidity are expected to be less abrupt, considering the results obtained for the SC [21]. In saturated salt solutions, the Young's modulus of the SC was observed to fall for values of < 100 MPa when A_w ~0.50, while in the vapour phase, a similar drop is observed when the relative humidity is greater than 80% [175].

Future studies should investigate the effects of relative humidity on the properties of corneocytes and particularly its relationship to the amount of natural moisturising factor (NMF). It is proposed that the inter-subject variability found in the mechanical

properties of the cells in the nominal dry state, apart from being partly correlated to CE maturity, is extremely dependent on the level of NMF, which is known to vary according to age [185], anatomical site [186], and in diseases such as Atopic Dermatitis [103]. The levels of these compounds may be controlling the properties of corneocytes in varying RH environments since they are responsible for retaining water inside the cells. However, this could not be investigated with the protocol followed in the current study since any incubation in liquid media may extract the small NMF molecules and so mask their effect in native SC.

Finally, the study of the rate-dependent properties and the calculation of the Herschel-Bulkley parameters (Appendix C) suggest that the plasticization of corneocytes by water decreases the resistance to flow, becoming less viscous and less resistant to deformation under shear which has been observed for hair, another keratinous material [187]. Furthermore, future studies should investigate the effects of pH relevant for skin integrity loss due to moisture damage. In fact, varying the pH has previously been observed to change the protonation and deprotonation ratio in amino acid side chains of keratin in hair, which in turn affected the ratio of salt bridges and hydrogen bonds, and protein solvation [251]. These affect the thermal properties, water sorption and dry tensile properties.

As discussed for SC, plasticization by water results in a rubbery-glassy transition, which causes in a reduction in the Young's modulus and the yield stress but an increase in the yield strain.

5.6 Conclusion

Moisture plays a crucial role in the "bricks and mortar" structure of the SC, assisting in the maintenance of the natural desquamation process by promoting the activity of

serine proteases responsible for the degradation of corneodesmosomes [188]. It also promotes the maturation of corneocytes (rigidity and hydrophobicity) [189, 190]. In the present study, corneocytes were found to swell in water by about 50% of their initial dry volume (Figure 5.1 and Table 5.1) and to become much more compliant with increasing water activity (the Young's modulus was ~ 630 MPa in the nominally dry state and decreased to 1.5–2 MPa in distilled water). This indicates that, when hydrated, corneocytes contribute to the flexibility and softness of the SC, with the cells becoming more capable of withstanding deformation without breaking or undergoing structural damage as reflected in an increase in the yield strain. However, prolonged water exposure has been observed to disrupt the lipid lamellae structure with "water pools" being formed in the SC after several hours of water exposure [191]. The expansion of the extracellular spaces between corneocytes and their swelling may weaken the structure of the corneodesmosomes, leading to impaired cell-to-cell adhesion [190]. This increases transepidermal water loss [192] and renders the skin surface more susceptible to the penetration of environmental irritants and microorganisms [193]. Therefore, hydration seems to play a dual opposing role in the SC. While being very important in promoting a healthy skin barrier, prolonged exposure to moisture may be disruptive for the SC structure. Further studies should investigate the effects of prolonged exposure on both the mechanical properties of corneocytes, but also on the cell-to-cell adhesion. By fully characterizing the mechanical resistance of the SC under such conditions, it should be possible to gain a comprehensive understanding of the impact of prolonged hydration on skin health.

CHAPTER VI - CHARACTERIZATION OF SUPERFICIAL CORNEOCYTES IN THE SKIN AREAS OF THE FACE EXPOSED TO PROLONGED USAGE OF RESPIRATORS BY HEALTHCARE PROFFESIONALS DURING COVID-19 PANDEMIC

This chapter is based on Évora, A.S., et al., *Characterisation of superficial corneocytes in skin areas of the face exposed to prolonged usage of respirators by healthcare professionals during COVID-19 pandemic* published in the Journal of Tissue Viability (2023).

6.1 Abstract

Background: During the COVID-19 pandemic healthcare workers (HCWs) have used respiratory protective equipment for prolonged periods, which has been associated with detrimental effects on the underlying skin. The present study aims to evaluate changes in the main SC cells (corneocytes) following prolonged and consecutive use of respirators.

Methods: 17 HCWs who wore respirators daily during routine hospital practice were recruited to a longitudinal cohort study. Corneocytes were collected via tape stripping from a negative control site (area outside the respirator) and from the cheek which was in contact with the device. Corneocytes were sampled on three occasions and analysed for the level of positive-involucrin CEs and the amount of Dsg1, as indirect measurements of immature CEs and corneodesmosomes (CDs), respectively. These were related to biophysical measurements (TEWL, and SC hydration) at the same investigation sites.

Results: A large degree of inter-subject variability was observed, with maximum coefficients of variation of 43% and 30% for the level of immature CEs and Dsg1, respectively. Although there was not an effect of prolonged respirator usage on the properties of corneocytes, the level of CDs was greater at the cheek than the negative control site ($p<0.05$). Furthermore, low levels of immature CEs correlated with greater TEWL values after prolonged respirator application ($p<0.01$). It was also noted that a smaller proportion of immature CEs and CDs was associated with a reduced incidence of self-reported skin adverse reactions ($p<0.001$).

Conclusion: This is the first study that investigated changes in corneocyte properties in the context of prolonged mechanical loading following respirator application.

Although differences were not recorded over time, the levels of CDs and immature CEs were consistently higher in the loaded cheek compared to the negative control site and were positively correlated with a greater number of self-reported skin adverse reactions. Further studies are required to evaluate the role of corneocyte characteristics in the evaluation of both healthy and damaged skin sites.

6.2 Introduction

To undertake clinical commitments during the COVID-19 pandemic, healthcare workers (HCWs) were required to wear personal protective equipment (PPE) in order to reduce the transmission of the infection in different care settings [194]. In the context of PPE, respiratory protective equipment (RPE) is particularly essential for avoiding airborne particle transmission, involving a filtration level of 95 to 99% via a respirator that is tightly fastened to the face in order to create a seal. However, the prolonged use of such devices can affect skin health, resulting in a variety of problems ranging from erythema, acne, dermatitis, and skin breakdown in the form of pressure ulcers (PUs) [195, 196]. These adverse reactions are the result of non-uniform pressure, shear, and frictional forces at the skin–respirator interface [197], together with changes in the microclimate, which includes increased moisture and temperature from excess sweating due to mental and physical stress [198]. Indeed, moisture is known to increase skin friction [199, 200] and has been attributed to an increase in the contact area due to its plasticising action [199, 200] that reduces the stiffness and strength of the skin layers [21, 201]. This is a direct result of compression of the surface topographical features of skin, which may also become smoother with increasing hydration [21, 201].

Han et al. analysed the biophysical responses to medical mask and respirator application, showing consistent lower values of skin hydration in those regions of interest (~56-62 a.u.) compared to uncovered areas (~68-79 A.U.) [202]. In a cohort of 17 HCWs, a recent study by Abiakam et al. evaluated various biophysical skin parameters as well as the levels of certain inflammatory cytokines in sites exposed to prolonged respirator application [203]. The main finding included the consistent

upregulation in TEWL response particularly at the bridge of the nose, which coincided with high interface pressures at that location [204].

Although biophysical and biochemical markers are usually assessed in studies pertaining to the integrity of skin [205], the study of the effects of mechanical insults on the stratum corneum (SC) and its relationship to its main cells, the corneocytes, has been limited. Indeed, the SC represents the primary skin barrier that is exposed to friction, pressure, and shear, and corneocytes represent the building blocks of the SC, which impart stiffness and create the skin barrier function [70, 85, 86]. Moreover, these cells are known to undergo a complex process of maturation [125], the so-called cornification process, which includes the cross-linking of certain precursor proteins e.g., involucrin and loricrin, and the covalent attachment of lipids to produce a rigid and hydrophobic CE [71]. In addition, a gradual degradation of corneodesmosomes (CDs) occurs in the central region of the cell, originating a residual honeycomb formation of cell junctions. It is this honeycomb pattern that is believed to underpin the barrier function resulting in lower values of TEWL when compared to the inner SC or body locations where this maturation is impaired or not achieved e.g., palms of hands and soles of feet [85, 86, 206]. The honeycomb feature of a mature SC results in improved flexibility of the whole layer by attenuating mechanical insults, such as bending or flexing, and allowing minimal relative sliding of the outer SC over the inner SC [90]. Corneodesmosomes are usually observed indirectly by immunostaining of Dsg1 [85, 86], which is a cadherin-type cell-cell adhesion molecule found in stratified epithelial desmosomes, expressed in the suprabasal layer of the epidermis [85].

The complex mechanisms leading to SC maturation and desquamation depend on intrinsic [207, 208] and extrinsic factors [93, 209, 210] and may influence the way in which skin

responds to the mechanical insults. Therefore, there is a need to evaluate the effects of the RPE that are related to mechanical and thermal insults on the SC and its relationship to its main cells.

The present paper presents a complementary methodology and analysis of a previously published study on the biophysical and biochemical changes in skin health in HCWs during the COVID-19 pandemic [203]. It is focused on establishing the characteristics of superficial corneocytes, namely CE maturation and corneodesmosome distribution, in areas exposed to prolonged mechanical loading. Changes will be compared to the biophysical skin responses and perceived skin damage in the same cohort of HCWs to evaluate the role of corneocytes in skin surface integrity for understanding the role of corneocytes in skin surface integrity.

6.3 Materials and methods

6.3.1 Participants and study protocol

The study was conducted as previously published by Abiakam et al. [203]. To review briefly, a convenience sample of 17 HCWs were recruited from specific departments treating COVID-19 patients in a UK University Hospital Trust. Participants were included if they were aged over 18 years, wore FFP2/3 respirators daily while attending to clinical commitments and were on duty for at least three consecutive shifts per week. Except for those using N95 masks, all participants were fit tested according to standardised procedures (CITE fit2fit guideline) [211]. Those presenting with broken skin were excluded from the study. The study was approved by the UK Health Research Authority committee (IRAS 285764) and written informed consent was obtained from participants prior to commencing the study.

The study was conducted during the second wave of the COVID-19 pandemic in the UK (December 2020 to March 2021). Anatomical locations on the face, namely an area outside the perimeter of respirator application (site A) and either the right or left the cheek (site C) were investigated (Figure 6.1a). The assessment of biophysical skin parameters at these sites was performed as described previously in Abiakam et al. [203]. In summary, TEWL, (Tewameter, Courage + Khazaka electronic GmbH, Germany), stratum corneum hydration (Corneometer, Courage + Khazaka electronic GmbH, Germany) and erythema was collected in the indicated order. This was followed by the sampling of skin surface sebum using Sebutapes, while corneocytes were the last samples to be collected. Biophysical skin parameters and sebum collection were performed pre- and post-respirator application. The skin response to respirator application (TEWL and SC hydration) was calculated as the ratio between pre- and post-shift biophysical skin values (normalized values), as previously described and presented in Abiakam et al. [203].

Corneocytes were collected in three distinct sessions after the working shift of the HCW (Figure 6.1b). During the test session, each participant acclimatized in an indoor environment and the skin on their face was dried with paper towels (Tork®, Bedfordshire, UK) prior to measurements. Corneocyte collection was only performed post-respirator application. This was done to avoid the possibility that the act of tape stripping immediately prior to wearing RPE makes the skin more susceptible to respirator-induced damage.

All test sessions were conducted in a temperature and humidity-controlled laboratory (room temperature of 22.5± 0.7ºC and relative humidity of 42± 6%). Data

collection was performed following established and published patterns to minimise interferences [212].

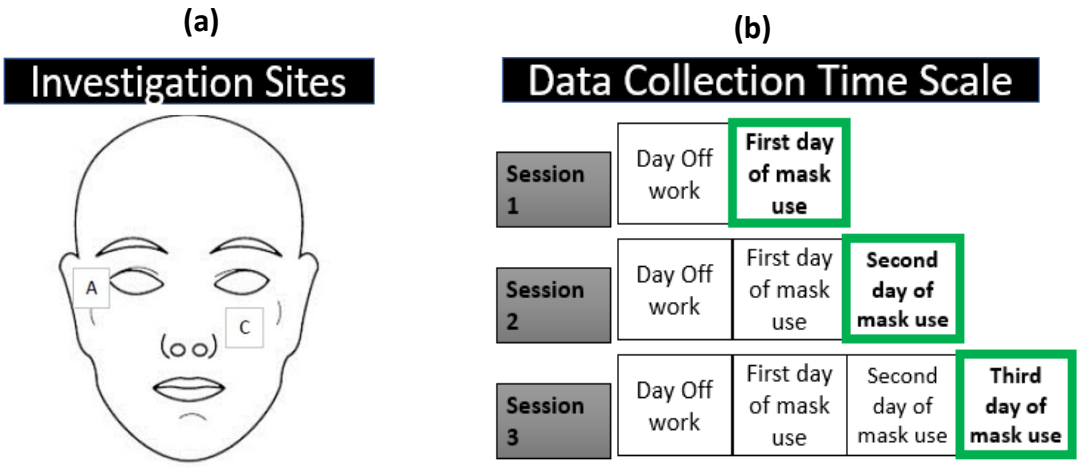

Figure 6.1. Study protocol. (a) Investigation sites for the analysis of the properties of corneocytes. A - area outside the perimeter of respirator application (negative control); C – left cheek. **(b)** Scheme of sample collection. After a day off work, tape stripping was performed after one, two or three days of consecutive respirator usage. Corneocytes were collected after assessment of biophysical skin parameters and sebum collection. Corneocyte collection was only performed post-respirator application to avoid the possibility that the act of tape stripping immediately prior to wearing RPE that could make the skin more susceptible to respirator-induced damage. TEWL and stratum corneum hydration were measured pre- and post- respirator application. The periods between consecutive test sessions varied for practical reasons, ranging between 1 to 8 weeks. The corresponding analysis depicts the number of consecutive days wearing a FFP2 or FFP3 masks, denoted as test sessions.

Two cell collection sites with three distinct data collection sessions were used as highlighted in Figure 6.1:

- Session 1: participant first day of respirator usage following return to work after a period of absence (minimum of 24 hours).
- Session 2: second consecutive day of respirator usage in a given working week.
- Session 3: third consecutive day of respirator usage in a given working week.

6.3.2 Collection and isolation of corneocytes

At the end of each shift, and following the biophysical assessment procedures, corneocytes were collected from the two sites (Figure 6.1a), after sebum collection using commercially available Sebutapes (CuDerm, Dallas, TX, USA) as described in our published study on the analysis of the same subjects [203]. The cells were sampled via tape stripping (Sellotape, UK) by pressing the tape gently onto the skin with gloved hands and gently removing by peeling the tape. Each tape strip was cut in half and used for the assessment of CE maturation and indirect visualization of CDs by the immunostaining of a CD protein – desmoglein-1 (Dsg1).

6.3.3 CE maturity assay: CE extraction and immunostaining for involucrin and Nile red staining for lipids

Cornified envelopes were isolated from the tape using an established methodology [75]. Briefly, half of each tape was extracted with 750 mL of dissociation buffer containing 100 mM Tris-HCl pH 8.0, 5 mM EDTA (ethylenediaminetetraacetic acid), 2% SDS (sodium dodecyl sulphate) and 20 mM DL-dithiothreitol (Sigma Aldrich Dorset, UK). Tapes were extracted in the dissociation buffer for 10 min at 75 °C and centrifuged at room temperature for 10 min at 5000 g. The extracted CEs were washed (three times) in washing buffer: 20 mM Tris-HCl pH 9.0, 5 mM EDTA, 0.2% SDS and 10 mM DL-dithiothreitol and suspended in 1 × PBS buffer (Sigma Aldrich Dorset, UK).

Extracted CEs were transferred onto a Polysine-coated microscope slide (5 µL, VWR international Ltd, Leicestershire, UK) for the immunostaining protocol, as previously described [75]. This included an overnight incubation in a humidity chamber at 4°C in the primary monoclonal antibody (1:100, mouse anti-human involucrin SY5,

ABCAM, Cambridge, UK). The antibody solution was washed with PBS three times for 5 min before adding the secondary antibody Alexa-Fluor 488-labeled goat anti-mouse IgG antibody (1:200, ABCAM, Cambridge, UK) for 60 min at room temperature (in the dark). The slides were washed with 1 × PBS (three times for 5 min) and mounted with 20 µg/mL Nile red (Sigma Aldrich, Dorset, UK) in 75% glycerol solution.

6.3.4 Immunostaining for Dsg1

The immunostaining protocol for Dsg1 was followed as presented in Chapter IV [85]. Corneocytes attached to the tape were washed with 1 × PBS (10 min) and incubated with a P23 mouse monoclonal antibody against the extracellular domain of Dsg1 (Progen, Heidelberg, Germany) at 4 °C overnight. This was followed by incubation with an Alexa-Fluor 488-labeled goat anti-mouse IgG antibody (1:200, ABCAM, Cambridge, UK), for 60 min at room temperature in the dark. The samples were mounted with anti-fade fluorescence mounting medium (ABCAM, Cambridge, UK).

6.3.5 Image and data analysis

Five non-overlapping images were taken in total for each CE and each Dsg1 sample with a field of view of 720 × 580 µm. The fluorescence images were acquired at a 10× objective magnification and analysed using a Leica DMRBE microscope (Leica Microsystems, USA) equipped with PL-Fluotar 5 × /0.12 and 10 × /0.30 lenses mounted with a Cool-LED pE-300 series blue-illumination source at the wavelength of 460 nm and with a Motic Pro 252 microscope camera. Image quality control was performed using a QC pipeline [30] on the open-source software Cell Profiler (http://cellprofiler.org/). Images were analysed using Image J® version 1.53a (National Institutes of Health, Bethesda, MD, USA).

CE maturation was evaluated using a sequential approach (Figure 6.2a). After application of a Gaussian filter, images were converted to either an 8-bit map (for total cell number count) or divided in RGB channels (to count cells staining for Alexa-Fluor 488, i.e., positive to involucrin). The Huang threshold followed by Watershed command was applied to define CE borders and the cells with a surface area of 300-2000 µm^2 were counted based on the reported average values [125].

$$\%\,\mathrm{INV}+ \;= \frac{\text{number of INV} + \text{cells}}{\text{total number of cells}} \times 100$$

For the distribution of Dsg1, the ratio of pixels expressing Dsg1 to the total area in pixels was counted in two random regions of interest (ROIs) of 70 x 70 µm (see yellow boxes in Figure 6.2b) that contained corneocytes, as previously established and described in [86, 125]. Images were, first, transformed in 8-bit maps and a Huang threshold was applied. This was followed by the Watershed command and using “Analyse Particle” command to count number of pixels (Figure 6.2b).

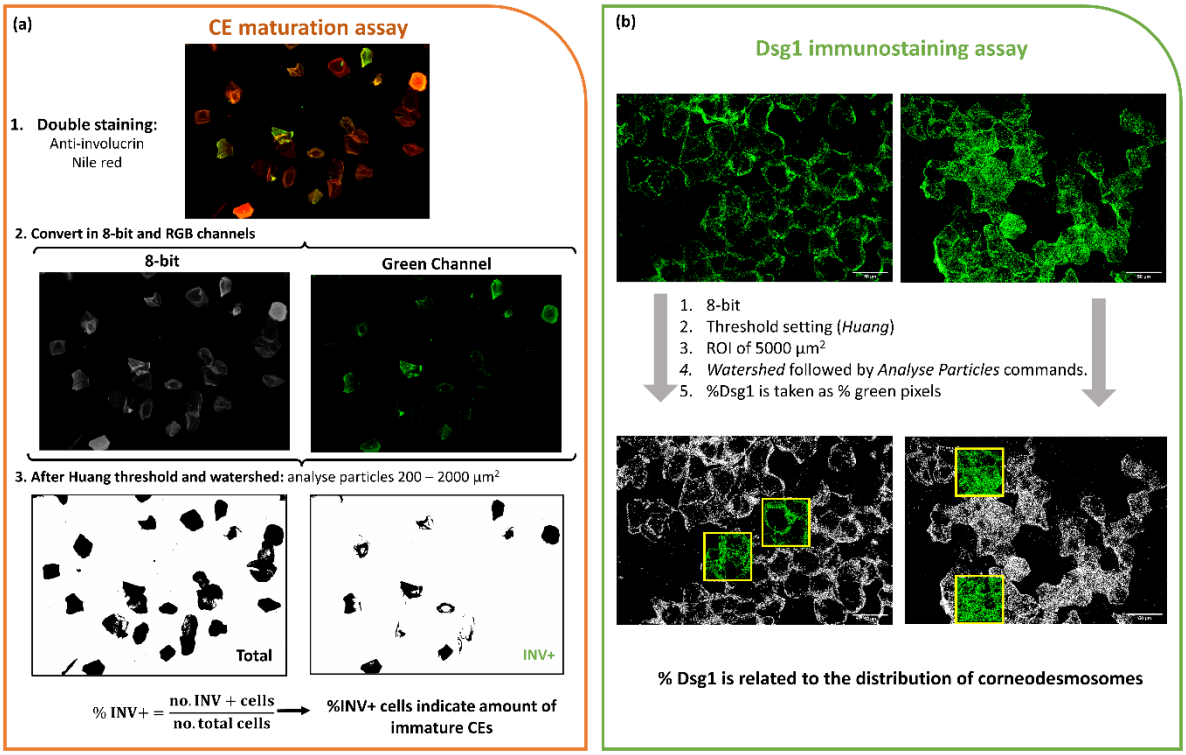

Figure 6.2. Scheme of image analysis procedures. For each sample, 5 images were analysed for each assay. **(a)** Design of maturation assay image analysis. 8-bit and RGB (green) channel are used to count the total number of cells and those staining with Alexa-fluor 488 (INV+), respectively. The Huang threshold is applied to the images, followed by watershed segmentation. The ratio between the number of green/total cells is calculated to obtain % of immature cells (% INV+). **(b)** Design of Dsg1 immunostaining assay image analysis. Raw images of Alexa-fluor fluorescence are transformed in 8-bit images. Huang threshold followed by watershed command were applied, and two ROIs are analysed using the "Analyse particles" command: the percentage of green pixels against the total number of pixels in the two ROIs are taken as the percentage of Dsg1 in each image. Image scale bar = 50 µm.

6.3.6 Data analysis

The median of five repeat images for each body site and session was calculated for each participant and imported into IBM® SPSS® Statistics (version 27) for analysis and assessed for normality using probability plots and the Shapiro-Wilk test, which revealed a non-normal distribution across participants. Accordingly, the Friedman test was employed to investigate whether the challenges to the skin were able to induce temporal variations in cell properties. It was followed by the Wilcoxon Signed Ranks

Test to investigate whether there were differences in cell properties between the control site and the cheek at the different time points. Tests were considered statistically significant at a 5% level ($p<0.05$).

The Spearman's correlational analysis was employed to investigate the relationships between the properties of corneocytes and biophysical parameters as presented in Abiakam et al. [203] as well as for self-reported adverse reactions and body mass index BMI. A rank-sum was used for the properties of skin cells and biophysical markers, by summing the ranks of corneocyte properties and of the pre-respirator application values of TEWL and SC hydration to study the relationship between barrier function and cell properties in unloaded skin. Additionally, a rank sum of normalised TEWL values (post/pre-respirator application ratio) at the cheek was used to correlate the effect of respirator usage with corneocyte properties. Self-reported skin adverse reactions were scored (0 – no reactions, 4 – maximum reported reactions) and plotted against the two corneocyte properties.

6.4 Results

The study recruited 17 HCWs (15 females and 2 males) who used N95 or FFP3 during established clinical shift patterns as described in Abiakam et al. [203]. The age of the participants ranged between 22 and 61 years (mean ± SD was 33 ± 11 years), and the BMI was 25.1 ± 5.4 kg/m^2. Participants shift length ranged from 8 to 12 hours and breaks ranged from 1 to 4 per shift, being consistent for each participant, as they followed an established working pattern.

6.4.1 Cheek presented higher levels of immature CEs and Dsg1 compared to the control site

Representative immunostaining images for two participants, P5 and P10 corresponding to individuals with low and high levels of immature CEs and Dsg1, respectively, are shown on Figure 6.3, for the cheek at each session.

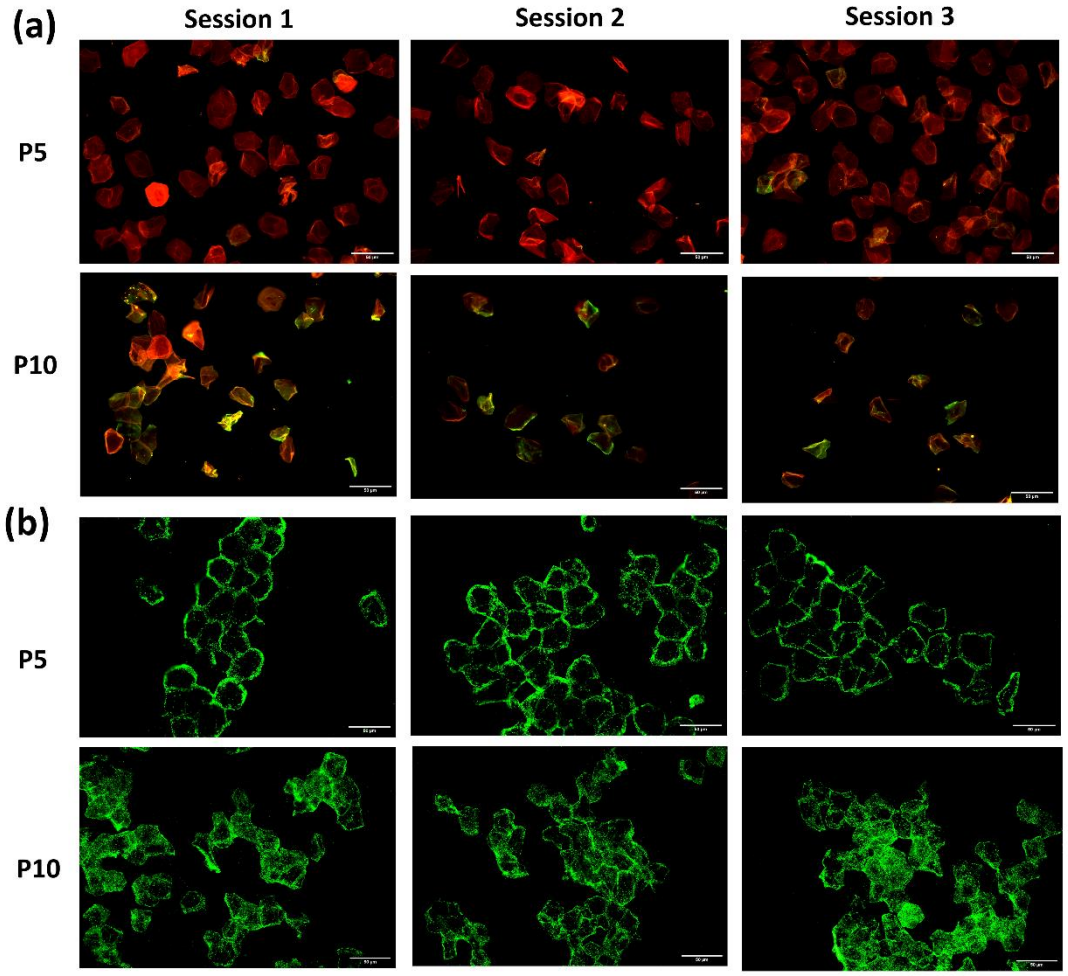

Figure 6.3. Representative immunostaining images of CE maturity and Dsg1 assays. Images showcase the case of low (P5) and high (P10) levels of INV+ CEs **(a)** and Dsg1 **(b)** at the cheek. (a) Low level of CE maturity is represented by a high number of CEs positive for involucrin (median = 31, 35, 54% on sessions 1, 2 and 3, respectively for P10), while high level of maturity is characterized by hydrophobic CEs (median = 17, 23 and 8% for sessions 1, 2 and 3 respectively for P5). (b) Honeycomb pattern of Dsg1 is observed for P5 (median =22, 12, 15% Dsg1 on sessions 1, 2 and 3, respectively), while CDs are present ubiquitously over the cell surface for P10 (median = 46, 45 and 39% Dsg1 on sessions 1, 2 and 3 respectively). P5 – participant 5; P10 – participant 10. Scale bar = 50 µm.

The properties of corneocytes across the three sessions for each participant are shown in Figure 6.4. The median levels of immature CEs based on five repeat images ranged from 11 to 50%, while the median levels of Dsg1 ranged from 12 to 56% at the two sites across the sessions (Table 6.1). The inter-subject variability was measured between participants for the three sessions, and the maximum coefficient of variation (CV) for the level of immature CEs was found to be 33% and 43% for the cheek and the control site, respectively. Similar values were found for the level of Dsg1, with maximum values of 30% at both sites.

Although there was a variability between participants, a positive correlation ($r=0.81$, $p<0.001$) was found between the two anatomical locations, i.e., participants with higher levels of Dsg1 at the control site, also generally presented higher values at the cheek. The same positive trend was found for the level of CE maturity ($r=0.47$, $p=0.061$).

When considering the median values of the cohort, significant differences were not found between the test sessions for either of the anatomical locations. However, differences were identified between anatomical sites for each session (Table 6.1), with higher levels of Dsg1 ($p<0.05$ for each session) in the loaded cheek compared to the control. Similar trends were also observed for the level immature CEs, although statistical significance was only achieved at session 2.

Table 6.1. Summary of corneocyte properties of the 17 HCWs cohort at each of the three test sessions.

Parameter (%)	Session 1					Session 2					Session 3				
	Control		Cheek			Control		Cheek			Control		Cheek		
	Median	Range	Median	Range	*p-value*	Median	Range	Median	Range	*p-value*	Median	Range	Median	Range	p-value
INV+	24.3	11-39	29.9	11-50	0.100	25.9	16-36	29.9	22-38	0.028*	26.2	11-46	*33.9*	10-49	0.496
Dsg1	35.7	19-45	37.9	16-48	0.015*	31.5	16-48	41.1	12-56	0.025*	28.7	14-47	36.9	19-46	0.023*

6.4.2 High levels of mature CEs and low levels of Dsg1 correlate with increased SC hydration at unloaded skin

A correlational analysis of the rank-sums across test sessions was employed to investigate the relationship between the SC structure and the skin barrier function at the two facial locations of unloaded skin (Figure 6.5), i.e., by investigating the relationship between SC cell properties and pre-respirator application skin biophysical parameters. Indeed, corneocytes were only collected post-respirator application, but considering that these are dead cells, any biochemical alteration to their maturation properties would not be expected to occur during a single shift, since these can take several days to manifest [213]. The correlations between the properties of corneocytes and TEWL were not statistically significant (Figures .6.5a and c), with the exception of a positive correlation in the values of Dsg1 at the cheek ($p<0.05$) However, when SC hydration values were correlated to both the levels of immature CEs and Dsg1 a significant negative relationship was evident at both the control and cheek sites (Figures 6.5b and 6.5d), i.e., an increasingly hydrated SC correlates with lower levels of immature CEs and corneodesmosomes.

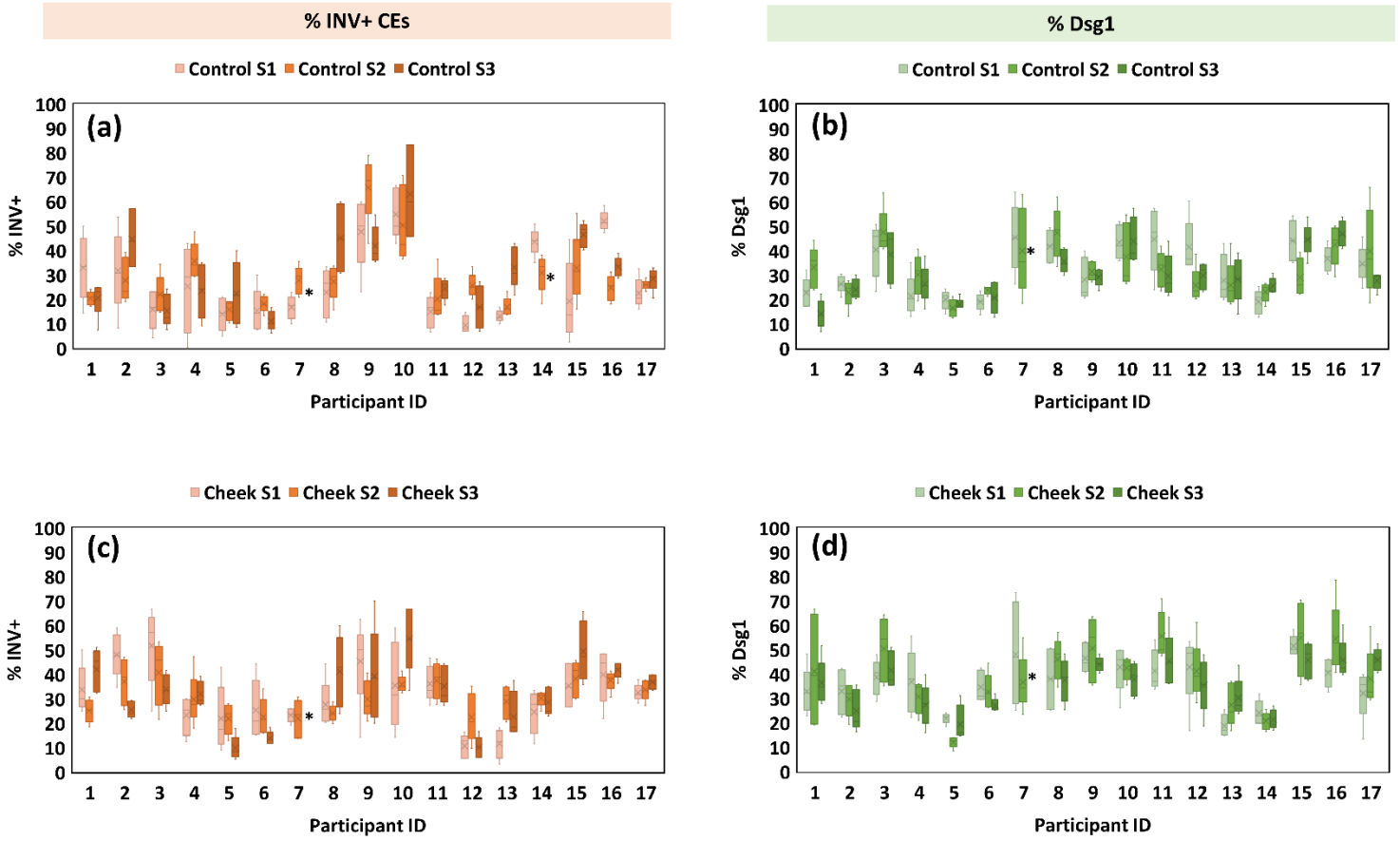

Figure 6.4. Individual data concerning the level of immature CEs and Dsg1. (a) and (c) Percentage of immature CEs in the negative control site and cheek expressed as the percentage of cells positive for involucrin. **(b) and (d)** Percentage of Dsg1 puncta stained at the surface of corneocytes from the negative control site and cheek. All data are shown as box-plots. The box boundaries indicate the 25th and 75th percentiles, while the whiskers represent the 10th and 90th percentile. The mean is shown by the cross (×) and the median by the line (—). (* indicates missing data).

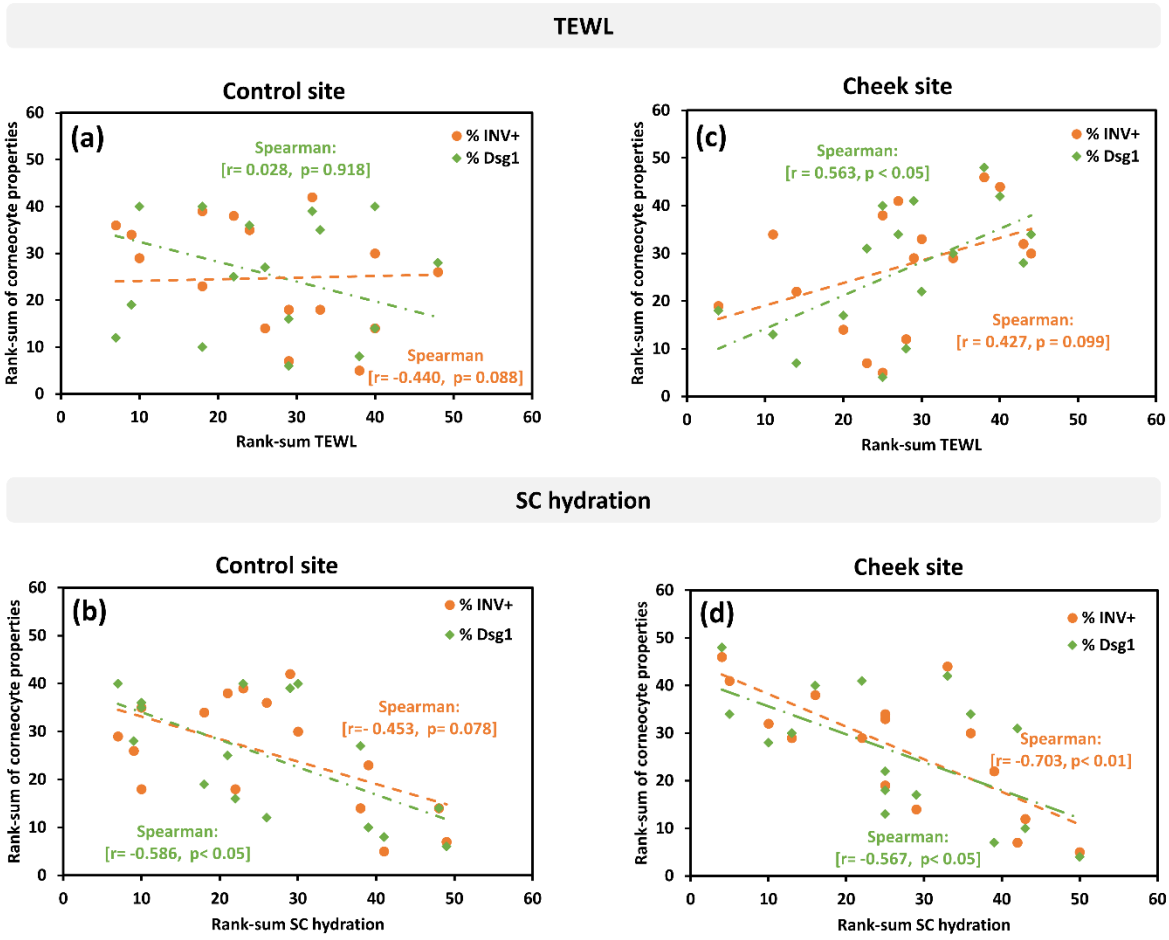

Figure 6.5. Correlations between the rank-sums of the properties of corneocytes (% INV+ and % Dsg1) and biophysical parameters. (a and c) TEWL and **(b and d)** SC hydration measured pre-respirator application across test sessions for the control site (a and b) and the cheek (c and d).

6.4.3 Low levels of immature CEs correlate with barrier function disruption after prolonged respirator usage

In our previous analysis of the same subjects, we found changes in the barrier function of the cheek after each test session [203]. Indeed, 2-fold-changes were recorded in 24% and 19% of the participants in test sessions 2 and 3, respectively, measured as the ratio post/pre-respirator application for TEWL. Consequently, a correlational analysis was employed between the rank-sums (of all three sessions) of both % INV+ and

% Dsg1 and the skin response to insult measured as the normalized (pre- to post-respirator application) value of TEWL (Figure 6.6).

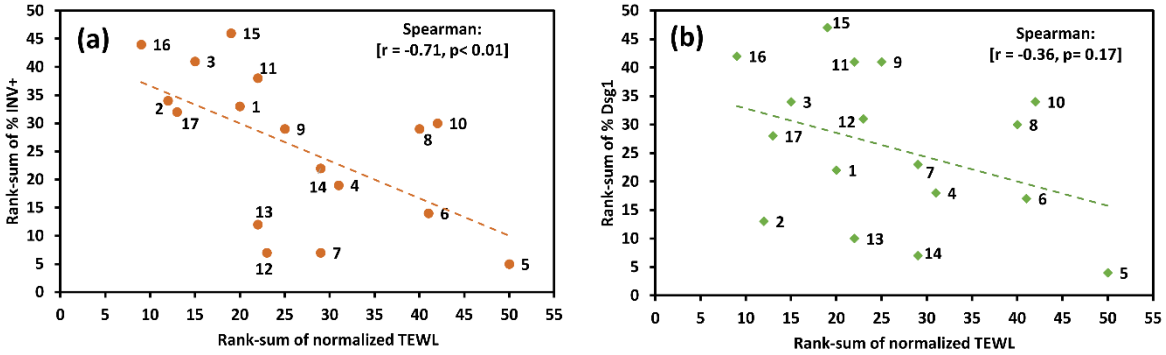

Figure 6.6. Correlational analysis between skin barrier disruption and corneocyte properties. Relationship between the rank-sum of (**a**) %INV+ and (**b**) % Dsg1 on the rank-sum of normalized TEWL (i.e., rank-sum of the ratio pre/post-respirator application) at the cheek.

Interestingly, a negative correlation ($p<0.01$) was observed between the number of immature CEs and the TEWL response to respirator application (Figure 6.6a). By contrast, the corresponding negative correlation with %Dsg1 was not statistically significant (Figure 6.6b).

6.4.4 A higher level of self-reported skin adverse reactions correlates with high level of immature CEs and Dsg1

Finally, the relationship between the properties of the corneocytes and skin adverse reactions reported by the participants was investigated (Table 6.2). The reactions were graded from 0 to 4, where 0 corresponded to no adverse reaction and 4 to reports of a combination of dry skin, spots, itchiness, and rashes (i.e., one point per reaction). The categorical score of skin adverse reactions was plotted as a function of the rank-sum of values of % INV+ and Dsg1 of the loaded site of the cheek, as shown in Figure 6.7.

Table 6.2. Adverse reactions to the skin reported by the participants following respirator usage.

Participant ID	Adverse reactions	Score
1	spots, dry skin	2
2	itchiness, excessive sweating	1
3	spots, itchiness	2
4	none	0
5	spots, lumps	1
6	none	0
7	spots, itchiness	2
8	excessive sweating	0
9	spots, dry skin	2
10	spots, dry skin, excessive sweating, headache	2
11	itchiness, spots, excessive sweating	2
12	none	0
13	spots	1
14	none	0
15	dry skin, rashes, spots, itchiness	4
16	dry skin, rashes, spots, itchiness, excessive sweating	4
17	dry skin	1

The analysis revealed that each of the 17 participants reporting 2 or more skin adverse reactions, presented a high level of immature CEs (rank sum % INV+ across sessions was above 25), while the majority of these (6 out of 7) also presented high levels of Dsg1 (rank sum above 30). By contrast, those with fewer self-reported skin reactions had a lower rank of immature CEs and Dsg1. In fact, when performing a correlational analysis (Spearman coefficient), a positive correlation was found for the rank-sum of immature CEs ($r=0.797$, $p< 0.001$) and for %Dsg1 ($r=0.743$, $p< 0.001$).

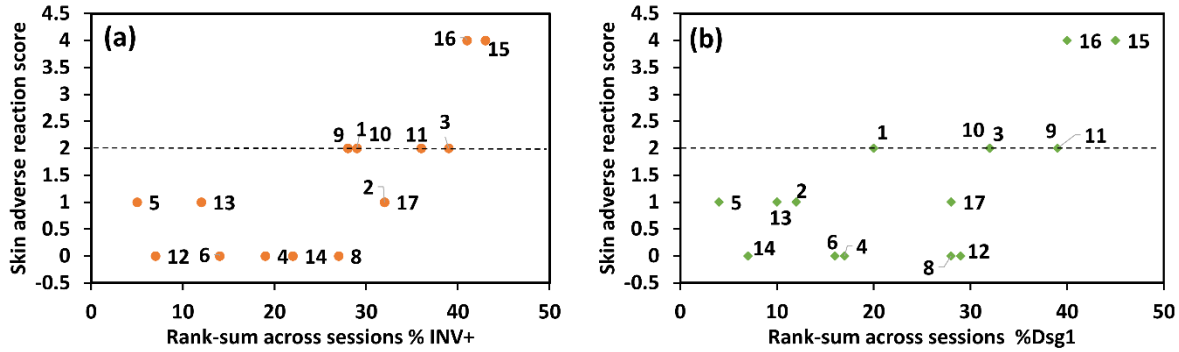

Figure 6.7. Relationship between the score of self-reported skin reactions and corneocyte properties. The number of skin adverse reactions registered were scored from 0 to 4 and related to the rank-sum of % INV+ **(a)** and % Dsg1 **(b)** at the cheek.

6.5 Discussion

The extensive use of personal protective equipment (PPE) during the outbreak of the coronavirus pandemic led to ubiquitous reports of adverse skin reactions in HCWs [195, 196, 198]. In our published study on the analysis of the same subjects we demonstrated how the integration of biophysical and biochemical markers could provide a comprehensive analysis of changes in local skin health following respirator usage [203]. However, there is still a limited understanding of the actual mechanisms in the skin leading to those changes. Therefore, the primary aim of this complementary study was to investigate the properties of superficial corneocytes in the context of prolonged respirator application to broaden the knowledge of skin surface physiology. While an effect of respirator usage was not observed for corneocyte maturity and CD distribution over time, the level of CDs was higher in the skin site at the loaded cheek site compared to an area outside the perimeter of the respirator, representing a negative control site, for all three sessions. Furthermore, a greater number of self-reported skin adverse reactions was shown to correspond with a greater number of immature CEs and CDs at the cell surface (Figure 6.7).

In the present study, the properties of corneocytes were observed to vary between individuals. In the context of CE maturity, the maximum coefficients of variation (CVs) between participants (considering the three sessions analysed) of 33% and 43% were found for the cheek and the control site, respectively. Equally high CVs have been observed previously by Guneri et al. [75] for cells of the cheek and post-auricular areas (54 and 27%, respectively). Similar inter-subject variability was also found for the level of Dsg1, with a maximum CV between participants of 30% at both sites. However, such variability did not appear to arise from intrinsic factors such as age or BMI, since no

significant correlations between these factors were observed (see Appendix D). In fact, this was expected considering the age range of the cohort, which was between 21-41 years (with two participants aged 57 and 61). A prominent effect of age is expected only when comparing adult and aged skin [40, 214].

When analysing the temporal effects of respirator usage on the properties of superficial cells, there were not any statistically significant differences between the test sessions. However, the level of Dsg1 was higher for the loaded cheek site compared to the unloaded control site ($p < 0.05$ for all 3 test sessions). Furthermore, similar trends existed for the level of immature CEs, although the difference was only statistically significant for session 2 (Table 6.1). This could be due to a temporal adaptation of the cheek to respirator application involving mechanical loading or be caused by the stripping of superficial SC layers due to rubbing of respirator against the skin. The current study was performed during the second wave of COVID-19 in the UK, when respirators had been mandated in the clinical settings for over 12 months, and hence adaptation of the SC may have occurred. Indeed, the disruption of the SC has been observed in *in vitro* histological studies, following 24 hours of severe loading (200 mmHg) [215]. Recently, Caggiari et al. observed high interface pressures at the nasal bridge (>70 mmHg) for four different respirators [197]. However, there has not yet been a study that has investigated the effects of persistent loading on the physiology of the SC. Alternatively, this difference between anatomical sites could suggest that spatially close anatomical regions can be differently regulated, as observed previously by Guneri et al. [75] and in Chapter IV.

Previously, TEWL and SC hydration have been correlated with SC cohesion, associated with the pattern and number of CDs [85, 86]. However, such observations have

been mainly used to correlate different anatomical sites [36], and in tape stripping procedures in which the outer layers of skin are removed to compare SC properties at different depths [75, 85]. This motivated the present correlational analysis between the biophysical markers and the properties of corneocytes to further investigate the role of corneocytes in the skin barrier function. When correlating the integrated rank-sum of cell properties with the biophysical markers measured prior to the HCW shift, a statistically significant association was evident for SC hydration at both sites (Figures 6.5c and 6.5d), and for TEWL at the cheek (Figure 6.5b). This supports the assertion that the skin barrier function depends on a mature SC, characterized by a honeycomb distribution of CDs at the cell's edge and rigid and hydrophobic CEs [85, 86, 166].

However, this relationship was not observed with the values of biophysical markers measured after respirator application. Participants with a high TEWL ratio pre- to post respirator application, tended to have lower levels of immature CEs ($p < 0.01$). Although seemingly contradictory, this observation may pertain to information underlying the different mechanisms and functions of the SC. It is hypothesised that while a mature SC, with a honeycomb pattern of CDs and hydrophobic CEs, may be a requirement for a well-maintained barrier function, with lower TEWL values, it may be detrimental when exposed to mechanical insults such as respirator application. This would be consistent with the properties of the anatomical regions, such as the palm of the hand or plantar region of the foot, which are adapted to grip and load-bearing functions, presenting an immature SC [216]. Future studies should focus on understanding this apparent dichotomy between load-bearing and barrier functions, particularly by comparing glabrous and non-glabrous skin.

When analysing the trends between self-reported adverse skin reactions and the studied cell properties, it was observed that participants reporting dry skin, spots, itchiness, rashes, and excessive sweating usually presented greater levels of immature CEs and Dsg1 (Figure 6.6). This indicates that a mature SC is associated with less adverse reactions after prolonged use of respirators, which seems to contradict the relationships found with biophysical markers. However, it must be emphasised that such reactions may be induced by different mechanisms than those provoking changes in TEWL, and consequently a direct comparison and causal associations cannot be made. As an example, itchiness associated with dry skin may be related to the properties of corneocytes, such as an interrupted corneodesmosome remodelling as occurs in ichthyosis vulgaris [207].

This study was limited by the relatively small HCW cohort from a single UK acute care provider, and necessarily most participants were female of white (Caucasian) ethnicity [203]. These factors and the small variations in BMI and age of the participants limit the generalisability of the findings. Also, it should be emphasised that the study was conducted over varying time periods (1-8 weeks), which might have impacted on the properties of superficial corneocytes, since it is known that the upper SC characteristics vary with both external and seasonal conditions [217]. Furthermore, future studies should focus on the effect of respirator application causing potential rubbing of the most superficial layers of the SC, which could explain a lack of mature SC registered at the cheek.

Furthermore, prolonged use of respirators, which limits airflow and creates occlusion, can result in a moist microenvironment. This can lead to the softening of corneocytes in the superficial skin layers, which, as investigated in the previous

chapter, can have an impact on their mechanical properties, making them more pliable and less rigid. This softening can affect their mechanical behaviour, potentially rendering them more susceptible to deformation under mechanical stresses. This may be detrimental to the skin barrier function, since a soft SC may be more prone to damage by friction and shear.

Although biophysical markers can provide insights on the status of the skin barrier function, they may be insufficient to understand the mechanisms leading to the loss of skin integrity in the context of mechanical insults. Superficial corneocytes, which are easily collected by tape stripping, are an interesting candidate for a skin integrity biomarker. The present work confirms previous claims relating barrier function with SC structure [85, 86], but raises questions concerning the role of this layer in adapting to prolonged pressure and shear insults. Future studies should focus on the role of corneocytes in skin surface integrity and challenge the relationships between barrier function and mechanical resistance.

6.6 Conclusion

The current study examined two surface properties of corneocytes, namely, the levels of immature CEs and Dsg1, at two skin sites on the face of healthcare workers following prolonged wearing of respiratory protective equipment during routine clinical shifts. While there was minimal effect of respirator usage on corneocyte maturity and CD distribution over time, the levels of CDs and immature CEs were consistently higher in the loaded cheek site compared to the negative unloaded control site. Furthermore, participants with a greater number of self-reported skin adverse reactions presented a larger number of immature CEs and larger level of Dsg1. These results contrasted with relationships observed for biophysical parameters, such as skin barrier function

measured by TEWL. These findings raise questions about the role of corneocytes in maintaining skin integrity. Further investigation is necessary to determine if the properties of corneocytes associated with a healthy barrier function are detrimental when the SC is subjected to pressure, shear, and frictional forces.

CHAPTER VII - CHANGES IN THE PROPERTIES OF SUPERFICIAL CORNEOCYTES OVER A CATEGORY I PRESSURE ULCER: A COHORT STUDY

This chapter is based on Évora, A.S., et al., *Changes in the properties of superficial corneocytes over a category I pressure ulcer: a cohort study* submitted to the Journal of Dermatological Science.

7.1 Abstract

Pressure ulcers (PUs) are chronic wounds that are detrimental to the quality of life of patients. Despite advances in monitoring skin changes, the structure and function of skin cells over the site of pressure ulcers are not fully understood. The present study aims to evaluate local changes in the properties of corneocytes in category 1 PU sites sampled from a cohort of hospitalised patients. Cells were collected from a PU-compromised site and an adjacent control area and their topographical, maturation and mechanical properties were analysed. Corneocytes at the PU-compromised site were characterized by higher levels of immature cornified envelopes ($p<0.001$) and greater amounts of desmoglein-1 (corneodesmosomal protein) ($p<0.001$) compared to the adjacent control area. The cells at the control site presented the typical ridges-and-valleys topographical features of sacrum corneocytes, by contrast the PU cells presented circular nano-objects at the cell surface, and, for some patients, the cell topography was deformed. Although differences were not observed in the mechanical properties of the cells, those of the elderly patients were much softer compared with young subjects previously studied. Further research is required to elucidate if these changes in corneocytes can be used to monitor and predict changes in skin integrity.

7.2 Introduction

A pressure ulcer (PU) has been defined as localised damage to the skin and/or underlying tissue, as a result of pressure alone or in combination with shear, usually occurring over a bony prominence and may also be related to the application of a medical device or other objects [10, 218]. However, as suggested by late Emeritus Professor Dan Bader in his recent editorial "*The last hurrah"*, there has been a recent overemphasis on deep tissue injury (DTI) in the literature [219, 220]. This ignores the fact that most PUs are classified as category I and II and are initiated at the superficial dermal and epidermal layers, with interactions of pressure, shear, friction and moisture [3]. Although the role of the dermis on the architecture and mechanical function of the skin has been studied [121, 122], the potential role of the epidermis, and particularly that of the Stratum Corneum (SC) is usually neglected.

The SC can be considered a thin stiff film of dead cells on top of softer viable tissues [21, 125, 221]. At low relative humidities (RH ~30–40%), the SC acts as a polymer in a glassy state, with Young's moduli values of the order of GPa [125], i.e., a factor of 10^5 greater that of the dermis [222]. As a result of the characteristic mechanical properties, the role of the SC, and that of its main cells (corneocytes) on early indications of skin damage should be investigated with a focus. Indeed, corneocytes suffer a maturation process as they move upwards in the SC, with the loss of intercellular junctions (corneodesmosomes, CDs) and the maturation of the cornified envelope (CE) [125]. Recently, the authors have characterized the changes in the properties of these cells in healthcare professionals following the prolonged application of respirator protective equipment (RPE) [168]. The results revealed higher levels of immature CEs and Dsg1, a cadherin-type cell-cell adhesion molecule found in stratified

epithelial desmosomes, at the sites of mechanical load exposure from the respirator application (cheek) compared to a control site (Chapter VI) [168].

The current authors investigated changes in biophysical parameters of skin and the inflammatory cytokine responses in a cohort of hospitalised patients presenting with category I PUs [223, 224]. Significant spatial changes in skin barrier function were revealed (TEWL), and evident upregulation in proinflammatory biomarker IL-1α, suggesting that the tissue homeostasis was compromised. However, to date there has not been any investigation of the changes in the properties of skin cells from the sites of PUs. Therefore, the aim of the current study was to characterise the maturation and mechanical properties of corneocytes over the site of a category I PU from a sub-group of a cohort presenting such PUs from our previous study [223].

7.3 Materials and Methods

7.3.1 *Study Protocol*

The current investigation represents a secondary analysis from a cohort observational study conducted by Abiakam et al. in a large teaching hospital in the UK [223]. It was approved by the Health Research Authority committee (IRAS 301685) and written informed consent was obtained from patients prior to commencing the study. A sub-set of patients (n=17) from the original cohort of 30 who presented with category 1 PUs from elderly care and surgical hospital wards were selected. Corneocytes were collected from the investigation sites, i.e., PU-compromised area and a control site, located 10 cm lateral to the PU site (Appendix E - Figure E1). Cells were collected via tape stripping (Sellotape, UK) (Figure E1b – first tape strip was used), by pressing the tape gently onto the skin with gloved hands and removing via peeling. Each tape strip

was cut into three equal parts and used for topographical and mechanical analysis via Atomic Force Microscopy (AFM) (Figure E1d), and for assessment CE maturation and corneodesmosomes distribution (Figure E1e and E1f).

7.3.2 Atomic Force Microscopy

Atomic force microscopy (AFM) imaging and nanoindentation experiments were performed in air (Nanowizard 4, JPK). Standard imaging tips (NCHV-A, Bruker AFM Probes, Inc), with a nominal spring constant of 40 N/m and resonance frequency of 300 kHz, were used. Cell roughness was measured as root mean square height deviations (S_q) and arithmetic mean height deviations (S_a) from fitted mean planes using Gwyddion software [132], by analysing three random regions of 25 μm^2 per cell. The geometry of each AFM tips was calibrated as described in Appendix E (E2). Corneocytes were extracted from the tape by pressing the tape onto a microscope glass slide by overnight incubation in xylene. Cells attached to the slide were imaged in Tapping Mode (512 x 512 pixels, 40 x 40 µm). Nanoindentation experiments consisted of 64 indents on an 8 x 8 matrix, with points spaced 625 nm apart. Five cells were evaluated per sample. Force curves consisted of loading-pause-unloading cycles, with a maximum applied force of 1–2 µN. When this force setpoint was reached during loading, the cell was allowed to relax for a period of 4 s at a constant height. After this period, the AFM probe was retracted from the surface. The Young's modulus of corneocytes was calculated using the Oliver-Pharr analysis, as described in the Appendix E (E3).

7.3.3 CE maturity assay: CE extraction and immunostaining for involucrin and Nile red staining for lipids

Cornified envelopes were isolated from the tape using an established methodology [75] and processed using a standardised protocol [168]. In summary, half of each tape was extracted with 750 mL of dissociation buffer containing 100 mM Tris-HCl pH 8.0, 5 mM EDTA (ethylenediaminetetraacetic acid), 2% SDS (sodium dodecyl sulphate) and 20 mM DL-dithiothreitol (Sigma Aldrich Dorset, UK). The tapes were extracted in the dissociation buffer for 10 min at 75 °C and centrifuged at room temperature for 10 min at 5000 g. The extracted CEs were washed three times and suspended in 1 × PBS buffer (Sigma Aldrich Dorset, UK). Extracted CEs were transferred onto a Polysine-coated microscope slide (5 µL, VWR International Ltd, Leicestershire, UK) and incubated overnight in a humidity chamber at 4°C with a primary monoclonal antibody against involucrin (1:100, mouse anti-human involucrin SY5, ABCAM, Cambridge, UK). The antibody solution was washed with PBS three times for 5 min before adding the secondary antibody Alexa-Fluor 488-labeled goat anti-mouse IgG antibody (1:200, ABCAM, Cambridge, UK) for 60 min at room temperature (in the dark). The slides were washed with 1 × PBS (three times for 5 min) and a cover slip was mounted with 20 µg/mL Nile red (Sigma Aldrich, Dorset, UK) in 75% glycerol solution (w/w).

7.3.4 *Immunostaining for dsg1*

The prevalence of corneodesmosomes was indirectly measured by immunostaining of desmoglein-1 (Dsg1). The immunostaining protocol for Dsg1 was adapted from a previous study [168]. Here, corneocytes were extracted from the tape onto a glass slide via overnight immersion in xylene to avoid residual fluorescent background from the

tape (Figure E1c). Attached cells were washed with 1 × PBS (10 min) and incubated with a P23 mouse monoclonal antibody against the extracellular domain of Dsg1 (Progen, Heidelberg, Germany) at 4 °C overnight. This was followed by incubation with Alexa-Fluor 488-labeled goat anti-mouse IgG antibody (1:200, ABCAM, Cambridge, UK), for 60 min at room temperature in the dark. The samples were mounted with anti-fade fluorescence mounting medium (ABCAM, Cambridge, UK).

7.3.5 *Image analysis*

Optical image analysis was performed as previously described and presented in Chapter VI [168]. Briefly, five non-overlapping images were taken in total for each CE and Dsg1 sample at a 10× objective magnification and analysed using a Leica DMRBE microscope (Leica Microsystems, USA) equipped with PL-Fluotar 5×/0.12 and 10×/0.30 lenses mounted with a Cool-LED pE-300 series blue-illumination source at the wavelength of 460 nm and with a Motic Pro 252 microscope camera. Images were analysed using ImageJ® version 1.53a (National Institutes of Health, Bethesda, MD, USA).

CE maturation was evaluated using a sequential approach [168]. Images were converted to either an 8-bit map (for total cell number count) or divided in RGB channels (to count cells staining for Alexa-Fluor 488, i.e., positive to involucrin). The Huang threshold followed by the Watershed command was applied to define CE borders and the cells with a surface area of 300-2000 μm^2 were counted. For the distribution of Dsg1, the ratio of pixels expressing Dsg1 to the total area in pixels was counted in two random regions of interest (ROIs) of 70 x 70 µm containing corneocytes.

7.3.6 Statistical analysis

Raw data were imported into IBM® SPSS® Statistics (version 27) for analysis and assessed for normality using probability plots and the Shapiro-Wilk test for each site, which revealed a normal distribution for morphological and maturation properties (% INV+ and Dsg1) and a non-normal distribution for the Young's modulus. Accordingly, a t-student or Mann-Whitney test was employed to investigate whether the anatomical sites presented differences in morphological and maturation properties, and moduli values, respectively. Tests were considered statistically significant at a 5% level ($p < 0.05$).

7.4 Results

A cohort of 17 patients (13 males and 4 females) presenting with category 1 PUs were recruited for the study. Patients were of a white ethnic background and ages ranging between 71 and 95 years (mean age = 86.4 ± 6.7 years) with a mean height and weight of 1.69 ± 0.08 m and 66.0 ± 17.7 kg, respectively. 41% were bedridden and 59% needed assistance with mobility. Moreover, 24% of the patients presented a history of PUs and 59% were incontinent for urine or faeces, or both.

7.4.1 *Corneocytes at PU site presented altered topography and size compared to the control site*

Representative topographical images obtained using TM AFM of superficial corneocytes collected at a site of category1 PU and a control site (10 cm adjacent to PU site) from six of the 17 patients are presented in Figure 7.1. All images for the patient cohort can be found in Appendix E (Figure E3). At the control site, corneocytes were characterized by ridges and valleys, with average roughness values (Table 7.1).

However, some patients presented circular nano-objects (CNOs) at the cell surface (Figure 7.1 – P6, Figure E3 – P8, P11, P14, P17). Patient 9 presented deformed topography without visible recognisable features (Figure 7.1).

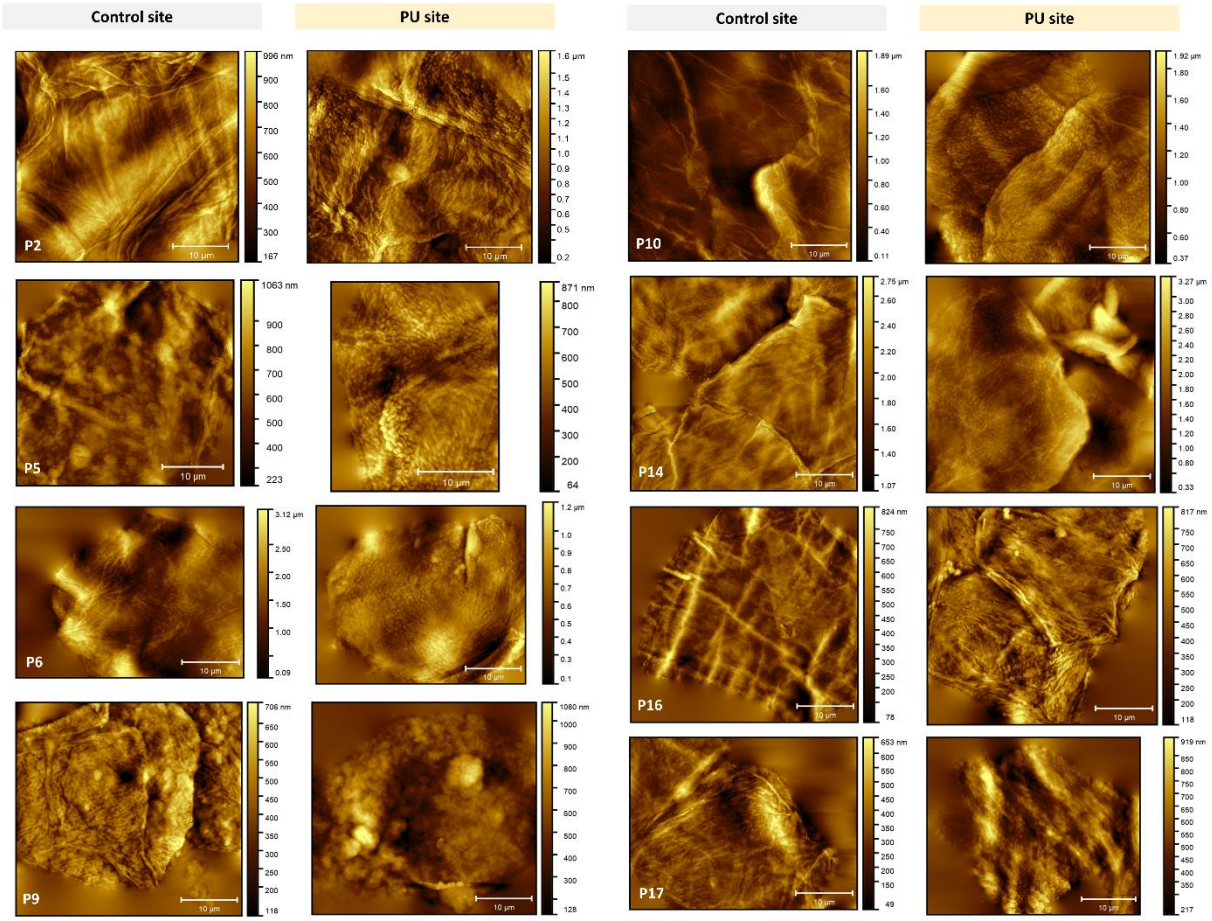

Figure 7.1. AFM analysis of superficial corneocytes revealed differences in the topography at the sites of the category 1 PUs. While at the control sites, cells showed typical features of ridges, valleys, and peaks, with only a few patients (e.g., P6 and P17) showing CNOs at the cell surface. Cells at the PU sites exhibited an abundance of CNOs (e.g., P5, P6, P10) or a deformed topography (P9, P16). The results for 8 patients are shown, but representative images for all 17 patients can be found in Supplementary Information.

By contrast, at the PU site, most patients exhibited visible changes in topography, frequently presenting CNOs (Figure 7.1 – P2, P5, P10, P17), or deformed topography (Figure 7.1 – P9, P16). These differences between the PU and control sites were

quantified as an increase in roughness values (Table 7.1), with averages of 84.1 ± 18.1 nm at the PU site compared to the control site of 55.4 ± 18.5 nm ($p < 0.001$).

The corneocyte and CE sizes were also measured using AFM with Nile red staining of isolated CEs (Table 7.1). CEs were smaller at the PU site compared to the control site ($p<0.05$).

Table 7.1. Roughness values measured from TM AFM images of corneocytes. S_q (root mean square height) and S_a (arithmetic mean height) of three 5 × 5 µm regions (n =5 cells per site per participant). ns – not significant.

Parameter	Control Site	PU site	p-value
S_q (nm)	55.4 ± 18.5	84.1 ± 18.1	<0.001
S_a (nm)	44.3 ± 14.9	67.6 ± 14.8	<0.001
Size AFM (nm^2)	963.7 ± 149.4	884.9 ± 188.0	ns
Size CEs (nm^2)	667.5 ± 110.7	593.8 ± 90.4	<0.05

7.4.2 Levels of immature CEs were elevated at category 1 PU site

The level of immature CEs was studied at the PU and control sites, as the ratio between INV+ CEs and the total number of CEs. The results are shown in Figure 7.2 for the patients showing the greatest changes between the two sites. Representative microscopy images for all patients can be found in Appendix E (Figure E4).

Most patients, except P1, P3 and P4, had higher levels of immature CEs at the PU site compared to the control site (Figure 7.2, 7.3a and E4). There was a significant difference (Figure 7.3b, $p<0.001$) in levels of immature CEs between the PU (mean ± standard deviation = 44.7 ± 12.1%) and control site (mean ± standard deviation = 26.9 ± 10.1%) within the cohort.

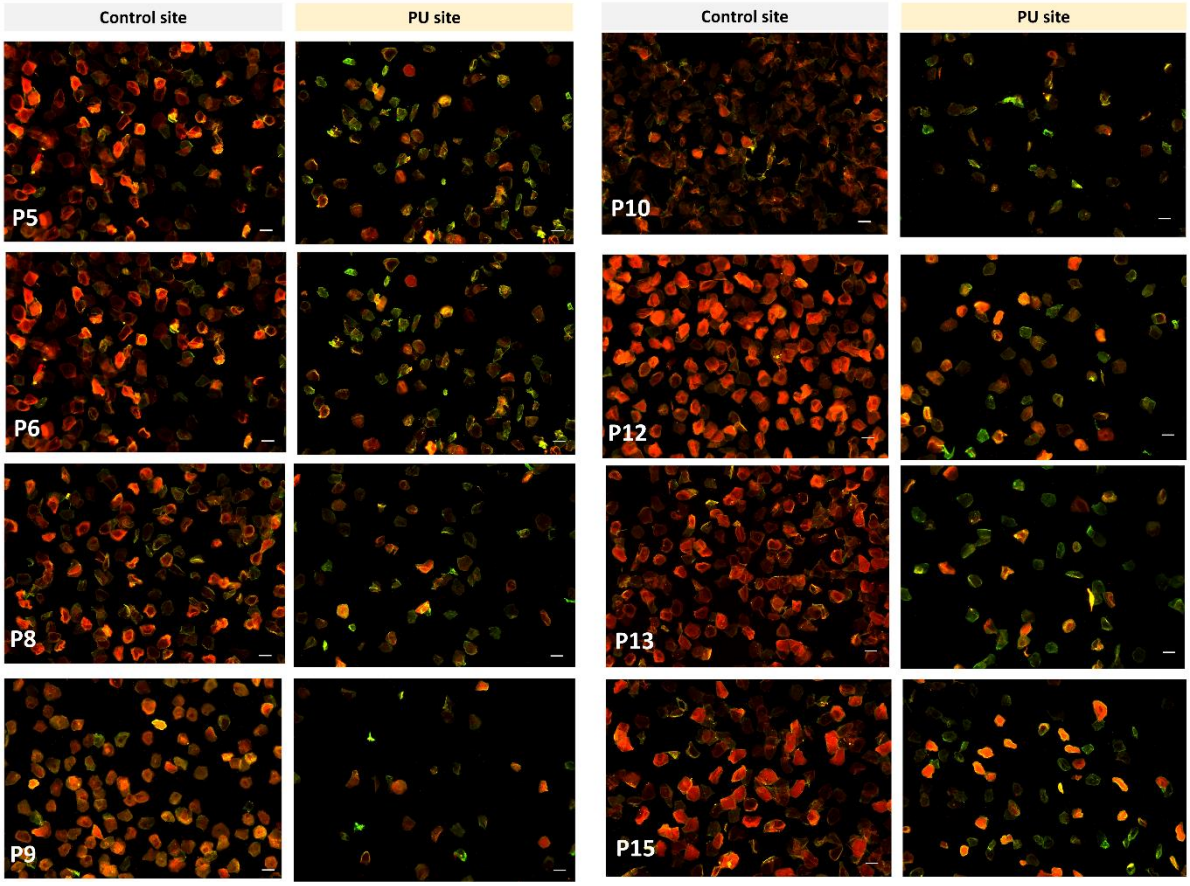

Figure 7.2. PU corneocytes presented high levels of immature CEs. Imaging of the control and PU sites of the superficial CEs using a double staining: immunostaining against INV (green) and Nile red (red) against lipids to quantify the degree of CE maturation for patients 5, 7, 8, 9, 10, 12, 13 and 15. The control site corneocytes stained strongly with Nile red, while the PU corneocytes presented less lipids at the surface as observed by staining green to INV. Scale bar = 50 µm.

7.4.3 Levels of Dsg1 were elevated at category I PU site

Representative images from the immunostaining of Dsg1 are shown in Figure 7.4 for the patients showing the largest changes between the two sites of investigation, with the entire image data set for the 17 patients provided in Appendix E.

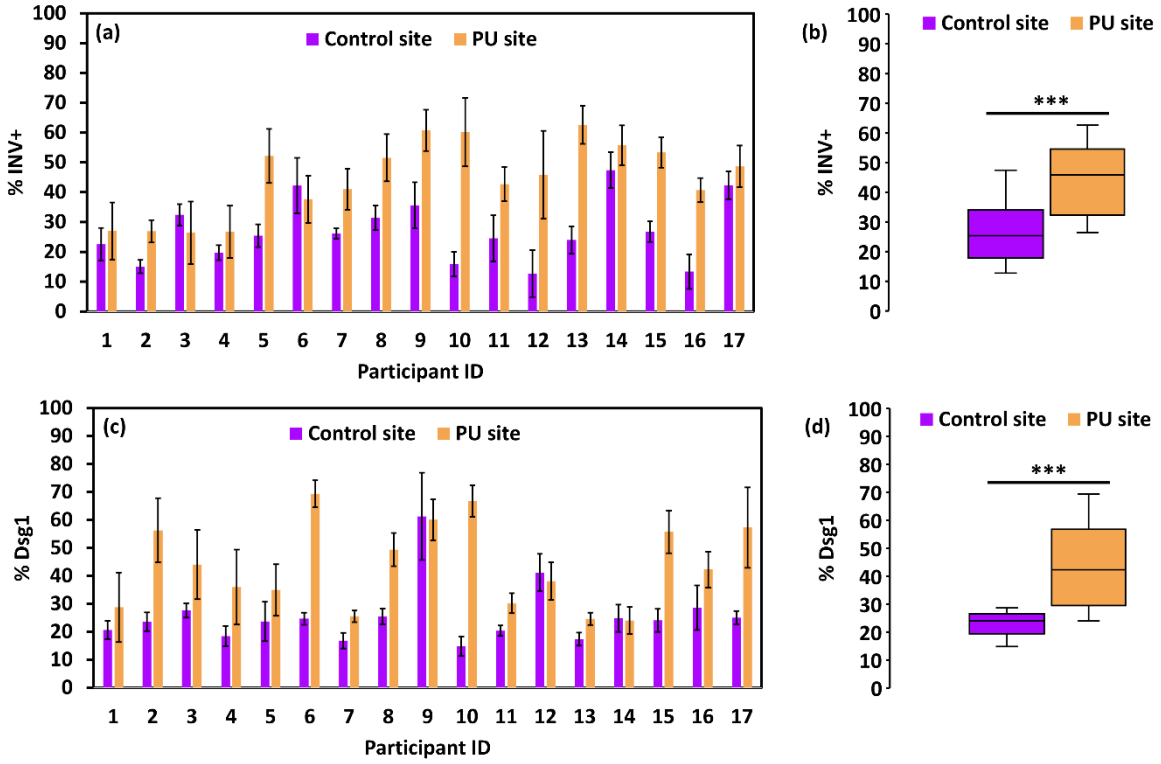

Figure 7.3. Individual data for the levels of immature CEs and Dsg1. (a) Individual level of % INV CEs and **(c)** % Dsg1 associated with the 17 patients. The cohort results are shown in plots **(b)** and **(d)** for % INV+ and % Dsg1, respectively as box-and-whisker plots. The box boundaries indicate the 25th and 75th percentiles, while the whiskers represent the 10th and 90th percentile. The median is represented by the line (—). Independent sample t-tests were performed. ***p<0.001

A honeycomb pattern of Dsg1 was prevalent for control site samples, except for participant P9 and P12 whose samples had a uniform distribution of Dsg1 signal over the cell surface. In contrast, at the PU sites, Dsg1 was present not just at the cell periphery, but also in the central regions of the cells for all patients except P7, P12 and P14. Individual data is shown in Figure 7.3c and shows greater levels of Dsg1 for 12 out of 17 participants (namely P2, P3, P4, P6, P7, P8, P10, P11, P13, P15, P16 and P17). Indeed, the average Dsg1 value for the PU site samples was 43.7 ± 14.6%, which was significantly higher (Figure 7.3d, p<0.001) than for control site samples (25.8 ± 10.6%).

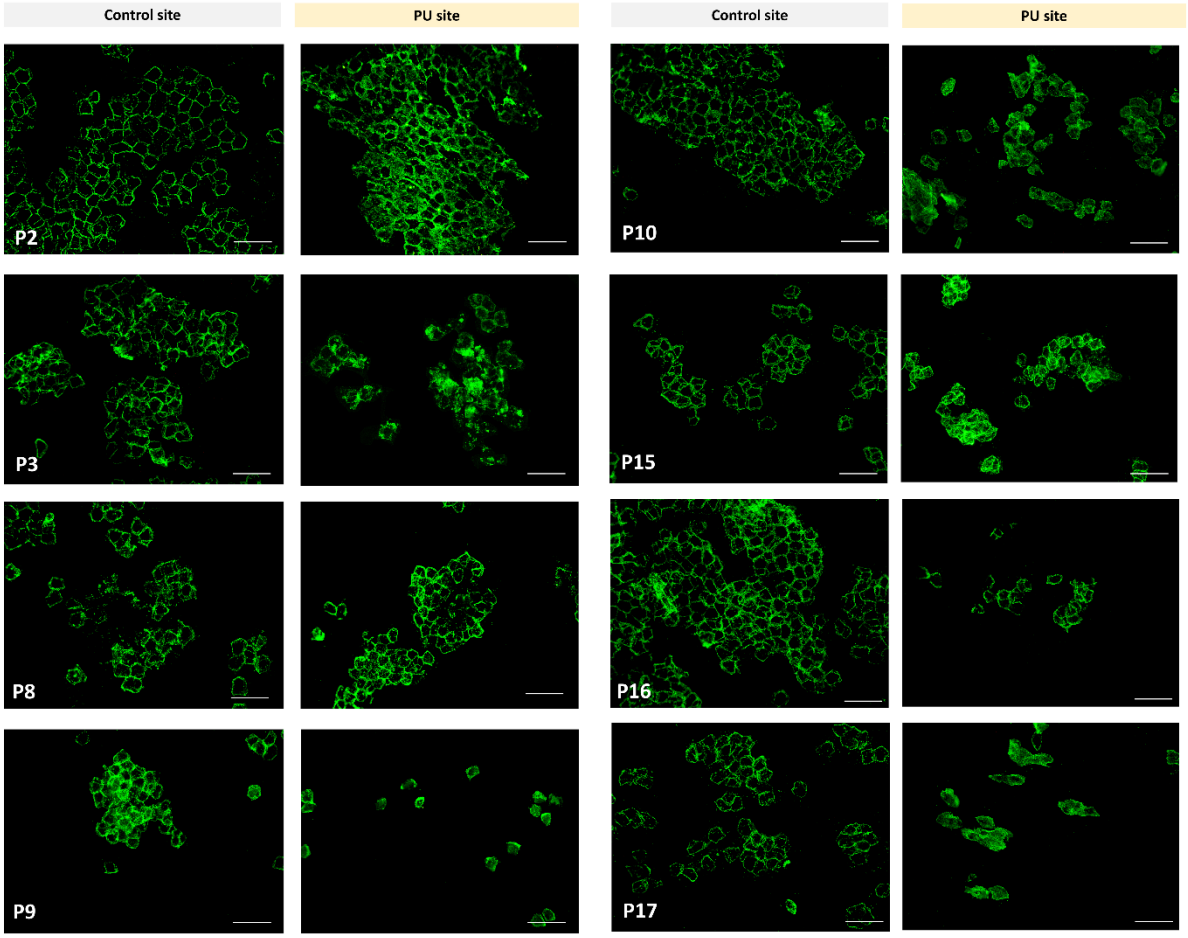

Figure 7.4. PU samples presented higher levels of Dsg1 staining. Distribution of Dsg1 at the surface of superficial corneocytes as an indirect measure of CDs. Most patients had a typical honeycomb pattern with Dsg1 mostly at the cell periphery of the control site. However, the corneocytes at the PU sites showed varying degrees of a more uniform distribution of Dsg1 over the cell surface across the cohort. Scale bar = 100 µm.

7.4.4 Corneocytes at category I PU sites present similar stiffness values to the control site

The Young's modulus of the corneocytes was measured using AFM and the results are presented in Figure 7.5. There were no significant differences in the cell stiffnesses between the two sites (Figure 7.5b). However, there was a high degree of inter-subject variability (Figure 7.5a), with coefficients of variation of 43% and 46% for the control and PU sites, respectively. For example, at the PU site, while patients P2, P12, P13,

P14 and P15 had relatively larger values of the modulus (medians were 514, 530, 435, 586 and 598 MPa, respectively), other patients, such as P3, P9, P10, P11 and P17 had lower moduli values (medians were 175, 195, 193, 152 and 140 MPa, respectively).

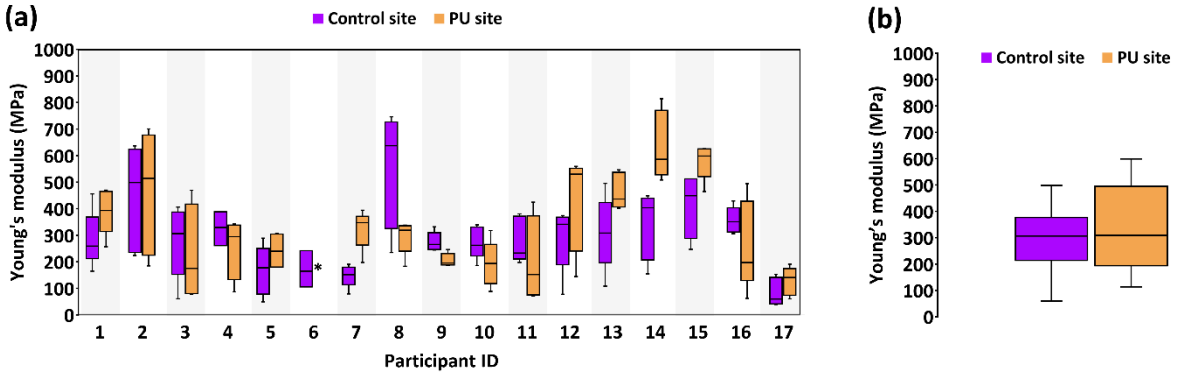

Figure 7.5. Box-and-whisker plots of individual cell stiffness data. (a) Young's modulus and **(b)** cohort results. The upper and lower whiskers represent the highest and lowest datum within 1.0 interquartile range. (n = 5 cells per site per participant) *indicates missing data

7.5 Discussion

The mechanisms underlying the superficial changes in skin over a PU site are still not fully understood and the role of the SC in both loss of tissue integrity and recovery have been mostly neglected. In this context, the aim of the present study was to investigate the properties of corneocytes collected from category 1 PU and an adjacent control site. The maturation, topography, and stiffness of corneocytes were analysed to characterise local changes in cell properties. The results revealed altered topography of PU corneocytes, characterized by the presence of CNOs, which was reflected in increased cell roughness values. Moreover, changes in the maturation properties of cells at the PU sites were observed, with increased levels of immature CEs and Dsg1. These differences could correspond to local changes in the skin barrier function and be a potential marker for diagnosing early signs of damage.

The topographical analysis of superficial corneocytes revealed changes in the surface features and morphology of cells in category 1 PUs (Figure 7.2 and Table 7.1). Cells at the control site were generally smooth (Table 7.1), characterized by cross-over ridges and valleys (Figure 7.2). By contrast, PU corneocytes were rough ($p<0.001$), presenting CNOs over the cell surface. Two patients, P9 and P16, displayed a distorted cell surface with little or no distinct topographical features (Figure 7.2). CNOs have been previously detected for certain skin conditions [101, 103, 117, 225], such as Atopic Dermatitis [103]. They have also been associated with the exposure of chemicals on the skin such as sodium dodecyl sulphate [225]. In those studies, the presence of such structures was related to changes in the skin barrier function (TEWL) [103, 225]. Indeed, in our previous published study, a significant increase in TEWL was registered at the PU sites, while control sites 5 and 10 cm away generally conformed to normative values [223].

Furthermore, CNOs have been previously shown to harbour corneodesmosin, a glycoprotein located in the core of corneodesmosomes [103, 226]. These structures were suggested to likely be involved in cell-to-cell attachment [101]. Interestingly, in addition to the increase in CNOs, an increase in the levels of Dsg1 (a component of corneodesmosomes) was also found at the PU sites compared to the control sites (Figure 7.3c, E3 and E4). This non-peripheral distribution (homogenous pattern) of Dsg1 has been suggested to lead to cracking of the SC with the formation of hexagonal scaling clinical features when the skin is subjected to lateral-pulling forces [90]. The consequences of increased levels of Dsg1 in PU corneocytes should be further investigated, since an increase in SC cohesion (cells strongly attached to each other) may influence skin resistance to pressure and shear forces.

Moreover, the current study has revealed an increase in the level of immature CEs at the PU sites ($p<0.001$). Increased levels of immature CEs have been previously observed in irritated skin [81] and scaly inflammatory dermatoses [80, 227] and related to impaired barrier function [81]. The formation of a mature CE is a complex process regulated by factors such as a calcium gradient and certain cytokines. These signalling molecules control the expression of structurally important proteins involved in building the CE (interleukin-31), as well as in the lipid composition of the CE (interferon-γ) and in cell-to-cell adhesion (interleukin-1α, IL-1α) [227]. A complimentary analysis of the category 1 PU patients in the present study revealed an upregulation of IL-1α, compared to a negative control site [224]. Therefore, the increased level of immature CEs found in this study may be due a cytokine action on certain signalling pathways, namely the release of pro-inflammatory proteins.

The study of corneocyte stiffness revealed high inter-subject variability, with Young's moduli ranging from 60 to 640 MPa at the control site, and 140 to 600 MPa at the PU site (Figure 7.5a), but without significant differences between the PU and control sites, since the median at both sites $\approx$ 310 MPa (Figure 7.5b). However, while the topographical and maturation properties of control site cells were like those of young healthy skin at the sacrum, the mechanical properties of the cells were distinctly different [181]. In fact, patient cells, even at the control site, were much more compliant than those of young healthy skin that have a modulus in the range of 0.45–1.88 GPa (median = 1.15 GPa) as presented in Chapter IV [181]. This may be the result of keratin and CE structural differences in aged skin. CEs of aging skin have a reduced amount of loricrin and filaggrin, and an increase in small proline-rich proteins [228]. Moreover, the reduced levels of filaggrin may compromise the keratin assembly and cross-linking.

These structural changes may result in more compliant cells. A more compliant SC may be more susceptible to microclimate changes, particularly to increased levels of moisture. Together with more cohesive SC layers (i.e., homogenous distribution of corneodesmosomes), these features may lead to cracking of the SC when the skin is subjected to lateral-pulling forces.

The current study is limited by the relatively small sample size (17 patients) and a homogeneous cohort of elderly Caucasian individuals, which limits the generalisability of the results to other age groups and ethnic backgrounds. Furthermore, corneocytes were collected from a control site away from the PU site, but there was no control for elderly healthy subjects. Previous studies have shown that cells from aged skin are usually thinner and larger in area [229], but with no alteration of the number of CNOs [102]. Moreover, studies on isolated SC have observed an increase in the values of the Young's modulus of SC with age [170, 230], which contradicts our data on single cells. Future studies on the modulus of individual corneocytes collected from elderly healthy subjects should be performed. These would allow the comparison between hospitalized and healthy individuals and assist in establishing thresholds for maturation and mechanical properties of superficial cells of healthy and compromised skin.

Detection of early skin damage is of critical importance for the implementation of optimal preventive strategies to enable skin integrity to be recovered. However, even experienced clinicians face the challenges of a subjective evaluation by visual observations to detect PUs [231, 232]. Corneocytes, which can be easily collected via tape stripping, may give important information regarding changes occurring at the skin surface in early-stage skin breakdown, together with biophysical and biochemical objective parameters. In this study, a modified topography, and lower degree of cell

maturation of superficial cells indicate alterations of the most external layer of the skin in category 1 PUs. Thus far, theories on the causes of PUs have ignored the role of the mechanical properties of the SC in affecting tissue integrity, but here it has been observed that even in early skin damage, superficial corneocytes are affected. Future studies should investigate the pathways leading to these changes. Understanding if these result from inflammatory processes or from the direct action of the microclimate and mechanical forces peeling off the most superficial cell layers, may give a more effective insight into the aetiology of PU.

7.6 Conclusion

The present study revealed distinct changes in the topographical, maturation and mechanical properties of superficial corneocytes in category 1 PUs when compared to a healthy adjacent site. Topographic features in the PU sites included the presence of CNOs, as well as increased levels of Dsg1 in the central surface regions of the cells. Moreover, an increase in the levels of immature CEs was observed, in the absence of mechanical stiffness differences. Thus, this study demonstrates that early skin damage can be characterised by changes in superficial skin cells, which are active components of the first skin barrier i.e., the SC. Future research should focus on the changes of elderly skin cells compared to those from young skin, and different skin damage mechanisms e.g., moisture, biochemical and mechanical, to understand the role of the SC in maintaining skin tissue integrity.

CHAPTER VIII - SUMMARY AND FUTURE WORK

The mechanisms underlying the loss of skin integrity due to mechanical insults are still not fully understood. The complexity of the problem involves mechanical, biochemical, and physiological factors, and depends on the interactions between the skin, the contact surface, and the microclimate at the interface [10]. The skin layer most exposed to the interface microclimate, as well as to friction and pressure is the SC. As such, the work presented in this thesis considered the potential role of SC cells, corneocytes, in the skin mechanical function. The mechanical and maturation properties of corneocytes, such as stiffness, CE maturity and Dsg1 levels, were shown to be influenced by factors such as hydration and anatomical location. Moreover, the potential use of corneocytes as biomarkers for early skin damage by mechanical stresses was explored in two cohort studies: i) in the application on respirators during the COVID19 pandemic and ii) in category I pressure ulcers. Overall, this thesis shows that sampling and analysing superficial skin cells, apart from allowing a deeper understanding of the physiology of the SC across anatomical sites and subjects, may serve as a prediction tool for skin integrity.

In Chapter III, atomic force microscopy was used as a nanoindentation tool to determine the mechanical properties of single corneocytes. It builds on the existing literature by addressing the uncertainties associated with using AFM force spectroscopy for biomechanical analysis and by standardizing a protocol for the study of corneocyte properties. This chapter highlights that the tape commonly used for stripping and collecting corneocytes is unsuitable as a substrate for AFM indentation measurements, as it is much more compliant than these skin cells. Furthermore, it shows that an elastomer reference material (in this case, polydimethylsiloxane, PDMS) can be used to provide an accurate effective geometry of a standard imaging AFM tip.

Finally, it concludes that corneocytes exhibit elastic behaviour at small stresses but viscoplastic behaviour when the stress reaches the yield value. The behaviour could be described by the Herschel-Bulkley material model. This protocol is used in the subsequent studies to investigate the mechanical properties of corneocytes under various conditions and at different anatomical sites, as demonstrated in Chapter IV. In this particular study, the topographical, maturation, and biomechanical characteristics of corneocytes collected from young skin at five anatomical sites are presented: forearm, cheek, neck, sacrum, and medial heel. The findings confirm that the cheek and medial heel exhibit higher levels of immature corneocytes, and desmoglein-1 compared to the forearm, neck, and sacrum. Topographically, cheek corneocytes display CNOs (circular nano-objects), while medial heel cells exhibit villi-like structures, whereas the remaining sites are characterized by ridges and valleys. Additionally, male participants tend to have larger cells with a higher proportion of immature corneocytes and desmoglein-1. Although no significant differences were observed in the mechanical properties of corneocytes across anatomical sites, this study reveals a significant positive correlation between the proportion of mature corneocytes and cell stiffness. In other words, individuals with a higher concentration of mature corneocytes generally display increased cell stiffness.

Chapter V, inspired by the work of Park and Baddiel [21, 175,182], presents the effects of water activity on the topographical and mechanical behaviour of volar forearm and medial heel corneocytes. The swelling of cells when immersed in water is accompanied by the plasticization of the keratin matrix, which results in a rubbery-glassy transition, with a reduction in the Young's modulus and the yield stress, but an increase in the yield strain. The effects of hydration and overhydration are extremely relevant to the

barrier function of the SC. While promoting the natural desquamation process, maturation of corneocytes, and enhancing flexibility and plumpness of the SC, prolonged exposure to water can disrupt the lipid lamellae structure, weaken corneodesmosomes, increase transepidermal water loss, and make the skin more vulnerable to environmental irritants and microorganisms. Future studies should investigate the effects of prolonged exposure on corneocyte properties, particularly in the case of incontinence associated dermatitis (IAD), where urine acts as both plasticizer and irritant to the skin.

In order to explore the potential of corneocytes as biomarkers for skin integrity, two collaborative studies were conducted in conjunction with the University of Southampton. The first study, in Chapter VI, investigated the effects of the prolonged use of respiratory protective equipment in healthcare workers during the COVID-19 pandemic. The levels of Dsg1 and immature CEs were consistently higher in a loaded cheek site compared to a negative unloaded control site. Additionally, participants with a greater number of self-reported skin adverse reactions presented a greater number of immature CEs and larger level of Dsg1. Although further studies are required to confirm that this type of mechanical loading has a direct effect on corneocyte properties, this study suggests that an immature SC is associated with adverse skin reactions following pressure and shear insults to the skin.

Finally, in Chapter VII, the topographical, maturation, and mechanical properties of corneocytes over category I PUs were investigated. The PU site was characterized by greater levels of immature CEs and demosglein-1. Cells presented distinct topographical features, such as CNOs. Some cells presented completely deformed surface topography. Although there were no significant mechanical differences

between a control and the PU site, corneocytes collected from the cohort of this study (elderly subjects with age mean of 86 years old) were much more compliant than those collected from healthy young individuals (mean age 29 years old), presented in Chapter IV. This is an interesting finding, considering that aged skin presents mature SC characteristics, i.e., larger, and thinner cells [233, 234], and levels of CE maturity comparable to those of young skin (Chapters IV). However, this difference in stiffness may result from an altered CE composition and keratin assembly. Aged corneocytes are thought to present a reduced amount of loricrin and filaggrin, and increased amount of small proline-rich proteins in their CE [228]. Moreover, the reduced levels of filaggrin may compromise the assembly and cross-linking of the keratin matrix [228]. Thus, although larger and thinner, aged skin corneocytes may be more fragile. Fragile corneocytes in combination with prolonged exposure to moisture, as in the case of IAD may render the SC unable to sustain load, resulting in greater stresses in deeper live skin layers [70].

This work also holds significant relevance for cosmetic science, especially in skincare product development and comprehending skin health dynamics. For example, understanding how the mechanical properties of corneocytes change under different hydration conditions may help in understanding diffusion paths of compounds through the CE. Additionally, the discovery that corneocytes in elderly individuals exhibit higher compliance may provide a mechanistic pathway for tailored anti-aging products. Finally, this work shows the importance of maintaining skin integrity under high-stress scenarios, highlighting the implications for cosmetic product development that are designed to enhance skin health. In summary, this research provides valuable information about the mechanical properties of corneocytes and their role in skin health

and damage. Cosmetic scientists and companies may find this information relevant when developing skincare products and formulations aimed at maintaining and improving skin barrier function, addressing age-related skin changes, and promoting skin integrity.

Overall, the work presented in this thesis showed that the mechanical and maturation properties of corneocytes are affected by various factors such as anatomical site, water activity and skin integrity. The potential use of corneocytes as indicators of early signs of skin damage was demonstrated. However, future work should focus in understanding why the properties of corneocytes are affected in skin damage. Are the changes observed in early skin damage due to inflammation, i.e., corneocyte maturation is altered due to signals sent by the live epidermis? Or rather, is it friction, shear, and moisture responsible for exfoliating the upper layers of the SC, exposing the lower, less mature layers of corneocytes? It is possible that both mechanisms are involved and might have relatively different contributions depending on the type of insult, the magnitude of pressure and friction, as well as the time of exposure to those mechanical insults. Future research should also investigate the origins of intra and inter-subject variability in skin cell properties. Understanding why different subjects react differently to similar insults, may be the key to predict and avoid skin damage, such as pressure ulcers.

Moreover, future work should account for the preliminary results presented in the Appendices F and G, exploring the effects of urine, urea, and pH on the mechanical and maturation properties of corneocytes. These preliminary results indicate that a strong lateral attachment between superficial mature corneocytes may be disadvantageous when the SC is subjected to mechanical insults, since the exposed

cells, which are not attached to interior SC layers, may be easily detached from the surface of the skin. This may be exacerbated due to cell swelling provoked by moisture, which, in combination with friction, may facilitate the detachment of upper SC layers. This reinforces the hypothesis of a dichotomy in the role of SC maturation. Although extremely important in ensuring barrier function, i.e., healthy looking and hydrated skin, a mature SC, as characterized in non-glabrous skin, may be disadvantageous when subjected to mechanical insults. Future research is needed to elucidate the effect of moisture and overhydration, as well as pH in the mechanics and maturation of the SC, since these are some of the most important risk factors in early skin damage associated with pressure and friction in combination with shear and patients' incontinence.

REFERENCES

1. Edsberg LE, Black JM, Goldberg M, McNichol L, Moore L, Sieggreen M. Revised national pressure ulcer advisory panel pressure injury staging system: revised pressure injury staging system. *J Wound Ostomy Continence Nurs* **43**, 585-597 (2016).
2. Moore Z, Avsar P, Conaty L, Moore DH, Patton D, O'Connor T. The prevalence of pressure ulcers in Europe, what does the European data tell us: a systematic review. *J Wound Care* **28**, 710-719 (2019).
3. Bader DL. The last hurrah. *J Tissue Viability* **31**, 373 (2022).
4. Daniel RK, Priest DL, Wheatley DC. Etiologic factors in pressure sores: an experimental model. *Arch Phys Med Rehabil* **62**, 492-498 (1981).
5. Kosiak M. Etiology of decubitus ulcers. *Arch Phys Med Rehabil* **42**, 19-29 (1961).
6. Miller GS, J. Lymphatic clearance during compressive loading. *Lymphology*, 161-166 (1981).
7. Reddy NP, Cochran GVB, Krouskop TA. Interstitial fluid flow as a factor in decubitus ulcer formation. *J Biomech* **14**, 879-881 (1981).
8. Herrman EC, Knapp CF, Donofrio JC, Salcido R. Skin perfusion responses to surface pressure-induced ischemia: implication for the developing pressure ulcer. *J Rehabil Res Dev* **36**, 109-120 (1999).
9. Peirce SM, Skalak TC, Rodeheaver GT. Ischemia-reperfusion injury in chronic pressure ulcer formation: a skin model in the rat. *Wound Repair Regen* **8**, 68-76 (2000).

10. Gefen A, Brienza DM, Cuddigan J, Haesler E, Kottner J. Our contemporary understanding of the aetiology of pressure ulcers/pressure injuries. *Int Wound J* **19**, 692-704 (2022).
11. Bouten CC, Bosboom EMH, Oomens CC. The aetiology of pressure sores : a tissue and cell mechanics approach. In *Biomedical aspects of manual wheelchair propulsion: the state of the art II*. IOS Press. (1999).
12. Tanaka Y*, et al.* Cutaneous ischemia-reperfusion injury is exacerbated by IL-36 receptor antagonist deficiency. *J Eur Acad Dermatol Venereol* **36**, 295-304 (2022).
13. Vande Berg JS, Rudolph R. Pressure (decubitus) ulcer: variation in histopathology-a light and electron microscope study. *Hum Pathol* **26**, 195-200 (1995).
14. Landsman AS, Meaney DF, Cargill RS, 2nd, Macarak EJ, Thibault LE. 1995 William J. Stickel Gold Award. High strain rate tissue deformation. A theory on the mechanical etiology of diabetic foot ulcerations. *J Am Podiatr Medl Assoc* **85**, 519-527 (1995).
15. Bouten CV, Knight MM, Lee DA, Bade DL. Compressive deformation and damage of muscle cell subpopulations in a model system. *Ann Biomed Eng* **29**, 153-163 (2001).
16. Lee SH, Jeong SK, Ahn SK. An update of the defensive barrier function of skin. *Yonsei Med J* **47**, 293-306 (2006).
17. Talreja P, Kleene N, Pickens W, Wang T, Kasting G. Visualization of the lipid barrier and measurement of lipid pathlength in human stratum corneum. *AAPS PharmSciTech* **3**, E13-E13 (2001).

18. Menon G, Cleary G, Lane M. The structure and function of the stratum corneum. *Int J Pharm* **435**, 3-9 (2012).
19. Ishida-Yamamoto A, Igawa S. The biology and regulation of corneodesmosomes. *Cell Tissue Res* **360**, 477-482 (2015).
20. Egawa M, Hirao T, Takahashi M. In vivo estimation of stratum corneum thickness from water concentration profiles obtained with Raman spectroscopy. *Acta Derm Venereol* **87**, 4-8 (2007).
21. Park A, Baddiel C. Rheology of stratum corneum-I: A molecular interpretation of the stress-strain curve. *J Soc Cosmet Chem* **23**, 3-12 (1972).
22. van Kuilenburg J, Masen MA, van der Heide E. Contact modelling of human skin: What value to use for the modulus of elasticity? *P I Mech Eng J-J Eng,* **227**, 349 - 361 (2013).
23. Wong R, Geyer S, Weninger W, Guimberteau J, Wong J. The dynamic anatomy and patterning of skin. *Exp Dermatol* **25**, 92-98 (2016).
24. Honari G, Maibach H. Chapter 1 - Skin Structure and Function. In: *Applied Dermatotoxicology*. Academic Press (2014).
25. Deo P, Deshmukh R. Pathophysiology of keratinization. *J Oral Maxillofac Pathol* **22**, 86-91 (2018).
26. Mauldin E, Peters-Kennedy J. Chapter 6 - integumentary system. In: *Jubb, Kennedy & Palmer's Pathology of Domestic Animals: Volume 1 (Sixth Edition)*. W.B. Saunders (2016).
27. Matsui T, Amagai M. Dissecting the formation, structure and barrier function of the stratum corneum. *Int Immunol* **27**, 269-280 (2015).

28. Feingold K, Elias P. Role of lipids in the formation and maintenance of the cutaneous permeability barrier. *Biochim Biophys Acta* **1841**, 280-294 (2014).

29. Segre J. Epidermal barrier formation and recovery in skin disorders. *J Clin Invest* **116**, 1150-1158 (2006).

30. Lane E, McLean W. Keratins and skin disorders. *J Pathol* **204**, 355-366 (2004).

31. Elias P. Stratum corneum defensive functions: an integrated view. *J Invest Dermatol* **125**, 183-200 (2005).

32. Eckhart L, Lippens S, Tschachler E, Declercq W. Cell death by cornification. *Biochim Biophys Acta* **1833**, 3471-3480 (2013).

33. Hunter R, Pinkus H, Steele C. Examination of the epidermis by the strip method: III. the number of keratin cells in the human epidermis. *J Invest Dermatol* **27**, 31-34 (1956).

34. Plewig G, Marples R. Regional differences of cell sizes in the human stratum corneum. Part I. *J Invest Dermatol* **54**, 13-18 (1970).

35. Plewig G. Regional differences of cell sizes in the human. stratum corneum part II. effects of sex and age. *J Invest Dermatol* **54**, 19-23 (1970).

36. Mohammed D, Matts P, Hadgraft J, Lane M. Variation of stratum corneum biophysical and molecular properties with anatomic site. *AAPS J* **14**, 806-812 (2012).

37. Lee S, Lee S. Regional and sexual differences in corneocytes among young korean adults. *Yonsei Med J* **27**, 213-218 (1986).

38. Kashibuchi N, Hirai Y, O'Goshi K, Tagami H. Three-dimensional analyses of individual corneocytes with atomic force microscope: morphological changes

related to age, location and to the pathologic skin conditions. *Skin Res Technol* **8**, 203-211 (2002).

39. Guz NV, Gaikwad RM, Dokukin ME, Sokolov I. A novel in vitro stripping method to study geometry of corneocytes with fluorescent microscopy: example of aging skin. *Skin Res Technol* **15**, 379-383 (2009).
40. Gorzelanny C, Goerge T, Schnaeker E-M, Thomas K, Luger TA, Schneider SW. Atomic force microscopy as an innovative tool for nanoanalysis of native stratum corneum. *Exp Dermatol* **15**, 387-391 (2006).
41. Plewig G, Scheuber E, Reuter B, Waidelich W. Thickness of corneocytes. In: *Stratum Corneum*. Springer (1983).
42. Gorcea M, Lane M, Moore D. A proof-of-principle study comparing barrier function and cell morphology in face and body skin. *Int J Cosmet Sci* **41**, 613-616 (2019).
43. Feuchter D, Heisig M, Wittum G. A geometry model for the simulation of drug diffusion through the stratum corneum. *Comput Vis Sci* **9**, 117-130 (2006).
44. Allen T, Potten C. Significance of cell shape in tissue architecture. *Nature* **264**, 545-547 (1976).
45. Leveque JP, MC; Derigal, J; Kligman, AM Are corneocytes elastic? *Dermatologica* **176**, 65-69 (1988).
46. Évora A, Zhang Z, Adams M. Unpublished data. (2020).
47. Harding CR*, et al.* The cornified cell envelope: an important marker of stratum corneum maturation in healthy and dry skin. *Int J Cosmet Sci* **25**, 157-167 (2003).

48. Luengo GS, Potter A, Ghibaudo M, Baghdadli N, Enea R, Song Z. Stratum Corneum Biomechanics (Mechanics and Friction): Influence of Lipids and Moisturizers. In: *Agache's Measuring the Skin: Non-invasive Investigations, Physiology, Normal Constants*. Springer International Publishing (2017).

49. Gaikwad R, Vasilyev S, Datta S, Sokolov I. Atomic force microscopy characterization of corneocytes: effect of moisturizer on their topology, rigidity, and friction. *Skin Res Technol* **16**, 275-282 (2010).

50. Dulińska-Molak I, Lekka M, Lewandowska M, Pasikowska M, Tyszczuk B, Eris I. Preliminary studies on the characteristics of corneocytes using atomic force microscopy (AFM). *Pol J Cosmetol* **15**, 50-57 (2012).

51. Beard JD, Guy RH, Gordeev SN. Mechanical tomography of human corneocytes with a nanoneedle. *J Invest Dermatol* **133**, 1565-1571 (2013).

52. Milani P, Chlasta J, Abdayem R, Kezic S, Haftek M. Changes in nano-mechanical properties of human epidermal cornified cells depending on their proximity to the skin surface. *J Mol Recognit* **31**, e2722 (2018).

53. Jacobs T, Mate C, Turner K, Carpick R. Understanding the tip-sample contact: An overview of contact mechanics at the nanoscale. In: *Scanning Probe Microscopy for Industrial Applications: Nanomechanical Characterization*. Wiley (2013).

54. Oliver WC, Pharr GM. An improved technique for determining hardness and elastic modulus using load and displacement sensing indentation experiments. *J Mater Res* **7**, 1564-1583 (1992).

55. Richter T, Müller J, Schwarz U, Wepf R, Wiesendanger R. Investigation of the swelling of human skin cells in liquid media by tapping mode scanning force microscopy. *Appl Phys A* **72**, S125-S128 (2001).

56. Norlén L. Stratum corneum keratin structure, function and formation - a comprehensive review. *Int J Cosmet Sci* **28**, 397-425 (2006).

57. Wang F, Zieman A, Coulombe P. Skin keratins. *Methods Enzymol* **568**, 303-350 (2016).

58. Bragulla H, Homberger D. Structure and functions of keratin proteins in simple, stratified, keratinized and cornified epithelia. *J Anat* **214**, 516-559 (2009).

59. Collin C, Moll R, Kubicka S, Ouhayoun J, Franke W. Characterization of human cytokeratin 2, an epidermal cytoskeletal protein synthesized late during differentiation. *Exp Cell Res* **202**, 132-141 (1992).

60. Fu DJ*, et al.* Keratin 9 is required for the structural integrity and terminal differentiation of the palmoplantar epidermis. *J Invest Dermatol* **134**, 754-763 (2014).

61. Freedberg I, Tomic-Canic M, Komine M, Blumenberg M. Keratins and the keratinocyte activation cycle. *J Invest Dermatol* **116**, 633-640 (2001).

62. Lulevich V, Yang H, Isseroff R, Liu G. Single cell mechanics of keratinocyte cells. *Ultramicroscopy* **110**, 1435-1442 (2010).

63. Knobel M, O'Toole E, Smith F. Keratins and skin disease. *Cell Tissue Res* **360**, 583-589 (2015).

64. Ramms L*, et al.* Keratins as the main component for the mechanical integrity of keratinocytes. *PNAS* **110**, (2013).

65. Akinshina A, Jambon-Puillet E, Warren P, Noro M. Self-consistent field theory for the interactions between keratin intermediate filaments. *BMC Biophys* **6**, 12 (2013).

66. Jokura Y, Ishikawa S, Tokuda H, Imokawa G. Molecular analysis of elastic properties of the stratum corneum by solid-state 13C-nuclear magnetic resonance spectroscopy. *J Invest Dermatol* **104**, 806-812 (1995).

67. Yano S, Komine M, Fujimoto M, Okochi H, Tamaki K. Mechanical stretching in vitro regulates signal transduction pathways and cellular proliferation in human epidermal keratinocytes. *J Invest Dermatol* **122**, 783-790 (2004).

68. Gormar F, Bernd A, Bereiter-Hahn J, Holzmann H. A new model of epidermal differentiation: induction by mechanical stimulation. *Arch Dermatol Res* **282**, 22-32 (1990).

69. Yamaguchi Y, Itami S, Tarutani M, Hosokawa K, Miura H, Yoshikawa K. Regulation of keratin 9 in nonpalmoplantar keratinocytes by palmoplantar fibroblasts through epithelial-mesenchymal interactions. *J Invest Dermatol* **112**, 483-488 (1999).

70. Boyle CJ*, et al.* Morphology and composition play distinct and complementary roles in the tolerance of plantar skin to mechanical load. *Sci Adv* **5**, eaay0244 (2019).

71. Candi E, Schmidt R, Melino G. The cornified envelope: a model of cell death in the skin. *Nat Rev Mol Cell Biol* **6**, 328-340 (2005).

72. Eckert R, Sturniolo M, Broome A, Ruse M, Rorke E. Transglutaminase function in epidermis. *J Invest Dermatol* **124**, 481-492 (2005).

73. Michel S, Schmidt R, Shroot B, Reichert U. Morphological and biochemical characterization of the cornified envelopes from human epidermal keratinocytes of different origin. *J Invest Dermatol* **91**, 11-15 (1988).

74. Lin T*, et al.* Cellular changes that accompany shedding of human corneocytes. *J Invest Dermatol* **132**, 2430-2439 (2012).

75. Guneri D, Voegeli R, Gurgul SJ, Munday MR, Lane ME, Rawlings AV. A new approach to assess the effect of photodamage on corneocyte envelope maturity using combined hydrophobicity and mechanical fragility assays. *Int J Cosmet Sci* **40**, 207-216 (2018).

76. Wertz P, Swartzendruber D, Kitko D, Madison K, Downing D. The role of the corneocyte lipid envelopes in cohesion of the stratum corneum. *J Invest Dermatol* **93**, 169-172 (1989).

77. Nemes Z, Steinert P. Bricks and mortar of the epidermal barrier. *Exp Mol Med* **31**, 5-19 (1999).

78. Elias P*, et al.* Formation and functions of the corneocyte lipid envelope (CLE). *Biochim Biophys Acta* **1841**, 314-318 (2014).

79. Lopez O, Cocera M, Wertz P, Lopez-Iglesias C, de la Maza A. New arrangement of proteins and lipids in the stratum corneum cornified envelope. *Biochim Biophys Acta* **1768**, 521-529 (2007).

80. Hirao T*, et al.* Ratio of immature cornified envelopes does not correlate with parakeratosis in inflammatory skin disorders. *Exp Dermatol* **12**, 591-601 (2003).

81. Hirao T, Denda M, Takahashi M. Identification of immature cornified envelopes in the barrier-impaired epidermis by characterization of their hydrophobicity and antigenicities of the components. *Exp Dermatol* **10**, 35-44 (2001).

82. Mohammed D, Matts P, Hadgraft J, Lane M. Depth profiling of stratum corneum biophysical and molecular properties. *Br J Dermatol* **164**, 957-965 (2011).

83. Richters R, Uzunbajakava N, Timofeeva N, van de Kerkhof P, van Erp P. Development of a novel approach to studying corneodesmosomes and stratum corneum adhesion: extending knowledge on the pathophysiology of sensitive skin. *Skin Pharmacol Physiol* **32**, 81-93 (2019).

84. Ishida-Yamamoto A, Igawa S, Kishibe M. Order and disorder in corneocyte adhesion. *J Dermatol* **38**, 645-654 (2011).

85. Naoe Y, Hata T, Tanigawa K, Kimura H, Masunaga T. Bidimensional analysis of desmoglein 1 distribution on the outermost corneocytes provides the structural and functional information of the stratum corneum. *J Dermatol Sci* **57**, 192-198 (2010).

86. Goto H, Tada A, Ibe A, Kitajima Y. Basket-weave structure in the stratum corneum is an important factor for maintaining the physiological properties of human skin as studied using reconstructed human epidermis and tape stripping of human cheek skin. *Br J Dermatol* **182**, 364-372 (2020).

87. Chapman S, Walsh A, Jackson S, Friedmann P. Lipids, proteins and corneocyte adhesion. *Arch Dermatol Res* **283**, 167-173 (1991).

88. Jonca N, Leclerc E, Caubet C, Simon M, Guerrin M, Serre G. Corneodesmosomes and corneodesmosin: from the stratum corneum cohesion to the pathophysiology of genodermatoses. *Eur J Dermatol* **21 Suppl 2**, 35-42 (2011).

89. Kitajima Y. Desmosomes and corneodesmosomes are enclosed by tight junctions at the periphery of granular cells and corneocytes, suggesting a role

in generation of a peripheral distribution of corneodesmosomes in corneocytes. *J Dermatol Sci* **83**, 73-75 (2016).

90. Kitajima Y. Implications of normal and disordered remodeling dynamics of corneodesmosomes in stratum corneum. *Dermatol Sin* **33**, 58-63 (2015).
91. Rawlings A, Harding C, Watkinson A, Banks J, Ackerman C, Sabin R. The effect of glycerol and humidity on desmosome degradation in stratum corneum. *Arch Dermatol Res* **287**, 457-464 (1995).
92. Biniek K, Levi K, Dauskardt R. Solar UV radiation reduces the barrier function of human skin. *PNAS* **109**, 17111-17116 (2012).
93. Lipsky ZW, German GK. Ultraviolet light degrades the mechanical and structural properties of human stratum corneum. *J Mech Behav Biomed Mater* **100**, 103391 (2019).
94. Mils V, Vincent C, Croute F, Serre G. The expression of desmosomal and corneodesmosomal antigens shows specific variations during the terminal differentiation of epidermis and hair follicle epithelia. *J Histochem Cytochem* **40**, 1329-1337 (1992).
95. Heilmann B, Ryckmanns F, Plewig G. Scanning electron microscopy of human corneocytes. In: *Stratum Corneum* (eds Marks R, Plewig G). Springer Berlin Heidelberg (1983).
96. Fredonnet J, Gasc G, Serre G, Séverac C, Simon M. Topographical and nano-mechanical characterization of native corneocytes using atomic force microscopy. *J Dermatol Sci* **75**, 63-65 (2014).
97. Fluhr J*, et al.* Development and organization of human stratum corneum after birth: electron microscopy isotropy score and immunocytochemical corneocyte

labelling as epidermal maturation's markers in infancy. *Br J Dermatol* **171**, 978-986 (2014).

98. Koppes S*, et al.* Stratum corneum profiles of inflammatory mediators in patch test reactions to common contact allergens and sodium lauryl sulfate. *Br J Dermatol* **176**, 1533-1540 (2017).

99. Engebretsen K*, et al.* Concentration of filaggrin monomers, its metabolites and corneocyte surface texture in individuals with a history of atopic dermatitis and controls. *J Eur Acad Dermatol Venereol* **32**, 796-804 (2018).

100. Soltanipoor M*, et al.* Specific barrier response profiles after experimentally induced skin irritation in vivo. *Contact Derm* **79**, 59-66 (2018).

101. Riethmüller C. Assessing the skin barrier via corneocyte morphometry. *Exp Dermatol* **27**, 923-930 (2018).

102. Franz J*, et al.* Nanoscale alterations of corneocytes indicate skin disease. *Skin Res Technol* **22**, 174-180 (2016).

103. Riethmuller C*, et al.* Filaggrin breakdown products determine corneocyte conformation in patients with atopic dermatitis. *J Allergy Clin Immunol* **136**, 1573-1580.e1572 (2015).

104. Rankl C, Zhu R, Luengo G, Donovan M, Baghdadli N, Hinterdorfer P. Detection of corneodesmosin on the surface of stratum corneum using atomic force microscopy. *Exp Dermatol* **19**, 1014-1019 (2010).

105. Simon M*, et al.* Refined characterization of corneodesmosin proteolysis during terminal differentiation of human epidermis and its relationship to desquamation. *J Biol Chem* **276**, 20292-20299 (2001).

106. Danzberger J*, et al.* Glycan distribution and density in native skin's stratum corneum. *Skin Res Technol* **24**, 450-458 (2018).

107. Walsh A, Chapman S. Sugars protect desmosome and corneosome glycoproteins from proteolysis. *Arch Dermatol Res* **283**, 174-179 (1991).

108. Guo S*, et al.* Anisotropic cellular forces support mechanical integrity of the stratum corneum barrier. *J Mech Behav Biomed Mater* **92**, 11-23 (2019).

109. R M, SP B. The significance of the size and shape of corneocytes. In: *Stratum Corneum*. Springer (1983).

110. Marks R, Nicholls S, King C. Studies on isolated corneocytes. *Int J Cosmet Sci* **3**, 251-259 (1981).

111. Marks R. The stratum corneum barrier: the final frontier. *J Nutr* **134**, 2017S-2021S (2004).

112. Collinsworth A, Zhang S, Kraus W, Truskey G. Apparent elastic modulus and hysteresis of skeletal muscle cells throughout differentiation. *Am J Physiol-Cell Physiol* **283**, C1219-C1227 (2002).

113. Haga H, Sasaki S, Kawabata K, Ito E, Ushiki T, Sambongi T. Elasticity mapping of living fibroblasts by AFM and immunofluorescence observation of the cytoskeleton. *Ultramicroscopy* **82**, 253-258 (2000).

114. Macheleidt O, Kaiser H, Sandhoff K. Deficiency of epidermal protein-bound omega-hydroxyceramides in atopic dermatitis. *J Invest Dermatol* **119**, 166-173 (2002).

115. Ohnishi Y, Okino N, Ito M, Imayama S. Ceramidase activity in bacterial skin flora as a possible cause of ceramide deficiency in atopic dermatitis. *Clin Vaccine Immunol* **6**, 101-104 (1999).

116. Kita K*, et al.* Activation of bacterial ceramidase by anionic glycerophospholipids: possible involvement in ceramide hydrolysis on atopic skin by Pseudomonas ceramidase. *Biochem J* **362**, 619-626 (2002).

117. Feuillie C*, et al.* Adhesion of staphylococcus aureus to corneocytes from atopic dermatitis patients is controlled by natural moisturizing factor levels. *mBio* **9**, e01184-01118 (2018).

118. van Drongelen V, Haisma E, Out-Luiting J, Nibbering P, El Ghalbzouri A. Reduced filaggrin expression is accompanied by increased Staphylococcus aureus colonization of epidermal skin models. *Clin Exp Allergy* **44**, 1515-1524 (2014).

119. Chaturvedi P, Worsley PR, Zanelli G, Kroon W, Bader DL. Quantifying skin sensitivity caused by mechanical insults: A review. *Skin Res Technol* **28**, 187-199 (2022).

120. Hess CT. Did you know? The difference between friction and shear. *Adv Skin Wound Care* **17**, 222 (2004).

121. Jor JWY, Parker MD, Taberner AJ, Nash MP, Nielsen PMF. Computational and experimental characterization of skin mechanics: identifying current challenges and future directions. *Wiley Interdiscip Rev Syst Biol Med* **5**, 539-556 (2013).

122. Lynch B*, et al.* A mechanistic view on the aging human skin through ex vivo layer-by-layer analysis of mechanics and microstructure of facial and mammary dermis. *Sci Rep* **12**, 849 (2022).

123. Deng X*, et al.* Application of atomic force microscopy in cancer research. *J Nanobiotechnology* **16**, 102 (2018).

124. Paz Ramos A, Gooris G, Bouwstra J, Molinari M, Lafleur M. Raman and AFM-IR chemical imaging of stratum corneum model membranes. *Can J Chem* **98**, 495-501 (2020).

125. Évora AS, Adams MJ, Johnson SA, Zhang Z. Corneocytes: relationship between structural and biomechanical properties. *Skin Pharmacol Physiol* **34**, 146-161 (2021).

126. Rheinlaender J*, et al.* Cortical cell stiffness is independent of substrate mechanics. *Nat Mater* **19**, 1019-1025 (2020).

127. Sneddon IN. The relation between load and penetration in the axisymmetric Boussinesq problem for a punch of arbitrary profile. *Int J Eng Sci* **3**, 47-57 (1965).

128. Fujinami S, Nakajima K. Cone–paraboloid transition of the Johnson–Kendall–Roberts-type hyperboloidal contact. *Langmuir* **36**, 11284-11291 (2020).

129. Wang Z, Volinsky AA, Gallant ND. Crosslinking effect on polydimethylsiloxane elastic modulus measured by custom-built compression instrument. *J Appl Polym Sci* **131**, (2014).

130. Qian Z, McKenna GB. On the extreme depth dependence of the hardness of PDMS rubber: A problem of false surface detection. *J Polym Sci, Part B: Polym Phys* **55**, 30-38 (2017).

131. M. M*, et al.* Temperature compensated $LiTaO_3$/sapphire bonded SAW substrate with low loss and high coupling factor suitable for US-PCS application. In: *IEEE Ultrasonics Symposium, 2004*) (2004).

132. Sader JE*, et al.* A virtual instrument to standardise the calibration of atomic force microscope cantilevers. *Rev Sci Instrum* **87**, 093711 (2016).

133. Briscoe BJ, Arvanitaki A, Adams MJ, Johnson SA. The friction and adhesion of elastomers. *Tribology Series* **39**, 661-672 (2001).

134. Gao Y*, et al.* Hierarchical self-assembly of adhesive and conductive gels with anion-coordinated triple helicate junctions. *Angew Chem Int Ed* **61**, e202201793 (2022).

135. Chen C, Hendrickson A. Microhardness phenomena in silver. In: *Technical Progress Report no. COO-916-23. Michigan Technological Univ* (1973).

136. Persch G, Born C, Utesch B. Nano-hardness investigations of thin films by an atomic force microscope. *Microelectron Eng* **24**, 113-121 (1994).

137. Hosseini N, Neuenschwander M, Peric O, Andany SH, Adams JD, Fantner GE. Integration of sharp silicon nitride tips into high-speed SU8 cantilevers in a batch fabrication process. *Beilstein J Nanotechnol* **10**, 2357-2363 (2019).

138. Nečas D, Klapetek P. Gwyddion: an open-source software for SPM data analysis. *Eur J Phys* **10**, 181-188 (2012).

139. Józwiak G, Henrykowski A, Masalska A, Gotszalk T, Ritz I, Steigmann H. The regularized blind tip reconstruction algorithm as a scanning probe microscopy tip metrology method. *arXiv*, (2011).

140. Wu CE, Lin KH, Juang JY. Hertzian load–displacement relation holds for spherical indentation on soft elastic solids undergoing large deformations. *Tribol Int* **97**, 71-76 (2016).

141. Efremov YM, Wang WH, Hardy SD, Geahlen RL, Raman A. Measuring nanoscale viscoelastic parameters of cells directly from AFM force-displacement curves. *Sci Rep* **7**, 1541 (2017).

142. Garcia R. Nanomechanical mapping of soft materials with the atomic force microscope: methods, theory and applications. *Chem Soc Rev* **49**, 5850-5884 (2020).

143. Caron A. Quantitative hardness measurement by instrumented AFM-indentation. *J Vis Exp*, (117), e54706 (2016).

144. Popov VL, Heß M, Willert E. Normal Contact Without Adhesion. In: *Handbook of Contact Mechanics: Exact Solutions of Axisymmetric Contact Problems*. Springer (2019).

145. Zhenxing H, Gaosheng L, Huimin X, Tao H, Pengwan C, Fenglei H. Measurement of Young's modulus and Poisson's ratio of human hair using optical techniques. In: *Proceedings of SPIE* (2010).

146. Fischer-Cripps AC. Contact Mechanics. In: *Nanoindentation*. Springer (2002).

147. Oliver WC, Pharr GM. Measurement of hardness and elastic modulus by instrumented indentation: Advances in understanding and refinements to methodology. *J Mater Res* **19**, 3-20 (2004).

148. Jansen LE, Birch NP, Schiffman JD, Crosby AJ, Peyton SR. Mechanics of intact bone marrow. *J Mech Behav Biomed Mater* **50**, 299-307 (2015).

149. Bowden PB. The elastic modulus of an amorphous glassy polymer. *Polymer* **9**, 449-454 (1968).

150. Papir YS, Hsu KH, Wildnauer RH. The mechanical properties of stratum corneum. I. The effect of water and ambient temperature on the tensile properties of newborn rat stratum corneum. *Biochim Biophys Acta* **399**, 170-180 (1975).

151. Ezawa Y, Nagase S, Mamada A, Inoue S, Koike K, Itou T. Stiffness of human hair correlates with the fractions of cortical cell types. *Cosmetics* **6**, 24 (2019).

152. Bornschlögl T*, et al.* Keratin network modifications lead to the mechanical stiffening of the hair follicle fiber. *PNAS* **113**, 5940-5945 (2016).

153. Yan Y, Zhang Z, Stokes JR, Zhou Q-Z, Ma G-H, Adams MJ. Mechanical characterization of agarose micro-particles with a narrow size distribution. *Powder Technol* **192**, 122-130 (2009).

154. Johnson KL. *Contact Mechanics*. Cambridge University Press (1985).

155. Mattice JM, Lau AG, Oyen ML, Kent R. Spherical indentation load-relaxation of soft biological tissues. *J Mater Res* **21**, 2003-2010 (2006).

156. Choe C, Schleusener J, Lademann J, Darvin ME. Keratin-water-NMF interaction as a three layer model in the human stratum corneum using in vivo confocal Raman microscopy. *Sci Rep* **7**, 15900 (2017).

157. Lekka M. Discrimination between normal and cancerous cells using AFM. *BioNanoScience* **6**, 65-80 (2016).

158. Sun TT, Green H. Keratin filaments of cultured human epidermal cells. Formation of intermolecular disulfide bonds during terminal differentiation. *J Biol Chem* **253**, 2053-2060 (1978).

159. Rheinlaender J, Schäffer TE. Mapping the creep compliance of living cells with scanning ion conductance microscopy reveals a subcellular correlation between stiffness and fluidity. *Nanoscale* **11**, 6982-6989 (2019).

160. Chen WW, Zhou K, Keer LM, Wang QJ. Modeling elasto-plastic indentation on layered materials using the equivalent inclusion method. *Int J Solids Struct* **47**, 2841-2854 (2010).

161. Perzyna P. The constitutive equations for rate sensitive plastic materials. *Q Appl Math* **20**, 321-332 (1963).

162. Saramito P. A new elastoviscoplastic model based on the Herschel–Bulkley viscoplastic model. *J Nonnewton Fluid Mech* **158**, 154-161 (2009).

163. Dayan N, Wertz PW. *Innate immune system of skin and oral mucosa: Properties and impact in pharmaceutics, cosmetics, and personal care products*. John Wiley & Sons (2011).

164. Kalia YN, Alberti I, Sekkat N, Curdy C, et al. Normalization of stratum corneum barrier function and transepidermal water loss in vivo. *Pharm Res* **17**, 1148-1150 (2000).

165. Leyva-Mendivil MF, Page A, Bressloff NW, Limbert G. A mechanistic insight into the mechanical role of the stratum corneum during stretching and compression of the skin. *J Mech Behav Biomed Mater* **49**, 197-219 (2015).

166. Kunii T, Hirao T, Kikuchi K, Tagami H. Stratum corneum lipid profile and maturation pattern of corneocytes in the outermost layer of fresh scars: the presence of immature corneocytes plays a much more important role in the barrier dysfunction than do changes in intercellular lipids. *Br J Dermatol* **149**, 749-756 (2003).

167. Igawa S*, et al.* Aberrant distribution patterns of corneodesmosomal components of tape-stripped corneocytes in atopic dermatitis and related skin conditions (ichthyosis vulgaris, Netherton syndrome and peeling skin syndrome type B). *J Dermatol Sci* **72**, 54-60 (2013).

168. Évora AS*, et al.* Characterisation of superficial corneocytes in skin areas of the face exposed to prolonged usage of respirators by healthcare professionals during COVID-19 pandemic. *J Tissue Viability*, (2023).

169. Engebretsen K*, et al.* Changes in filaggrin degradation products and corneocyte surface texture by season. *Br J Dermatol* **178**, 1143-1150 (2018).

170. Biniek K, Kaczvinsky J, Matts P, Dauskardt RH. Understanding age-induced alterations to the biomechanical barrier function of human stratum corneum. *J Dermatol Sci* **80**, 94-101 (2015).

171. Chirikhina E, Chirikhin A, Xiao P, Dewsbury-Ennis S, Bianconi F. In vivo assessment of water content, trans-epidermial water loss and thickness in human facial skin. *Appl Sci* **10**, 6139 (2020).

172. Raj N*, et al.* A fundamental investigation into aspects of the physiology and biochemistry of the stratum corneum in subjects with sensitive skin. *Int J Cosmet Sci* **39**, 2-10 (2017).

173. Fluhr JW, Pelosi A, Lazzerini S, Dikstein S, Berardesca E. Differences in corneocyte surface area in pre- and post-menopausal women. *Skin Pharmacol Physiol* **14(suppl 1)**, 10-16 (2001).

174. Kottner J*, et al.* Pressure ulcer/injury classification today: An international perspective. *J Tissue Viability* **29**, 197-203 (2020).

175. Park A, Baddiel C. Rheology of stratum corneum. II. A physico-chemical investigation of factors influencing the water content of the corneum. *J Soc Cosmet Chem* **23**, 13-21 (1972).

176. Norlén L, Emilson A, Forslind B. Stratum corneum swelling. Biophysical and computer assisted quantitative assessments. *Arch Dermatol Res* **289**, 506-513 (1997).

177. Richter T*, et al.* Dead but highly dynamic--the stratum corneum is divided into three hydration zones. *Skin Pharmacol Physiol* **17**, 246-257 (2004).

178. Evans ME, Roth R. Shaping the skin: the interplay of mesoscale geometry and corneocyte swelling. *Phys Rev Lett* **112**, 038102 (2014).

179. Lademann J, Jacobi U, Surber C, Weigmann HJ, Fluhr JW. The tape stripping procedure – evaluation of some critical parameters. *Eur J Pharm Biopharm* **72**, 317-323 (2009).

180. Nakagawa H, Oyama T. Molecular basis of water activity in glycerol-water mixtures. *Front Chem* **7**, 731 (2019).

181. Évora AS, Johnson SA, Zhang Z, Adams MM. Characterization of topographical, biomechanical and maturation properties of corneocytes with respect to anatomical location. *Submitted*, (2023).

182. Park AC, Baddiel CB. The effect of saturated salt solutions on the elastic properties of stratum (1972).

183. Björklund S, Andersson JM, Pham QD, Nowacka A, Topgaard D, Sparr E. Stratum corneum molecular mobility in the presence of natural moisturizers. *Soft Matter* **10**, 4535-4546 (2014).

184. Chen HJ*, et al.* Moisture retention of glycerin solutions with various concentrations: a comparative study. *Sci Rep* **12**, 10232 (2022).

185. Du J-X, Zhai C-M, Ye Y-Q. Face aging simulation and recognition based on NMF algorithm with sparseness constraints. *Neurocomputing* **116**, 250-259 (2013).

186. Takada S, Naito S, Sonoda J, Miyauchi Y. Noninvasive in vivo measurement of natural moisturizing factor content in stratum corneum of human skin by attenuated total reflection infrared spectroscopy. *Appl Spectrosc* **66**, 26-32 (2012).

187. Yu Y, Yang W, Wang B, Meyers MA. Structure and mechanical behavior of human hair. *Mater Sci Eng C Mater Biol Appl* **73**, 152-163 (2017).

188. Watkinson A, Harding C, Moore A, Coan P. Water modulation of stratum corneum chymotryptic enzyme activity and desquamation. *Arch Dermatol Res* **293**, 470-476 (2001).

189. Guneri D. The Development and Validation of Novel Biomarkers to Assess the Skin Barrier FunctionUniversity College London (2020).

190. Hirao T. Involvement of transglutaminase in ex vivo maturation of cornified envelopes in the stratum corneum. *Int J Cosmet Sci* **25**, 245-257 (2003).

191. Warner RR, Stone KJ, Boissy YL. Hydration disrupts human stratum corneum ultrastructure. *J Invest Dermatol* **120**, 275-284 (2003).

192. Fluhr JW, Lazzerini S, Distante F, Gloor M, Berardesca E. Effects of prolonged occlusion on stratum corneum barrier function and water holding capacity. *Skin Pharmacol Appl Skin Physiol* **12**, 193-198 (1999).

193. Falloon SS, Abbas S, Stridfeldt C, Cottenden A. The impact of microclimate on skin health with absorbent incontinence product use: an integrative review. *J Wound Ostomy Continence Nurs* **45**, 341-348 (2018).

194. Smith LE, Serfioti D, Weston D, Greenberg N, Rubin GJ. Adherence to protective measures among healthcare workers in the UK: a cross-sectional study. *Emerg Med J* **39**, 100 (2022).

195. Yuan X*, et al.* Online survey on healthcare skin reactions for wearing medical-grade protective equipment against COVID-19 in Hubei Province, China. *PLoS One* **16**, e0250869 (2021).

196. Abiakam N*, et al.* Personal protective equipment related skin reactions in healthcare professionals during COVID-19. *Int Wound J* **18**, 312-322 (2021).

197. Caggiari S*, et al.* Biomechanical and physiological evaluation of respiratory protective equipment application. *Medical devices (Auckland, NZ)* **15**, 241-252 (2022).

198. Peko L, Ovadia-Blechman Z, Hoffer O, Gefen A. Physiological measurements of facial skin response under personal protective equipment. *J Mech Behav Biomed Mater* **120**, 104566 (2021).

199. Adams MJ, Briscoe BJ, Johnson SA. Friction and lubrication of human skin. *Tribol Lett* **26**, 239-253 (2007).

200. Comaish S, Bottoms E. The skin and friction: deviations from Amonton's laws, and the effects of hydration and lubrication. *Br J Dermatol* **84**, 37-43 (1971).

201. Dąbrowska AK*, et al.* In vivo confirmation of hydration-induced changes in human-skin thickness, roughness and interaction with the environment. *Biointerphases* **11**, 031015 (2016).

202. Han HS, Shin SH, Park JW, Li K, Kim BJ, Yoo KH. Changes in skin characteristics after using respiratory protective equipment (medical masks and

respirators) in the COVID-19 pandemic among healthcare workers. *Contact Derm*, 10.1111/cod.13855 (2021).

203. Abiakam NS, Jayabal H, Mitchell K, Bader DL, Worsley PR. Biophysical and biochemical changes in skin health of healthcare professionals using respirators during COVID-19 pandemic. *Skin Res Technol*, (2022).

204. Worsley PR, Stanger ND, Horrell AK, Bader DL. Investigating the effects of cervical collar design and fit on the biomechanical and biomarker reaction at the skin. *Medical Devices (Auckland, NZ)* **11**, 87 (2018).

205. Hua W*, et al.* Short-term skin reactions following use of N95 respirators and medical masks. *Contact Derm* **83**, 115-121 (2020).

206. Taylor NA, Machado-Moreira CA. Regional variations in transepidermal water loss, eccrine sweat gland density, sweat secretion rates and electrolyte composition in resting and exercising humans. *Extreme Physiol Med* **2**, 4-4 (2013).

207. Mori S*, et al.* Characterization of skin function associated with obesity and specific correlation to local/systemic parameters in American women. *Lipids Health Dis* **16**, 214 (2017).

208. Boireau-Adamezyk E, Baillet-Guffroy A, Stamatas GN. Age-dependent changes in stratum corneum barrier function. *Skin Res Technol* **20**, 409-415 (2014).

209. Vyumvuhore R, Tfayli A, Duplan H, Delalleau A, Manfait M, Baillet-Guffroy A. Effects of atmospheric relative humidity on Stratum Corneum structure at the molecular level: ex vivo Raman spectroscopy analysis. *Analyst* **138**, 4103-4111 (2013).

210. Katagiri C, Sato J, Nomura J, Denda M. Changes in environmental humidity affect the water-holding property of the stratum corneum and its free amino acid content, and the expression of filaggrin in the epidermis of hairless mice. *J Dermatol Sci* **31**, 29-35 (2003).

211. Health and Safety Executive (HSE). Fit2Fit' mission statement. (2021).

212. Kottner J, Ludriksone L, Garcia Bartels N, Blume-Peytavi U. Do repeated skin barrier measurements influence each other's results? An explorative study. *Skin Pharmacol Physiol* **27**, 90-96 (2013).

213. Guneri D*, et al.* The importance of 12R-lipoxygenase and transglutaminase activities in the hydration-dependent ex vivo maturation of corneocyte envelopes. *Int J Cosmet Sci* **41**, 563-578 (2019).

214. Darlenski R, Berardesca E, Fluhr JW. Corneocyte Size and Cell Renewal: Effects of Aging and Sex Hormones. In: *Textbook of Aging Skin*. Springer (2017).

215. Bronneberg D. Biochemical markers for early detection of superficial pressure ulcers.). Technische Universiteit Eindhoven (2007).

216. Poonja P. Skin barrier changes in T1DM and T2DM. *Int J Diabetes Clin Res* **9**, 156 (2022).

217. Kikuchi K, Kobayashi H, Le Fur I, Tschachler E, Tagami H. The winter season affects more severely the facial skin than the forearm skin: comparative biophysical studies conducted in the same japanese females in later Summer and winter. *Exogenous Dermatology* **1**, 32-38 (2002).

218. Bouten C, Oomens C, Colin D, Bader D. The Aetiopathology of Pressure Ulcers: A Hierarchical Approach. In: *Pressure Ulcer Research: Current and Future Perspectives*. Springer (2005).

219. Berlowitz DR, Brienza DM. Are all pressure ulcers the result of deep tissue injury? A review of the literature. *Ostomy Wound Manage* **53**, 34-38 (2007).

220. Ankrom MA*, et al.* Pressure-related deep tissue injury under intact skin and the current pressure ulcer staging systems. *Adv Skin Wound Care* **18**, (2005).

221. Mackenzie IC. The Cellular Architecture of the Stratum Corneum. In: *Stratum Corneum* Springer (1983).

222. Kalra A, Lowe A, Jumaily AA. An overview of factors affecting the skins youngs modulus. *J Aging Sci* **4**, 1-5 (2016).

223. Abiakam NS, Jayabal H, Filingeri D, Bader DL, Worsley PR. Spatial and temporal changes in biophysical skin parameters over a category I pressure ulcer. *Int Wound J* **n/a**, (2023).

224. Jayabal H, Abiakam NS, Filingeri D, Bader DL, Worsley PR. Inflammatory biomarkers in sebum for identifying skin damage in patients with a Stage I pressure ulcer in the pelvic region: A single centre observational, longitudinal cohort study with elderly patients. *Int Wound J*, (2023).

225. Vater C*, et al.* Changes in skin barrier function after repeated exposition to phospholipid-based surfactants and sodium dodecyl sulfate in vivo and corneocyte surface analysis by atomic force microscopy. *Pharmaceutics* **13**, (2021).

226. Jonca N*, et al.* Corneodesmosin, a component of epidermal corneocyte desmosomes, displays homophilic adhesive properties. *J Biol Chem* **277**, 5024-5029 (2002).

227. Hänel KH, Cornelissen C, Lüscher B, Baron JM. Cytokines and the skin barrier. *Int J Mol Sci* **14**, 6720-6745 (2013).

228. Streubel MK, Rinnerthaler M, Bischof J, Richter K. Changes in the Composition of the Cornified Envelope During Skin Aging: A Calcium Centric Point of View. In: *Textbook of Aging Skin*. Springer (2014).

229. Rawlings AV. The Stratum Corneum and Aging. In: *Textbook of Aging Skin*. Springer (2017).

230. Hara Y, Masuda Y, Hirao T, Yoshikawa N. The relationship between the Young's modulus of the stratum corneum and age: a pilot study. *Skin Res Technol* **19**, 339-345 (2013).

231. Payne D. Not just another rash: management of incontinence-associated dermatitis. *Br J Community Nurs* **21**, 434-440 (2016).

232. Kottner J, Dassen T. Pressure ulcer risk assessment in critical care: Interrater reliability and validity studies of the Braden and Waterlow scales and subjective ratings in two intensive care units. *Int J Nurs Stud* **47**, 671-677 (2010).

233. Berardesca E, Fluhr J. Corneocyte size and cell renewal: effects of aging and sex hormones. In: *Textbook of Aging Skin*. Springer Berlin Heidelberg (2010).

234. Tagami H. Location-related differences in structure and function of the stratum corneum with special emphasis on those of the facial skin. *Int J Cosmet Sci* **30**, 413-434 (2008).

235. Pierard GE, Goffin V, Hermanns-Le T, Pierard-Franchimont C. Corneocyte desquamation. *Int J Mol Med* **6**, 217-238 (2000).

236. Gray M*, et al.* Incontinence-associated dermatitis: a comprehensive review and update. *J Wound Ostomy Continence Nurs* **39**, 61-74 (2012).

237. Beeckman D. A decade of research on Incontinence-Associated Dermatitis (IAD): evidence, knowledge gaps and next steps. *J Tissue Viability* **26**, 47-56 (2017).

238. Lumbers M. Moisture-associated skin damage: cause, risk and management. *Br J Nurs* **27**, S6-S14 (2018).

239. Leyden JJ, Katz S, Stewart R, Kligman AM. Urinary ammonia and ammonia-producing microorganisms in infants with and without diaper dermatitis. *Arch Dermatol* **113**, 1678-1680 (1977).

240. Ichikawa-Shigeta Y, Sanada H, Konya C, Yusuf S, Syafiie S, Sugama J. Risk assessment tool for incontinence-associated dermatitis in elderly patients combining tissue tolerance and perineal environment predictors: a prospective clinical study. *Chronic Wound Care Manage Res* **I**, 41-47 (2014).

241. Fluhr JW, Dickel H, Kuss O, Weyher I, Diepgen TL, Berardesca E. Impact of anatomical location on barrier recovery, surface pH and stratum corneum hydration after acute barrier disruption. *Br J Dermatol* **146**, 770-776 (2002).

242. Bostan LE, Worsley PR, Abbas S, Bader DL. The influence of incontinence pads moisture at the loaded skin interface. *J Tissue Viability* **28**, 125-132 (2019).

243. Koudounas S*, et al.* Bacterial invasion into the epidermis of rats with sodium lauryl sulphate-irritated skin increases damage and induces incontinence-associated dermatitis. *Int Wound J* **20**, 191-200 (2023).

244. Feasibility study for fibroblast autologous skin grafts. https://ClinicalTrials.gov/show/NCT01964859.

245. Celleno L. Topical urea in skincare: A review. *Dermatol Ther* **31**, e12690 (2018).

246. Piquero-Casals J, Morgado-Carrasco D, Granger C, Trullàs C, Jesús-Silva A, Krutmann J. Urea in dermatology: A review of its emollient, moisturizing, keratolytic, skin barrier enhancing and antimicrobial properties. *Dermatol Ther (Heidelb)* **11**, 1905-1915 (2021).

247. Starace M, Alessandrini A, Piraccini BM. Clinical evidences of urea at high concentration on skin and annexes. *Int J Clin Pract* **74**, e13740 (2020).

248. Koudounas S, Bader DL, Voegeli D. An exploratory study of the effects of the pH of synthetic urine on skin integrity in healthy participants. *Skin Pharmacol Physiol* **35**, 166-173 (2022).

249. Kohta M*, et al.* Selective detection of urease-producing bacteria on the genital skin surface in patients with incontinence-associated dermatitis. *Int Wound J*, (2023).

250. Schreml S, Szeimies RM, Karrer S, Heinlin J, Landthaler M, Babilas P. The impact of the pH value on skin integrity and cutaneous wound healing. *J Eur Acad Dermatol Venereol* **24**, 373-378 (2010).

251. Malinauskyte E, Cornwell PA, Reay L, Shaw N, Petkov J. Effect of equilibrium pH on the structure and properties of bleach-damaged human hair fibers. *Biopolymers* **111**, e23401 (2020).

252. Whitlock J. SSKIN bundle: preventing pressure damage across the health-care community. *Br J Community Nurs* **18**, S32-S39 (2013).

253. Jayabal H, Bader DL, Worsley P. Development of an efficient extraction methodology to analyse potential inflammatory biomarkers from sebum. *Skin Pharmacol Physiol*, (2022).

254. Mayrovitz HN, Sims N. Biophysical effects of water and synthetic urine on skin. *Adv Skin Wound Care* **14**, (2001).

255. Garidel P. Mid-FTIR-Microspectroscopy of stratum corneum single cells and stratum corneum tissue. *Phys Chem Chem Phys* **4**, 5671-5677 (2002).

256. Lucassen G. W., van Veen G. N., Jansen J. A. Band analysis of hydrated human skin stratum corneum attenuated total reflectance fourier transform infrared spectra in vivo. *J Biomed Opt* **3**, 267-280 (1998).

257. Zhang Z., Saunders R., Thomas C. R. Mechanical strength of single microcapsules determined by a novel micromanipulation technique. *J Microencapsul* **16**, 117-124 (1999).

258. Chen J. Nanobiomechanics of living cells: a review. *Interface Focus* **4**, 20130055 (2014).

APPENDIX A

Chapter III Supplementary Information

A1 Methodology for calibration of AFM tip geometry using a reference elastomer

1A. Sample

Sample: exposed-side of cast Sylgard 184 PDMS.

Elastic modulus, E^* = 3.79 ± 0.21 MPa (from micromanipulation measurements, See A5).

Poisson's ratio, ν = 0.5.

Environment: immersed in dilute surfactant to minimise adhesion forces.

1B. Indentation test conditions and raw PDMS loading curves

AFM head displacement velocity = 500 nm/s.

AFM maximum force set point = 250 nN.

Probe force as a function of AFM head height.

1C. Pre-analysis: zero force, contact point determination and compliance correction

- The cantilever stiffness (N/m) was obtained from its resonance behaviour, as well as the cantilever deflection sensitivity (m/V) that are required for force calibration (N/V) using the JPK software. See A3 and Manuscript Methods.
- The indentation zero force for each loading curve is set by a baseline offset and tilt correction in the JPK software.
- The contact point of each PDMS loading curve is determined in Matlab from a linear fit of the initial 1–2 nN contact data (about 10 force/depth points spaced by

0.5 nm), on the assumption that the fit should extrapolate to $F = 0$ at $h = 0$. This allows the raw displacement data to be converted from the AFM head height to the probe indentation depth, after the probe height is compliance-corrected using the cantilever stiffness value. See Figure A1.

- Only loading data for $F > 1$ nN ($h > 5$ nm, if the initial slope is ca. 0.2 N/m) are included in subsequent power law or polynomial fits (twice the noise level of 0.5 nN p-p), since points with $F < 1$ nN are assumed to be too susceptible to noise and local roughness.

1D. Calibrated PDMS loading curves

Indentation force, F (nN), as a function of indentation depth (i.e. the total penetration depth), h (nm).

Number of data points = ca. 1000 per loading curve.

Number of curves = 64 in each of 3 zones.

Maximum, F_{max} = 250–253 nN (AFM set point = 250 nN).

Maximum indentation depth, h_{max} = 430–460 nm.

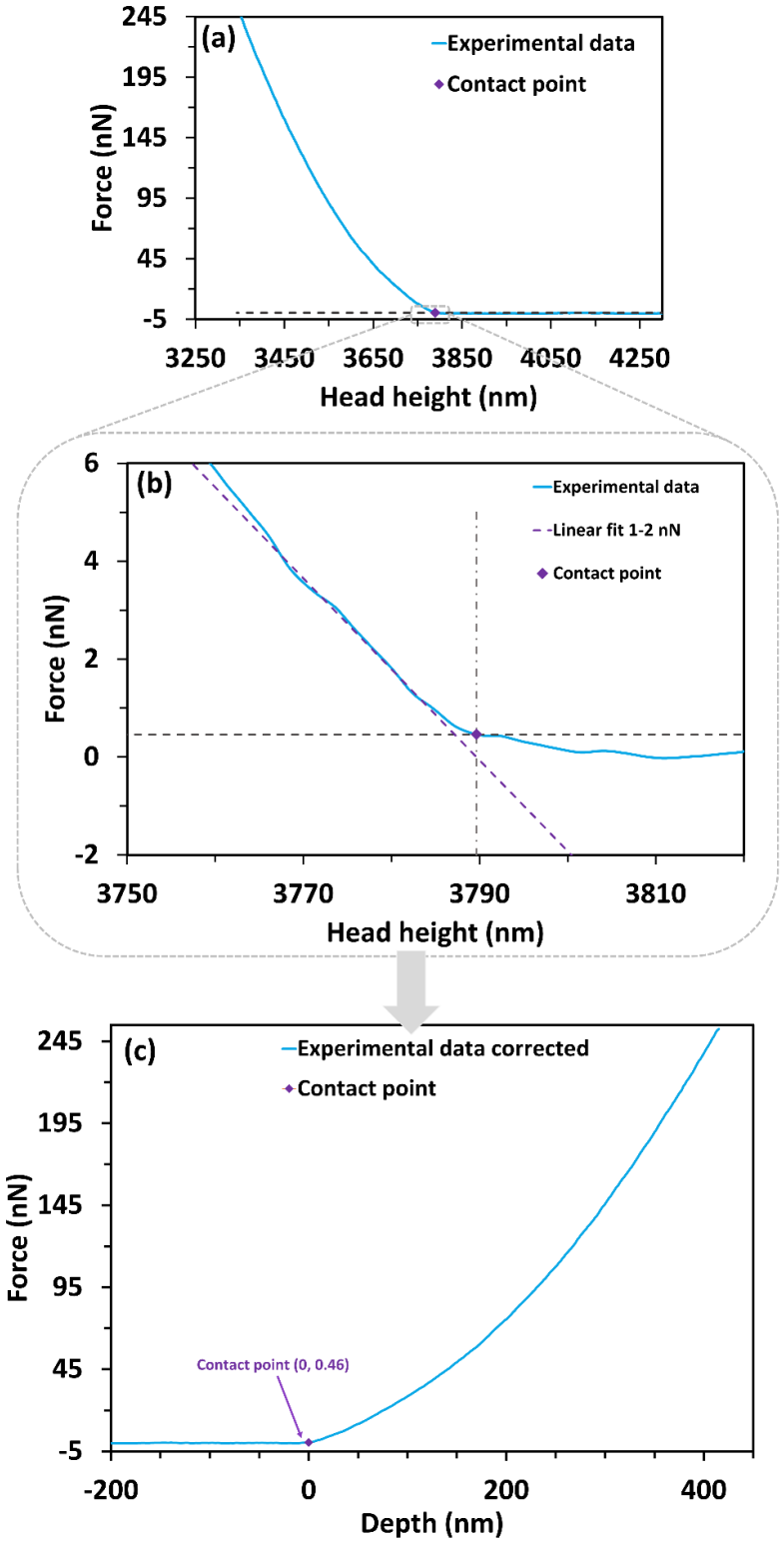

Figure A1. Contact point of AFM force curves. (a) Raw data for a single PDMS loading curve. **(b)** The contact point of each loading curve was determined from a linear fit of the initial 1–2 nN contact data, on the assumption that the fit should extrapolate to F = 0 at h = 0. **(c)** Compliance-corrected loading curve as a function of indentation depth, based on this estimate of the contact point which, in this example, is at 0 nm and 0.46 nN.

1E. Power law fitting of a loading curve:

$$F = bh^m \quad \text{A1}$$

$$S = \frac{dF}{dH} = mbh^{m-1} \quad \text{A2}$$

$$S = 2E^* a \quad \text{A3}$$

$$a = \frac{mbh^{m-1}}{2E^*} \quad \text{A4}$$

$$\frac{F}{S} = \frac{h}{m} \quad \text{A5}$$

$$m = \frac{Sh}{F} \quad \text{A6}$$

The experimental loading curves for PDMS of known elastic modulus fitted to Eq. A1 can be used to obtain the contact radius, *a*, as a function of indentation depth, *h*, using Eq. A4. However, for the current AFM probe, a single power law does not satisfactorily fit the data over the entire load range. Experimentally, the *m* value of the best-fit power law ranges from ca. *m* = 1.1 for fitting just the data close to contact, and towards ca. *m* = 1.7 for data at deep depths (*h* = 400 nm).

1F. Two-term polynomial fitting of loading curve:

$$F = b_1 h + b_2 h^2 \quad \text{A7}$$

$$S = \frac{dF}{dH} = b_1 + 2b_2 h \quad \text{A8}$$

$$S = 2E^* a \quad \text{A9}$$

$$a = \frac{b_1}{2E^*} + \frac{b_2 h}{E^*} \quad \text{A10}$$

A 2nd order polynomial with a zero intercept (Eq. A7) provides a more satisfactory fit over the entire range of a PDMS loading curve than a single power law (Eq. A1). Hence

Eq. A10 implies that the probe geometry is better approximated by a truncated cone/pyramid rather than a single power law such as a paraboloid (*m* = 1.5).

1G. Power law tip geometry, and loading curve analysis using a combination of power law equations and two term polynomial fits:

$$h_c = ca^n \quad \text{A11}$$

$$n = \frac{1}{m-1} \quad \text{A12}$$

$$\kappa = \sqrt{\pi}\frac{\Gamma\left(\frac{n+2}{2}\right)}{\Gamma\left(\frac{n+1}{2}\right)} \quad \text{A13}$$

$$h = \kappa h_c \quad \text{A14}$$

$$a = \frac{mb\kappa^{m-1}h_c^{m-1}}{2E^*} \quad \text{A15}$$

$$a = \frac{b_1}{2E^*} + \frac{b_2\kappa h_c}{E^*} \quad \text{A16}$$

The tip geometry can also be described in power law form by Eq. A11. From the two fitted polynomial parameters, b_1 and b_2, Eq. A7 and Eq. A8 can be used to calculate predicted values of *F* and *S* as a function of indentation depth, *h*; namely *F*(*h*) and *S*(*h*). These predicted values of *F* and *S* can be used to calculate a number of parameters as a function of indentation depth:

- *m*(*h*): Eq. A6
- *b*(*h*): Eq. A1
- *a*(*h*): Eq. A4
- *n*(*h*): Eq. A12

- $\kappa(h)$: Eq. A13
- $h_c(h)$: Eq. A14

These allow $a(h)$ to be expressed as $a(h_c)$ in Eq. A16, where the semi-included angle, α, of the equivalent cone is given by $\tan^{-1}\alpha = b_2\kappa/E^*$ and the radius of the truncation is given by $a(h_c = 0) = b_1/2E^*$. The tip contact radius function, $a(h_c)$, is a description of the tip geometry and can be expressed, equivalently, by Eq. A15 where b, m and κ vary continuously as a function of h. Essentially, for each point on a predicted loading curve generated from a polynomial fit, $F(h)$, there is a unique power law that gives the same predicted force and slope (contact stiffness) at the same indentation depth. Similarly, for each point on the tip radius function, $a(h_c)$ there is a unique power law that gives the same predicted contact radius and slope at the same contact depth, h_c.

For corneocytes, the Oliver & Pharr analysis [54] for an elastoplastic contact is used to obtain the value of h_c associated with h_{max} by measuring the initial unloading stiffness S_0. Eq. A16 can then be used to obtain a from h_c . The elastic modulus then follows from Eq. A9.

1H. Power law tip geometry, and loading curve analysis using a combination of six-term polynomial smoothing and power law equations

$$F = b_1h + b_2h^2 + b_3h^3 + b_4h^4 + b_5h^5 + b_6h^6 \quad \text{A17}$$

$$S = \frac{dF}{dh} = b_1 + 2b_2h + 3b_3h^2 + 4b_4h^3 + 5b_5h^4 + 6b_6h^5 \quad \text{A18}$$

$$S = 2E^*a \quad \text{A19}$$

$$a = \frac{b_1}{2E^*} + \frac{b_2h}{E^*} + \frac{3b_3h^2}{2E^*} + \frac{2b_4h^3}{E^*} + \frac{5b_5h^4}{2E^*} + \frac{3b_6h^5}{E^*} \quad \text{A20}$$

$$a = d_0 + d_1 h_c + d_2 h_c^2 + d_3 h_c^3 + d_4 h_c^4 + d_5 h_c^5 + d_6 h_c^6 \quad \text{A21}$$

A significantly better fit to each loading curve results from using the 6th order polynomial with a zero intercept as shown in Eq. A17. In particular, this reduces small, but significant, percentage systematic deviations between experimental loading curves and those predicted using Eq. A7 in the region 20 nm < *h* < 200 nm. These are attributed to deviations of the actual tip shape from a perfect flat-ended truncated cone. Any residual deviations are random, and a 6-term polynomial reduces each ca. 1000 point experimental loading curve to a set of 6 coefficients. This procedure acts as a smoothing function for the entire loading curve without residual tip-shape related systematic deviations.

By analogy with the procedures described above in A1G, the following steps are taken to numerically generate the tip function from a single AFM loading curve. All except the first step were implemented in Matlab.

A. Force zero set by tilt and offset correction in JPK software (see A1C).

B. Contact point set by linear back extrapolation of first 1-2 nN of data (see A1C).

C. 6th order polynomial with zero intercept fit from 1 nN and upwards of entire loading curve.

D. Create ca. 450-point arrays from h = 1 nm to $h = h_{max}$ in 1 nm steps using 6 fitted coefficients of:

E. $F(h)$: Eq. A17

F. $S(h)$: Eq. A18

G. $m(h)$: Eq. A6

H. $b(h)$: Eq. A1

I. $a(h)$: Eq. A4

J. $n(h)$: Eq. A12

K. $\kappa(h)$: Eq. A13

L. $h_c(h)$: Eq. A14

M. $a(h_c)$: Eq. A15. This tip contact radius function is valid for h = 5 nm to h_{max}, since it is the range in which the polynomial fit to the loading curve is confined.

N. $c(h_c)$: Eq. A11

O. 6th order polynomial fit with fitted intercept (Eq. A21) of $a(h_c)$ from h_c = 10 nm to h_c = 200 nm, which includes the complete range of values obtained from the Oliver & Pharr analysis of corneocytes.

1I. Tip contact radius function and corneocyte indentation

Multiple loading curves with the AFM probe for the PDMS specimen are averaged after performing Step E on them all, and this mean loading curve $F(h)$ is processed through the subsequent steps to produce a mean tip contact radius function array for fitting in Step O. The resulting 7 coefficients from an example fit to Eq. A21 are shown in Figure A2. The parameter arrays from intermediate steps can be used to calculate the mean and standard deviations, for example, at specific h or h_c values as shown in Table A1. These coefficients can then be used to calculate a from h_c obtained from corneocyte unloading curves using this AFM tip and the well-established Oliver & Pharr elastoplastic analysis procedure.

1J. Assumptions:

- Eq. A13 can be used in Eq. A14, even when the actual indenter tip shape has n varying with h_c.
- The Young's modulus of cast Sylgard 184 is independent of depth.

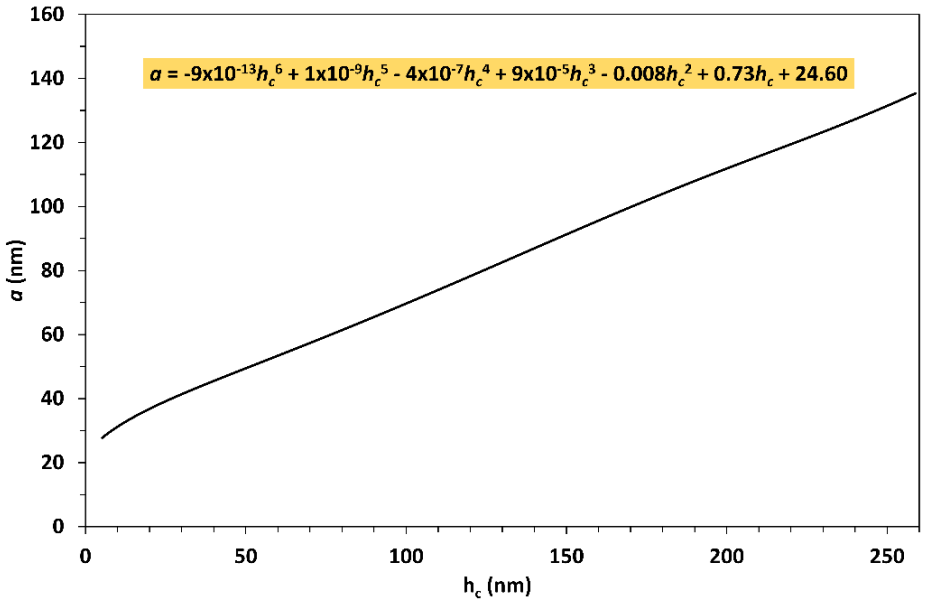

Figure A2. Example of a tip contact radius function for zone 3 of PDMS (average of 64 loading curves), which is valid for h = 5 nm to h_{max}.

Table A1. Elastic analysis of PDMS. The parameters of the indenter geometry obtained from an elastic analysis of PDMS. The power law load index, m, was calculated at different indentation depths based on polynomial fitting of multiple loading curves. The derived parameters c and n define the geometry of the AFM tip at different contact depths, h_c.

h_c (nm)	m	n	c (μm^{1-n})
5	1.150 ± 0.025	7.55 ± 0.20	(7.90 ± 3.90) x 10^{-11}
10	1.184 ± 0.004	5.41 ± 0.10	(7.80 ± 3.11) x 10^{-8}
15	1.217 ± 0.005	4.62 ± 0.11	(1.26 ± 0.40) x 10^{-6}
20	1.240 ± 0.004	4.61 ± 0.08	(5.90 ± 1.31) x 10^{-6}
30	1.278 ± 0.003	3.59 ± 0.04	(4.55 ± 0.63) x 10^{-5}
40	1.311 ± 0.003	3.21 ± 0.03	(1.85 ± 0.21) x 10^{-4}
50	1.344 ± 0.002	2.90 ± 0.02	(5.89 ± 0.50) x 10^{-4}
60	1.380 ± 0.002	2.63 ± 0.01	(1.65 ± 0.01) x 10^{-3}
70	1.414 ± 0.002	2.42 ± 0.01	(3.85 ± 0.20) x 10^{-3}
80	1.450 ± 0.002	2.22 ± 0.01	(8.26 ± 0.20) x 10^{-3}
90	1.484 ± 0.003	2.07 ± 0.01	(1.56 ± 0.05) x 10^{-2}
100	1.518 ± 0.004	1.93 ± 0.02	(2.70 + 0.11) x 10^{-2}
110	1.550 ± 0.005	1.82 ± 0.02	(4.31 ± 0.21) x 10^{-2}
120	1.580 ± 0.006	1.73 ± 0.02	(6.38 ± 0.32) x 10^{-2}
130	1.605 ± 0.006	1.65 ± 0.02	(8.63 ± 0.42) x 10^{-2}
140	1.628 ± 0.006	1.59 ± 0.01	0.112 ± 0.005
150	1.648 ± 0.005	1.54 ± 0.01	0.139 ± 0.005
160	1.663 ± 0.005	1.51 ± 0.01	0.162 ± 0.005
170	1.674 ± 0.004	1.48 ± 0.01	0.180 ± 0.003
180	1.680 ± 0.003	1.47 ± 0.01	0.192 ± 0.003
190	1.683 ± 0.003	1.46 ± 0.01	0.197 ± 0.005
200	1.682 ± 0.003	1.47 ± 0.01	0.196 ± 0.007
210	1.681 ± 0.004	1.47 ± 0.01	0.19 ± 0.01
220	1.682 ± 0.006	1.47 ± 0.01	0.20 ± 0.01
230	1.687 ± 0.009	1.46 ± 0.02	0.20 ± 0.02
240	1.695 ± 0.012	1.44 ± 0.03	0.22 ± 0.02
250	1.700 ± 0.014	1.41 ± 0.04	0.26 ± 0.04

A2 Methodology flow chart for corneocyte extraction and analysis

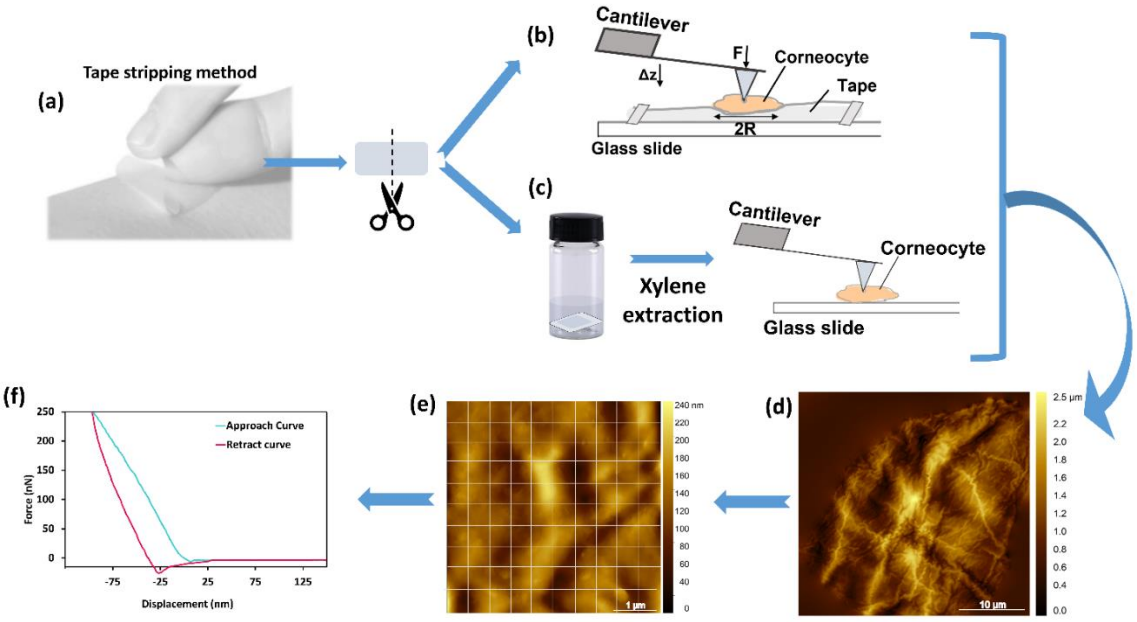

Figure A3. The workflow for the collection and analysis of corneocytes using AFM: (a) the tape stripping method was used to collect cells from the volar forearm of 3 healthy subjects using regular Sellotape and (**b**) half of the tapes were used directly for AFM measurements. **(c)** The remaining half of the tapes were pressed on glass slides and immersed in xylene overnight. This removed the tape and adhesion glue, transferring the corneocytes onto the slides. **(d)** Topographical images of single corneocytes were obtained using AFM TM; **(e)** Zoom-in image (5 × 5 µm) showing the 100 force curves grid used for the force spectroscopy experiments. **(f)** Example of loading and unloading curves obtained for a typical corneocyte attached to tape.

A3 AFM sensitivity calibration

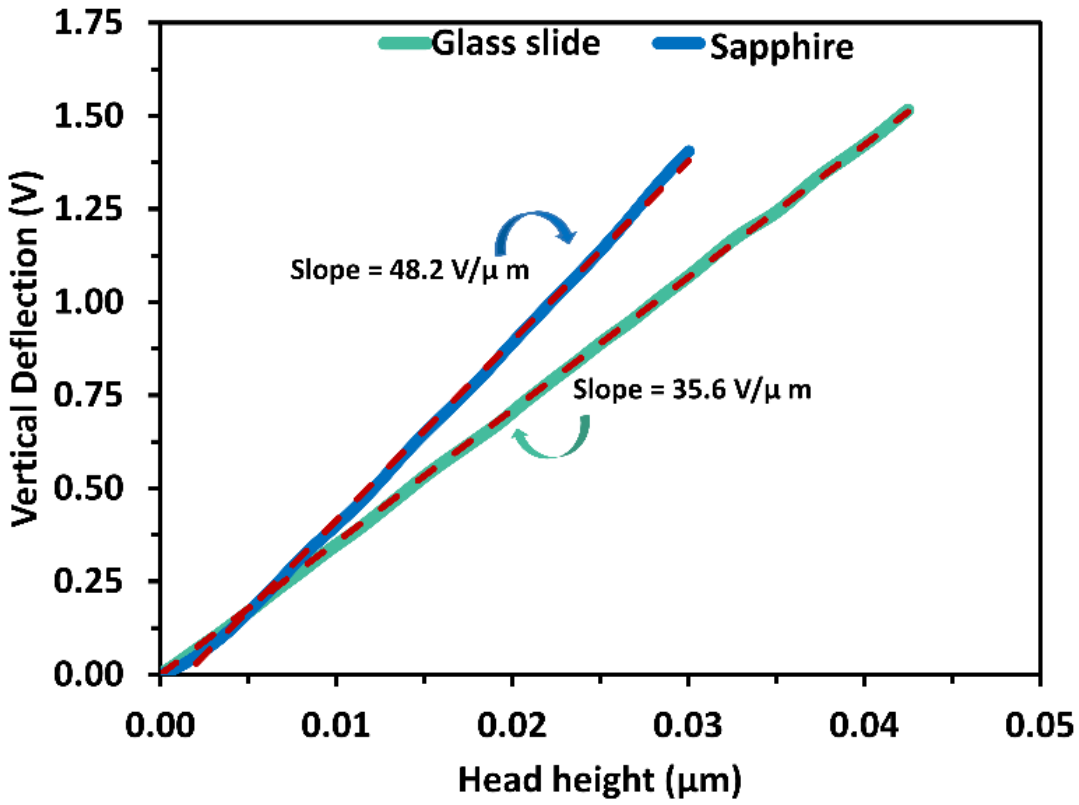

Figure A4. AFM Sensitivity calibration. The deflection sensitivity was calculated after each set of experiments by pressing the tip onto a 'relatively' rigid material (e.g., glass slide or sapphire), on the basis that there would not be significant indentation and, thus, the deflection of the cantilever should represent the sensitivity of the system (V/nm). Representative examples of the sensitivity values calculated for the stiff substrates were 28.1 nm/V (slope = 35.6 V/µm) for the glass slide and 20.7 nm/V (slope = 48.2 V/µm) for the sapphire sample. Sapphire was used for sensitivity calibration due to its greater stiffness compared to the glass and the AFM tip (made of silicon).

A4 Attenuated Total Reflection Fourier Transform (ATR-FTIR) spectroscopy

To explore any effects of xylene immersion, corneocytes were analysed using ATR-FTIR spectroscopy with a Nicolet 860 Fourier transform infrared microscope with OMNIC software on the computer interfaced to the spectrometer (Thermo Fisher Scientific UK Ltd., Loughborough, Leicestershire, LE11 5RG, UK). The spectra of corneocytes were obtained on tape, and after xylene extraction and re-adherence to the tape. In addition, spectra of the tape were acquired. Each spectrum consisted of

64 scans recorded in the wave-number range 600–4000 cm^{-1} and with a resolution of 4 cm^{-1}. Peak identification was done by consulting the literature [255, 256]. Fourier self-deconvolution (FSD) of the infrared spectra covering the Amide I region (1595−1705 cm^{-1}) was conducted using OMNIC software (Thermo Scientific, USA). Deconvolution was automatically performed using the Gaussian/Lorentzian line shape with a noise reduction factor of 0.3. The peak band assignment was based on literature [186].

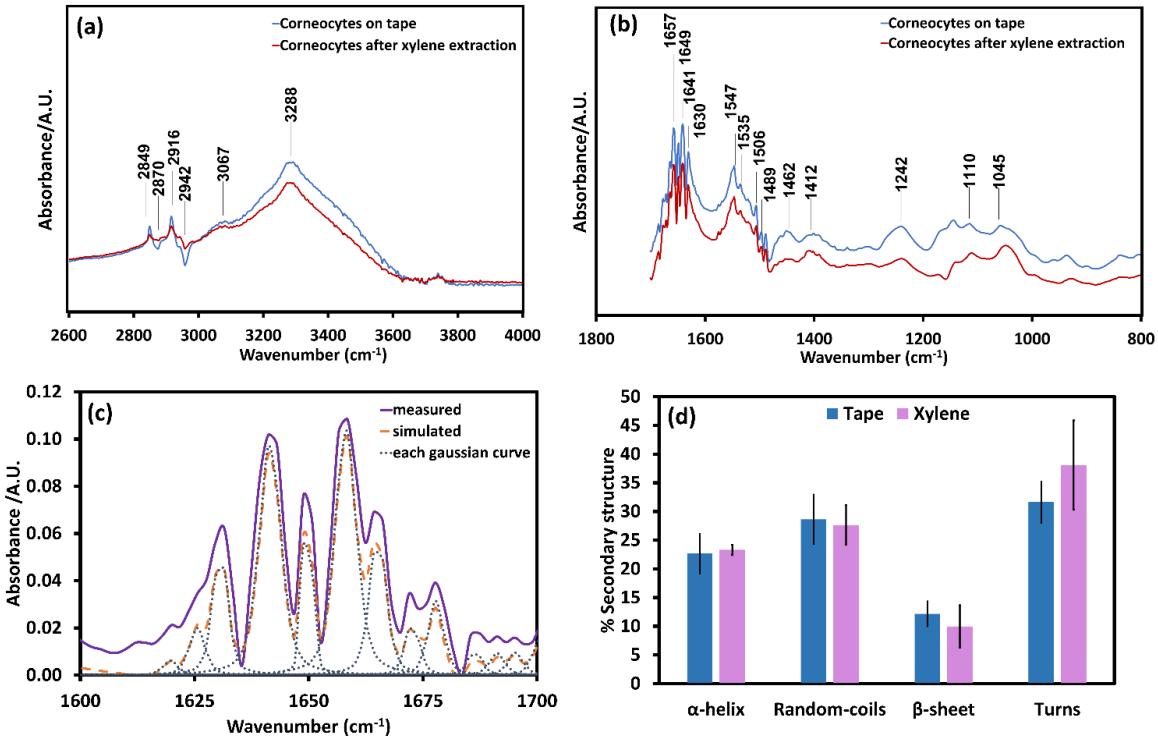

Figure A5. Attenuated total reflection Fourier transform infrared (ATR-FTIR) absorbance spectra of corneocytes (a) Cells on tape) before and **(b)** after xylene extraction in the spectral region of **(a)** 2600–4000 cm^{-1} and **(b)** 800–1700 cm^{-1}. **(c)** typical example of multiple Gauss curve-fitting to corneocyte ATR-FTIR spectrum for the Amide I band (1595–1705 cm^{-1}) spectrum. **(d)** secondary structures content based on Amide I band deconvolution for corneocytes on tape and after xylene extraction.

Typical ATR-Fourier transform infrared spectra for corneocytes before and after xylene extraction are shown in Figures A5a and A5b and the main peaks are identified and assigned in Table A2. There were not any apparent differences observed in the spectra for the range 700–1700 cm^{-1} and 2600–3800 cm^{-1}. The more prominent bands

were consistent with the work of Garidel [255] for corneocytes extracted from SC sheet, by removing the lipid fraction with chloroform. Furthermore, the band found at 1410.5/1412 cm^1 was attributed to amino acids belonging to the Natural Moisturising Factor (NMF), as described by Takada et al. [186]. Corneocytes are mainly composed of fibrous proteins like keratins and filaggrin and thus, to account for the secondary structure of the proteins, a deconvolution of the Amide I band was done to evaluate any effect of the xylene extraction. In Figure A5c, a typical example of multiple Gauss curve-fitting is shown. Xylene did not seem to affect the secondary structure of proteins since there were no differences found before and after tape extraction (Figure A5d).

Table A2. Assignments of the most prominent infrared absorption regions of corneocyte spectra on tape and after xylene extraction.

Tape		Xylene extraction	
Frequency range (cm^1)	**Assignment**	**Frequency range (cm^1)**	**Assignment**
3288.1	ν(OH) of water	3286.7	ν(OH) of water
2916.5	$\nu(CH_2)$ asymmetric	2916.1	$\nu(CH_2)$ asymmetric
2849.4	$\nu(CH_2)$ symmetric	2848.8	$\nu(CH_2)$ symmetric
1657.8	Amide I (α-helix)	1657.6	Amide I (α-helix)
1649.3	Amide I (random-coils)	1649.1	Amide I (random-coils)
1641.7	Amide I (random-coils)	1641.4	Amide I (random-coils)
1630.9	Amide I (β-sheet)	1630.9	Amide I (β-sheet)
1547.2	Amide II	1547.3	Amide II
1412.4	$\nu_{syn}(—COO^-)$	1410.5	$\nu_{syn}(—COO^-)$
1044.8	ν(C-OP) stretch	1047.9	ν(C-OP) stretch

A5 Elastomer calibration using a micromanipulation system

A bespoke micromanipulation system with a CCD camera was used for characterizing the mechanical properties of PDMS as a reference material for AFM nanoindentation.

Details of the system configuration are described elsewhere [257]. Force transducers 403A and 405A (Aurora Scientific Inc., Canada) were mounted with end-polished 24 μm diameter glass needles. The system compliance was evaluated 5 times and the mean value was used to compensate the force transducer and stage displacements. 10 randomly selected regions of a PDMS sample were indented until the maximum displacement load was reached.

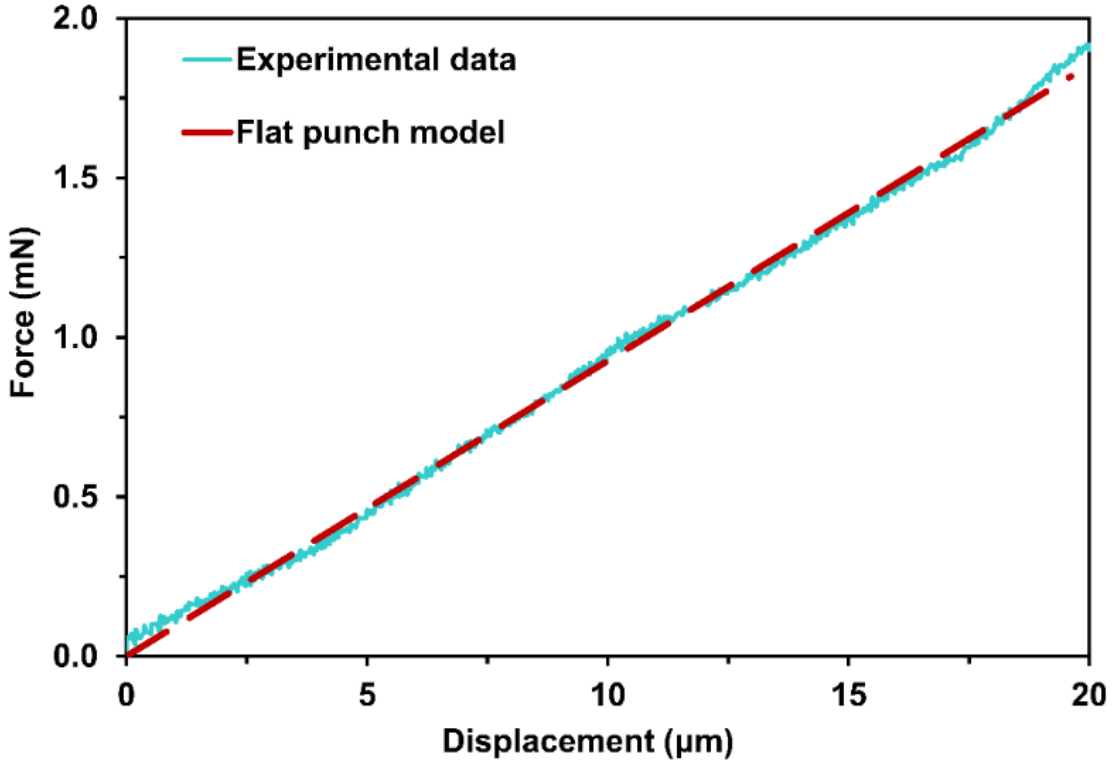

Figure A6. Force-displacement curve obtained using a flat punch indented on a PDMS sample surface up to 20 μm indentation depth.

The Young's of PDMS was calculated using on the basis of a flat punch indenting an isotropic linear elastic half-space (flat-punch theory) [258]:

$$F = 2RE^{*}\delta \tag{A22}$$

where F is applied force, R is the radius of the flat punch (12 μm), and δ is the displacement and E^{*} of the PDMS is given by the following expression by assuming that the probe is rigid compared to the PDMS:

$$E^* = \frac{E}{1-\nu^2} \quad \text{(A23)}$$

where E and ν are the Young's and Poisson's ratio of the PDMS, which was taken as 0.5 since it is considered incompressible.

APPENDIX B

Chapter IV Supplementary Information

B1. Geometry parameters of AFM tips

The tip geometry of each of the three AFM probes used in this study was calibrated using a reference specimen of silicone elastomer (polydimethylsiloxane, PDMS). This specimen had a plane strain elastic modulus, *E**, of 3.79 ± 0.21 MPa. This value was obtained independently at a larger scale by indentation with a cylindrical flat punch. The specimen was relatively smooth with a mean roughness, S_a, of 2.1 nm as calculated from AFM Tapping Mode scans over a 25 μm^2 area. Multiple AFM loading curves for each tip were obtained on the PDMS specimen in the presence of dilute aqueous surfactant to reduce adhesion. These curves were fitted to a 6th order polynomial equation for averaging and smoothing. This function, $F(h)$, was used to calculate the contact radius, a, as a function of the indentation depth, h, using [144]:

$$S = \frac{dF}{dh} = \frac{2E}{1-\nu^2}a = 2E^*a \qquad \text{(B1)}$$

where S is the contact stiffness, F is the indentation force and h is the indentation depth. E and ν are the Young's modulus and Poisson's ratio of the elastomer (ν = 0.5 for PDMS).

The tip radius profile can be expressed as the contact radius, a, as a function of the contact depth, h_c. This profile, $a(h_c)$, represents the geometry of the tip and can be derived from $a(h)$ by utilising indentation equations for a generalised power law indenter profile, and its associated power law loading curve [144]:

$$h_c = ca^n \tag{B2}$$

$$F = bh^m \tag{B3}$$

where c and n are the power law indenter profile coefficient and indenter profile index respectively, and b and m are the corresponding power law load coefficient and load index respectively. The load index as a function of indentation depth, $m(h)$, can be obtained from the fitted polynomial, $F(h)$, and its differential, $S(h)$, thus:

$$m = \frac{Sh}{F} \tag{B4}$$

The two indices are related as follows:

$$n = \frac{1}{m-1} \tag{B5}$$

The relationship between h and h_c is given by:

$$h = \kappa h_c \tag{B6}$$

where the scaling factor, κ, is a function of n through an equation containing gamma functions, $\Gamma(.)$:

$$\kappa = \sqrt{\pi}\frac{\Gamma\left(\frac{n+2}{2}\right)}{\Gamma\left(\frac{n+1}{2}\right)} \tag{B7}$$

This accounts for the surface deflection of the elastomer beyond the contact boundary, $h_s\ (= h - h_c)$. Eqs (B6) and (B7) allow $h_c(h)$ to be obtained and hence $a(h_c)$ from $a(h)$.

Finally, a best fit polynomial equation from h_c = 10 nm to h_c = 100 nm is derived for $a(h_c)$:

$$a = d_0 + d_1 h_c + d_2 h_c^2 + d_3 h_c^3 + d_4 h_c^4 + d_5 h_c^5 + d_6 h_c^6 \quad \text{(B8)}$$

This covers the complete range of h_c values obtained from the corneocyte indentation measurements in this study. The data below 10 nm are excluded since the experimental data are more variable in the near contact region than at deeper depths. Table B1 gives the load index and geometric parameters for each tip at selected depths, and Figure B1 shows the corresponding fitted tip radius functions.

Table B1. Elastic analysis of PDMS. Tip shape calibration was carried out by indenting a PDMS reference elastomer (64 force curves in 3 regions for each tip) with a known elastic modulus, E^* = 3.79 ± 0.21 MPa. This value was obtained from independent indentation experiments at a larger scale. The power law load index, *m*, was calculated at different indentation depths based on polynomial fitting of multiple loading curves. The derived parameters *c* and *n* define the geometry of the AFM tip at different contact depths, h_c.

Contact depth	**Cantilever 1**			**Cantilever 2**			**Cantilever 3**		
h_c **(nm)**	***m***	***n***	***c* (μm^{1-n})**	***m***	***n***	***c* (μm^{1-n})**	***m***	***n***	***c* (μm^{1-n})**
8	1.132 ± 0.004	7.55 ± 0.20	(7.91 ± 3.86) x 10^{-11}	1.229 ± 0.041	4.51 ± 0.80	(2.04 ± 1.06) x 10^{-6}	1.290 ± 0.010	3.58 ± 0.11	(5.70 ± 3.18) x 10^{-6}
10	1.184 ± 0.004	5.44 ± 0.13	(7.80 ± 3.11) x 10^{-8}	1.286 ± 0.047	3.59 ± 0.59	(2.97 ± 1.91) x 10^{-5}	1.380 ± 0.054	2.71 ± 0.08	(1.52 ± 0.63) x 10^{-4}
20	1.240 ± 0.004	4.61 ± 0.08	(5.90 ± 1.31) x 10^{-6}	1.316 ± 0.050	3.24 ± 0.51	(8.53 ± 7.95) x 10^{-5}	1.454 ± 0.013	2.27 ± 0.07	(1.02 ± 0.25) x 10^{-3}
40	1.311 ± 0.003	3.21 ± 0.03	(1.85 ± 0.21) x 10^{-4}	1.335 ± 0.038	3.02 ± 0.34	(1.10 ± 0.10) x 10^{-4}	1.501 ± 0.028	2.12 ± 0.12	(1.99 ± 1.16) x 10^{-3}
60	1.380 ± 0.002	2.63 ± 0.01	(1.65 ± 0.01) x 10^{-3}	1.361 ± 0.003	2.77 ± 0.03	(5.57 ± 5.56) x 10^{-5}	1.516 ± 0.039	2.11 ± 0.17	(2.39 ± 1.72) x 10^{-3}
80	1.450 ± 0.002	2.22 ± 0.01	(8.26 ± 0.20) x 10^{-3}	1.452 ± 0.031	2.22 ± 0.16	(2.16 ± 1.49) x 10^{-3}	1.481 ± 0.032	2.23 ± 0.16	(1.26 ± 0.10) x 10^{-3}
100	1.518 ± 0.004	1.93 ± 0.02	(2.70 ± 0.11) x 10^{-2}	1.480 ± 0.032	2.09 ± 0.14	(3.74 ± 2.37) x 10^{-3}	1.448 ± 0.021	2.26 ± 0.01	(1.01 ± 0.10) x 10^{-3}

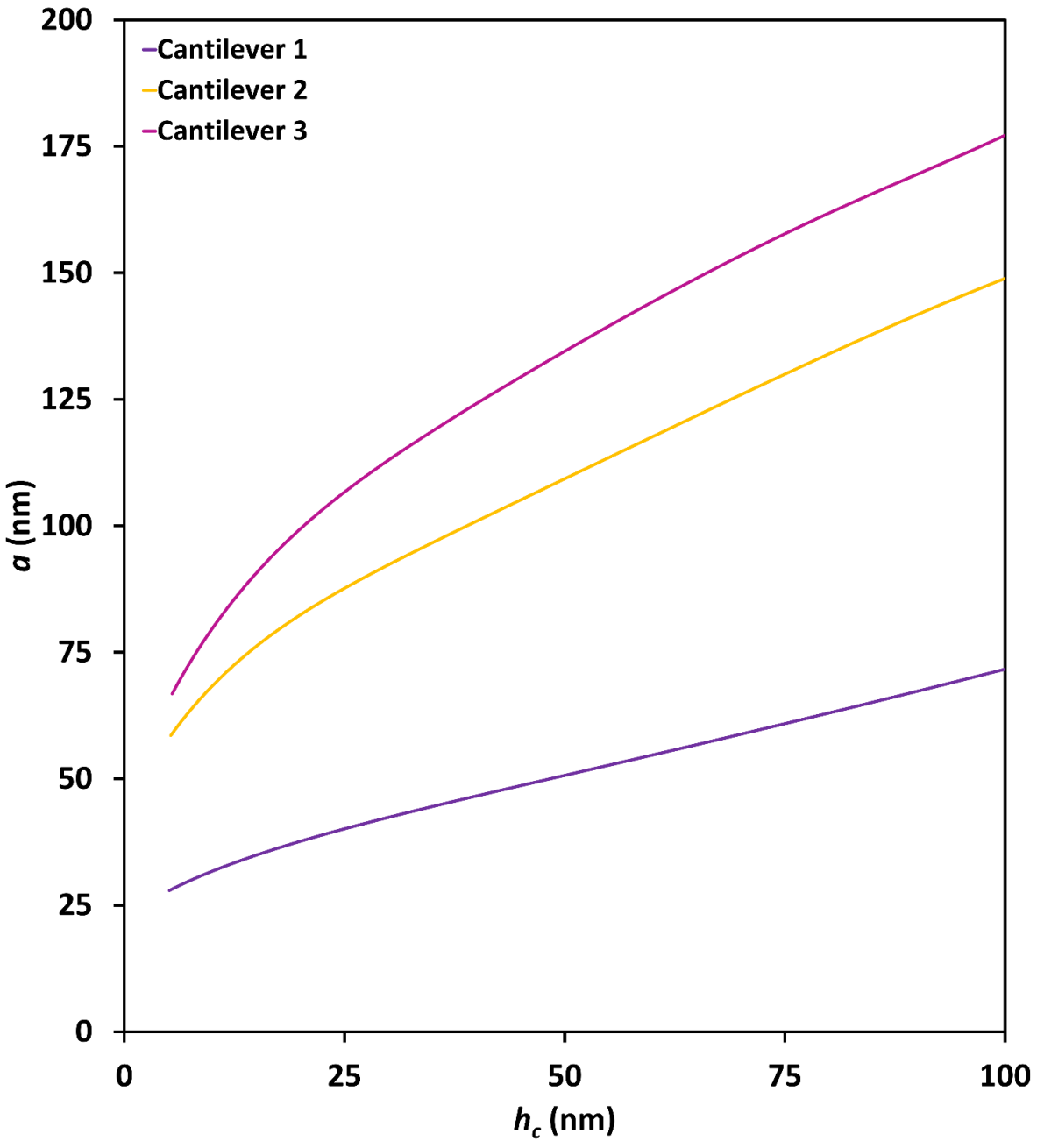

Figure B1. Tip contact radius function for the three cantilevers used in this study. This was based on the indentation of three regions of a PDMS reference specimen (each region is the average of 64 loading curves) which is valid for h_c = 10–100 nm.

APPENDIX C

Chapter V Supplementary Information

C1 Geometry parameters of AFM tips

The tip geometry of each of the five AFM probes used in this study were calibrated using a reference specimen of silicone elastomer (polydimethylsiloxane, PDMS), which had a plane strain Young's modulus, E^*, of 3.79 ± 0.21 MPa. This value was obtained independently at a larger scale by indentation with a cylindrical flat punch. The specimen was relatively smooth with a mean roughness, S_a, of 2.1 nm as calculated from AFM Tapping Mode scans over a 25 μm^2 area. Multiple AFM loading curves for each tip were measured on the PDMS specimen in the presence of dilute aqueous surfactant to reduce adhesion. These curves were fitted to a 6th order polynomial equation for averaging and smoothing. This function, $F(h)$, was used to calculate the contact radius, a, as a function of the indentation depth, h, using [144]:

$$S = \frac{dF}{dh} = \frac{2E}{1-\nu^2}a = 2E^*a \qquad \text{(C1)}$$

where S is the contact stiffness, F is the indentation force and h is the indentation depth. E and ν are the Young's modulus and Poisson's ratio of the elastomer (ν = 0.5 for PDMS).

The tip radius profile can be expressed as the contact radius, a, as a function of the contact depth, h_c. This profile, $a(h_c)$, represents the geometry of the tip and can be derived from $a(h)$ by utilising indentation equations for a generalised power law indenter profile, and its associated power law loading curve [144]:

$$h_c = ca^n \tag{C2}$$

$$F = bh^m \tag{C3}$$

where c and n are the power law indenter profile coefficient and indenter profile index respectively, and b and m are the corresponding power law load coefficient and load index respectively. The load index as a function of indentation depth, $m(h)$, can be obtained from the fitted polynomial, $F(h)$, and its differential, $S(h)$, thus:

$$m = \frac{Sh}{F} \tag{C4}$$

The two indices are related as follows:

$$n = \frac{1}{m-1} \tag{C5}$$

The relationship between h and h_c is given by:

$$h = \kappa h_c \tag{C6}$$

where the scaling factor, κ, is a function of n through an equation containing gamma functions, $\Gamma(.)$:

$$\kappa = \sqrt{\pi}\frac{\Gamma\left(\frac{n+2}{2}\right)}{\Gamma\left(\frac{n+1}{2}\right)} \tag{C7}$$

This accounts for the surface deflection of the elastomer beyond the contact boundary, h_s $(= h - h_c)$. Eqs (C6) and (C7) allow $h_c(h)$ to be obtained and hence $a(h_c)$ from $a(h)$. Finally, a best fit polynomial equation from h_c = 10 nm to h_c = 100 nm is derived for $a(h_c)$:

$$a = d_0 + d_1 h_c + d_2 h_c^2 + d_3 h_c^3 + d_4 h_c^4 + d_5 h_c^5 + d_6 h_c^6 \tag{C8}$$

This covers the complete range of h_c values obtained from the corneocyte indentation measurements in this study. The data for < 10 nm were excluded since they are more variable in the near contact region than at deeper depths. Table C1 gives the load

index and geometric parameters for each tip at selected depths, and Figure C1 shows the corresponding fitted tip radius functions.

Table C1. Elastic analysis of PDMS. Tip shape calibration was carried out by indenting a PDMS reference elastomer (64 force curves in 3 regions for each tip) with a known elastic modulus, E^* = 3.79 ± 0.21 MPa. This value was obtained from independent indentation experiments at a larger scale. The power law load index, m, was calculated at different indentation depths based on the polynomial fitting of multiple loading curves. The derived parameters c and n define the geometry of the AFM tip at different contact depths, h_c.up to 100 nm.

Contact depth h_c (nm)	Cantilever 1			Cantilever 2			Cantilever 3		
	m	***n***	***c* (μm^{1-n})**	***m***	***n***	***c* (μm^{1-n})**	***m***	***n***	***c* (μm^{1-n})**
20	1.315 ± 0.013	3.17 ± 0.13	(1.51 ± 0.1) x 10^{-4}	1.312 ± 0.062	3.32 ± 0.56	(7.18 ± 2.59) x 10^{-5}	1.227 ± 0.010	4.09 ± 0.11	(1.38 ± 0.52) x 10^{-5}
40	1.354 ± 0.028	2.83 ± 0.24	(6.12 ± 3.90) x 10^{-4}	1.335 ± 0.045	2.94 ± 0.31	(4.33 ± 0.79) x 10^{-4}	1.338 ± 0.028	2.87 ± 0.18	(1.12 ± 0.6) x 10^{-3}
60	1.394 ± 0.039	2.56 ± 0.27	(1.91 ± 1.10) x 10^{-3}	1.395 ± 0.011	2.45 ± 0.05	(5.48 ± 1.37) x 10^{-3}	1.448 ± 0.039	2.23 ± 0.13	(1.12 ± 0.53) x 10^{-2}
80	1.450 ± 0.032	2.23 ± 0.16	(5.92 ± 2.68) x 10^{-3}	1.507 ± 0.035	1.99 ± 0.11	(4.14± 0.8) x 10^{-2}	1.49 ± 0.031	1.86 ± 0.08	(4.25 ± 1.35) x 10^{-2}
100	1.508 ± 0.025	1.97 ± 0.10	(1.63 + 0.42) x 10^{-2}	1.650 ± 0.065	1.64 ± 0.12	0.17 ± 0.02	1.624 ± 0.014	1.64 ± 0.04	(9.77 + 1.44) x 10^{-2}

Contact depth h_c (nm)	Cantilever 4			Cantilever 5		
	m	***n***	***c* (μm^{1-n})**	***m***	***n***	***c* (μm^{1-n})**
20	1.300 ± 0.102	3.39 ± 1.38	(2.03 ± 1.00) x 10^{-6}	1.244 ± 0.024	4.28 ± 0.61	(1.57 ± 1.16) x 10^{-5}
40	1.352 ± 0.071	3.03 ± 0.65	(2.01 ± 1.50) x 10^{-3}	1.220 ± 0.050	4.50 ± 0.97	(1.28 ± 0.10) x 10^{-5}
60	1.416 ± 0.036	2.44 ± 0.23	(4.03 ± 3.22) x 10^{-3}	1.249 ± 0.057	3.41 ± 0.34	(1.78 ± 0.98) x 10^{-4}
80	1.493 ± 0.009	2.03 ± 0.03	(1.37 ± 0.38) x 10^{-2}	1.341 ± 0.048	2.41 ± 0.30	(8.10 ± 0.42) x 10^{-3}
100	1.560 ± 0.007	1.80 ± 0.02	(3.47 ± 0.13) x 10^{-2}	1.457 ± 0.033	1.91 ± 0.24	(5.74 ± 3.43) x 10^{-2}

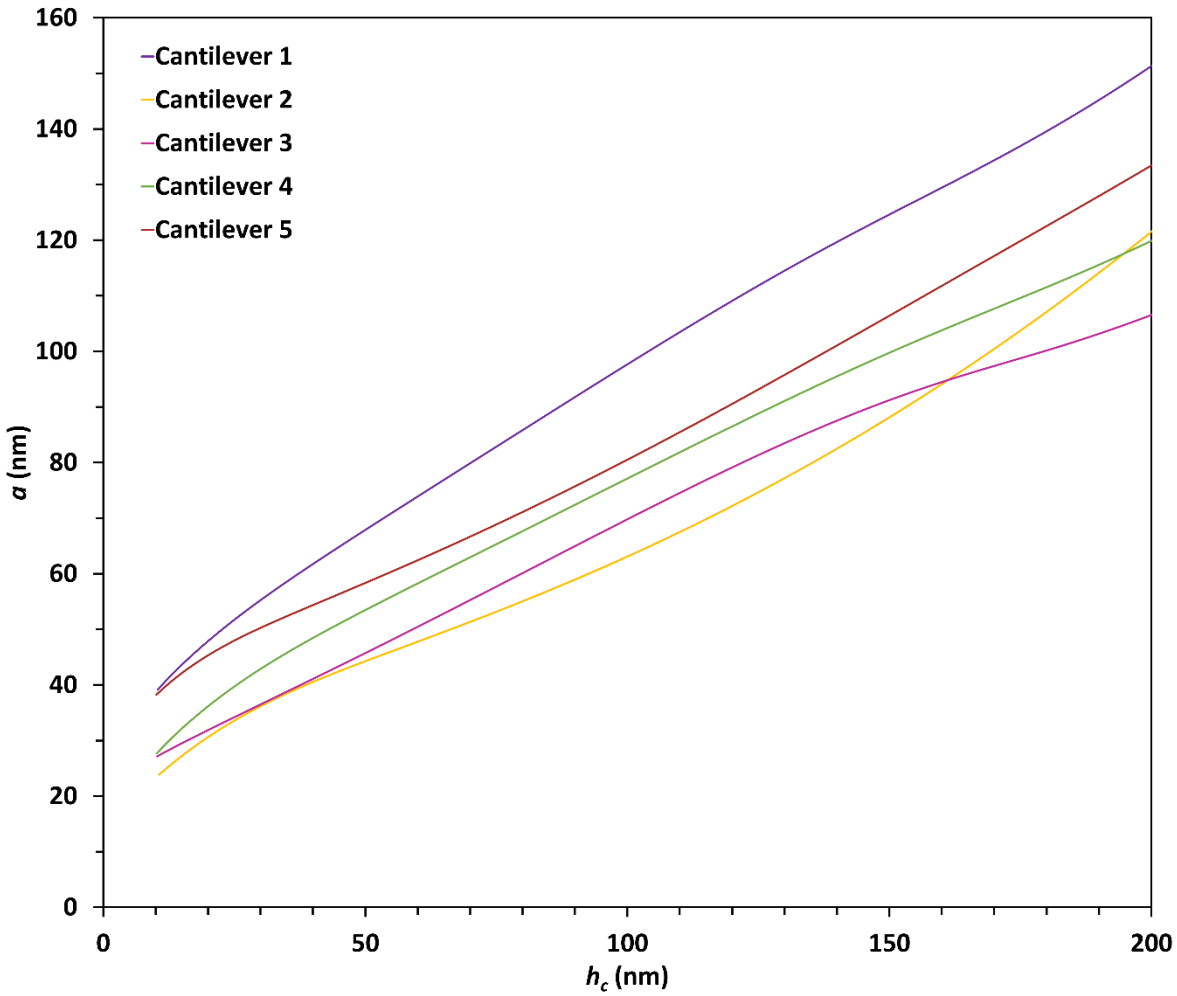

Tip-radius function

Cantilever 1: $a = -7.84\text{x}10^{-12}h_c^6 + 6.23\text{x}10^{-9}h_c^5 - 1.88\text{x}10^{-6}h_c^4 + 2.7\text{x}10^{-4}h_c^3 - 0.02h_c^2 + 1.4h_c + 27.0$

Cantilever 2: $a = -5.25\text{x}10^{-12}h_c^6 + 4.19\text{x}10^{-9}h_c^5 - 1.35\text{x}10^{-6}h_c^4 + 2.3\text{x}10^{-4}h_c^3 - 0.02h_c^2 + 1.2h_c + 13.16$

Cantilever 3: $a = -4.07\text{x}10^{-12}h_c^6 + 3.39\text{x}10^{-9}h_c^5 - 1.03\text{x}10^{-6}h_c^4 + 1.4\text{x}10^{-4}h_c^3 - 0.008h_c^2 + 0.68h_c + 20.8$

Cantilever 4: $a = -4.58\text{x}10^{-12}h_c^6 + 4.13\text{x}10^{-9}h_c^5 - 1.41\text{x}10^{-6}h_c^4 + 2.3\text{x}10^{-4}h_c^3 - 0.02h_c^2 + 1.3h_c + 16.2$

Cantilever 5: $a = -4.90\text{x}10^{-11}h_c^6 + 2.65\text{x}10^{-8}h_c^5 - 5.75\text{x}10^{-6}h_c^4 + 6.4\text{x}10^{-4}h_c^3 - 0.04h_c^2 + 1.5h_c + 26.5$

Figure C1. Tip contact radius functions for the five cantilevers used in this study. They are each based on indentation in three regions of the PDMS specimen (each region is the average of 64 loading curves) and are valid for h_c= 10–200 nm.

C2 Herschel-Bulkley material parameters

Given that corneocytes are elastoplastic [51] with a time dependent yield stress, it is possible to apply the Herschel-Bulkley model to describe the material properties. To obtain this rate-dependent material model from the time dependent data, it may be

assumed that the relaxation arises from a conversion of the elastic, ε_e, to the plastic, ε_p, strain so that the total strain, ε, may be decomposed additively as follows:

$$\varepsilon = \varepsilon_e + \varepsilon_p \tag{C9}$$

and assuming $d\varepsilon/dt = 0$ and a constant value of the Young's modulus $E^* = \sigma/\varepsilon_e$, where σ is the unconfined bulk stress:

$$d\varepsilon_p/dt = -d\varepsilon_e/dt = -d(\sigma/E^*)/dt \approx -\frac{1}{E^*}d\sigma/dt \tag{C10}$$

Substituting the derivative of Eq. (19) with the mean stress, $H = \bar{\sigma} = 3\sigma$, the uniaxial strain rate is given by:

$$d\varepsilon_p/dt = \frac{3}{E^*}\left(\frac{C_1}{\tau_1}e^{-t/\tau_1} + \frac{C_2}{\tau_2}e^{-t/\tau_2}\right) \tag{C11}$$

so that a material model can be obtained from a plot of σ as a function of $d\varepsilon_p/dt$. Generally, viscoplastic materials are described by a stress overshoot model to account for the strain rate hardening [161]. However, the Herschel-Bulkley model is applied here since it is equivalent to uniaxial deformation [162]:

$$\sigma = \sigma_Y + k\left(d\varepsilon_p/dt\right)^j \tag{C12}$$

where σ_Y is the quasi-static uniaxial yield stress, k is the plastic flow consistency and j is plastic flow index. It should be noted that this is a rigid-viscoplastic model since it is assumed that yielding occurs at a zero strain. That is, elastic deformation within the yield surface is treated separately. The quasi-static uniaxial yield stress, the plastic flow consistency and plastic flow index calculated for corneocytes in different water activities are shown in Table C2, together with R^2 values of the fits to Eq. (12).

Table C2. Herschel-Bulkley material parameters. Results are presented as mean ± 1 SD based on 5 cells per participant and per anatomical site.

Hydration level		σ_Y (MPa)		j		k (MPa s^n)		R^2	
		Forearm	Medial Heel	Forearm	Medial Heel	Forearm	Medial Heel	Forearm	Medial Heel
Air (RH)	35%	29.73 ± 17.01	38.83 ± 9.29	0.42 ± 0.09	0.42 ± 0.04	19.18 ± 9.63	24.17 ± 10.45	0.97 ± 0.01	0.94 ± 0.03
Glycerol 85% (A_w)	0.42	0.37 ± 0.13	0.28 ± 0.19	0.49 ± 0.03	0.51 ± 0.02	0.32 ± 0.06	0.22 ± 0.10	0.97 ± 0.02	0.96 ± 0.01
Glycerol 70% (A_w)	0.62	0.14 ± 0.06	0.19 ± 0.08	0.49 ± 0.07	0.50 ± 0.03	0.16 ± 0.03	0.13 ± 0.05	0.95 ± 0.03	0.97 ± 0.02
Glycerol 50% (A_w)	0.80	0.11 ± 0.03	0.14 ± 0.07	0.44 ± 0.08	0.48 ± 0.03	0.10 ± 0.02	0.13 ± 0.05	0.94 ± 0.02	0.97 ± 0.01
H_2O (A_w)	1.00	0.12 ± 0.01	0.14 ± 0.05	0.53 ± 0.03	0.52 ± 0.01	0.06 ± 0.01	0.11 ± 0.01	0.95 ± 0.02	0.98 ± 0.03

APPENDIX D

Chapter VI Supplementary Information

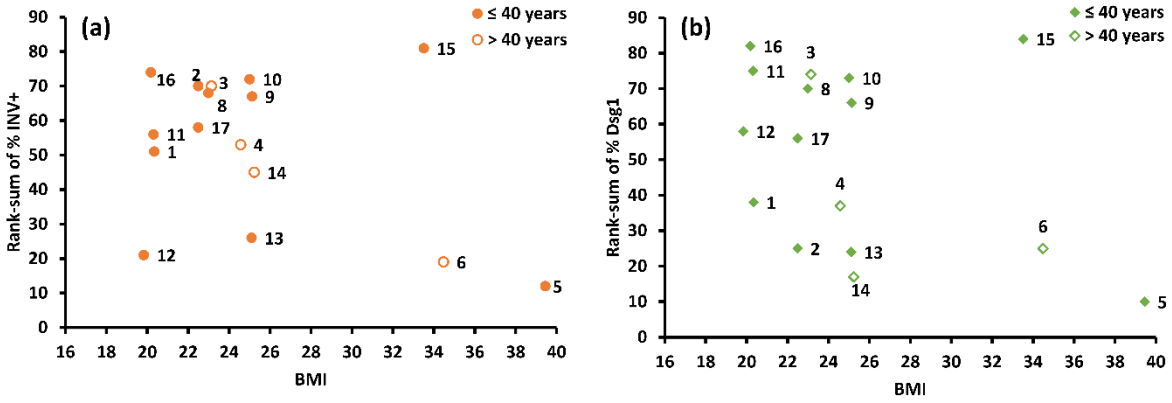

Figure D1. Rank sum analysis of the percentage of immature cells **(a)** and of Dsg1 **(b)** as a function of BMI for both anatomical sites (site A and C) across all sessions (session 1, 2 and 3). Correlational analysis did not show any significant relationship, as Spearman coefficients were r=-0.229 and p=0.394 for % INV+ and r=-0.403 and p=0.122 for % Dsg1.

APPENDIX E

Chapter VII Supplementary Information

E1. Methodology flow chart

A sub-set of patients (n=17) from the original cohort of 30 who presented with category 1 PUs from elderly care and surgical hospital wards were selected. Prior to being enrolled in the study, each patient presenting with redness and erythema on the skin surface was subjected to further assessment (non-blanching erythema test [252] to ensure that the local skin changes could be classified as category1 PU [223]. Corneocyte samples were collected following a biophysical assessment of the skin (TEWL and SC hydration) and sampling of the skin surface sebum using Sebutapes [253]. The protocol followed in this study is shown in Figure E1.

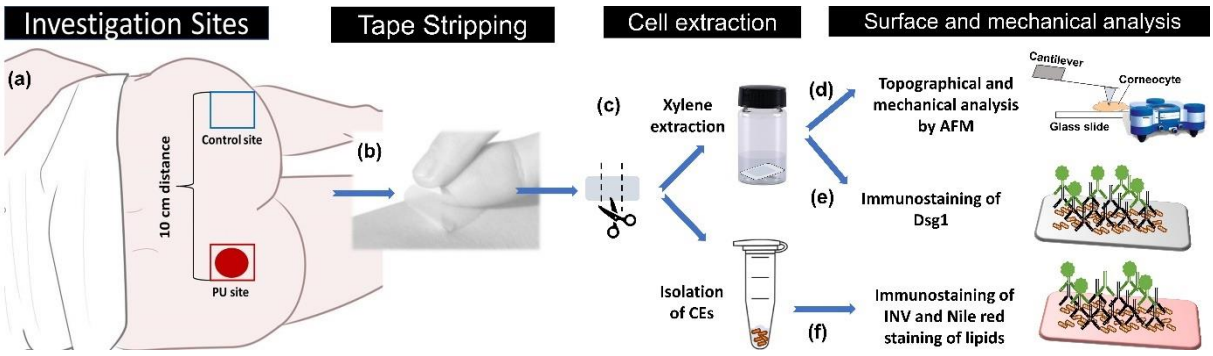

Figure E1. Methodology flow chart. (a) Investigation sites associated with the location of the category 1 PUs and at 10 cm from this location, the latter representing a control site. **(b)** Collection of corneocytes were performed via tape stripping. **(c)** Extraction of cells was carried out via xylene, directly fixing the cells on a glass slide for use in protocol **(d)** and **(e)**, or by buffer extraction of cells from a tape (isolation of CEs) for use in protocol **(f)**. **(d)** Topographical and mechanical properties were analysed via Atomic Force Microscopy. **(e)** Immunostaining of Dsg1 was used to indirectly visualise corneodesmosomes. **(f)** Double staining of involucrin (immunostaining) and surface lipids (Nile red) was performed to calculate the number of immature CEs.

E2. Geometric parameters of AFM tips

The tip geometry of each of the four AFM probes used in this study was calibrated using a reference specimen of silicone elastomer (polydimethylsiloxane, PDMS). This specimen had a plane strain elastic modulus, *E**, of 3.79 ± 0.21 MPa. This value was obtained independently at a larger scale by indentation with a cylindrical flat punch. The specimen was relatively smooth with a mean roughness, S_a, of 2.1 nm as calculated from AFM Tapping Mode scans over a 25 μm^2 area. Multiple AFM loading curves for each tip were obtained on the PDMS specimen in the presence of dilute aqueous surfactant to reduce adhesion. These curves were fitted to a 6th order polynomial equation for averaging and smoothing. This function, $F(h)$, was used to calculate the contact radius, a, as a function of the indentation depth, h, using [144]:

$$S = \frac{dF}{dh} = \frac{2E}{1-\nu^2}a = 2E^*a \qquad \text{(E1)}$$

where S is the contact stiffness, F is the indentation force and h is the indentation depth. E and ν are the Young's modulus and Poisson's ratio of the elastomer (ν = 0.5 for PDMS).

The tip radius profile can be expressed as the contact radius, a, as a function of the contact depth, h_c. This profile, $a(h_c)$, represents the geometry of the tip and can be derived from $a(h)$ by utilising indentation equations for a generalised power law indenter profile, and its associated power law loading curve [144]:

$$h_c = ca^n \qquad \text{(E2)}$$

$$n = \frac{1}{m-1} \tag{E3}$$

where c and n are the power law indenter profile coefficient and indenter profile index respectively, and b and m are the corresponding power law load coefficient and load index respectively. The load index as a function of indentation depth, $m(h)$, can be obtained from the fitted polynomial, $F(h)$, and its differential, $S(h)$, thus:

$$m = \frac{Sh}{F} \tag{E4}$$

The two indices are related as follows:

$$n = \frac{1}{m-1} \tag{E5}$$

The relationship between h and h_c is given by:

$$h = \kappa h_c \tag{E6}$$

where the scaling factor, κ, is a function of n through an equation containing gamma functions, $\Gamma(.)$:

$$\kappa = \sqrt{\pi}\frac{\Gamma\left(\frac{n+2}{2}\right)}{\Gamma\left(\frac{n+1}{2}\right)} \tag{E7}$$

This accounts for the surface deflection of the elastomer beyond the contact boundary, $h_s\ (= h - h_c)$. Eqs (E6) and (E7) allow $h_c(h)$ to be obtained and hence $a(h_c)$ from $a(h)$. Finally, a best fit polynomial equation from h_c = 10 nm to h_c = 100 nm is derived for $a(h_c)$:

$$a = d_0 + d_1 h_c + d_2 h_c^2 + d_3 h_c^3 + d_4 h_c^4 + d_5 h_c^5 + d_6 h_c^6 \tag{E8}$$

This covers the complete range of h_c values obtained from the corneocyte indentation measurements in this study. The data below 10 nm are excluded since the experimental data are more variable in the near contact region than at deeper depths. Table E1 gives the load index and geometric parameters for each tip at selected depths, and Figure E2 shows the corresponding fitted tip radius functions.

Table E1. Elastic analysis of PDMS. Tip shape calibration was carried out by indenting a PDMS reference elastomer (64 force curves in 3 regions for each tip) with a known elastic modulus, E^* = 3.79 ± 0.21 MPa. This value was obtained from independent indentation experiments at a larger scale. The power law load index, *m*, was calculated at different indentation depths based on polynomial fitting of multiple loading curves. The derived parameters *c* and *n* define the geometry of the AFM tip at different contact depths, h_c.

Contact depth h_c (nm)	Cantilever 1			Cantilever 2		
	m	***n***	***c* (μm^{1-n})**	***m***	***n***	***c* (μm^{1-n})**
5	1.030 ± 0.003	33.04 ± 3.19	(6.99 ± 3.12) x 10^{-65}	1.240 ± 0.009	4.17 ± 0.15	(3.42 ± 2.10) x 10^{-6}
10	1.041 ± 0.002	24.60 ± 0.95	(1.85 ± 1.01) x 10^{-51}	1.329 ± 0.008	3.03 ± 0.07	(1.49 ±0.50) x 10^{-4}
20	1.071 ± 0.002	14.10 ± 0.32	(5.29 ± 4.18) x 10^{-30}	1.409 ± 0.014	2.45 ± 0.08	(1.33 ± 0.48) x 10^{-3}
40	1.123 ± 0.002	8.12 ± 0.11	(2.78 ± 2.03) x 10^{-17}	1.463 ± 0.010	2.16 ± 0.05	(3.96 ± 0.80) x 10^{-3}
60	1.113 ± 0.006	8.88 ± 0.44	(2.37 ± 2.00) x 10^{-18}	1.483 ± 0.010	2.07 ± 0.04	(5.78 ± 0.94) x 10^{-3}
80	1.161 ± 0.015	6.26 ± 0.57	(4.06 ± 3.50) x 10^{-12}	1.500 ± 0.013	2.01 ± 0.05	(7.47 ± 0.15) x 10^{-3}
100	1.240 ± 0.023	4.19 ± 0.40	(8.22 + 7.01) x 10^{-8}	1.503 ± 0.017	1.98 ± 0.07	(8.60 ± 2.47) x 10^{-3}

Contact depth h_c (nm)	Cantilever 3			Cantilever 4		
	m	***n***	***c* (μm^{1-n})**	***m***	***n***	***c* (μm^{1-n})**
5	1.117 ± 0.029	8.45 ± 0.11	(4.09 ± 1.44) x 10^{-14}	1.132 ± 0.004	7.55 ± 0.20	(7.91 ± 3.86) x 10^{-11}
10	1.164 ± 0.041	6.09 ± 0.17	(5.04 ± 2.74) x 10^{-10}	1.184 ± 0.004	5.44 ± 0.13	(7.80 ± 3.11) x 10^{-8}
20	1.217 ± 0.051	4.61 ± 0.10	(1.46 ± 0.46) x 10^{-8}	1.240 ± 0.004	4.61 ± 0.08	(5.90 ± 1.31) x 10^{-6}
40	1.277 ± 0.050	3.61 ± 0.08	(8.69 ± 2.31) x 10^{-6}	1.311 ± 0.003	3.21 ± 0.03	(1.85 ± 0.21) x 10^{-4}
60	1.328 ± 0.047	3.05 ± 0.07	(9.11 ± 2.21) x 10^{-5}	1.380 ± 0.002	2.63 ± 0.01	(1.65 ± 0.01) x 10^{-3}
80	1.374 ± 0.043	2.68 ± 0.07	(4.59 ± 1.15) x 10^{-4}	1.450 ± 0.002	2.22 ± 0.01	(8.26 ± 0.20) x 10^{-3}
100	1.412 ± 0.039	2.43 ± 0.07	(1.34 ± 0.38) x 10^{-3}	1.518 ± 0.004	1.93 ± 0.02	(2.70 ± 0.11) x 10^{-2}

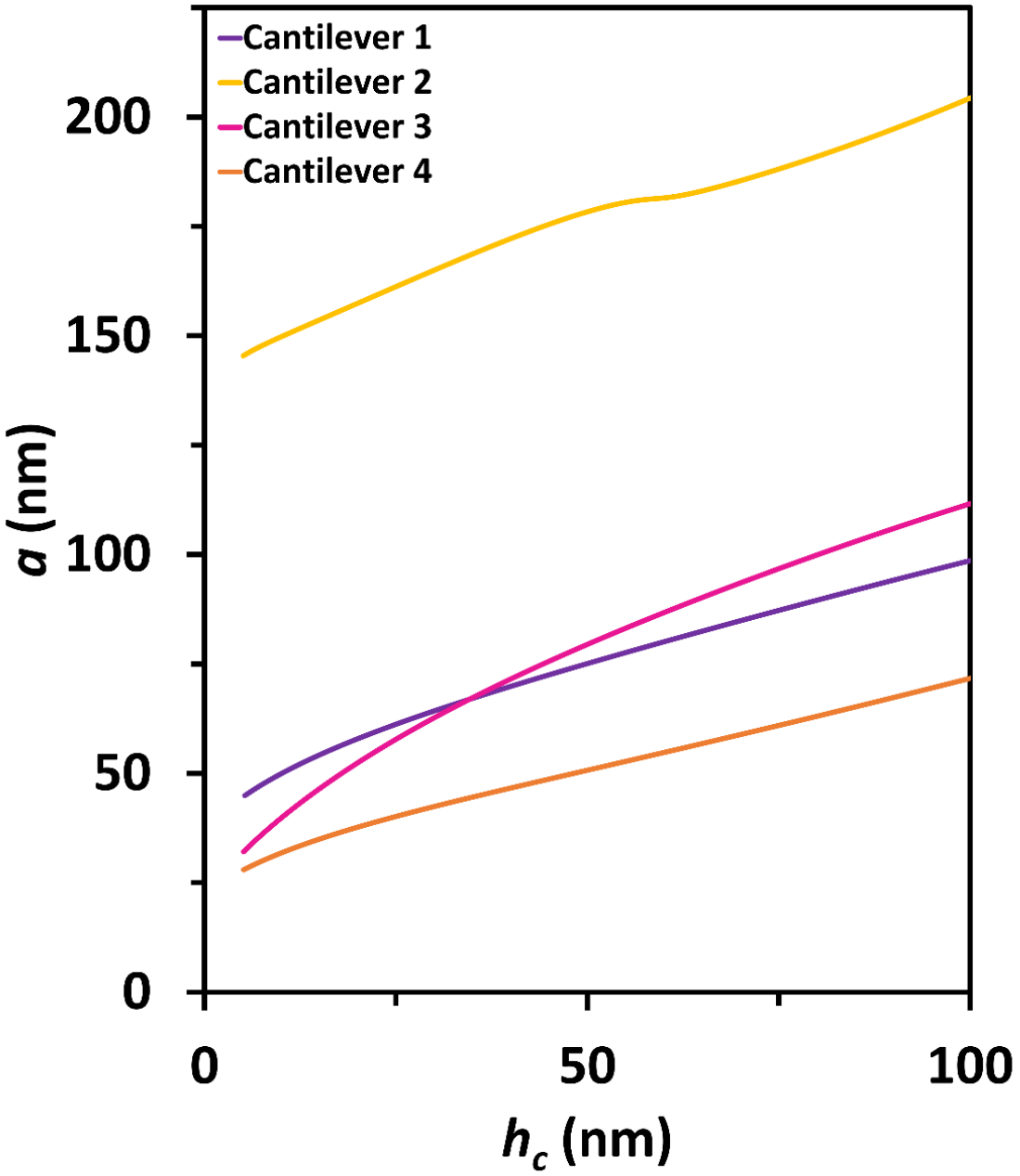

Tip contact radius functions:

$a = -1.5\text{x}10^{-11}h_c^6 + 9.7\text{x}10^{-9}h_c^5 - 2.4\text{x}10^{-6}h_c^4 + 3.1\text{x}10^{-4}h_c^3 - 0.02h_c^2 + 1.3h_c + 38$
$a = -1.3\text{x}10^{-10}h_c^6 + 3.8\text{x}10^{-8}h_c^5 - 3.4\text{x}10^{-6}h_c^4 + 1.1\text{x}10^{-4}h_c^3 - 0.005h_c^2 + 0.95h_c + 140$
$a = -1.2\text{x}10^{-11}h_c^6 + 7.8\text{x}10^{-9}h_c^5 - 2.1\text{x}10^{-5}h_c^4 + 2.8\text{x}10^{-4}h_c^3 - 0.02h_c^2 + 1.8h_c + 23$
$a = -1.0\text{x}10^{-12}h_c^6 + 1.1\text{x}10^{-9}h_c^5 - 6.2\text{x}10^{-7}h_c^4 + 1.0\text{x}10^{-4}h_c^3 - 0.01h_c^2 + 0.8h_c + 25$

Figure E2. Tip contact radius function for the four cantilevers used in this study based on three regions (each zone is the average of 64 loading curves) which is valid for h = 10–100 nm.

E3. AFM data analysis

The Young's modulus of the corneocytes was calculated from the unloading curves using the Oliver-Pharr method [54]:

$$E = \frac{\sqrt{\pi}}{2}(1-\nu^2)\frac{S_0}{\sqrt{A}} \quad \text{(E9)}$$

where S_0 is the stiffness at the maximum force of the unloading curve, F_{max}, corresponding to the maximum indentation depth, h_{max} , and $A = \pi a^2$ is the contact area [144]. The Poisson's ratio for corneocytes, ν, was assumed to be 0.4, on the basis of the value for keratin [145]. The tip contact radius function, which was calibrated with PDMS (see Table E1 and Figure E2), was used to obtain a, given that, for an elastoplastic contact, the contact depth, h_c, is related to h_{max} by the expression [54]:

$$h_c = h_{max} - h_s \quad \text{(E10)}$$

where h_s is the surface elastic deflection at the perimeter of the contact, which is given by the following expression [54]:

$$h_s = \phi\frac{F_{max}}{S_0} \quad \text{(E11)}$$

The unloading stiffness, $S_0 = dF/dh$ was obtained by differentiating the following polynomial fit to the upper 80% the unloading curve with respect to *h*, and determining the slope at h_{max} [146]:

$$F = C_e h^2 - \left(2C_e h_f\right)h + C_e h_f^2 \quad \text{(E12)}$$

where C_e and h_f are fitting parameters. The geometric factor, ϕ, was assumed to be 0.73 for a conical indenter, following the work of Oliver and Pharr [147].

E4. Supplementary Figures

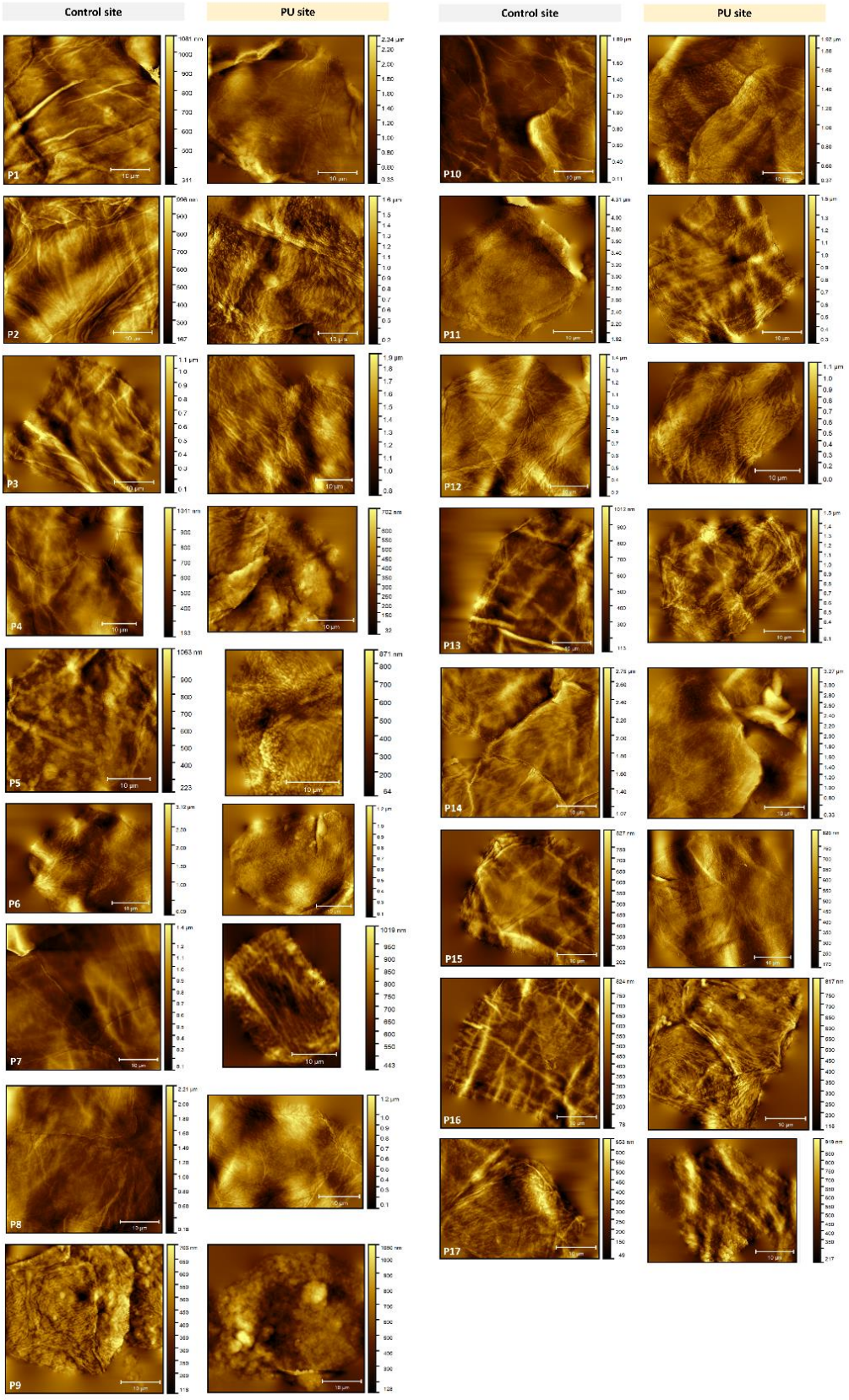

Figure E3. AFM analysis of superficial corneocytes revealed differences in the topography of superficial corneocytes at the site of category 1 pressure ulcers. At the control site, cells presented typical features of ridges, valleys, and peaks, with only a few patients (e.g., P6 and P17) showing CNOs at the cell surface. Cells at the PU site exhibit an abundance of CNOs (e.g., P5, P6, P10) or a deformed topography (P9, P16).

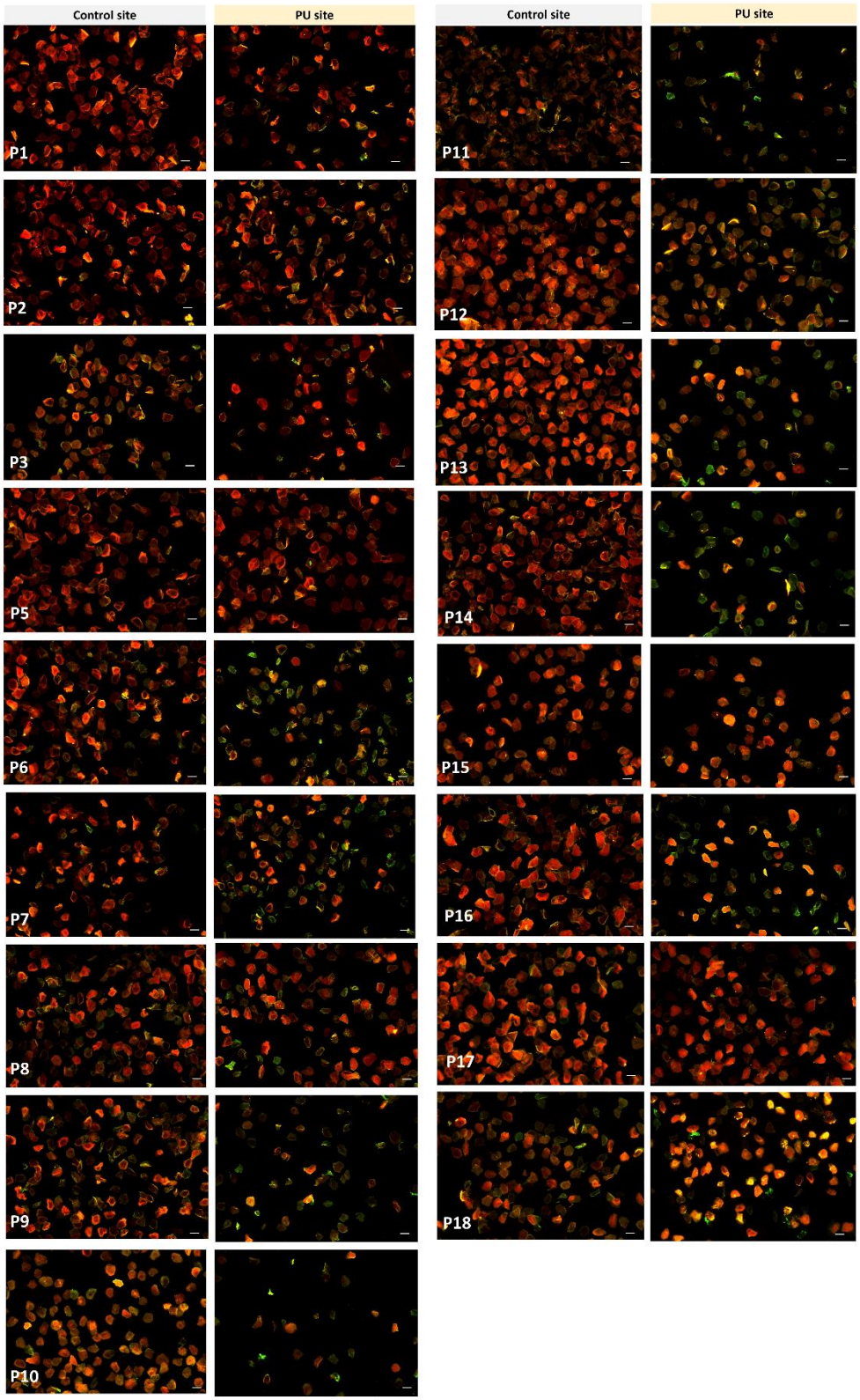

Figure E4. Imaging of the superficial CEs from the control and PU sites. Double staining: immunostaining against INV (green) and Nile red (red) against lipids to quantify the degree of CE maturation. The control site corneocytes stained strongly with Nile red, while PU corneocytes presented less lipids at the surface, staining green to INV. Scale bar = 50 µm.

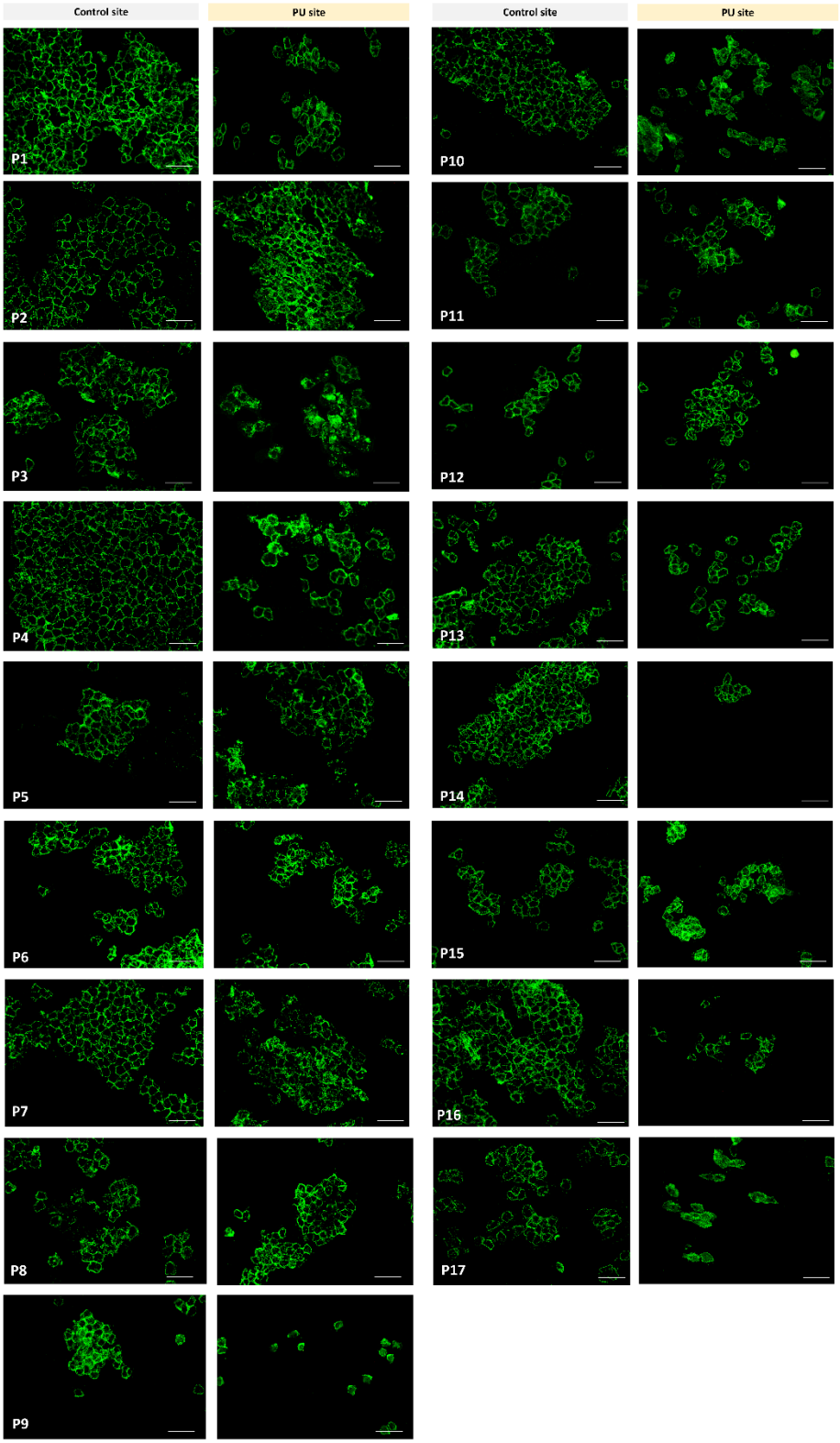

Figure E5. Distribution of Dsg1 at the surface of superficial corneocytes as an indirect measure of CDs. Most patients had a typical honeycomb structure with Dsg1 mostly exhibited at the cell periphery of the control site. The PU corneocytes sho

APPENDIX F

Chapter VIII Supplementary Information

F1. Introduction

The maturation of corneocytes is a complex process that involves enzymatic mechanisms that are capable of responding to external and internal stimuli [235]. As mentioned in Chapter V, over-hydration may have harmful effects on the SC. In fact, when moisture is a result of body waste products, namely urine and/or faeces, this could lead to the development of IAD [236]. Clinical manifestation of IAD ranges from excoriations, erythema to skin breakdown [237]. Urine is considered to be the main cause of IAD formation due to its ability to over-hydrate the skin, release harmful enzymes when interacting with stools, and decrease tissue tolerance to friction and pressure [238, 239, 240]. In particular, the concentration of ammonia in urine can shift the skin pH from acid to neutral or even alkaline levels. This causes a disruption of the skin acidic mantle, promoting bacterial colonisation and overgrowth, diminishing stratum corneum cohesion, and resulting in impaired skin barrier function [241, 242, 243]. However, the mechanisms leading to the loss of skin integrity associated with IAD are still not fully understood. Therefore, future research should investigate changes in skin health following the prolonged exposure to moisture and/or urine, as well as the effects of pH on physiology and mechanical properties of the SC. In this section, preliminary studies performed to investigate the effects of synthetic urine (S-urine) and pH in corneocyte maturation and mechanical properties are presented.

F.2 Methodology for the preliminary study of corneocyte properties following moisture and pressure insult

F2.1 Study protocol

This study was performed in collaboration with the University of Southampton. Nkemjika Abiakam was responsible for the study protocol and sample collection. Three separate sites (A, B, C) on the sacrum of each participant were marked using a non-permanent marker (Figure F1). To ensure clear differences between each test site, a 40 and 60 mm vertical and horizontal separation was maintained between sites. Sites A and B were exposed to the fabric T (incontinence nonwoven fabric provided by Essity AB, Gothenburg, Sweden) dry and 100% saturated with S-urine (pH 8), respectively. Site C represented the negative control skin site, which remained unchallenged throughout the test period. Samples of incontinence products were held in place via the use of strips of impermeable adhesive dressing (3M™ Tegaderm™, United Kingdom). The product was saturated with 15 mL of S-urine, formulated based on the composition and protocol as reported by Mayrovitz and colleagues [254]. The S-urine formulation was kept refrigerated at 4ºC and allowed to acclimatize to room temperature prior to each test session. The pH of the SU was monitored at each session using a pH meter (pH 213 Microprocessor pH Meter, HANNA Instruments, UK) to ensure consistency. S-urine was dispensed into the pads via serological pipettes until saturation was achieved, as observed by a small leakage of fluid from the pad samples. Each sample was left to equilibrate with the environment for 15 minutes to ensure equal distribution of the liquid within the product.

A standardised protocol, as summarised by the timeline in Figure F1b, was employed to challenge the skin of the participants. To review briefly, after 15 min of

acclimatization, the baseline values for each skin parameter (TEWL and SC hydration) were recorded at each test site. Subsequently, the sacral sites were exposed to samples of fabric T, in a dry or saturated state for 60 min. At the end of this period, the incontinence products were removed for a brief period in order to allow an intermediate skin measurement using biophysical and biomarker methods. This was followed by a further 60 minutes of skin exposure to incontinence products with the participants adopting a high sitting position (semi-Fowler's position). In this posture, participants were positioned on their back with the head and trunk raised to a 45 degrees bed angle, with the foot of the bed raised at the knee to flex the legs. At the end of the test period, equivalent to 120 min from the beginning of the test session, the individual samples were removed, and the skin of the participants blotted to remove an excess of fluid. The skin parameters were again assessed at each site. Participants were allowed a further 30 min of recovery prior to a final skin assessment. TEWL was assessed using an open-chamber method (Tewameter TM 300, Courage & Khazaka, Germany) and SC hydration was measured using a Corneometer (CM 825, Courage & Khazaka, Germany).

F2.2 Corneocyte maturation properties

Cells were collected at time points 0 and 150 (Figure F1) from three sacral sites (A, B and C) via the tape stripping (Sellotape, UK). Each tape strip was cut in half and used for the assessment of CE maturation and Dsg1 distribution. The level of CE maturity and Dsg1 were assessed by immunocytochemistry techniques and image analysis, as previously described in detail in Chapter VI.

F2.3 Statistical analysis

The skin parameters were imported into Microsoft Excel (Microsoft 365, USA) and normalised to the baseline values (i.e., post insult value/baseline value). Closer inspection of the collected data revealed their distribution was not normal in nature and, as such, non-parametric analyses were used. The Mann–Whitney U test was used to assess the independence of responses at the different specific time points of data collection. To investigate the relationship between barrier function and corneocyte properties the Spearman correlation analysis was employed. This was performed between corneocyte properties (sum of ranks for % INV+ and % Dsg1 at time points 0 ant 150 min) and rank-sum of the normalized skin biophysical parameters at site B (time point 60, 120 and 150 min). Tests were considered to be statistically significant at a 5% level ($p < 0.05$).

F.3 Results

Twelve healthy volunteers, four males and eight females with a Body Mass Index (BMI) ranging from 18.5-37.7 kg/m² were recruited for this study. Subjects' ages ranged from 32 to 62 years old, with a corresponding mean of 45.4 ± 10.6 years. The protocol followed in this study is shown in Figure F1.

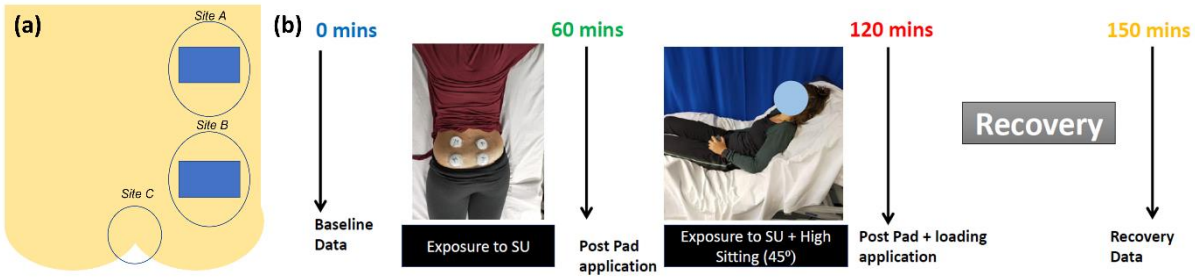

Figure F1. Effects of S-urine and load test protocol. **(a)** experimental test sites: A – Fabric T (dry), B – Fabric T saturated with S-urine (pH 8) and C – control site (no pad and no treatment) on the sacral region of each participant and **(b)** timescale of skin challenge and data collection. Corneocytes were collected at time 0 and at 150 min.

Briefly, the effects of S-urine and loading on corneocyte maturation properties were investigated in the sacral region when the skin was in contact with a fabric (Fabric T), which is the nonwoven layer of a commercial incontinence pad (Essity AB). Three test sites on the sacral region were investigated: A – Fabric T in the dry state, B – Fabric T saturated with S-urine (pH 8) and C – control site with no treatment and no pad. Corneocytes were collected via tape stripping at times 0 (baseline) and 150 min (after the recovery period) and the maturation properties were investigated as described in Chapter VI.

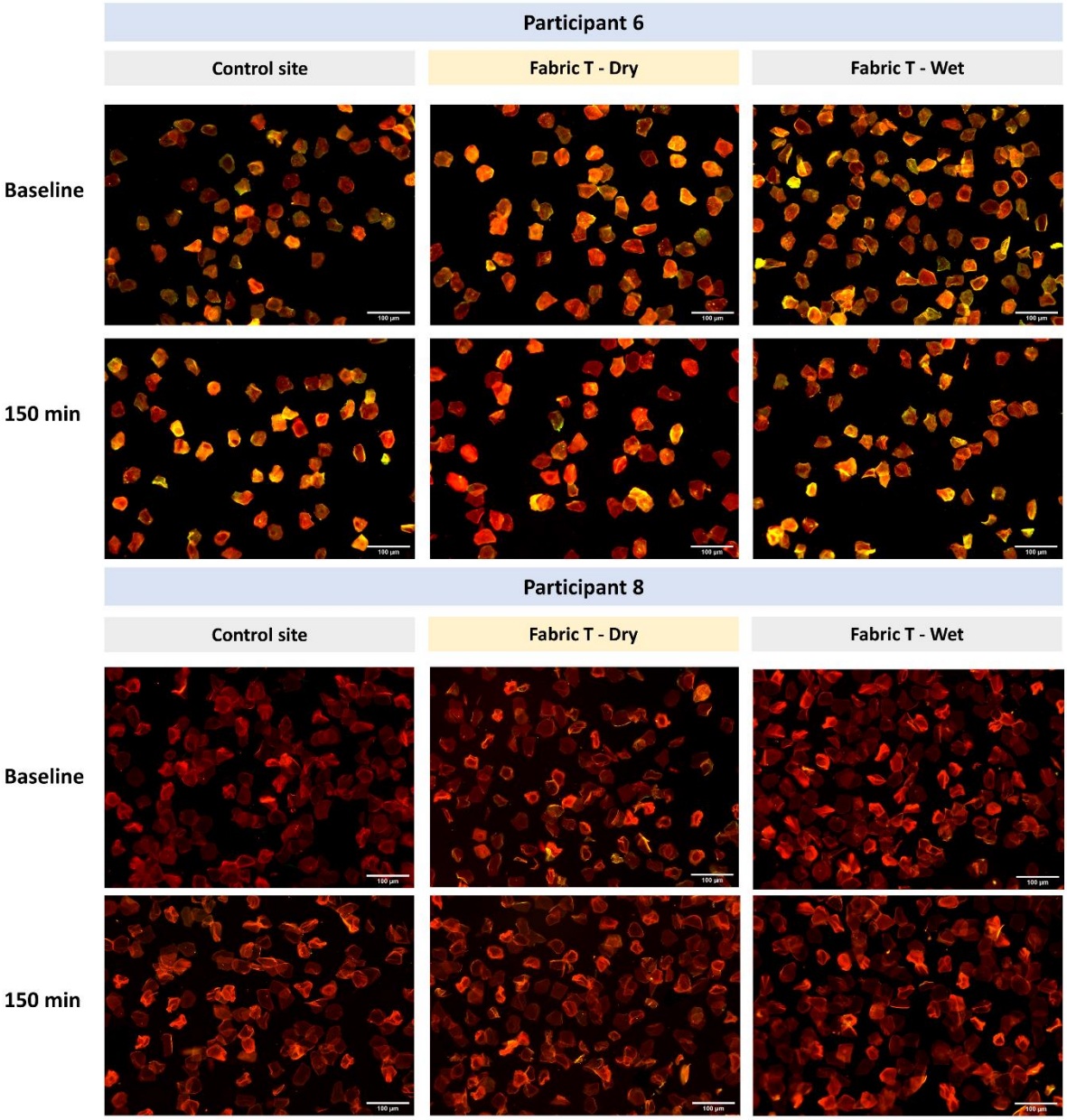

Figure F2. CE maturity levels in sacral corneocytes. Images of sacrum superficial CEs using double staining: immunostaining against INV (green) and Nile red (red) against lipids to quantify the degree of CE maturation. Participants 6 and 8 are presented as representative of low and high CE maturity. Similar levels of CE maturity were observed between baseline and time point 150 min (recovery). Scale bar = 100 µm.

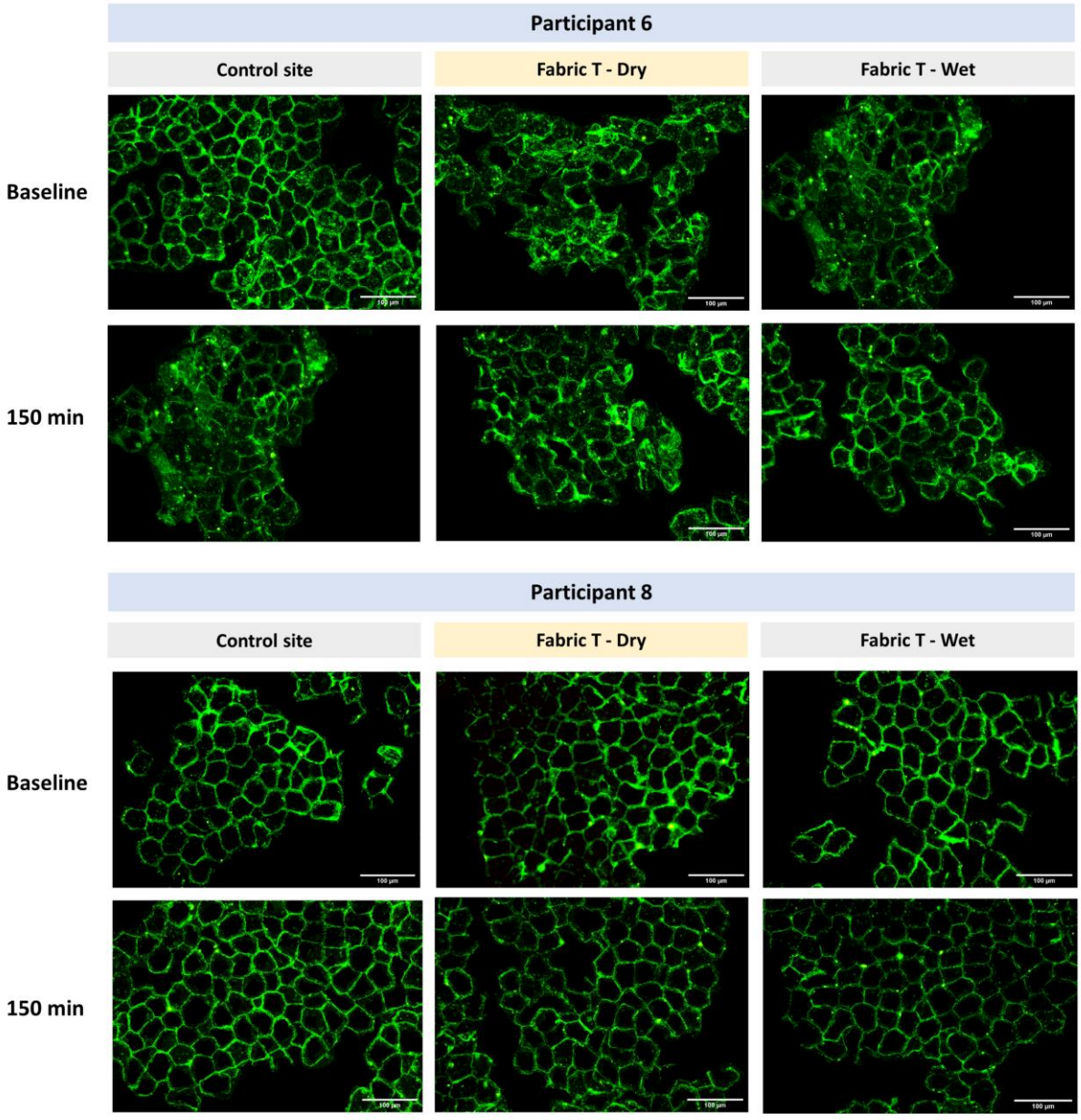

Figure F3. Level of Dsg1 in sacral corneocytes Distribution of Dsg1 at the surface of superficial corneocytes as an indirect measure of CDs for participant 6 and 8, representing high and low levels of Dsg1. Participant 6 presented ubiquitous distribution of Dsg1, while participant 8 presented the typical honeycomb pattern, hallmark of a mature SC and barrier function. Scale bar = 100 µm.

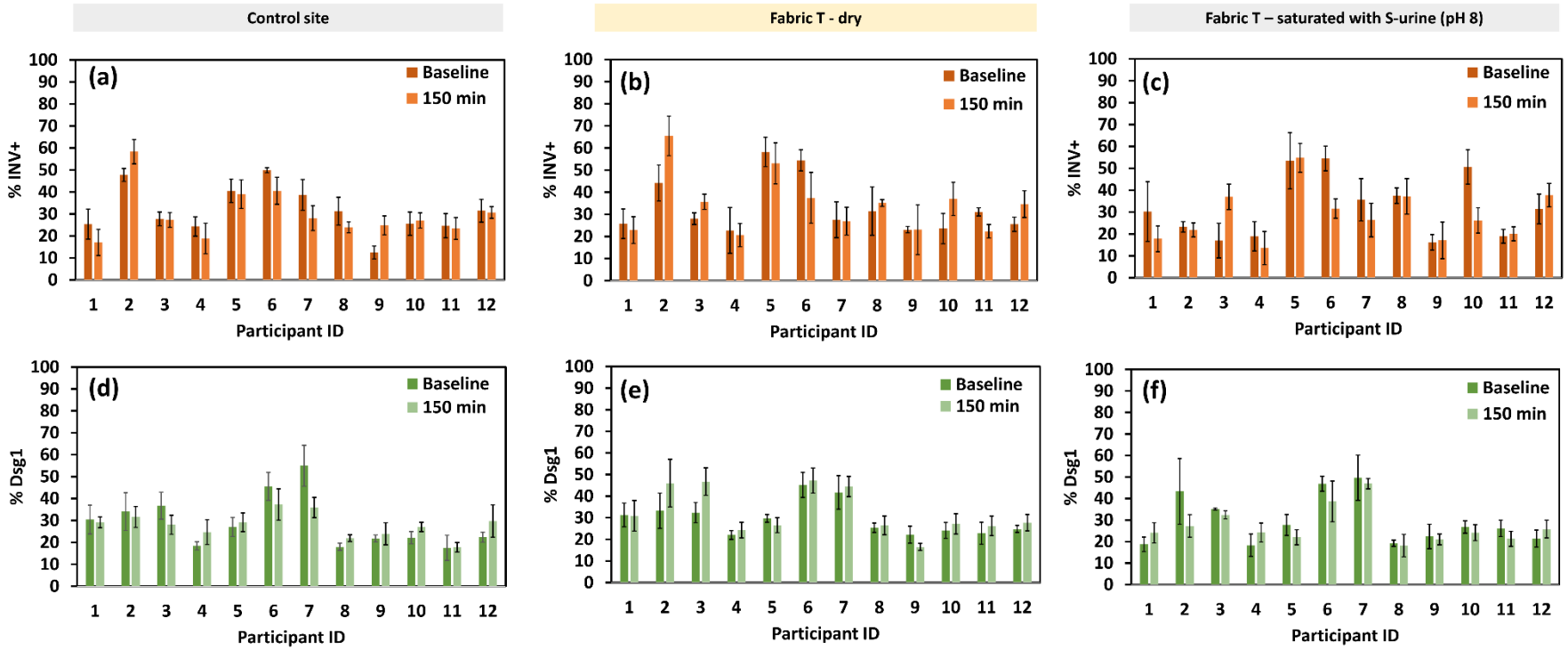

Figure F4. Individual data of corneocyte maturation properties. (a, b, and c) Levels of immature CEs (% INV+) and **(d, e, and f)** Dsg1 for each participant at three sacral sites (control site, fabric T in the dry state and fabric T saturated in s-urine pH 8) for time points 0 (baseline) and 150 min (recovery).

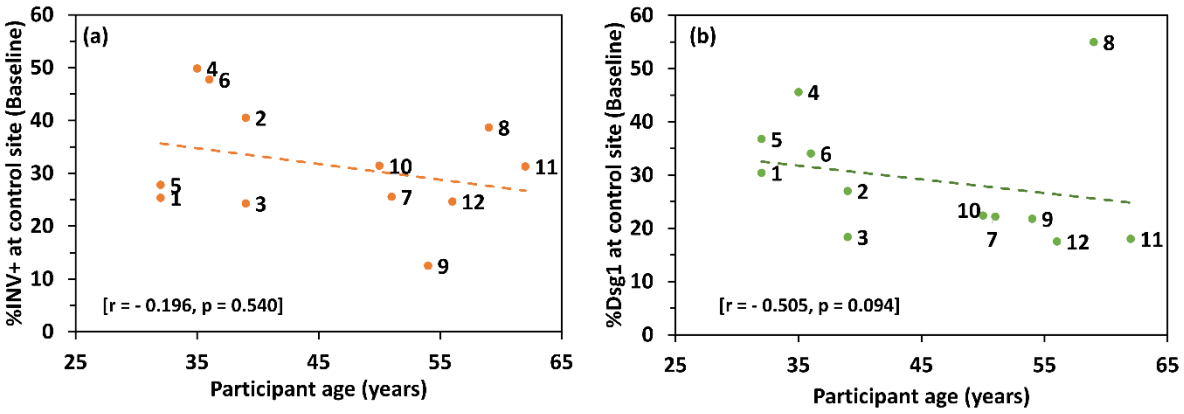

Figure F5. Spearman correlation analysis between corneocyte maturation properties and participant age. Older participants (age > 45 years) tended to present lower levels of immature CEs **(a)** and Dsg1 **(b)**, although these trends were not statistically significant.

The levels of immature CEs and Dsg1 were evaluated in the three test sites and revealed inter-subject variability (Figure F3). Absolute values of immature CEs ranged between 13% (P4 at site B) and 58% (P2 at control site) and levels of Dsg1 ranged between 17% (P11 at control site) and 47% (P6 at site A). Representative images for high and low levels of INV+ CEs and Dsg1 for participants P6 and P8 can be found in Figure F1 and F2. Consistent temporal trends were not observed at any of the sites. As mentioned on Chapter V, moisture is known to regulate the processes of CE maturation and degradation of corneodesmosomes [91, 213]. However, these processes are relatively slow (several days) compared to the time periods used in this protocol [213], which may explain why no effects of overhydration were observed. Additionally, weak trends were found with age, i.e., older individuals presenting greater levels of Dsg1 and immature CEs (Figure F5).

In a previous study by Abiakam et al. (not published), biophysical markers, namely TEWL and SC hydration, were measured at all the time points presented in Figure F1.

The greatest changes were observed for fabric T saturated with S-urine at both 60 and 120 min (2–5.7 ratio change in TEWL and 1.5–2 ratio change in SC hydration). To understand the role of corneocytes in skin health, a correlational analysis was employed between their properties and the biophysical parameters (Figure F6). The ranks of % INV+ and % Dsg1 were taken for time points 0 and 150 min, summed, and plotted against the sum of ranks of normalized TEWL and SC hydration values (for 60, 120 and 150 min). The correlational analysis showed similar trends for both maturation hallmarks, i.e., high levels of mature CEs and Dsg1, tended to correlate with high TEWL and SC hydration following mechanical and moisture insult.

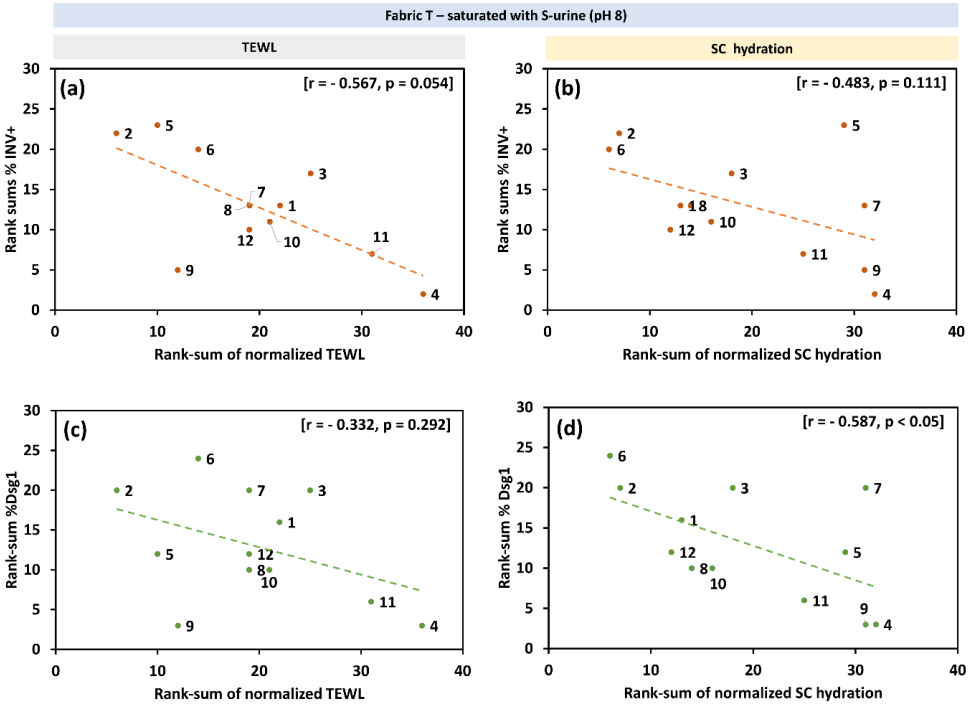

Figure F6. Correlations between the skin response to insults and corneocyte properties. The skin response was measured as TEWL and SC hydration following overhydration with S-urine and pressure at time points 60-, 120- and 150-min (normalized to baseline – time point 0-min) and plotted against the rank sum for % INV+ and % Dsg1 for time points 0- and 150-min.

F.3 Discussion

These findings are consistent with the weak trends found in a previous study on the effects of respirator application in healthcare workers during the COVID19 pandemic (Chapter VI). A strong lateral attachment between superficial mature corneocytes may be disadvantageous when the SC is subject to mechanical insults, as the exposed cells, which are not attached to lower SC layers, may be easily detached from the surface of the skin. This may be exacerbated due to cell swelling provoked by moisture, which, in combination with friction, may facilitate the detachment of upper SC layers. This reinforces the hypothesis of a dichotomy in the role of SC maturation. Although extremely important in ensuring barrier function, i.e., healthy looking and hydrated skin, a mature SC, as characterized in non-glabrous skin, may be disadvantageous when subjected to mechanical insults. In fact, plantar and palmar SC, while not being characterized by the typical hallmarks of a mature SC, are well equipped to deal with mechanical stresses, for example, by presenting high amounts of corneodesmosomes, and so assuring strong adhesion between SC cells.

Future research should focus on the differences between palmoplantar and non-palmoplantar skin to better comprehend how the mechanical resistance of skin can be maintained. In fact, this may open new opportunities not just in the prediction or diagnosis of early skin damage using superficial skin cells, but also in the treatment of pressure ulcers through grafting of autologous palmoplantar skin [244].

APPENDIX G

Chapter VIII Supplementary Information – Effect of urea and pH on corneocyte properties

G1. Introduction

Prolonged hydration influences the permeability and mechanical properties of skin [191, 213], with the disruption of the lipid structure and degradation of corneodesmosomes [213]. Permeation of certain compounds may be enhanced by the effects of structural changes to the lipid lamellae, since SC lipids constitute the primary permeability barrier. The cohesion of the SC is usually related to the degree of attachment between the corneocytes [125]. In fact, corneocytes that are deep in the SC are firmly attached, constituting a more cohesive sublayer, than those at the surface [85]. The progressive degradation of these structures is a well-controlled process (regulated, e.g., by pH and hydration) and is a requirement of efficient desquamation. Moreover, urea, a component of the natural moisturizing factor of the skin, plays an important role in the preservation of skin hydration and integrity [245]. As such, an *ex vivo* maturation assay as presented by Guneri et al. [189], was aimed at understanding the influence of the exposure time of moisture and urea (the main component of urine) on the maturation properties of corneocytes.

G2. Methodology for the study of the effect of S-urine in the ex vivo maturation of volar forearm corneocytes

A schematic of the protocol followed to obtain these preliminary results is presented in Figure G1. Briefly, corneocytes were collected via tape stripping from three healthy young participants and two anatomical sites (forearm and cheek). Cells were incubated in different conditions at 70% RH and 37 °C for 1 h. The different test conditions were control (no treatment), incubation in 1 × PBS, 5% urea and 20% urea (aqueous solutions w/v). After 1 h, the excess solutions were discarded and the tapes were maintained at 70% RH and 37 °C for 72 h, being allowed to mature under *ex vivo* conditions.

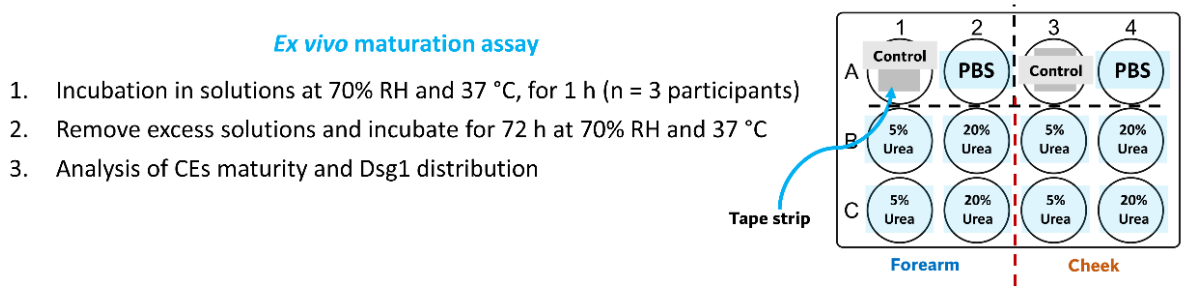

Figure G1. *Ex vivo* maturation assay protocol. Volar forearm and cheek corneocytes were tape stripped from three healthy young participants. Tape strips were incubated for 1 h at 70% RH and 37 °C in different conditions: control (no treatment), in PBS buffer, and in 5 and 20% urea aqueous solutions (w/w). Excess solutions were discarded after one hour, and ex vivo maturation was performed for 72 h at 70% RH and 37 °C. Following this period, tape strips were processed for the analysis of CE maturity and Dsg1 levels as described in Chapter VI.

G3 Effect of urea on the *ex vivo* maturation of corneocytes

Following the incubation periods, samples were processed for analysis of the levels of immature CEs and Dsg1, as previously described in a detailed manner in Chapter VI. Figure G2 presents representative images of %INV+ and %Dsg1 for participant 1 (P1) and individual data is presented in Figure G3.

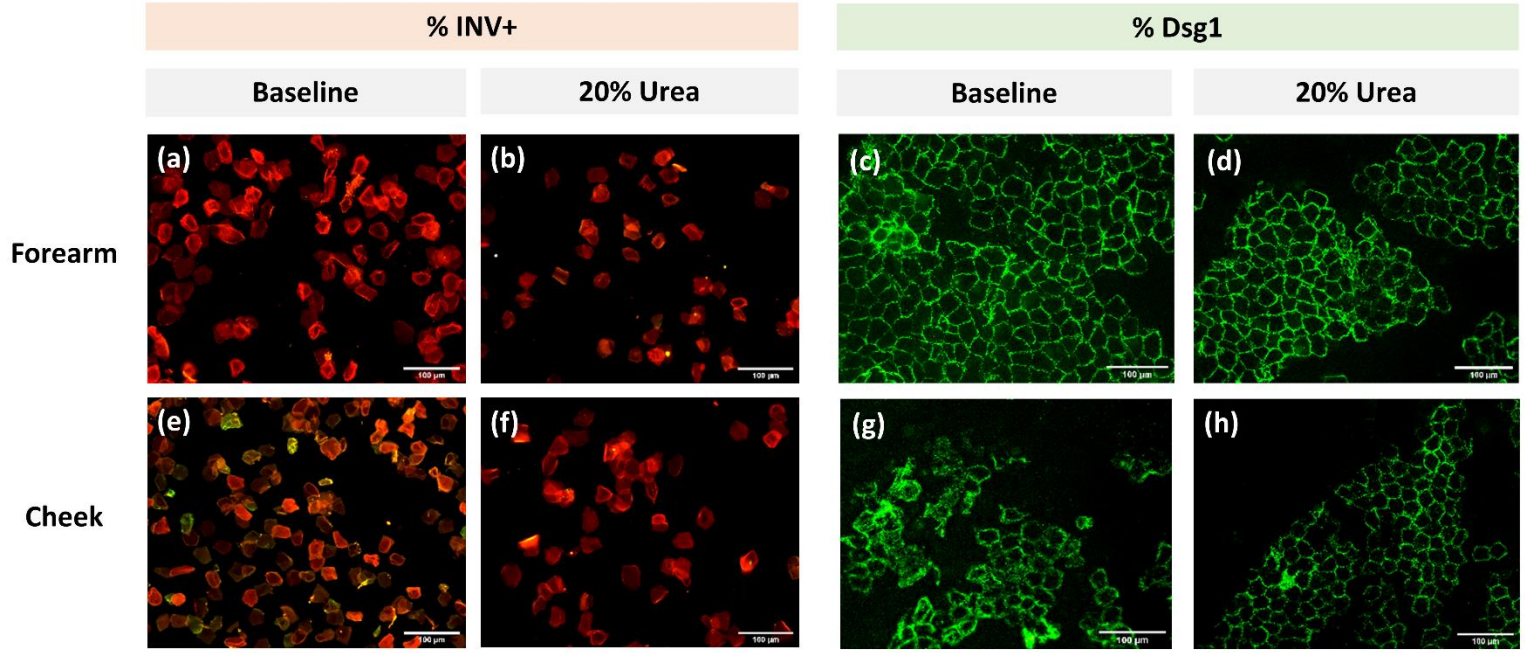

Figure G2. Ex vivo maturation assay. Volar forearm and cheek corneocytes were incubated with 20% urea aqueous solution for 1 h and allowed to mature for 72 h for participant 1. **(a-d)** Ex vivo maturation had small effects on forearm cells. However, cheek corneocytes suffered maturation when exposed to 20% urea, with an increase in mature CEs **(e and f)** and an apparent decrease in Dsg1 signal **(g and h)**.

Although no apparent effect of PBS or urea solutions was found for the level of immature CEs for P1 at the forearm (Figure G2), P2 and P3 presented a decrease in %INV+ when incubated with 5 and 20% urea solutions (Figure G3). Interestingly, no apparent effect of either PBS of urea solutions on the levels of Dsg1 was found at the forearm (Figure G2 and G3). Moreover, the effect of urea was clear on cheek cells, with an increase of > 50% in cell maturity for all participants, while the effect on Dsg1 levels was not so clear (Figure G3).

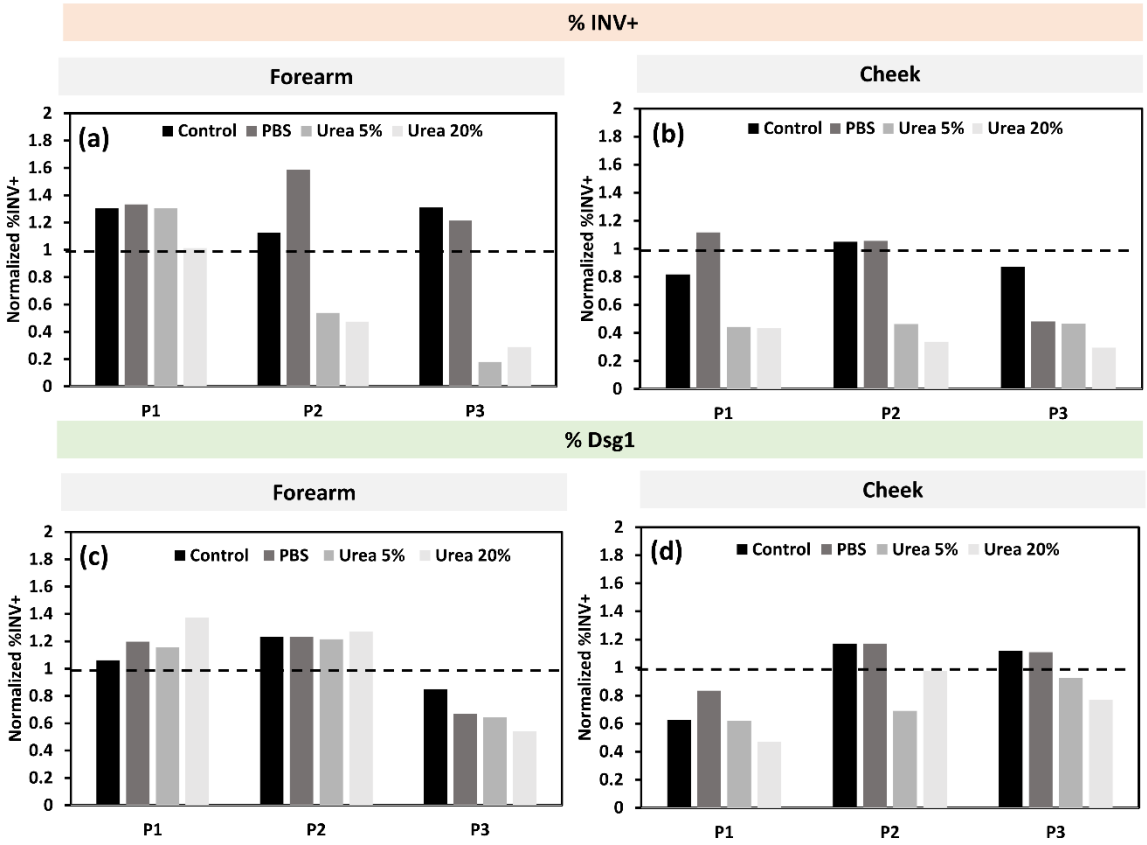

Figure G3. Individual data of ex vivo maturation assay after exposure to urea. (a) There was a decrease in immature CEs for participants 2 and 3 (P2 and P3) after incubation with 5 and 20% urea at the forearm, and **(b)** for all participants at the cheek. **(c)** No apparent effects were observed on the level of Dsg1 at the forearm. **(d)** Although there are indications of the effect of 5% and 20% urea on Dsg1 signal at the cheek, further studies are required to confirm these trends.

Urea is usually used in personal and dermatological products as a skin moisturizer (at lower doses ≤10%), and as a keratolytic factor, for higher concentrations (>10% urea) [245, 246]. In fact, the effects registered in these preliminary results shows that both 5 and 20% urea solutions act in promoting the CE maturation, while not having a strong role in CD degradation (Figure G3). This may be due to a direct effect of urea on enzyme activity (transglutaminase), as previously observed for the *ex vivo* maturation of cheek corneocytes following cells incubation with 5% glycerol [189]. The absence of abnormal corneocyte shape after incubation with 20% urea shows that, in these conditions, the keratolytic effect of urea may be minimal.

This preliminary study was limited by the number of participants, as well the type of incubation performed, i.e., excess solution was discarded after 1 h incubation, but there was no post-incubation washing step. This was done to avoid washing away any intracellular urea. However, as a result crystal residues of urea could not be avoided and may interfere with the maturation of cells, while not simulating real-life conditions. Future research should also investigate the effects of concentrations or urea > 20% on the mechanical properties of corneocytes. In fact, the keratolytic effect of this compound, is thought to be related to its denaturing action on the keratin filaments [247]. Although the effects of over-hydration in the case of IAD may mask any effect of urea on SC structure and maturation, understanding the role of individual factors (such as urea) on corneocyte properties can assist in developing a more comprehensive understanding of the interactions that occur at the interface of the insult.

G4 Effect of pH on the mechanical properties of corneocytes

One of the mechanisms thought to be involved in the loss of SC integrity in IAD is related to pH, which has been observed to be increased in the skin following exposure to S-urine [248]. The increase in pH of urine and/or microclimate in IAD is thought to be related to an increase in ammonia, as a product of the degradation of urea by certain microorganisms. In fact, urease-producing bacteria have been recently observed to be increased in IAD patients [249]. Moreover, bacteria invasion of damaged rat epidermis was observed to induce IAD [243]. This is exciting research in the field of IAD that helps unveil the role of pH in skin integrity loss. However, the specific mechanism of the action of pH on skin physiology, and particularly of the SC barrier function and integrity is still not fully understood. Apart from playing a role in controlling bacteria colonization and enzyme activity [250], the pH might have a direct effect on the mechanics of the SC.

This section presents the preliminary results on the effects of pH on the mechanical properties of corneocytes. As described in Chapter III, AFM force spectroscopy was used as a nanoindentation tool to study the stiffness of corneocytes. Sacral corneocytes collected from a single participant were immersed in varying pH solutions of S-urine and buffers: S-urine pH 5, 7 and 9, citrate buffer (pH 5), PBS buffer (pH 7) and Trizma buffer (pH 9). Analysis of AFM force curves was performed as described in Chapter III, using the Oliver-Pharr analysis to calculate the Young's modulus of the cells.

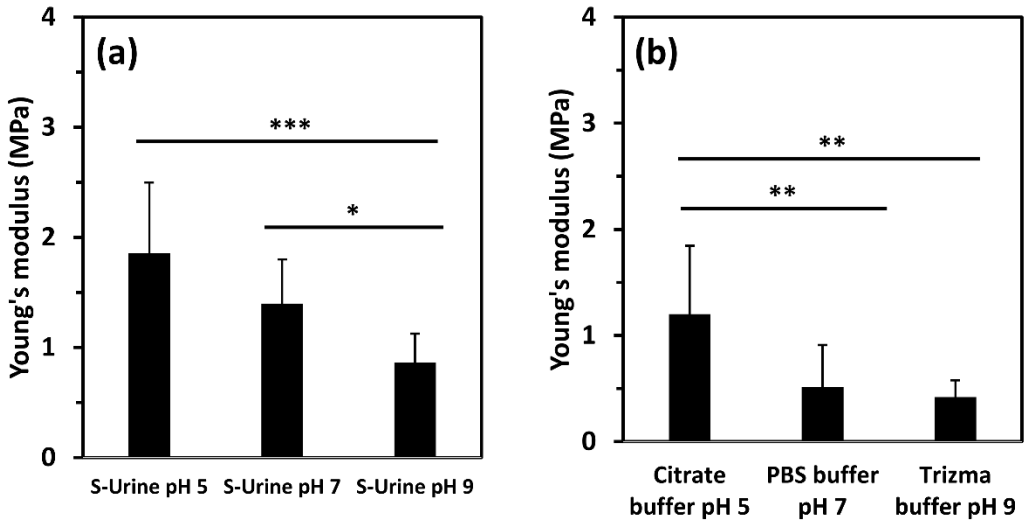

Figure G4. Effect of pH on the Young's modulus of sacral corneocytes. (a) Corneocytes immersed in S-urine solutions **(b)** in different buffer solutions. One-way ANOVA was performed to calculate differences between pH conditions. n = 5 cells and a single healthy participant. *p< 0.05, **< 0.01 and ***p< 0.001

Both S-urine and buffer solutions induced a decrease in the Young's modulus of single corneocytes with increasing pH (Figure G4). Previously, varying the pH was observed to change the protonation and deprotonation ratio in amino acid side chains of keratin in hair, which in turn affected the ratio of salt bridges and hydrogen bonds, and protein solvation [251]. These affected the thermal properties, water sorption and dry tensile properties. A decrease in SC stiffness may result in losing its ability to withstand pressure, so that the viable layers of the epidermis and subsequent lower layers may be vulnerable to higher stresses and strains.

G5. Conclusion

These preliminary studies provide insights into the effects of urine and pH on corneocytes, crucial for maintaining skin barrier function. High levels of mature corneocytes and Dsg1 were found to correlate with increased TEWL and SC hydration after moisture and mechanical insults, suggesting their susceptibility to detachment

under stress. Urea, a urine component, was found to promote corneocyte maturation without significant CD degradation. Additionally, both urine and buffer solutions decreased the Young's modulus of immersed corneocytes as the pH increased. These findings highlight the importance of understanding how external factors interact with corneocyte properties to maintain skin health and improve interventions for conditions like IAD. Further research including the study of prolonged exposure to moisture/urine and pH is needed to enhance our knowledge and clinical management of skin damage and pressure ulcers.